T 177

50500

STUDIES ON THE INTERACTION OF METAL AND SEMICONDUCTOR NANOPARTICLES WITH POLYMERS

A thesis submitted in partial fulfillment of the
requirements for the degree of
Doctor of Philosophy

by

Anamika Dutta, M.Sc.

Registration no. 069 of 2003

Department of Chemical Sciences
School of Science and Technology
Tezpur University
Napaam, Tezpur-784028
Assam, India

April, 2011

This thesis is dedicated to,
My parents,
My husband, sister, brothers,
and
My extended family,
For their love, support and encouragements

STUDIES ON THE INTERACTION OF METAL AND SEMICONDUCTOR NANOPARTICLES WITH POLYMERS

Abstract

The present thesis deals with synthesis and characterization of metal (copper and nickel) and semiconductor (cadmium sulphide and copper sulphide) nanoparticles using simple chemical synthesis route. Considerable efforts have been devoted to the synthesis of polyaniline based nanocomposites using the synthesized metal and semiconductor nanoparticles. The thesis also provides an account of optical and electrical behaviour of polyaniline based metal and semiconductor nanocomposites. The contents of the thesis have been compiled into five chapters.

Chapter1 contains a general introduction to nanoscience and technology. The two strategies top-down and bottom-up are briefly introduced followed by uniqueness of nanoparticles, their classification and colloidal synthesis route for their preparation. The role of capping agent to achieve stable colloidal dispersion is also described. A general overview of the nanocomposite materials specially based on conducting polymers is also given in this part. The general synthetic methods for the preparation of metal nanoparticles/conducting polymers and semiconductor nanoparticles/conducting polymers nanocomposite are also described.

Chapter 2 is related to the synthesis, characterization and properties evaluation of copper (Cu) and nickel (Ni) nanoparticles and their corresponding composites with polyaniline (PANI). Stable colloidal dispersion of Cu and Ni nanostructures are achieved by simple, economic and environmentally benign chemical synthesis route. Tannic acid (TA), a biomolecule is used as reducing as well as capping agent for synthesis of metal nanoparticles in ethylene glycol medium. The factors affecting the morphology of metal nanostructures are discussed thoroughly. The synthesized Ni and Cu nanoparticles are characterized using different techniques. A time delay study is performed to observe any morphological changes of nanostructures. *In-situ* polymerization technique is employed to get nanocomposites based on PANI and metal nanoparticles. Depending upon the nature of metal nanoprticles incorporated, nanocomposites show different morphologies and properties. A comparative study of optical and conductivity behaviour of pure PANI and nanocomposites based on PANI and metal nanoparticles has been discussed in detail.

Chapter 3 deals with the synthesis, characterization and property evaluation of cadmium sulphide (CdS) nanostructures and their composites with PANI. Stable colloidal dispersion of CdS nanoparticles is synthesized by employing cadmium acetate dihydrate as the cadmium source and sodium thiosulphate as the sulphur source. 3-mercaptopropionic acid (MPA) has been used as stabilizing agents in the synthesis process. Controlling the reaction parameters, the size and shapes of CdS nanoparticles can be tailored from simple *1-D* structure to *3-D* architecture and hence, their properties. A series of CdS/PANI nanocomposites based on different types of CdS nanostructures have been synthesized using *in-situ* polymerization technique and characterized using different techniques. It has been found that morphologies of the resultant composites depend upon the shape and size of the CdS nanoparticles incorporated and hence, optical and conductivity behaviour of the composites.

Chapter 4 describes the synthesis, characterization and properties evaluation of copper sulphide (CuS) nanoparticles and their composites with PANI. CuS nanoparticles are synthesized by employing copper acetate monohydrate as the copper source and thiourea as the sulphur source. Sodium dodecyl sulfate (SDS), poly(N-vinyl-2-pyrrolidone) (PVP) and Na-AOT were used as stabilizing agents in the synthesis process. The influence of thiourea concentration on conversion of golden brown copper sulphide sol to green form is also studied. The factors affecting the stability of the dispersion have also been investigated. CuS/PANI nanocomposites have been synthesized and characterized. The optical and electrical properties of the synthesized composites are investigated.

Chapter 5 outlines the concluding remarks, highlights of the findings followed by future scopes of the present investigation. It is concluded that inorganic-organic nanocomposite, which could merge the best properties of conducting PANI and metal or semiconductor nanoparticles such as Cu, Ni, CdS and CuS can be utilized as a new functional material. Controlling the size and shape of nanoparticles, the morphology and the properties of the nanocomposite can be tailored.

DECLARATION BY THE CANDIDATE

The thesis entitled "***Studies on the interaction of metal and semiconductor nanoparticles with polymers***" is being submitted to the Tezpur University in partial fulfillment for the award of the degree of Doctor of Philosophy in the Department of ***Chemical Sciences*** is a record of bonafide research work accomplished by me under the supervision of ***Prof. S. K. Dolui.***

All helps received from various sources have been duly acknowledged.

No part of this thesis has been submitted elsewhere for award of any other degree.

Anamika Dutta

Date: 12-04-2011

Place: Tezpur

Anamika Dutta

Department of Chemical Sciences
Tezpur University
Assam, India

TEZPUR UNIVERSITY
(A Central University by an Act of Parliament)
Napaam, Tezpur-784028
DISTRICT: SONITPUR:: ASSAM:: INDIA

Ph: 03712-267004(O) 9957198489 (M) Fax: 03712-267006 *Email : dolui@tezu.ernet.in*

CERTIFICATE OF THE PRINCIPAL SUPERVISOR

This is to certify that the thesis entitled "***Studies on the interaction of metal and semiconductor nanoparticles with polymers***" submitted to the School of ***Science and Technology***, Tezpur University in partial fulfillment for the award of the degree of Doctor of Philosophy in the ***Department of Chemical Sciences*** is a record of research work carried out by ***Anamika Dutta*** under my supervision and guidance.

All help received by him from various sources have been duly acknowledged.

No part of this thesis has been submitted elsewhere for award of any other degree.

Date: 12.4.11
Place: Tezpur

S. K. Dolui
Professor
Department of Chemical Sciences
School of Science and Technology
Tezpur University
Assam, India

TEZPUR UNIVERSITY
(A Central University by an Act of Parliament)
Napaam, Tezpur-784028
DISTRICT: SONITPUR:: ASSAM:: INDIA

Ph: 03712-267004(O) 9957198489 (M) Fax: 03712-267006 *Email : adm@tezu.ernet.in*

Certificate of the External Examiner and ODEC

This is to certify that the thesis entitled "**Studies on the interaction of metal and semiconductor nanoparticles with polymers**" submitted by **Anamika Dutta** to Tezpur University in the **Department of Chemical Sciences** under the school of **Science and Technology** in partial fulfillment of the requirement for the award of the degree of Doctor of Philosophy in **Chemical Sciences** has been examined by us on ____________________ and found to be satisfactory.

Signature of:

Principal Supervisor ***External Examiner***

Associate Supervisor

Co-Supervisor

Date:

Preface

The ability to tailor the physical properties in a controlled manner by adjusting only size and shape is a core feature of nanoscience, and it makes nanomaterials attractive for potential applications as building blocks for various nanodevices and nanosystems. However, most explorations of nano-based materials in practical applications require the metastable nanoparticles to be stabilized in an appropriate matrix with retention of their initial unique properties, where aggregation and agglomeration should be suppressed. Compared with inorganic materials, polymeric materials have allured considerable attention in recent years due to their relatively low cost, architectural flexibility and simple fabrication process. Based on the excellent concomitant properties of polymer materials, incorporation of metal and semiconductor nanoparticles into the polymer allows improved processability and stability of the nanomaterials for applications in various device systems. Compatibility between the nanoparticles and polymer matrix is important in this regard and hence studies on interaction between nanoparticles and polymer is of exigent importance.

Conducting polymer based nanocomposites represent a new concept in the development of systems exhibiting functional properties resulting from the synergistic interaction between the disperse phase and the matrix. Many properties of conducting polymers like non-corrosiveness, light weight, mechanical strength, and the possibility to tune electrical conductivity and dielectric behavior can be utilized along with luminescence properties of metal and semiconductor nanoparticles to make multifunctional structures. Polyaniline, being a conducting polymer possessing all the aforementioned characteristics is a suitable material for the development of nano-based device. The present thesis deals with synthesis and characterization of metal and semiconductor nanoparticles and their corresponding composites with polyaniline. The thesis also provides an account of optical and electrical properties of synthesized nanocomposites. We hope that this study contributes a little knowledge to the rapidly advancing field of conducting polymer based nanocomposites and also opens up the possibilities of further research on the subject.

This research was carried out in the Department of Chemical Sciences, Tezpur University with financial assistance from the Department of Science and Technology, Govt. of India (Grant No. SR/S1/PC-40/2004).

Anamika Dutta

ACKNOWLEDGEMENT

This PhD thesis is simply the fruit of a few years of ardent learning and research experience. The words in these pages is not just words but each word acknowledges my deep gratitude to all those who played a pivotal role during my PhD years and without whom this thesis would not have been possible.

At first, I would like to thank to almighty for giving me encouragement to complete this step.

With the deepest sense of gratitude, I would like to express my sincerest thanks to my research supervisor, Prof. Swapan Kr. Dolui for his unwavering support and guidance throughout the years. He is not only a great teacher with deep vision but also and most importantly a kind person. I am most indebted to him for exposing me to this exciting and interesting field of research. His tireless enthusiasm was always a source of motivation and inspiration throughout my work. Words are not enough to thank him for all the concern he has shown, and all the support he has rendered to ensure my personal well-being.

I take this opportunity to express my sincere thanks to the Head, Department of Chemical Sciences, for giving me the opportunity to work in this department and making all the facilities available for my research work. With a deep sense of gratitude, I would like to thank the faculty members of the Department of Chemical Sciences for their help and instruction in my academic study as well as my professional career.

I would also like to thank Jose and Anjali, NEHU, Shilong and Len, UCC for TEM images; NEIST, Jorhat for FTIR spectra; Benjamin, UCC, for TGA; Peter, UCC for XPS analysis.

I am particularly thankful to technical staff, for arranging instrumental and laboratory facilities throughout the study. Special thanks also go to office staff, Chemical Sciences Department. They are always there for the students.

I cannot express enough my gratitude to my fellow research scholars from my lab, Jatin, Binod, Lakhya, Muhsina, Surajit, Isha, and Amar for being always available when I needed their help, their stimulating suggestions and encouragement helped me in all the time of research and completion of this thesis. Thank you very much for being my wonderful friend.

I had the good fortune of having so many people here at Tezpur University. I had my share *of fun in interacting with each of them academically as well as otherwise. Today I fondly remember them and it is only practical that I do not attempt to put their names here, as the list is exceedingly long. There are some people whom I know for a period that is a little more than a decade, and some others whom I met more recently. They are all amazing people and are very dear to me. I thank them all for being with me through thick and thin.*

I gratefully acknowledged Mrs. Sutapa Dolui and Swapnil for their constant encouragement, hospitality and warmth.

I am thankful to library staff and administrative staff of TU for cooperation and DST for financial support in the form Junior Research Fellowship (Grant No. SR/S1/PC-40/2004).

Most importantly, I feel deepest sense of gratitude to my Mother Runu Dutta, my late father Haresh Dutta, uncle Bijoy, my aunt Devabala, Utpala, late Manjula, Nirmala,, Mamata, my Aita, my all Mahi, and Mama who embody all that is best in humanity by their selflessness, dedication and integrity. Indeed my doctoral thesis is the dream of my mother. The deepest thanks from the bottom of my heart should be dedicated to my brothers Arunav, Kaushik, Anirban, Anurag and especially to my sister, Mandakini who had always given me the moral support and time when I needed the most. Words fail me in expressing my sincere thanks to her. I am deeply indebted to my mother-in-law Renu Borah, my sister-in-laws Ruli,,Rubi and Rumi and brother-in-law, Jitu, for all the freedom and moral support they have given to my choice of career and life style.

Last but not the least; I am grateful to my husband Dipu without whose emotional support and dedication, this would never been possible. He is the person who was on my side with tremendous perseverance at each and every difficult stage during this work and I thank you Dipu for all the patience.

Anamika Dutta

Contents

Chapter 4: Synthesis of Copper Sulphide (CuS) Nanoparticles and Their Interaction with Polyaniline (PANI) 149-193

List of Publications

List of Tables

Chapter 1:

Chapter 2:

Chapter 3:

Chapter 4:

List of Figures

Chapter 1:

Chapter 2:

Chapter 3:

Chapter 4:

List of Schemes

Chapter 1:

Chapter 2:

Chapter 3:

Chapter 4:

Abbreviations and acronyms	**Meanings**
acac:	Acetylacetonate
AFM:	Atomic force microscope
^{o}C:	Degree centigrade
ca.:	Calculated
CdAc:	Cadmium acetate dihydrate $(Cd(CH_3COO)_2).2H_2O$
CdS:	Cadmium sulphide
CdS-1:	Cadmium sulphide synthesised with CdAc: STS: MPA molar ratio of 1: 1: 6
CdS-2:	Cadmium sulphide synthesised with CdAc: STS: MPA molar ratio of 1: 2: 2
CdS-3:	Cadmium sulphide synthesised with CdAc: STS: MPA molar ratio of 1: 3: 4
CdSe:	Cadmium selenide
CdS/PANI:	Cadmium sulphide/polyaniline
CdS-1/PANI:	Cadmium sulphide (CdAc: STS: MPA = 1: 1: 6)/polyaniline
CdS-2/PANI:	Cadmium sulphide (CdAc: STS: MPA = 1: 2: 2)/polyaniline
CdS-3/PANI:	Cadmium sulphide (CdAc: STS: MPA = 1: 3: 4)/polyaniline
CdTe:	Cadmium telluride
cm^{-1}:	Per centimetre
CMC:	Critical micelle concentration
^{o}C/min:	Degree centigrade/minute
CNT:	Carbon nanotube
CP:	Conducting polymer
CPS:	Counts per second
Cu:	Copper
Cu-2:	Copper nanoparticles synthesised with 0.02 M TA

Cu-4:	Copper nanoparticles synthesised with 0.04 M TA
Cu-6:	Copper nanoparticles synthesised with 0.06 M TA
CuAc:	Copper acetate monohydrate $(Cu(CH_3COO)_2)$. H_2O
Cu/PANI:	Copper nanoparticles/polyaniline
Cu-2/PANI:	Copper nanoparticles (synthesised with 0.02 M TA)/polyaniline
Cu-4/PANI:	Copper nanoparticles (synthesised with 0.04 M TA)/polyaniline
Cu-6/PANI:	Copper nanoparticles (synthesised with 0.06 M TA)/polyaniline
CuS:	Cupric sulphide or copper monosulphide (mineral covellite)
Cu_2S:	Cuprous sulphide (mineral chalcolite)
Cu_7S_4:	Anilite
$Cu_{1.95}S$:	Djurleite
CuS/PANI:	Cupric sulphide/polyaniline
Cu_2S/PANI:	Cuprous sulphide/polyaniline
CuS(THU):	Copper sulphide synthesised using thiourea as sulphur source
CuS(*THU*)/PANI:	Copper sulphide(thiourea)/polyaniline
CuS(STS):	Copper sulphide synthesised using sodium thiosulphate as sulphur source
CuS(*STS*)/PANI:	Copper sulphide(sodium thiosulphate)/polyaniline
1-D:	One-dimensional
2-D:	Two-dimensional
3-D:	Three-dimensional
DC:	Direct current
dmg:	Dimethylglyoximate
DOS	Density of states
DTA:	Differential thermal
DTG:	Differential thermogravimetry
EDTA:	Ethylenediaminetetraacetic acid
EG:	Ethylene glycol

eV:	Electron volt
fcc:	face-centred-cubic
FE-SEM:	Field emission-Scanning electron microscope
FTIR:	Fourier transform infrared spectrometer
FWHM:	Full width at half maximum
g:	Gram
g/l:	Gram/litre
GaN:	Gallium nitride
h:	Hour
HDA:	Hexadecylamine
HgS:	Mercury sulphide
HOMO:	Highest occupied molecular orbital
Hz:	Hertz
I:	Current
IR:	Infrared
InAs:	Indium arsenide
InP:	Indium phosphate
I-V:	Current-voltage
KPS:	Potassium peroxydisulphate ($K_2S_2O_8$)
kV:	Kilovolts
LED:	Light-emitting diode
LUMO:	Lowest unoccupied molecular orbital
M:	Molar
M-2:	Metal nanoparticles synthesised with 0.02 M TA
M-4:	Metal nanoparticles synthesised with 0.04 M TA
M-6:	Metal nanoparticles synthesised with 0.06 M TA
mA:	Miliampere
MEH-PPV:	Poly-[2-methoxy-5-(2¢-ethyl-hexyloxy)-1,4-phenylenevinylene]

MEH-PPV:	Poly-[2-methoxy-5-(2e-ethyl-hexyloxy)-1,4-phenylenevinylene]
mA:	Milliampere
M-6:	Metal nanoparticles synthesised with 0.06 M TA
M-4:	Metal nanoparticles synthesised with 0.04 M TA
M-2:	Metal nanoparticles synthesised with 0.02 M TA
M:	Molar
LUMO:	Lowest unoccupied molecular orbital
LED:	Light-emitting diode
KV:	Kilovolts
KPS:	Potassium peroxydisulphate ($K_2S_2O_8$)
I-V:	Current-voltage
InP:	Indium phosphate
InAs:	Indium arsenide
IR:	Infrared
I:	Current
Hz:	Hertz
HOMO:	Highest occupied molecular orbital
HgS:	Mercury sulphide
HDA:	Hexadecylamine
h:	Hour
GaN:	Gallium nitride
g/l:	Gram/litre
g:	Gram
FWHM:	Full width at half maximum
FTIR:	Fourier transform infrared spectrometer
FE-SEM:	Field emission-Scanning electron microscope
fcc:	Face-centred-cubic
eV:	Electron volt

metal/PANI:	Metal/polyaniline
mg:	Miligram
min:	Minute
min^{-1}:	Per minute
ml:	Mililitre
mm:	Milimeter
MPa:	Megapascal
MPA:	3-mercaptopropionic acid
MRI:	Magnetic resonance imaging
M_w:	Weight average molecular weight
N_2:	Nitrogen
Na-AOT:	Sodium (bis-2-ethylhexyl) sulphosuccinate
NaOH:	Sodium hydroxide
near-IR:	Near Infrared
Ni:	Nickel
Ni-2:	Nickel nanoparticles synthesised with 0.02 M TA
Ni-4:	Nickel nanoparticles synthesised with 0.04 M TA
Ni-6:	Nickel nanoparticles synthesised with 0.06 M TA
Ni/PANI:	Nickel nanoparticles/polyaniline
Ni-2/PANI:	Nickel nanoparticles (synthesised with 0.02 M TA)/polyaniline
Ni-4/PANI:	Nickel nanoparticles (synthesised with 0.04 M TA)/polyaniline
Ni-6/PANI:	Nickel nanoparticles (synthesised with 0.06 M TA)/polyaniline
nm:	Nanometer
N/m:	Newton/meter
NPs:	Nanoparticles
NSs:	Nanostructures
NSMs:	Nanostructures materials
PANI:	Polyaniline

PbS:	Lead sulphide
P3HT:	Poly(3-hexylthiophene)
PL:	Photoluminescence
PTh:	Polythiophene
PPV:	Poly(p-phenylene vinylene)
PPY:	Polypyrrole
PVP:	Poly (*N*-vinyl-2-pyrrolidone)
QDs:	Quantum dots
R:	Radius
s:	Second
s^{-1}:	Per second
S/cm:	Siemens/centimetre
SDS:	Sodium dodecyl sulphate
SEM:	Scanning electron microscope
STS:	Sodium thiosulphate ($Na_2S_2O_3 . 5H_2O$)
S/V:	Surface-to-volume
t:	Crystalline size
TA:	Tannic acid ($C_{76}H_{52}O_{46}$)
TEDA:	Triethylenediamine
TEM:	Transmission electron microscope
TEMA:	Tetramethylenethylenediamine
TG:	Thermo gravimetric
TGA:	Thermogravimetric analysis
THU:	Thiourea (NH_2CSNH_2)
TMV:	Tobacco mosaic virus
TOPO:	Trioctylphosphine oxide
UV-vis:	Ultraviolate-visible
V:	Voltage

XPS:	X-ray photoelectron spectrometer
XRD:	Powder X-ray diffraction
ZnSe:	Zinc selenide
α:	Alpha
θ:	Angle
Å:	Angstrom
μ:	Micro
μm:	Micrometer
%:	Percentage
π:	Pi
ρ:	Resistivity
Δ:	Temperature
λ:	Wavelength
ν:	Wavenumber

ν:	Wavenumber
λ:	Wavelength
Δ:	Temperature
ρ:	Resistivity
π:	Pi
%:	Percentage
μm:	Micrometer
μ:	Micro
Å:	Angstrom
θ:	Angle
α:	Alpha
ZnSe:	Zinc selenide
XRD:	Powder X-ray diffraction
XPS:	X-ray photoelectron spectrometer.

CHAPTER 1

Introduction

1.1. Introduction to nanoscience and technology

Richard P. Feynman in the year 1959 predicted the future of nanotechnology. He predicted that there should be nothing stopping us from creating products at the size of atoms. He also suggested that a machine could be created that makes a miniature replica of itself, which creates another miniature replica of itself, and so on until the replica was at the molecular level. His talk "***There's Plenty of Room at the Bottom***" could come road map of nanotechnology[1]. In 1974, the term "nanotechnology" was introduced by Taniguchi. The term was popularized by Drexler during the 1980s when he introduced the concept of molecular manufacturing[2-4]. Investigations of reactive species (free atoms, clusters, reactive particles) throughout the 1970s and 1980s, coupled with new techniques and instruments (innovations in mass spectrometry, vacuum technology, scanning tunneling microscopes, and more) nanotechnology has been prosperously developed with the ability to measure and visualize the novel phenomena, and to manipulate and manufacture the materials and devices with nanostructures of 100 nanometres or smaller.

Today, this field of nanostructures science and technology has become a broad and interdisciplinary area of worldwide research and development activity and has been growing enormously. It has already having a significant commercial impact, and it will certainly have a much greater impact in near future. From common people point of view, nanotechnology appears to be the fabrication of miniature machines, which will be able to travel through the human body and repair damaged tissues or supercomputers small enough to fit in a pocket. However, nanotechnology anticipated applications range from optoelectronics[5-8], single electron transistors and light emitters[9-13], non-linear optical devices[14,15], catalysis[16,17], solar energy conversion[18,19] photonic band gap materials[20] and biomedical applications[21-25]. In order to realize the practical devices with nanomaterials utilizing their unique properties, the individual nanoparticles (NPs) need to be assembled in a desired fashion. Two major approaches currently being envisaged for the generation of organized nanoscale particles are top-down approach and bottom-up approach.

"Top-down" approach begins with a suitable starting material and then "sculpts" the functionality from the material. This technique is similar to the approach used by the semiconductor industry in forming devices out of an electronic substrate (silicon), utilizing pattern formation (such as electron beam lithography) and pattern transfer processes (such as reactive ion etching) that have the requisite spatial resolution to achieve creation of structures at the nanoscale. This particular area of nanostructure formation has tremendous scope and is a driving issue for the silicon-integrated chip technology[26]. However, it has been realized that the current rate of miniaturization in silicon memory technology will be affected very soon by the physical limits of device dimensions imposed by ultra-violet, electron/ion beam and soft X-ray lithographic techniques (known as Moore's law). Another top-down approach is "ball-milling," the formation of nanostructure building blocks through controlled, mechanical attrition of the bulk starting material. Those nano building blocks are then subsequently assembled into a new bulk material.

In bottom-up approaches, the atoms and molecules are assembled into the smallest nanostructures using precursors in the liquid, solid, or gas phase employing either chemical or physical deposition processes that are integrated into building blocks within the final material structure. An ample of this approach is the formation of powder components through aerosol techniques and then the compaction of the components into the final material. These techniques have been used extensively in the formation of structural composite nanomaterials. Self-assembly of atoms and molecules into nanostructures can be classified as a bottom-up approach. In nature, self-assembly is often used to make complex structures.

1.2. Uniqueness of nanoparticles

It is usually assumed that the properties of solid semiconductors are independent of their size. However, this assumption is only valid for the solid containing a macroscopic number of atoms. Recent studies have shown that if the characteristic size of semiconductor particles is less than 10 nm, then many of their physicochemical properties appear to be essentially different from analogous properties macroscopic objects[27-29]. The two major phenomenons due to the effect of material size confinement are briefly described below.

1.2.1. Size effects on the density of electronic state

One of the defining features of a semiconductor is the energy gap separating the conduction and valence energy bands. The colour of light emitted by the semiconductor material is determined by the width of the gap. In natural bulk semiconductors, the gap width is a fixed parameter determined by the material's identity. The situation changes, however, in the case of nanoscale semiconductor and metal particles with sizes smaller than about 10 nanometres. This size range corresponds to the regime of quantum confinement, for which the spatial extent of the electronic wave function is comparable with the dot size. Because of these "geometrical" constraints, electrons "feel" the presence of the particle boundaries and respond to changes in particle size by adjusting their energy. This phenomenon is known as the quantum-size effect, and it plays a very important role in quantum dots (QDs). **Figure 1.1** illustrates the density of states (DOS) and energy level spacing change as a function of size. In the first approximation, the

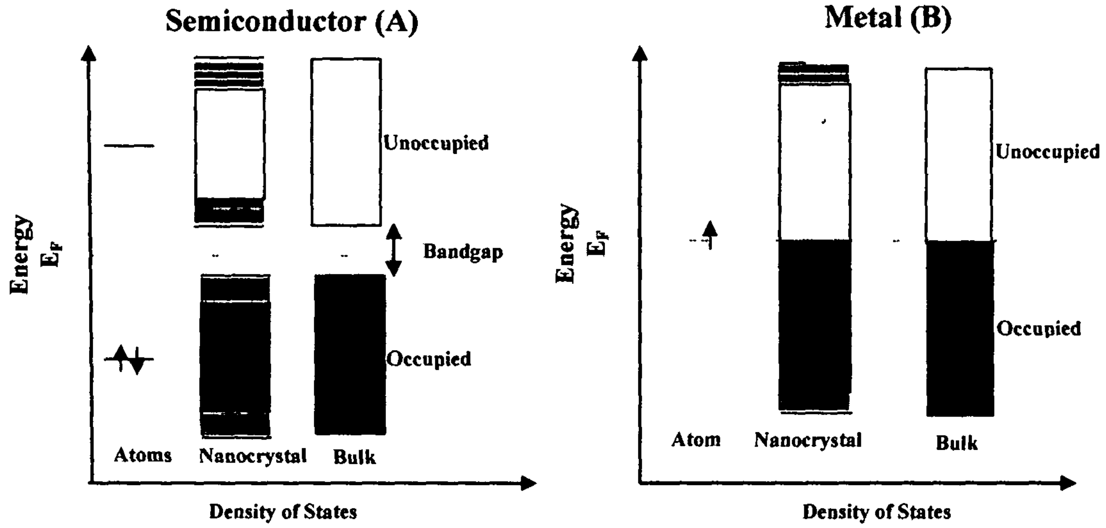

Figure 1.1. Schematic illustration of the energy levels as a function of density of states for different size systems for semiconductor (A) and metal (B).

quantum-size effect can be described by a simple "quantum box" model, in which the electron motion is restricted in all three dimensions by impenetrable walls. For a spherical QD with radius R, this model predicts that a size dependent contribution to the energy gap is simply proportional to $1/R^2$, implying that the gap increases as the QD size decreases[30]. In addition, quantum confinement leads to a collapse of the continuous energy bands of a bulk material into discrete, atomic-like energy levels[31-34]. The discrete structure of energy states leads to a discrete absorption spectrum of QDs, which is in contrast to the continuous absorption spectrum of a bulk semiconductor.

1.2.2. Size effects on the number surface atoms

Another important phenomenon that occurs due to size reduction is the extremely large surface-to-volume (S/V) ratio. The large percentage of surface atoms can introduce a high density of surface states. These surface states can fall within the band gap and trap charge carriers (electrons and holes), which in turn can significantly influence the charge carrier behaviour and other properties of the nanoparticles. The surface atoms contribute largely to the thermodynamic characteristics of solids and determine to a considerable extent the melting temperature and structural transitions for nanoparticles. The melting point of a solid, for example, is reached when the order of the lattice starts to be lost; as surface atoms have a smaller coordination number, they are easily rearranged. For typical bulk materials, the melting point is a physical constant, but only as long as the surface is negligibly small in comparison with the total volume. On reducing crystal size the number of surface atoms become equal or even exceeds that of the inner core atoms, as a result the melting process starts a lower temperature. Thus properties, which are usually determined by the molecular structure of the bulk lattice, now become increasingly dominated by the defect structure of the surface[35-38].

1.3. Nanostructured materials

Nanostructures materials (NSMs) are distinguished from conventional polycrystalline materials by the size of the structural units that compose them, and they often exhibit properties that are significantly different from those of conventional materials[39]. “**Nano**” derives from the Greek word “nanos” which means dwarf or extremely small. Nanomaterials are small clustered of atoms; at least one of their dimensions is less than 100 nm[40]. Nanostructured inorganic, organic and biological materials may have existed in nature since the evolution of life started on Earth. Some evident examples are microorganisms, fine grained minerals in rocks and nano size particles in bacterias and smoke. From a biological viewpoint, the DNA double helix has a diameter of about 2 nm (20 A°) while ribosomes have a diameter of 25 nm. Atoms have a size of 1-4 A°; therefore, nanostructured materials could hold tens of thousands of atoms all together. Moving to a micrometer scale, the diameter of a human hair is 50-100 µm[41]. **Figure 1.2** illustrates typical biological objects whose sizes belong to the

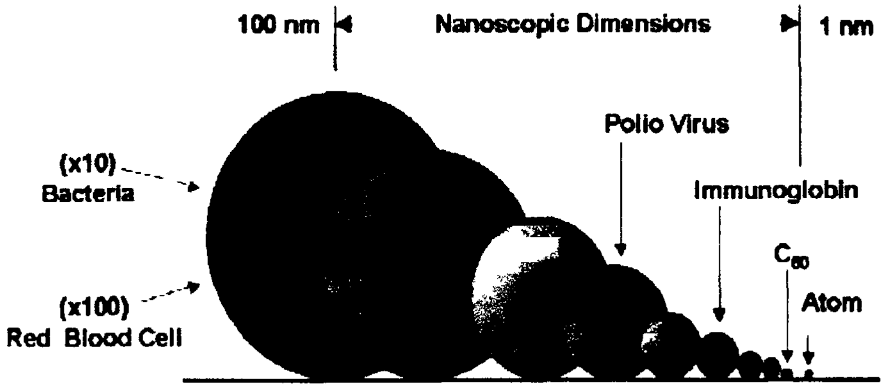

Figure 1.2. Size comparison of nanoparticles with bacteria, viruses and molecules.

significant gap existing between the two regimes, where particles of 1 to 100 nm (made of 10 to 106 atoms) can be found[42-44]. Although manmade nanostructured materials are of recent origin whose domain sizes have been precision engineered at an atomic level simply by controlling the size of constituent grains or building blocks, they actually have a very long history. Nanoparticles were used by artisans as far back as the 9th century in Mesopotamia for generating a glittering effect on the surface of pots. A Roman cup, called Lycurgus cup, used nanosized gold clusters to create different colours depending on whether it was illuminated from the front or the back. The cause of this effect was not known to those who exploited it. Michael Faraday provided the first description, in scientific terms, of the optical properties of nanometer-scale metals by synthesizing colloidal gold in his classic 1857 paper[45]. By the early 1940s, precipitated and fumed silica nanoparticle were used as substitutes for ultrafine "carbon black" particles for rubber reinforcement. Since then, nanosized silica have found large scale applications in many everyday consumer products, ranging from non-diary coffee creamer to automobile tires, optical fibers and catalyst supports. In the 1960s and 1970s metallic nano powders for magnetic recording tapes were developed[46]. Although research on nanostructured materials began about two decades ago but did not gain much impetus until the late 1990s. Since then the nano size length-scale has attracted increased attention and opened up a wide range of new opportunities for research and applications in the field of nanoscience and technology. Carbon black is the most famous example of a nanoparticulate material that has been produced in quantity of decades. Roughly, 1.5 million tons of the material is produced every year[41]. Among the nanostructured carbonaceous materials, fullerene and carbon nanotubes are the most popular materials. In fact, carbon nanotube is known as one of the most wanted material in 21st century. Both fullerene and carbon nanotubes have closed carbon cage structure. These two materials (in particular carbon nanotubes) have become topic of extensive experimental and theoretical investigations because of their unusual structure and properties that are in principal tunable by varying the diameter, the number of concentric shells, etc. The most common of the new generation of nanostructures being ceramics, which are best split into metal oxide ceramics, such as titanium, zinc, aluminium and iron oxides to name a prominent few, and silicate nanoparticles (silicates or silicon oxides are also ceramic), generally in the form of nanoscale flakes of clay. To date, nanostructures of ZnO, Fe_2O_3, SiO_2, MoS_2, CdS, CdSe, CdTe, HgS, GaP, Cd_3P_2, BiI_3, PbI_2 and a number of other semiconductors have been synthesized and investigated[47].

Among the nanostructured non carbonaceous II-VI materials, such as cadmium sulphide (CdS), cadmium selenide (CdSe), lead sulphide (PbS), and copper sulphide

(CuS), etc. as well as III-V elements, i.e., indium phosphide (InP), gallium nitride (GaN), indium arsenide (InAs), etc., are most important.

1.3.1. Copper and nickel

Over the past few years, considerable interest has been focused on metal nanoparticles due to their potential applications in diverse fields including catalysis, magnetic recording media, or microelectronics. Various methods are now known which enable one to prepare these nanoparticles with controlled size and shape; these include metal vapour deposition, electrochemical reduction, radiolytic reduction, thermal decomposition, mechanical attrition and chemical reduction. Among these methods, the solution method is found to be simple and most versatile for metal nanoparticles[48-56].

Copper is one of the most widely used materials in the world. It has a great significance in all industries, particularly in the electrical sector due to low cost. Copper has also been used as an antibacterial agent for many years[57]. The antifungal and antibacterial properties of copper nanoparticle-polymer composites have been reported[58-64]. Copper nanoparticles have been synthesized and characterized by different methods. Stability and reactivity are the two important factors that impede the use and development of the metal cluster in a new generation of nanoelectronic device.

Nickel nanoparticles have drawn additional interest as one of the most important catalysts for various reactions such as decomposition of ammonia[65], oxidative dehydrogenation[66], steam reforming[67], hydrogenation[68] and more recently, the formation of carbon nanotubes (CNTs)[69]. Extensive applications of nickel-based nanoparticles in biological systems are also reported. For example, Mirkin and co-workers demonstrated the efficient and selective separation of Histagged proteins using nickel-based nanorods with a diameter of about 300 nm[70]. Hyeon and co-workers have successfully proved that super paramagnetic Ni with NiO shells have a high affinity for polyhistidine and can be utilized for separating and purifying Histagged proteins from a multicomponent solution[71].

1.3.2. Copper sulphide and cadmium sulphide

Synthesis and characterization of nanocrystal of semiconducting copper sulphide (CuS), and cadmium sulphide (CdS) have been an intense field of research due to their interesting properties and potential applications.

Copper sulphides, belonging to space group 194, P63/mmc, are important semiconductors, which show metallic conductivity and transform at 1.6K into a superconductor[72]. In addition, copper sulphides exhibit fast-ion conduction at high temperature[73,74] and their many particular properties have been studied extensively[75,76]. Copper monosulphide crystallizes in the hexagonal crystal system, and this is the form of the mineral covellite. There is also an amorphous high pressure form[77], which on the basis of the Raman spectrum has been described as having a distorted covellite structure. The structure was described as "extraordinary" by Wells[78] and is quite different from copper (II) oxide, but similar to CuSe (klockmannite). The covellite unit cell contains 6 formula units (12 atoms) in which 4 Cu atoms have tetrahedral coordination, 2 Cu atoms have trigonal planar coordination, 2 pairs of S atoms are only 207.1 pm apart[79] indicating the existence of an S-S bond (a disulphide unit). The 2 remaining S atoms form trigonal planar triangles around the copper atoms, and are surrounded by five Cu atoms in a pentagonal bipyramid. The S atoms at each end of a disulphide unit are tetrahedrally coordinated to 3 tetrahedrally coordinated Cu atoms and the other S atom in the disulphide unit. Traditionally, many efforts have been made to synthesize CuS crystals, such as solid-state reactions[80], self-propagating high temperature synthesis[81-83], and hydrothermal synthesis of CuS nanoparticles[84]. Moreover, Henshaw and his co-workers have also prepared copper sulphides at low temperature via elemental reaction in liquid ammonia[85]. However, what they obtained was a mixture of $Cu_{1.8}S$, $Cu_{7.2}S_4$ and $Cu_{1.96}S$. Gautam and his co-worker prepared water-soluble CuS nanocrystals and nanorods by reacting copper acetate with thioacetamide in the presence of different surfactants and capping agents[86]. The size of the nanocrystals varied from 3-20 nm depending on the reaction parameters such as concentration, temperature, solvent and the capping agent. Lu et al. synthesized CuS nanoroads using liquid-crystal templates [87].

Cadmium sulphide (CdS) is a p-type semiconductor with Bohr radius of 2.4 nm and direct band gap of 2.40 eV[88] and is widely used as a commercial photodetector in the visible spectrum. It is also used as a promising material for buffer layers in thin film solar cells[89,90]. When combined with p-type semiconductor, it forms the core component of a photovoltaic solar cell. A CdS/Cu_2S solar cell was one of the first efficient cells to be reported in 1954[91,92]. When doped with for example Cu^+ ("activator'') and Al^{3+} ("coactivator"), CdS luminesces under electron beam excitation (cathodoluminescence) and is used as phosphor[93]. Cadmium sulphide has, like zinc sulphide, two crystal forms; the more stable hexagonal wurtzite structure (found in the mineral Greenockite) and the cubic zinc blende structure (found in the mineral Hawleyite). In both of these forms the cadmium and sulphur atoms are four coordinate[78]. There is also a high pressure form with the NaCl rock salt structure[78].

1.3.3. Dimensionally classification of nanostructures

First classification scheme of NSMs was proposed by Gleiter[94] and further was extended by Skorokhod et al.[95]. In the last decade, hundreds of new NSMs and

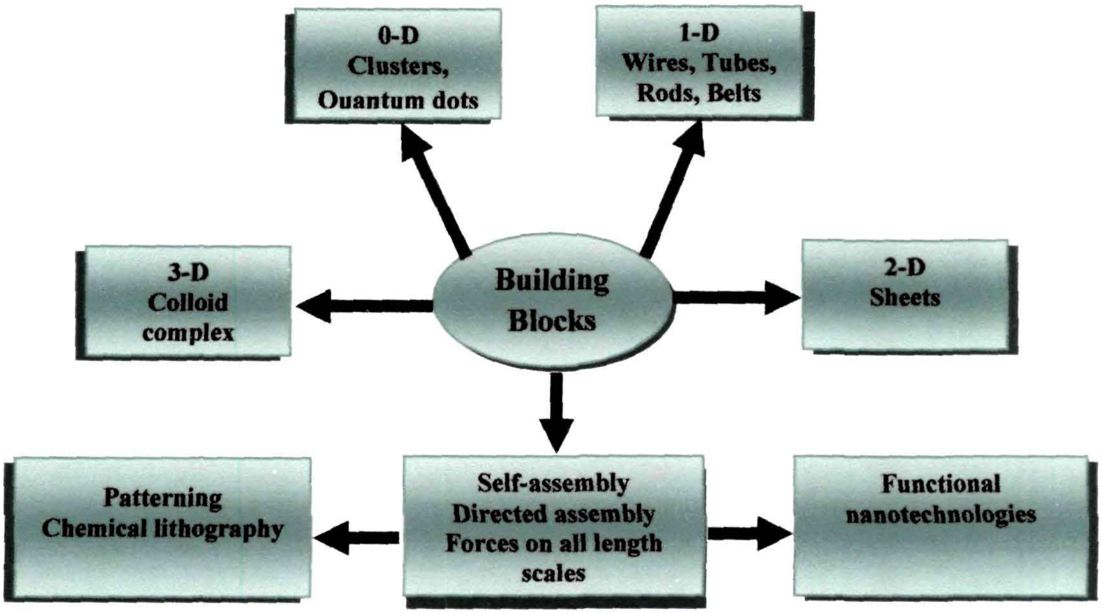

Figure 1.3. Schematic representation of different classes of dimensionally modulated nanostructured building blocks.

abundance of novel nanostructures (NSs) have been obtained and therefore, the need in their classification is ripened. Recently, Pokropivny and Skorokhod have proposed a classification of NSs based on their dimensionality namely, 0D, 1D, 2D, and 3D[96].

Table 1.1. 36 classes of nanostructures

0D	0D0 (Uniform particles arrays)	
	0D00 (Core-shell dendrimers)	
1D	1D0 (Molecular chain, Polymers)	
	1D00 (Heteropolymers)	
	1D1 (Bundles, Ropes)	
	1D11 (Heterochains, heterobundles)	
	1D10 (Beads, Pea-pods)	
2D	2D0 (Fullerene films)	2D11 (Films of fibers)
	2D1 (Nanostraw)	2D20 (Fullereno plate films)
	2D2 (Layered films)	2D21 (Fiber layer films)
	2D00 (Heterofilms)	2D22 (Hetero layers)
	2D10 (Films of pods)	2D210 (Fullarene fiber layer films)
3D	3D0 (Fog)	3D21 (Cross bar layers)
	3D1 (Skeleton of fibers)	3D22 (Heterolayers)
	3D2 (Honeycombs, Foams)	3D30 (Particles, pores in matrix)
	3D00 (sols, colloids, smogs)	3D31 (Fiber composites)
	3D10 (Skeletons of fibers-powders)	3D32 (Grain boundaries)
	3D11(Skeleton of heterofibers-nanotubes)	3D210 (Composites of layers)
		3D310 (Powder-fiber composites)
	3D20 (Intercalates)	3D320 (Powder- layers composites)
		3D321 (Layers-fibers composites in matrix)

Figure 1.3 represents the dimensionally modulated broad classification of NSs. All NSs can be built from elementary units (blocks) having lower dimensionality 0D, 1D, and 2D. The 3D units are excluded because they cannot be used to build low-dimensional NSs except 3D matrix. However, 3D structures can be considered as NSMs if they

involve the 0D, 1D, and 2D NSs. They introduce the notation of NSs as kDlmn......, where k is a dimensionality of NS as a whole, while the integers l, m, n denote the constituting units.

From the definition of NSs the condition leads, namely, $k \geq l,m,n$, and $k,l,m,n=0,1,2,3$. It follows from this conditions that restricted number of NSs classes exists, namely, 3 sorts of elementary units (0D, 1D, 2D), 9 single classes of kDl type built of 1 sort units, 19 binary classes of kDlm type built of 2 sort units, and a variety of ternary, tetradic, etc., classes. Restricting the classification by 5 main ternary structures of kDlmn type built of 3 sort units, we obtain in the result 3+9+19+5=36 classes of NSs as presented in **Table 1.1**.

1.3.4. Colloid chemical synthesis of nanostructures

The synthesis and processing of nanostructured materials with well defined architecture has attracted great attention because of the potential uses of nanostructures as building blocks for nanodevices and nanosystems. A number of methods have been explored to fabricate nanostructured materials. Methods for synthesis of nanostructures can be broadly divided into two categories as physical and chemical methods. Physical methods such as molecular beam epitaxy, evaporation, vacuum sputtering and metal organic chemical vapour deposition generally produced nanostructures on substrates [97-99]. The main limitations of this physical method are the cost of fabrication and lack of control over positioning of individual dots. In addition, there exists a limit on the physical size of a substrate and the number of substrates that may be processed during one single batch. Therefore, the throughput of the process is limited. Chemical synthesis methods are promising in terms of cost reduction and ability to produce large amounts of particles and there are no substrate issues.

Chemical synthesis in general involves reacting atomic or molecular species in a solvent/surfactant mixture. The solvent/surfactant mixture serves as a reaction medium in which reaction, nucleation and crystal growth occur. The surfactant is often an organic molecule which interacts dynamically with the surface of the growing nanostructures thus regulating the size and shape of the final nanostructures[97].

Depending upon the solvent used, chemical synthesis can be further classified as aqueous and nonaqueous synthesis. The nanostructures produced are freestanding and exist as colloids in solution.

Among various chemical synthetic methods developed, two approaches are most successful in creating stable colloids with good size dispersion. One is an organometallic synthesis based on the high temperature thermolysis of precursors, first reported by Murray *et al.*[100] and further improved later on[101]. The high reaction temperature (150-300 °C) facilitates the removal of crystalline defects and results in high-quality magnetic nanoparticles. However, the toxicity of the solvents, ligands and precursors used in these types of syntheses might limit their applications to a certain extent[102]. An alternative synthesis employs the synthesis from the starting reagents in solution by arresting the reaction at a definite moment of time. This is the so-called method of arrested precipitation[103,104]. Arrested precipitations in aqueous media in the presence of stabilizers such as polyphosphates[105], thiols[106], thioglycolic acid[107], triethylenediamine[108], sodium (bis-2-ethylhexyl) sulphosuccinate (Na-AOT)[86] are reported. This is a faster, simple, and inexpensive technique. However, the technique is very sensitive in terms of reproducibility of a particular size of particles. This is because various parameters e.g., volume of the reactants, stirring speed, rate of addition of reactants, time of stirring, temperature, and pH-value are involved in the synthesis and have to be reproduced for obtaining a particular size. Another important task is to minimize the size distribution in order to achieve monodispersed particles. For the case of nanoreactors, various cage-shaped functional materials such as reverse micelles[109], diblock copolymers[110], vesicles[111], etc., are used to control the growth of nanoparticles.

1.3.5. Means to achieve stable dispersion: role of capping ligands

In any solution phase synthesis of crystalline nanoparticles, there are three steps to consider: (i) nucleation of a sparingly soluble product under supersaturation conditions; (ii) growth of nuclei into crystalline nanoparticles and (iii) growth termination and nanoparticles stabilization. In theory, control in the size and shape distribution of nanoparticles prepared in solution can be achieved via the capability to

1.3.6. Nanocomposites materials

In the universe composite material are distributed widely and are considered to be the building blocks in planet formation processes. Some evident examples of composite materials that nature has created are timber, bamboo, feathers, wood, organic materials, like tissue surrounding the skeletal system, soil aggregates, minerals and rock. Bone is an organic-inorganic composite of protein (collagen) and minerals (calcium apatite) and bamboo is cellulose reinforced by silica. These combinations make a hard material with high impact strength. The cellulose cell structure of wood and fiber is bound together with lignin, a natural polymeric substance. Ancient society, imitating nature, used this approach as well to improve the quality of life. For example, people used construction materials like Adobe[113] to build sturdier houses and were made of mud bricks lined with straw and strips or mats of bamboo, canes to impart higher strength, for mud bricks. Ancient Pharaohs made their slaves use bricks with to straw to enhance the structural integrity of their buildings, some of which testify to wisdom of the dead civilization even today: safety and durability to the mud walls. Uses of papyrus reinforced bitumen in building fishing boats and of shellac as a stiff matrix material with reinforcements based on fibrous materials collected from forest were known to people in ancient Babylonia, Egypt and India. At a much later date, composites such as linoleum, asbestos, cement items, and reinforced concrete grew into prominence and universal acceptance. Contemporary composites results from research and innovation from past few decades have progressed from glass fibre for automobile bodies to particulate composites for aerospace and a range other ultra demanding applications. For instance, the term "FRP" (for Fibre Reinforced Plastic) usually indicates a thermosetting polyester matrix containing glass fibres, and this particular composite has the lion's share of today's commercial market[114].

The word ***composite***, as technically defined, means a macroscopic combination of two or more distinct materials having an identifiable interface between them, but more pointedly, the definition is confined to only such materials as would contain a fibrous or particulate reinforcement supported by a binder or matrix material. The discontinuous phase constituted of the fibre or particulate reinforcement is commonly stiffer and stronger than the continuous (matrix) phase[115]. The particulates may be powdered, crystalline or amorphous. They may be metallic or ceramic containing natural or artificially prepared materials. The matrix must be capable of being forced around the reinforcement during some stage in the manufacture of composite. There are a number of matrix materials, including carbon, ceramic, glass and polymers. Concrete and solid rocket propellants are familiar examples of particulate composites[116]. The difference between a composite and a filled system lies in the fact that while in composite the discontinuous phase imparts significant mechanical reinforcement, it only plays the role of a loading agent or diluents without property enhancement or reinforcement in what is called a filled system. Fillers however, may impart many advantages such as fire/flame retardancy, shrinkage control, improved thermal/electrical conductivity and above all, cost benefit. A composite is viewed as a laminate if the reinforcing fibres are arranged in layered fashion such as in the form of webs, fabrics or mats. Examples are automobile parts, like windshields and laminated glass, where, isotropic layers of materials are bonded together to form non-homogeneous composite laminates[115]. However, properties achieved by these traditional composites involve compromises. For example, stiffness is obtained at cost of toughness, which is also traded for optical clarity. Recently, nanoscale filled polymer composites give a new way to overcome the limitations of traditional counterparts.

The definition of "***nano-composite material***" has broadened significantly to encompass a large variety of systems such as one-dimensional, two-dimensional, three-dimensional materials, amorphous or crystalline, made of distinctly dissimilar components, which are mixed at the nanometer scale. Nanocomposite is a distinct form of composite materials, which involves embedding nano or molecular domain sized particles into an organic polymer, metal or ceramic matrix material. The incorporation of quantum dots into monodisperse polymer microbeads can give materials some unique properties, and numerous potential applications such as enhancement of conductivity[117,118], toughness[119], optical activity[120,121], catalytic activity[122], chemical selectivity[123,124], etc. Polymer based nanocomposite technology has been described as the next great frontier of material science. For example, nanotube fillers possess strength as high as 500 GPa and modulus as high as 1 TPa. Nanoparticles are optically active and do not scatter light significantly, which can be combined into a polymer to obtain the optical gain of the material. Very small fillers do not build large stress concentrations and therefore, do not compromise the ductility of the polymer. In addition, the small decrease in size of the fillers less than 100 nm leads to dramatically augmented interfacial area per unit volume or weight of the dispersed phase, which control the degree of interaction between the polymer and filler phase and thus controls the properties. Hence, the greatest challenge in making polymer nanocomposites is to learn how to control the interface.

1.4. Conducting polymers

Ever since the discovery by Shirakawa, Heeger and MacDiarmid, in 1976, conducting polymers (CP) and their composites has emerged as new field of research and development, directed to creation of new smart materials for use in modern and future technologies. In particular, electrochemistry-related aspects of nanostructurized conducting polymers have recently attracted a great deal of interest. The main expected electrochemistry related fields of application for nanostructurized conducting polymers are electric energy storage systems, chemical-to-electric or vice versa energy conversions, sensors and biosensors, and materials for corrosion protection[125-136]. They are called ***"fourth generation of materials"***. Along with semiconducting properties, conducting polymers extend lightweight, good strength, flexibility and easy processability. One of the remarkable features of conducting polymers is that it is possible to control the electrical conductivity of these polymers over a wide range from insulating to metallic and even to super conducting by proper doping with suitable dopants. Both n-type (electron donating, e.g., Na, K, Li, Ca, tetrabutylammonium) and p-type (electron accepting, e.g., PF_6, BF_4, Cl, AsF_6) dopants have been used. The doping typically is done using vapors or solutions of the dopant, or electrochemically. In some circumstances, the polymer and dopant are dissolved in the same solvent before forming the film or powder. The polymer backbone and dopant ions form a rich variety of new three-dimensional structures. Many of the CPs show good optical behaviour also[137]. CPs have an alternating sequence of single and double bonds along the polymer backbones. The overlap of π bonding and π^* antibonding molecular orbitals forms a continuous system of electron density along the polymer backbone. CPs are not ideal conjugated systems. There is a break in the conjugation length due to twists and kinks, as well as due to the chemical defects. The extent of this overlap (conjugation length) together with the bond alternation determines the HOMO-LUMO band gap. CPs have band gaps in the range of 1 to 4 eV, which makes them ideally suited for applications in optoelectronic devices operating in the visible light range. The vast majority of reports dealing with CPs involve the study of p-doped polymers, for example polyaniline (PANI)[138], polypyrrole (PPy)[139], poly(p-phenylene vinylene) (PPV)[140], polythiophene (PTh)[141] and their derivatives.

1.4.1. Polyaniline

Among all CPs, polyaniline (PANI) was the first stable metallic polymers which could be processed in the metallic form[126]. PANI has been investigated extensively for over 100 years and attracted a great deal of attention as a conducting materials for several important reasons; the monomer is inexpensive, the polymerization reaction is straight forward and proceeds with high yield and PANI has excellent stability[126,142,143]. One of the unusual characteristics of polyaniline is that it may be treated as an alternating block copolymer of benzenoid and quinoid units. This assumes a head to tail (that is 1, 4 bonding or para bonding) and an even oxidation state wherein there are 50% benzenoid and 50% quinoid units. This is nearly true when the polyaniline is in its emeraldine salt form. Between each benzenoid and quinoid there is a different nitrogen group. They are referred to as imino and amino groups. The generalized formula for different forms of PANI base can be described by the formula presented in the

Figure 1.4. These heteroatom moieties are often used as sites for selective acid doping and their ability to be protonated or deprotonated allows the PANI to be dissolved in strong acids or bases[144]. All these factors contribute to PANI being superior to other conducting polymers. PANI exists in a variety of forms that differ in chemical and physical properties[144-147]. Depending on the method of preparation, PANI bases may exist in three distinguished form; (a) fully reduced form (**leucoemeraldine**), (b) partially reduced form (**emeraldine**), and (c) fully oxidized form (**pernigraniline**) (**Figure 1.5**).

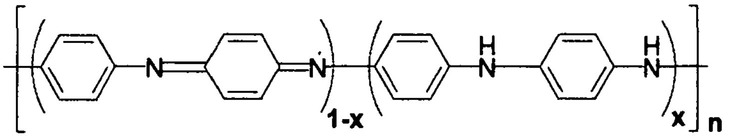

Figure 1.4. The general formula for different forms of PANI base.

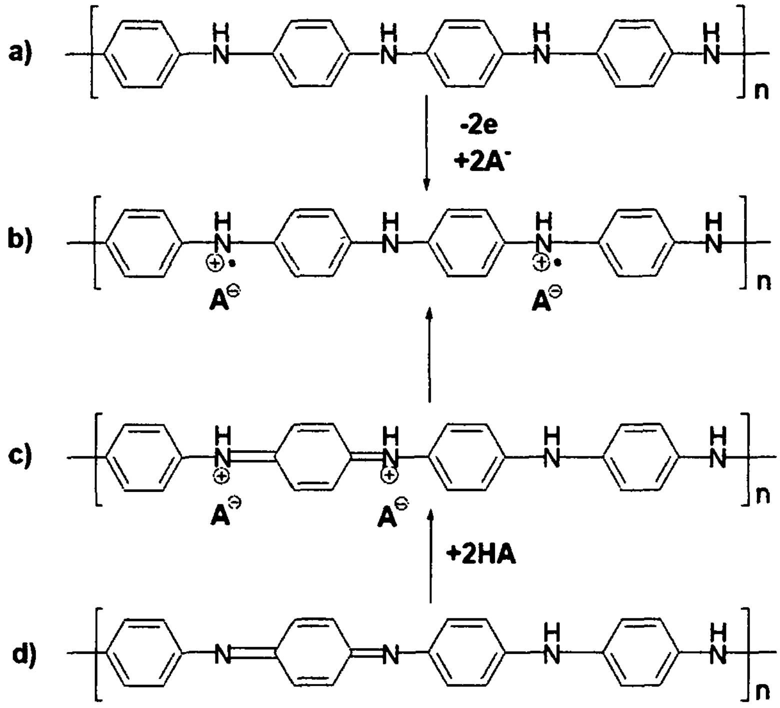

Figure 1.5. Principle of PANI doping.

Both fully reduced and fully oxidized are environmentally unstable. Leucoemeraldine (a) (white powder) is a strong reducing agent that easily reacts with air oxygen giving emeraldine (b) as the product[148]. Pernigraniline (c) (red-purple, partially crystalline powder) composed of oxidized units, easily undergoes hydrolytic type degradation via chain scission[144]. Emeraldine base (dark blue powder with metallic gloss)- semi-oxidized form of PANI is stable in air and can be stored for long time without chemical changes. Emeraldine is the most extensively studied form of PANI.

Several synthetic routes have been proposed for polymerization of aniline and its derivatives. The synthetic procedures are mainly aimed on the preparation of emeraldine base as this form of PANI is stable in ambient conditions. When pernigraniline or leucoemeraldine are required, the oxidation or the reduction of emeraldine usually obtains them. The oldest and still the most popular way for the preparation of polyaniline is chemical oxidative polymerisation. The efficient polymerization of aniline is achieved only in an acidic medium, where aniline exists as an anilinium cation. A variety of inorganic and organic acids of different concentration has been used in the syntheses of PANI; the resulting PANI, protonated with various acids, differs in solubility, conductivity, and stability[146]. Different inorganic oxidants such as: KIO_3, $KMnO_4$, $FeCl_3$, K_2CrO_4, $KBrO_3$, $KClO_3$, $(NH_4)_2S_2O_8$ have been used. Peroxydisulfate is the most commonly used oxidant, and its ammonium salt was preferred to the potassium counterpart because of its better solubility in water. The concentration of aniline hydrochloride was set to 0.2 M. Various oxidant/monomer ratios have been used in the literature[149]. To minimize the presence of residual aniline and to obtain the best yield of PANI, the stoichiometric peroxydisulfate/aniline ratio of 1.25 is recommended[149]. Chemical oxidative polymerisation of aniline using HCl and $(NH_4)_2S_2O_8$ can be described by the following **Scheme 1.1**.

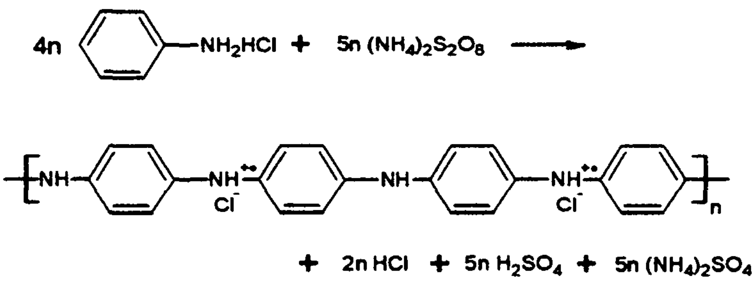

Scheme 1.1. Oxidative polymerization of aniline.

It is clear from **Scheme 1.1** that in acidic media emeraldine is obtained in its protonated state. If needed, it is usually transformed into the base form by deprotonation in 0.1 M ammonia aqueous solution.

Oxidative polymerisation of aniline can also be performed using the electrochemical route. Polyaniline can be synthetised potentiostatically, galvanostatically or by potential scanning (cyclic-voltammetry polymerisation). In the cyclic-voltametry method, the product is deposited layer-by layer on the anode. Using this technique the best quality homogenous polymer film was obtained in the eutectic mixture $NH_4F \cdot 2.35HF$ applying the potential from -0.2V to 0.7 V (vs. Cu/CuF_2)[150,151]. Electrochemical polymerisation can also be carried out in other media: aqueous solutions at low pH using inorganic acids such as HCl or H_2SO_4 and the systems composed of organic solvents and inorganic salts, i.e., lithium perchlorate-acetonitrile[152-155]. Electrochemical polymerisations are usually carried out at room temperature, but some comparative experiments have been done at 0 °C[156]. It has been found that the polymer obtained at lower temperatures exhibits better properties, among others, a higher molecular weight. Well-controlled conditions of the electrochemical polymerisation cause good reproducibility of the product.

1.5. Inorganic-organic materials interaction in nanocomposites

A great variety of nanocomposite materials can be formed by guest-host interactions between inorganic and organic species. Experimental work has generally shown that virtually all types and classes of nanocomposite materials lead to new and improved properties when compared to their macrocomposite counterparts. Therefore, nanocomposites promise new applications in many fields such as mechanically reinforced light weight components, non-linear optics, battery cathodes, sensors and optoelectronics.

Inorganic nanoparticles can be introduced into the matrix of a host-conducting polymer either by some suitable chemical route or by an electrochemical incorporation technique. However, each synthesis opens a way to a group of materials with complementary behavior between two components. The special properties viz. its colloidal stability, optical, catalytic, electrochemical, magnetic susceptibility, etc., always add new dimensions to the characteristic of the resulting composite. A wide variety of available inorganic components like three-dimensional framework systems of zeolites, two-dimensional layered materials such as clays, metal oxides, metal phosphates, chalcogenides, and even one-dimensional nanowires, nanotubes, $(Mo_3Se^{3-})_n$ chains and zero-dimensional materials such as CdS, CdSe nanoclusters have so far been encapsulated into the core of conducting polymers giving rise to a host of nanocomposites. These materials differ from pure polymers in some of the physical and chemical properties and at the same time differ from each other.

P. Poddar *et al.* used 15 nm manganese zinc ferrites (Mn0.68Zn0.25Fe2.07O3) synthesized in inverse micelles as the disperse phase for PANI/PPY-based nanocomposites[157]. Poddar's research was focused on the magnetic behavior of those compounds at different temperatures[157]. Lee *et al.* fabricated light-emitting devices using the polymer/layered silicate nanocomposite with good gas-barrier properties by blending poly-[2-methoxy-5-(2¢-ethyl-hexyloxy)-1,4-phenylenevinylene] (MEH-PPV) with organoclay[158]. The two-dimensional nanocomposite film shows higher photoluminescence (PL) output and better photo stability when compared with the pure MEH-PPV film of the same thickness[158]. The photovoltaic performance of CdSe /Poly(3-hexylthiophene) (P3HT) has been studied by Goodman *et al.*[159]. Improved photovoltaic performances of CPs due to the introducing NPs have been observed. Studies by Zhou *et al.* on the effect of metal NPs on the conjugation of poly(diacetylene) showed red-shift in the π-π^* absorption of polymer as Ag NPs increased in size upon UV irradiation[160,161]. Masuhara *et al.* reported a similar effect for Ag NPs surrounded by poly (1, 6-di(N-carbazolyl)-2, 4-hexadiyne) where the π-π^* absorption red-shifted ~20 nm than would be expected without the Ag particles[162]. NP/CP composites may also find utility as cathode materials. Embedding Ag or Pd NPs in a 2, 5-dimercapto-1, 3, 4-thiadiazole (DMcT)-polyaniline (PANI) composite resulted in an increase in redox activity compared to pristine material[163,164]. This increase in redox activity has been attributed to electroactivity of the NPs and improved conductivity of the nanocomposite.

This enhanced redox activity leads to better charge-discharge performance potentially making these useful as cathode materials in improved lithium rechargeable batteries. To improve the conductivity of PANI, Konwer *et al.* synthesized expanded graphite filled PANI composite by *in-situ* polymerization reaction[165].

1.6. Motivation and objectives of the present study

The field of nanotechnology has opened up new worlds of possibility and has spawned a proliferation of new terminology. Another feature of nanotechnology is an area of research and development that is truly multidisciplinary. Nanostructured materials have received steadily growing interest of their peculiar properties, organization to form superstructures and applications superior to their bulk counterparts.

Among the nanostructured non carbonaceous materials much attention has been paid to the synthesis of group I to group VI semiconductor materials e.g., cadmium sulphide (CdS), cadmium selenide (CdSe), copper sulphide (CuS), cadmium telluride (CdTe), zinc selenide (ZnSe), lead sulphide (PbS), mercury sulphide (HgS), and metallic silver, gold, copper, nickel, etc., due to their excellent prospective in catalysis, optical, electronic functionality, and so on.

Today, research on nanostructures has rapidly extended from simple structures to the assembly of nanocrystals into ordered superstructures aiming to achieve increased structural complexity and functionality. For example, tetrapods may be important alternatives to fibers and rods as additives for the mechanical reinforcement of polymers. However, it is challenging to develop simple and novel synthetic approaches for building hierarchically self-assembled fractal architectures of various system.

Conducting polymer based nanocomposites represent a new concept in the development of systems exhibiting functional properties resulting from the synergistic interaction between the disperse phase and the matrix. The many properties of conducting polymers like non-corrosiveness, light weight, mechanical strength, and the possibility to tune electrical conductivity and dielectric behavior can be utilized along with luminescence properties of metal and semiconductor nanoparticles to make multifunctional structures. In these regard, nanoparticles with complex architectures play an important role.

Accordingly, the overall goal of this research work can be described with the specific ***objectives*** as listed below:

- Preparation of Cu and Ni nanoparticles by chemical synthesis route.
- Preparation of CdS and CuS nanoparticles by chemical synthesis route.
- Synthesis of conducting polymer, PANI.
- Synthesis of Cu/PANI, Ni/PANI, CuS/PANI and CdS/PANI nanocomposites and their interaction study.
- Characterization of the prepared nanoparticles and polyaniline by UV-Visible Spectrophotometer (UV-vis), X-ray Diffraction (XRD), Fourier Transform Infrared Spectrophotometer (FTIR), Thermogravimetric Analysis (TGA), Scanning Electron Microscope (SEM), Transmission Electron Microscope (TEM), Atomic Force Microscope (AFM) and X-ray Photoelectron Spectroscopy (XPS) techniques.
- Investigation of optical properties of the synthesized materials.
- Investigation of conductivity behaviour of the synthesized materials.

References

1. Richard Feynman's classic talk on Dce. 1959, annual meeting of American Physical Soc., at the California Institute of Technology, published in Caltech's Engineering and Science, Feb (1960). (www.zyvex.com/nanotech/feynman.html)
2. http://www.fact-index.com/n/na/nanotechnology.html (2006)
3. LeBaron, P. C.; Pinnavaia, T. J. Clay nanolayer reinforcement of a silicone elastomer, *Chem. Mater* **13**, 3760-3765 (2001)
4. Tjong, S. C. Structural and mechanical properties of polymer nanocomposites, *Mater. Sci. Eng. R* **53**, 73-197 (2006)
5. Monti, O. L. A.; Fourkas, J. T.; Nesbitt, D. J. Diffraction-limited photogeneration and characterization of silver nanoparticles, *J. Phys. Chem. B* **108**, 1604-1612 (2004)
6. Jin, R. *et al.* Controlling anisotropic nanoparticle growth through plasmon excitation, *Nature* **425**, 487-490 (2003)
7. Schmid, G. *Clusters and Colloids: From theory to Application* (WILEY-VCH Verlag GmbH & Co KGaA, Weinheim, 1994)
8. Kamat, P. V.; Meisel, D. *Studies in Surface Science and Catalysis Semiconductor and Nanoclusters-Physical, Chemical, and Catalytic Aspects* (Elsevier, Amsterdam, 1997)
9. Klein, D. L.; Roth, R.; Lim, A. K. L.; Alivisatos, A. P.; McEuen, P. L. A single-electron transistor made from a cadmium selenide nanocrystal, *Nature* **389**, 699-701 (1997)
10. Weller, H. Transistors and light emitters from single nanoclusters, *Angew. Chem. Int. Ed.* **37**, 1658-1659 (1998)
11. Cui, J. B.; Burghard, M.; Kern, K. Room temperature single electron transistor based on chemically modified carbon nanotubes, *Nano Lett.* **2**, 117-120 (2002)
12. Björk, M. T. *et al.* Few-electron quantum dots in nanowires, *Nano Lett.* **4**, 1621-1625 (2004)

13. Liu, C. *et al.* High-density, ordered ultraviolet light-emitting ZnO nanowire arrays, *Adv. Mater.* **15**, 838-841 (2003)

14. Wang, Y. Nonlinear optical properties of nanometer-sized semiconductor clusters, *Acc. Chem. Res.* **24**, 133-139 (1991)

15. Yoffe, A. D. Low dimensional systems-quantum-size effects and elctronic properties of semiconductor microcrystallites (zero-dimensional systems) and some quasi-2-dimensional systems, *Adv. Phys.* **42**, 173-266 (1993)

16. Reetz, M. T.; Quaiser, S. A.; Breinbauer, R.; Teshe, B. A new strategy in heterogeneous catalysis: the design of cortex catalysts, *Angew. Chem. Int. Ed.* **34**, 2728-2730 (1995)

17. El-Sayed, M. A. Some interesting properties of metals confined in time and nanometer space of different shapes, *Acc. Chem. Res.* **34**, 257-264 (2001)

18. Hagfeldt, A.; Grätzel, M. Molecular photovoltaics, *Acc. Chem. Res.* **33**, 269-277 (2000)

19. Bueno, J. T.; Shchukina, N.; Ramos, A. A. A substantial amount of hidden magnetic energy in the quiet Sun, *Nature* **430**, 326-329 (2004)

20. Moran, C. E.; Steele, J. M.; Halas, N. J. Chemical and dielectric manipulation of the plasmonic band gap of metallodielectric arrays, *Nano Lett.* **4**, 1497-1500 (2004)

21. West, J. L.; Halas, N. J. Applications of nanotechnology to biotechnology: commentary, *Curr. Opin. Biotech.* **11**, 215-217 (2000)

22. Mornet, S.; Vasseur, S.; Grasset, F.; Duguet, E. J. Magnetic nanoparticle design for medical diagnosis and therapy, *J. Mater. Chem.* **14**, 2161-2175 (2004)

23. Roy, I. *et al.* Ceramic-based nanoparticles entrapping water-insoluble photosensitizing anticancer drugs: a novel drug-carrier system for photodynamic therapy, *J. Am. Chem. Soc.* **125**, 7860-7865 (2003)

24. Hirsch, L. R. *et al.* Nanoshell-mediated near-infrared thermal therapy of tumors under magnetic resonance guidance, *PNAS 100* 13549-13554 (2003)

25. Salata, O. V. Applications of nanoparticles in biology and medicine, *J. Nanobiotech.* **2**, 3 (2004)

26. Xia, Y.; Whitesides, G. M.; Soft Lithography, *Angew. Chem. Int. Ed.* **37**, 550-575 (1998)

27. Gibbs, H. M.; Khitrova, G. *Semiconductor Nanocrystals for Non-Linear Optical Devices, in Non-Linear Photoionics* (Springer, Berlin, Heidelberg, 1990)

28. Gaponenko, S. V. *Optical Properties of Semiconductor Nanocrystals* (Cambridge Univ. Press, 1998)

29. Weller, H. Colloidal semiconductor Q-particles: Chemistry in the transition region between solid state and molecules, *Angew. Chem. Int. Ed.* **32**, 41-53 (1993)

30. Bawendi, M. G.; Steigerwald, M. L.; Brus, L. E. The quantum mechanics of larger semiconductor clusters ("quantum dots"), *Annu. Rev. Phys. Chem.* **41**, 477-496 (1990)

31. Alivisatos, A. P. Perspectives on the physical chemistry of semiconductor nanocrystals, *J. Phys. Chem.* **100**, 13226-13239 (1996)

32. Alivisatos, A. P. Semiconductor clusters, nanocrystals, and quantum dots, *Science* **271**, 933-937 (1996)

33. de Jongh, J. *Physics and Chemistry of Metal Cluster Compounds* (Kluwer Academic Publishers, Dordrecht 1994)

34. Klabunde, K. J. *Nanoscale Materials in Chemistry* (Wiley-Interscience, New York, 2001)

35. Roberti, T. W.; Smith, B. A.; Zhang, J. Z. Ultrafast electron dynamics at the liquid-metal interface: femtosecond studies using surface plasmons in aqueous silver colloid, *J. Chem. Phys.* **102**, 3860-3866 (1995)

36. Faulhaber, A. E.; Smith, B. A.; Andersen, J. K.; Zhang, J. Z. Femtosecond electronic relaxation dynamics in metal nano-particles: effects of surface and size confinement, *Mol. Cryst. Liq. Cryst.* **283**, 25-30 (1996)

37. Wang, Y. Nonlinear optical properties of nanometer-sized semiconductor clusters, *Acc. Chem. Res.* **24**, 133-139 (1991)

38. Zhang, J. Z. Ultrafast studies of electron dynamics in semiconductor and metal colloidal nanoparticles: effects of size and surface, *Acc.Chem. Res.* **30**, 423-429 (1997)

39. Schoonman, J. Nanostructured materials in solid state ionics, *Solid State Ionics* **135**, 5-19 (2000)

40. http://www.evidenttech.com (2005)

41. Nalwa, H. S. *Hand Book of Nanostructured Materials and Nanotechnology-Electrical Properties* (Academic Press, 2000)

42. Klabunde, K. J. *Free Atoms, Cluster, and Nanoscale Particles* (Academic Press, San Diego, 1994)

43. Klabunde, K. J.; Mohs, C. *Chemistry of Advanced Materials: An Overview* (Wiley-VHC, New York, 1998)

44. Klabunde, K. J. *Nanoscale Materials in Chemistry* (Wiley, New York, 2001)

45. Faraday, M. The Bakerian lecture: experimental relations of gold (and other metals) to light, *Philos. Trans. Roy. Soc. London* **147**, 145-181 (1857)

46. Kubo, R. Electronic properties of metallic fine particles I, *J. Phys. Soc. Jpn.* **17**, 975-986 (1962)

47. Kharirutdinow, R. F. Chemistry of semiconductor nanoparticles. *Russ. Chem. Rev.* **67**, 109-122 (1998)

48. Schmit, G. *Clusters and Colloids: From Theory to Applications* (VCH, New York, 1994)

49. Suslick, K. S. *Ultrasound: Its Chemical, Physical and Biological Effect* (VCH, Weinheim, 1988)

50. Interrante, L. V.; Hampden-Smith, M. J. *Chemistry of Advanced Materials* (Wiley-VCH, New York, 1998)

51. Gates, B. C. Supported metal clusters: synthesis, structure, and catalysis, *Chem. Rev.* **95**, 511-522 (1995)

52. Pileni, M. P. Nanosized particles made in colloidal assemblies, *Langmuir* **13**, 3266-3276 (1997)

53. Reetz, M. T.; Helbig, W. J. Size-selective synthesis of nanostructured transition metal clusters, *J. Am. Chem. Soc.* **116**, 7401-7402 (1994)

54. Bandyopadhyay, S.; Chakravorty, D. J. Preparation of nanocrystalline copper by electrodeposition, *Mater. Res.* **12**, 2719-2724 (1997)

55. Davis, S. C.; Klabunde, K. J. Unsupported small metal particles: preparation, reactivity, and characterization, *Chem. Rev.* **82**, 153-208 (1982)

56. Lewis, L. N. Chemical catalysis by colloids and clusters, *Chem. Rev.* **93**, 2693-2730 (1993)

57. Avery, S. V.; Howlett, N. G.; Radice, S. Copper toxicity towards Saccharomyces cerevisiae: dependence on plasma membrane fatty acid composition. *Appl. Environ. Microbiol.* **62**, 3960- 3966 (1996)

58. Cioffi, N. *et al.* Antifungal activity of polymer-based copper nanocomposite coatings, *Appl. Phys. Lett.* **85**, 2417-2419 (2004)

59. Cioffi, N. *et al.* Copper nanoparticle/polymer composites with antifungal and bacteriostatic properties, *Chem. Mater.* **17**, 5255-5262 (2005)

60. Trapalis, C. C.; Kokkoris, M.; Perdikakis, G.; Kordas, G. Study of antibacterial composite Cu/SiO_2 thin coatings, *J. Sol-Gel Sci. Technol.* **26**, 1213-1218 (2003)

61. Esteban-Cubillo, A.; Pecharromán, C.; Aguilar, E.; Santarén, J.; Moya, J. S. Antibacterial activity of copper monodispersed nanoparticles into sepiolite, *J. Mater. Sci.* **41**, 5208-5212 (2006)

62. Kamrupi, I. R.; Dolui, S. K. Synthesis of copper–polystyrene nanocomposite particles using water in supercritical carbon dioxide medium and its antimicrobial activity, *J. Appl. Polym. Sci.* **120**, 1027-1033 (2011)

63. Gu, C.; Sun, B.; Wu, W.; Wang, F.; Zhu, M. Synthesis, characterization of copper-loaded carboxymethyl-chitosan nanoparticles with effective antibacterial activity, *Macromol. Symp.* **254**, 160-166 (2007)

64. Ramstedt, M. *et al.* Synthesis and characterization of poly (3-sulfopropylmethacrylate) brushes for potential antibacterial applications, *Langmuir* **23**, 3314-3321 (2007)

65. Li, X. K.; Ji, W. J.; Zhao, J.; Wang, S. J.; Au, C. T. Ammonia decomposition over Ru and Ni catalysts supported on fumed SiO_2, MCM-41, and SBA-15, *J. Catal.* **236**, 181-189 (2005)

66. Heracleous, E.; Lee, A. F.; Wilson, K.; Lemonidou, A. A. Investigation of Ni-based alumina-supported catalysts for the oxidative dehydrogenation of ethane to ethylene: structural characterization and reactivity studies, *J. Catal.* **231**, 159-171 (2005)

67. Fatsikostas, A. N.; Verykios, X. E. Reaction network of steam reforming of ethanol over Ni-based catalysts, *J. Catal.* **225**, 439-452 (2004)

68. Molina, A. I. *et al.* Nickel supported on porous silica as catalysts for the gas-phase hydrogenation of acetonitrile, *J. Catal.* **225**, 479-488 (2004)

69. Li, Y.; Zhang, B.; Xie, X.; Liu, J.; Xu, Y.; Shen, W. Novel Ni catalysts for methane decomposition to hydrogen and carbon nanofibers, *J. Catal.* **238**, 412-424 (2006)

70. Lee, K. B.; Park, S.; Mirkin, C. A. Multicomponent magnetic nanorods for biomolecular separations, *Angew. Chem. Int. Edn* **43**, 3048-3050 (2004)

71. Lee, I. S. *et al.* Ni/NiO core/shell nanoparticles for selective binding and magnetic separation of histidine-tagged proteins, *J. Am. Chem. Soc.* **128**, 10658-10659 (2006)

72. Liang, W.; Whangbo, M. H. Conductivity anisotropy and structural phase transition in covellite CuS, *Solid State Commun.* **85**, 405-408 (1993)

73. Nair, M. T. S.; Nair, P. K. Chemical bath deposition of Cu_xS thin films and their prospective large area applications, *Semicond. Sci. Technol.* **4**, 191-199 (1989)

74. Folmer, J. C. W.; Jellinek, F. The valence of copper in sulphides and selenides: an X-ray photoelectron spectroscopy study, *J. Less-common Met.* **76**, 153-162 (1980)

75. Paul, P. P.; Rauchfuss, T. B.; Wilson, S. R. General synthesis of metalloid polysulphide complexes from the elements: structures of Sb2S152- and InS8 (N-Melm), *J. Am. Chem. Soc.* **115**, 3316-3317 (1993)

76. Grijavala, H.; Inoue, M.; Buggavarapu, S.; Calvert, P. Amorphous and crystalline copper sulphides, CuS, *J. Mater. Chem.* **7**, 1157-1160 (1996)

77. Peiris, M.; Sweeney, J. S.; Campbell, A. J.; Heinz, D. L. Pressure-induced amorphization of covellite, CuS, *J. Chem. Phys.* **104**, 11-16 (1996)

78. Wells, A. F. *Structural Inorganic Chemistry* (Oxford Science Publications, 1984)

79. Jr. Evans, H. T.; Konnert, J. Crystal structure refinement of covellite, *Am. Mineral.* **61**, 996-1000 (1976)

80. Parkin, I. P. Solid state metathesis reaction for metal borides, silicides, pnictides and chalcogenides: ionic or elemental pathways, *Chem. Soc. Rev.* **25**, 199-207 (1996)

81. Yi, H. C.; Moore, J. J. Self-propagating high-temperature (combustion) synthesis (SHS) of powder-compacted materials, *J. Mater. Sci.* **25**, 1159-1168 (1990)

82. Mingos, D. M. P.; Baghurst, D. R. Applications of microwave dielectric heating effects to synthetic problems in chemistry, *Chem. Soc. Rev.* **20**, 1-47 (1991)

83. Ohtani, T.; Motoki, M.; Koh, K.; Ohshima, K. Synthesis of binary copper chalcogenides by mechanical alloying, *Mater. Res. Bull.* **30**, 1495-1504 (1995)

84. Zhu, H.; Ji, X.; Yang, D.; Ji, Y.; Zhang H. Novel CuS hollow spheres fabricated by a novel hydrothermal method, *Microporous Mesoporous Mater.* **80**, 153-156 (2005)

85. Henshaw, G.; Parkin, I. P.; Shaw, G. A. Convenient, room-temperature liquid ammonia routes to metalchalcogenides, *J. Chem. Soc., Dalton Trans.* **2**, 231-236 (1997)

86. Gautam, U. K.; Mukherjee, B. A simple synthesis and characterization of CuS nanocrystals, *Bull. Mater. Sci.* **29**, 1-5 (2006)

87. Lu, J.; Zhao, Y.; Chen, N.; Xie, Y. A novel in situ template-controlled route to CuS nanorods via transition metal liquid crystals, *Chem. Lett.* **32**, 30-31 (2003)

88. Shen, G.; Cho, J. H.; Yoo, Y. K.; Yi, G. C.; Lee, C. J. Synthesis of single-crystal CdS microbelts using a modified thermal evaporation method and their photoluminescence, *J. Phys. Chem .B.* **109**, 9294-9298 (2005)

89. Danaher, W. I.; Lyons, L. E.; Morris, G. C. Some properties of thin films of chemically deposited cadmium sulphide, *Sol. Energy Mater.* **12**, 137-148 (1985)

90. Weinhardt, L. *et al.* CdS and $Cd(OH)_2$ formation during Cd treatments of $Cu(In,Ga)(S,Se)_2$ thin-film solar cell absorbers, *Appl. Phys. Lett.* **82**, 571-573 (2003)

91. Luque, A.; Hegedus, S. *Handbook of Photovoltaic Science and Engineering* (John Wiley & Sons, 2003)

92. Reynolds, D.; Leies, G.; Antes, L.; Marburger, R. Photovoltaic effect in cadmium sulphide, *Phys. Rev.* **96**, 533-534 (1954)

93. Fouassier, C. *Luminescence in Encyclopaedia of Inorganic Chemistry* (John Wiley & Sons, ISBN 0471936200, 1994)

94. Gleiter, H. Nanostructured materials: basic concepts and microstructure, *Acta Mater.* **48**, 1-29 (2000)

95. Skorokhod, V. V.; Ragulya, A. V.; Uvarova, I. V. *Physico-Chemical Kinetics in Nanostructured Systems* (Academperiodica, Kid, 2001)

96. Pokropivny, V. V.; Skorokhod, V. V. Classification of nanostructures by dimensionality and concept of surface forms engineering in nanomaterial science, *Mater. Sci. Eng. C* **27**, 990-993 (2007)

97. Schmid, G. *Nanoparticles From Theory to Application* (WILEY-VCH, Verlaag Weinheim, Germany, 2004)

98. Lin, B.; Fu, Z.; Jia, Y. Green luminescent center in undoped zinc oxide films deposited on silicon substrates, *Appl. Phys. Lett.* **79**, 943-945 (2001)

99. Tanigaki, T.; Saito, Y.; Nakada, T.; Tsuda, N.; Kaito, C. Structure of carbon-coated or silicon-oxide-coated ZnTe, ZnSe and ZnS nanoparticles produced by gas evaporation technique, *J. Nanopart. Res.* **4**, 83-90 (2002)

100. Murray, C. B.; Norris, D. J.; Bawendi, M. G. Synthesis and characterization of nearly monodisperse CdE (E = sulfur, selenium, tellurium) semiconductor nanocrystallites, *J. Am. Chem. Soc.* **115**, 8706-8715 (1993)

101. Peng, X. G.; Schlamp, M. C.; Kadavanich, A. V.; Alivisatos, A. P. Epitaxial growth of highly luminescent CdSe/CdS core/shell nanocrystals with photostability and electronic accessibility, *J. Am. Chem. Soc.* **119**, 7019-7029 (1997)

102. Peng, Z. A.; Peng, X. Mechanisms of the shape evolution of CdSe nanocrystals, *J. Am. Chem. Soc.* **123**, 1389-1395 (2001)

103. Berry, C. R. Structure and optical absorption of AgI microcrystals, *Phys. Rev.* **161**, 848-851 (1967)

104. Rossetti, R.; Ellison, J. L.; Gibson, J. M.; Brus, L. E. Size effects in the excited electronic states of small colloidal CdS crystallites, *J. Chem. Phys.* **80**, 4464-4469 (1984)

105. Spanhel, L.; Hasse, M.; Weller, H.; Henglein, A. Photochemistry of colloidal semiconductors. 20. Surface modification and stability of strong luminescing CdS particles, *J. Am. Chem. Soc.* **109**, 5649-5655 (1987)

106. Gaponik, N. *et al.* Thiol-capping of CdTe nanocrystals: an alternative to organometallic synthetic routes, *J. Phys. Chem. B* **106**, 7177-7185 (2002)

107. Mandal, A.; Tamai, N. Influence of acid on luminescence properties of thioglycolic acid-capped CdTe quantum dots, *J. Phys. Chem. C* **112**, 8244-8250 (2008)

108. Lu, Q.; Gao, F.; Zhao, D. The assembly of semiconductor sulphide nanocrystallites with organic reagents as templates, *Nanotechnology* **13**, 741-745 (2002)

109. Pileni, M. P. II-VI semiconductors made by soft chemistry: syntheses and optical properties, *Catal. Today* **58**, 151-166 (2000)

110. Zhao, H.; Douglas, E. P.; Harrison, B. S.; Schanze, K. S. Preparation of CdS nanoparticles in salt-induced block copolymer micelles, *Langmuir* **17**, 8428-8433 (2001)

111. Zhou, H. S.; Honma, I.; Komiyama, H.; Haus, J. W. Coated semiconductor nanoparticles; the cadmium sulphide/lead sulphide system's synthesis and properties, *J. Phys. Chem.* **97**, 895-901 (1993)

112. Cushing, B. L.; Kolesnichenko, V. L.; O'Connor, C. J. Recent advances in the liquid-phase syntheses of inorganic nanoparticles, *Chem. Rev.* **104**, 3893-3946 (2004)

113. Gomez-Romero, P. Hybrid organic-inorganic materials-in search of synergic activity, *Adv. Mat.* **13**, 163-174 (2001)

114. Roylance, D. *Introduction to Composite Materials* (Massachusetts Institute of Technology, Cambridge 2000)

115. Ghosh, P. *Polymer Science and Technology: Plastic, Rubbers, Blends and Composites* (Tata McGraw-Hill Com., New Delhi, 2002)

116. Richardson, T. *Composites: A Design Guide* (Industrial Press Inc. 200 Madison Avenue, NewYork, 1987)

117. Coronado, E.; Galan-Mascaros, J. R.; Gomez-Garcia, C. J.; Laukhin, V. Coexistence of ferromagnetism and metallic conductivity in a molecule-based layered compound, *Nature* **408**, 447-449 (2000)

118. Croce, F.; Appetecchi, G. B.; Persi, L.; Scrosati, B. Nanocomposite polymer electrolytes for lithium batteries, *Nature* **394**, 456-458 (1998)

119. Pinnavaia, T. J. Intercalated clay catalysts, *Science* **220**, 365-371 (1983)

120. Wang, Y.; Herron, N. X-ray photoconductive nanocomposites, *Science* **273**, 632-634 (1996)

121. Winiarz, J. G.; Zhang, L. M.; Lal, M.; Friend, C. S.; Prasad, P. N. Observation of the photorefractive effect in a hybrid organic-inorganic nanocomposite, *J. Am. Chem. Soc.* **121**, 5287-5295 (1999)

122. Sidorov, S. N. *et al.* Platinum-containing hyper-cross-linked polystyrene as a modifier-free selective catalyst for l-sorbose oxidation, *J. Am. Chem. Soc.* **123**, 10502- 10510 (2001)

123. Merkel, T. C. *et al.* Ultrapermeable, reverse-selective nanocomposite membranes, *Science* **296**, 519-522 (2002)

124. Joly, C.; Smaihi, M.; Porcar, L.; Noble, R. D. Polyimide-silica composite materials: how does silica influence their microstructure and gas permeation properties?, *Chem. Mater.* **11**, 2331-2338 (1999)

125. Shirakawa, H.; Louis, E. J.; MacDiramid, A. G.; Chiang, C. K.; Heeger, A. J. Synthesis of electrically conducting organic polymers: halogen derivatives of polyacetylene, (CH)x, *Chem. Commun.* 578-580 (1977)

126. Heeger, A. J. Semiconducting and metallic polymers: the fourth generation of polymeric materials, *Synth. Met.* **125**, 23-42 (2001)

127. Hughes, G.; Bryce, M. R. Electron-transporting materials for organic electroluminescent and electrophosphorescent devices, *J. Mater. Chem.* **15**, 94-107 (2005)

128. Singh, T. B.; Sariciftci, N. S. Progress in plastic electronics devices, *Annu. Rev. Mater. Res.* **36**, 199-230 (2006)

129. Thomas III, S. W.; Joly, G. D.; Swager, T. M. Chemical sensors based on amplifying fluorescent conjugated polymers, *Chem. Rev.* **107**, 1339-1386 (2007)

130. Gunes, S.; Neugebauer, H.; Sariciftci, N. S. Conjugated polymer-based organic solar cells, *Chem. Rev.* **107**, 1324-1338 (2007)

131. Yang, X.; Loos, T. Toward high-performance polymer solar cells: the importance of morphology control, *Macromol.* **40**, 1353-1362 (2007)

132. Facchetti, A. Semiconductors for organic transistors, *Materials Today* **10**, 28-37 (2007)

133. Kalinoswki, J. Optical materials for organic light-emitting devices, *Opt. Mater.* **30**, 792-799 (2008)

134. Lutz, J. F.; Börner, H. G. Modern trends in polymer bioconjugates design, *Prog. Polym. Sci.* **33**, 1-39 (2008)

135. Rahman, M. A.; Kumar, P.; Park, D. S.; Shim, Y. B. Electrochemical sensors based on organic conjugated polymers, *Sensors* **8**, 118-141 (2008)

136. Smela, E. Conjugated Polymer Actuators, *MRS Bull.* **33**, 197-204 (2008)

137. Wang, H. L.; MacDiarmid, A. G.; Wang, Y. Z.; Gebler, D. D.; Epstein, A. J. Application of polyaniline (emeraldine base, EB) in polymer light-emitting devices, *Synth. Met.* **78**, 33-37 (1996)

138. Diaz, A. F.; Kanazava, K. K.; Gardini, G. P. Electrochemical polymerization of pyrrole, *J. Chem. Soc., Chem. Commun.* **24**, 635-636 (1979)

139. Burgmayer, P.; Murray, R.W. Faster ion gate membranes, *J. Electroanal. Chem.* **147**, 339-344 (1983)

140. Braun, D.; Heeger, A. J. Visible light emission from semiconducting polymer diodes, *Appl. Phys. Lett.* **58**, 1982-1984 (1991)

141. Tourillon, G.; Garnier, F. New electrochemically generated organic conducting polymers, *J. Eletroanal. Chem.* **135**, 173-178 (1982)

142. Pud, A.; Ogurtsov, N.; Korzhenko, A.; Shapoval, G. Some aspects of preparation methods and properties of polyaniline blends and composites with organic polymers, *Prog. Polym. Sci.* **28**, 1701-1753 (2003)

143. Cao, Y.; Smith, P.; Heeger, A. J. Counter-ion induced processibility of conducting polyaniline and of conducting polyblends of polyaniline in bulk polymers, *Synth. Met.* **48**, 91-97 (1992)

144. MacDiarmid, A. G.; Epstein, A. J. Polyanilines: a novel class of conducting polymers, *Fraraday Discuss. Chem. Soc.* **88**, 317-332 (1989)

145. Stejskal, J.; Kratochvil, P.; Jenkins, A. D. The formation of polyaniline and the nature of its structures, *Polymer* **37**, 367-369 (1996)

146. Trivedi, D. C.; Nalwa, H. S. (Ed.): *In Handbook of Organic Conductive Molecules and Polymers* (John Wiley & Sons Ltd, Wiley, Chichester, England, 1997)

147. Gospodinova, N.; Terlemezyan, L. Conducting polymers prepared by oxidative polymerization: polyaniline, *Prog. Polym. Sci.* **23**, 1443-1484 (1998)

148. Ray, A. *et al.* Polyaniline: doping, structure and derivatives, *Synth. Met.* **29**, 141-150 (1989)

149. Armes, S. P.; Miller, J. F. Optimum reaction conditions for the polymerization of aniline in aqueous solution by ammonium persulphate, *Synth. Met.* **22**, 385-393 (1988)

150. Genies, E. M.; Tsintavis, C. Redox mechanism and electrochemical behaviour of polyaniline deposits, *J. Electroanal. Chem.* **195**, 109-128 (1985)

151. Genies, E. M.; Łapkowski, M. Electrochemical in situ epr evidence of two polaron-bipolaron states in polyaniline, *J. Electroanal. Chem.* **236**, 199-208 (1987)

152. Kobayashi, T.; Yoneyama, H.; Tamura, H. Oxidative degradation pathway of polyaniline film electrodes, *J. Electroanal. Chem.* **177**, 293-297 (1984)

153. Wang, B.; Tang, J.; Wang, F. The effect of anions of supporting electrolyte on the electrochemical polymerization of aniline and the properties of polyaniline, *Synth. Met.* **13**, 329-334 (1986)

154. Watanabe, A.; Mori, K.; Mikuni, M.; Nakamura, Y.; Matsuda, M. Comparative study of redox reactions of polyaniline films in aqueous and nonaqueous solutions, *Macromol.* **22**, 3323-3327 (1989)

155. Teshima, K.; Yamada, K.; Kobayashi, N.; Hirohashi, R. M. Effect of electropolymerization temperature on structural, morphological and conductive properties of poly(aniline) deposits prepared in 1,2-dichloroethane without a proton donor, *J. Electroanal. Chem.* **426**, 97-102 (1997)

156. Gholamian, M.; Contractor, A. Q. Effect of the temperature of synthesis on the conductivity and electrochemical behaviour of polyaniline, *J. Electroanal. Chem.* **252**, 291-301 (1988)

157. Poddar, P.; Wilson, J. L.; Srikanth, H.; Morrison, S. A.; Carpenter, E. E. Magnetic properties of conducting polymer doped with manganese-zinc ferrite nanoparticles, *Nanotechnology* **15**, S570-S574 (2004)

158. Lee, T. W.; Park, O. O.; Kim, J. J.; Hong, J. M.; Kim, Y. C. Efficient photoluminescence and electroluminescence from environmentally stable polymer/clay nanocomposites, *Chem. Mater.* **13**, 2217-2222 (2001)

159. Goodman, M. D.; Xu, J.; Wang, J.; Lin, Z. Semiconductor conjugated polymer-quantum dot nanocomposites at the air/water interface and their photovoltaic performance, *Chem. Mater.* **21**, 934-937 (2009)

160. Zhou, H. S.; Wada, T.; Sasabe, H.; Komiyama, H. Synthesis and optical properties of nanocomposite silver-polydiacetylene, *Synth. Met.* **81**, 129-132 (1996)

161. Zhou, H. S.; Wada, T.; Sasabe, H.; Komiyama, H. Synthesis of nanometer-size silver coated polymerized diacetylene composite particles, *Appl. Phys. Lett.* **68**, 1288-1290 (1996)

162. Masuhara, A. *et al.* Hybridized microcrystals composed of metal fine particles and π-conjugated organic microcrystals, *Jpn. J. Appl. Phys. Part 2* **40**, L1129-L1131 (2001)

163. Park, J. E.; Kim, S.; Mihashi, S.; Hatozaki, O.; Oyama, N. Roles of metal nanoparticles on organosulfur-conducting polymer composites for lithium battery with high energy density, *Macromol. Symp.* **186**, 35-40 (2002)

164. Park, J. E.; Park, S. G.; Koukitu, A.; Hatozaki, O.; Oyama, N. Effect of adding Pd nanoparticles to dimercaptan-polyaniline cathodes for lithium polymer battery, *Synth. Met.* **140**, 121-126 (2004)

165. Konwer, S.; Gogoi, J. P.; Kalita, A. Dolui, S. W. Synthesis of expanded graphite filled polyaniline composites and evaluation of their electrical and electrochemical properties, *J. Mater. Sci. - Mater. Electron.* (DOI: 10.1007/s10854-010-0276-7)

CHAPTER 2

Synthesis of Copper (Cu) and Nickel (Ni) Nanoparticles and Their Interaction with Polyaniline (PANI)

2.1. Introduction

Size and shape play a very crucial role in determining the properties of metal nanostructures materials. Simply by controlling the morphology, properties of metal nanostructures can be tailored and this is the beauty of nanostructures materials. Today the field of research on metal nanostructures has greatly extended from simple *1-D* structure to the assembly of nanocrystals into ordered superstructures holding promise for advanced applications in electronics and optoelectronics, and hence an approach toward the future realization of functional nanodevices[1-6]. To get hold of desired morphology, it is indispensable to explore a proper synthesis pathway. However, it is still a challenge to develop simple synthesis pathway for acquiring hierarchically self-assembled architecture and hence it becomes an intensive research topic.

Self-assembly in solution phase has proved to be one of the simplest, versatile and cost effective fabrication approaches to get nanoparticles with different morphologies[7,8]. In solution based self-assembly process, surfactant molecule or capping ligands can act as a building units or shape modifier for spontaneously assembled objects into solution[9,10]. A growing number of literatures are being published on synthesis of complex architecture using different types of surfactants. Combination of oleic acid and oleylamine in a 1: 1 ratio has been used by Watt *et al.* to get branched Pd nanostructures[11]. Sodium dodecyl sulfate (SDS) also served as a shape modifier to facilitate the formation of highly faceted Au nanoparticles[12]. Similar approach has been used by Liu *et al.* to synthesize sea urchin-like metallic nickel nanocrystals[13]. Small chelating ligands such as citric acid, ethylenediaminetetraacetic acid (EDTA) have already been used as shape modifiers to control the morphology of the nanostructures[14,15]. Daxad 19, a sodium salt of polynaphthalene sulphonate formaldehyde condensate was used as a dispersing agent in the preparation of silver nanoparticles[16].

However, in recent times, the use of biomolecules such as DNA[17], peptides[18], proteins[19], amino acid[20] as capping agents find more interests among the scientific community for the synthesis of self-assembled metal nanoarchitectures. Living organism such as tobacco mosaic virus (TMV),[21] bacteria[22] can also serve as templates to get ordered superstructures. For example, gallic acid, a biomolecule has been utilized to get Au and Ag nanostructures[23]. Self-assembled cylindrical particles of wild type and recombinant TMV were used as organic templates for the controlled deposition and organization of Pt, Au, or Ag nanoparticles[24]. From green chemistry point of view, these biomimetic synthesis strategies regulating structures of nanoparticles by biomolecule or organism are very important and such materials have shown to have potential application in biosensors[25], chemical sensors[26] and in the construction of nanoelectronic devices[27].

Shape and size control synthesis of Cu nanoparticles have immense interest as they have potential applications in diverse fields including optical, catalytic, electronic systems[28-30]. For example, copper nanoparticles can be used as catalysts for the growth of single-walled carbon nanotubes[31], for water-gas shifts[32] and gas detoxification reactions[33]. Copper nanopareticles have application as lubricants and they are used as ink in inkjet printing technology and in metallic coating[34-36]. Use of silver ink in inkjet printing conductive traces has been well documented[37]. However, silver as a conductive material has problems due to ion migration at relatively high temperature, humidity conditions as well as cost benefit issues compared to copper, which is significantly low expensive[36,38]. In addition, copper nanoparticles containing polymer composites possess antibacterial and antifungal properties[39]. Different approaches are implemented for the fabrication of Cu nanoparticles including supercritical carbon dioxide[40], high-temperature decomposition of organometallic precursors[41], etc.

Synthesis of magnetic nanostructures with well-defined shapes and sizes have attracted considerable attention recently, owing to their scientific importance and widespread promising applications in magnetic fluid[42], sensors[43], data storage devices[44], high performance electromagnetic[45], as well as environmental remediation[46,47], and biomedical applications, such as magnetic resonance imaging (MRI)[48-50], cell and protein separation[51,52], drug delivery[53], and hyperthermia treatments[54], etc. Among the magnetic nanoparticles, nickel nanoparticles find additional interest among the scientific community, not only because of the magnetic property but also for the high catalytic activity for various reactions such as oxidative dehydrogenation[55], decomposition of ammonia[56], hydrogenation[57] and more recently the formation of carbon nanotubes (CNTs)[58]. Many synthesis approaches have been reported for Ni nanoparticles. The synthesis of pure black Ni powder through reduction of aqueous $NiSO_4$ with hydrazine has been reported by Li *et al.*[59]. Flower shaped Ni nanocrystals has been prepared using a hydrothermal chemical reduction containing a mixture of $Ni(N_2H_4)_3^{2+}$ and $Ni(dmg)_2$ (dmg = dimethylglyoximate) as the nickel source[60]. The solution reduction of $Ni(acac)_2$ (acac = acetylacetonate) by sodium borohydride or superhydride in the presence of hexadecylamine (HDA) and trioctylphosphine oxide (TOPO) in dichlorobenzene has been employed to produce nickel nanoparticles by Hou *et al.*[61]. Recently, Ni nanoparticles have been synthesized via a facile water-based method utilizing the neutral pluronic triblock copolymers and oleic acids as stabilizing agents[62].

There have been attempts to combine the advantages of metal nanoparticles and polyaniline by conjugating them into hybrid composites that can be cast into useful devices in thin film configurations. Enhanced catalytic, electrical, optical performance of nanoparticles composites materials have been reported[63-65].

This study reports a one-step synthesis route for the preparation of stable colloidal dispersions of Cu and Ni nanostructures in ethylene glycol using a biocompatible molecule, tannic acid as reducing as well as capping agent. Tannic acid is typically hydrolyzed tannin (present in woods like oak, walnut and mahogany), a mixed gallotannin composed of gallic acid esters of glucose, which has been used for the biomimetic growth of inorganic nanoparticles[66]. Compared to other approaches, this path way has some advantages: (1) the reaction is environmental friendly, simple, quick, and one-step approach; (2) the reagents are green; (3) there is no need to add extra stabilizing agent or capping agent; (4) no other toxic chemicals like TOPO, TOP, etc. are involved; (5) alkaline condition is not necessary; and importantly (6) the dispersion of nanoparticles is remarkably stable. Further, literature survey reveals that extensive work has been devoted to the preparation of noble metal/PANI nanocomposites like Au, Pd and Pt because of their stability and ease of preparation[67-69]. In this chapter, attempts have been made to synthesize Cu/PANI and Ni/PANI nanocomposites using a simple and general procedure. The effect of nanoparticles on the optical and electrical behaviour of the nanocomposites has also been investigated.

2.2. Materials and method

2.2.1. Materials.

Copper acetate monohydrate (CuAc) ($Cu(CH_3COO)_2.\ H_2O$), nickel chloride hexahydrate ($NiCl_2.6H_2O$), tannic acid (TA) ($C_{76}H_{52}O_{46}$), and aniline (99%, monomer) were obtained from Fluka. Potassium peroxydisulfate (KPS) ($K_2S_2O_8$) was purchased from Merck. Ethylene glycol (EG), ethanol and hydrochloric acid were of the highest purity commercially available and used without further purification. Double distilled water was used in all reactions.

2.2.2. Synthesis of metal nanoparticles

Both Cu and Ni nanoparticles were synthesized via a soft chemical synthesis route using environmentally benign reagents namely TA and EG. For metal nanoparticles synthesis, at first 30 ml of 0.004 M CuAc or $NiCl_2$ was dissolved in EG and then heated upto 90 °C under magnetic stirring inside a round bottom flask equipped with a condenser. Then 5 ml 0.04 M TA in EG was rapidly added into the metal salt solutions under vigorously stirred condition and temperature was allowed to raise up to 140 °C. Nitrogen was purged throughout the reaction. As reduction occurred, the colour of the CuAc suspension turned wine red within 2 h while the $NiCl_2$ suspension became yellow within 1 h. A few batches of metal nanoparticles were synthesized by varying TA concentrations (0.02 M and 0.06 M) to examine its effect on particle size, morphology and stability of metal nanoparticles.

2.2.3. Synthesis of polyaniline (PANI)

For the synthesis of PANI, 1 ml (0.01 mole) of aniline was dissolved in 10 ml of 1.5 M HCl solution in a 50 ml conical flask and cooled down to 0 °C. The oxidizing agent was prepared by dissolving 0.0166 g (0.0125 mole) of KPS in 5 ml 1.5 M HCl solution. KPS solution was added dropwise to the aniline solution while stirring and continued to add for 1 h keeping the reaction temperature at 0 °C. The reaction mixture was then left to warm up to room temperature. Afterwards the reaction mixture was filtered under gravity, washed with 1.5 M HCl and double distilled water until the washing liquid become colourless and finally dried at 60 °C for 24 h under vacuum to obtain a fine tint green powder.

2.2.4. Synthesis of metal nanoparticles/PANI nanocomposites

Metal nanoparticles composites with PANI have been synthesized by *in-situ* polymerization technique. The polymerization was carried out by injecting 1 ml aniline into 10 ml of 1.5 M HCl with 0.1 g of as-synthesized metal nanoparticles under constant stirring. After 2 h, 0.0166 g KPS (dissolved in 10 ml water) was then dropped into the solution with constant stirring. The polymerization was allowed to proceed for 5 h. The reaction mixture was then filtered under gravity, washed repeatedly with 1.5 M HCl followed by double distilled water, and finally dried at 60 °C for 24 h under vacuum. The final products were obtained in powdery form with green tint.

2.2.5. Characterization of metal nanoparticles and metal/PANI nanocomposites

2.2.5.1. Scanning electron microscope (SEM)

SEM is a characterization technique that can yield data about a sample's topography, morphology, composition and crystallography. The benefit of the SEM over other electron microscopes is that it provides a highly magnified image of the surface of a material that is very similar to what one would expect if one could actually "see" the surface visually.

Top-down SEM images of the samples were conducted in a high-resolution field emission scanning electron microscope (FEI INSPECT F, model no. FP 2031/11) operating at a voltage of 5 kV.

2.2.5.2. Transmission electron microscope (TEM)

TEM allows the imaging of individual particles and to some extent, to evaluate the statistical distribution of sizes and shapes of the particles in sample. High magnification imaging with lattice contrast allows imaging of individual crystallite morphologies. However, TEM is a local probe because only particles in a very small area can be probed, and it is not possible to get an impression of a large number of particles that are statistically oriented. Furthermore, it is tricky to find individual particles, and only a part of such particles can be seen under the microscope from which information on the shape and size is not completely disclosed.

Transmission electron microscopy (TEM) images were taken on JEOL-JEM-2000FX transmission electron microscope. The samples were prepared by sonication in EG for 10 min prior to transfer to copper grids. To obtain an accurate estimation of the average particle size, at least 100 particles were manually counted.

2.2.5.3. Atomic force microscope (AFM)

AFM provides images of overall morphology and structural details without any chemical treatment (etching or staining) of the specimens. It is possible to extract some information about the particle shape and size from the AFM image but difficulties arise especially for very small nanoparticles (~1 nm) because of the greater influence of the substrate. Moreover, the particles should be large enough and should not coalesce on the substrate. Furthermore, AFM is also a local probe and, similar to TEM, it does not give the statistical information about the particles.

AFM provides images of structural details without any chemical treatment (etching or staining) of the specimens. The AFM used was a DME 2452 DualScope Scanner DS Atomic Force Microscope. Scans were carried out in AC mode under ambient conditions with a silicon microcantilever probe tips, using the parameters: force constant: 60,000 N/m; force: 0.15 nN; loop gain: 1,000 loop filter: 3 Hz.

2.2.5.4. Fourier transform infrared spectrometer (FTIR)

FTIR is a useful method for the characterization of compounds. It is primarily used for the detection of functional groups, but analysis of spectra in the lower frequency finger print region can give evidence of the effect of substituent on the properties of the material concerned.

Spectra were recorded from pressed KBr pellets using a Perkin Elmer FT-IR spectrometer in the range of 4000-400 cm^{-1} at room temperature.

2.2.5.5. Powder X-ray diffraction (XRD)

XRD technique gives the information about the size and crystallographic structure, chemical composition and physical properties of materials. The particle size can be obtained either by direct computer simulation of the X-ray diffraction pattern or from the full width at half maximum (FWHM) of the diffraction peaks using the Debye-Scherrer formula (***Equation 2.1***).

$$t = \frac{K\lambda}{B\cos\theta} \qquad \textbf{(2.1)}$$

where t is the mean dimension of the nanoparticles, B is the corrected X-ray diffraction broadening, K is a constant dependent on crystalline shape, θ is Bragg angle and λ is the wavelength of X-ray. The line width depends on the crystalline regions within the particle. When the particles are not perfectly crystalline a problem arises in the size estimation. Particles smaller than 25 Å lead to significant broadening of the line width. Furthermore, the validity of Scherrer's equation, the effect of defects, shapes and size distributions on the X-ray diffraction patterns has to be examined. This is possible with a direct computer simulation approach.

XRD data were collected on a Rigaku Miniflex X-ray diffractometer with Cu K_α radiation (λ = 0.15418 nm) at 30 kV and 15 mA using a scan rate of 0.05° s^{-1} in 2θ ranges from 10° to 80°.

2.2.5.6. X-ray photoelectron spectrometer (XPS)

XPS gives not only qualitative and quantitative information of the various species in the sample under investigation but also probes the different chemical environment surrounding the species. Furthermore, it is a surface sensitive technique because even though the ionization occurs to a depth of 10-1000 nm by photons depending on energy and material, only those electrons that originate within few tens of Angstroms below the solid surface can leave the surface without energy loss.

Spectra were acquired on a PHI Quantum 2000 spectrometer with monochromated AlK_α 1486.6 eV X-ray radiation. Samples were loaded into the vacuum chamber within 1 h after being prepared and were subjected to XPS analysis. The analysis area was 1200 μm x 400 μm on each sample. The take off angle in the instrument was set at 90°.

2.2.5.7. Thermogravimetric analysis (TGA)

The thermal characteristics of materials including degradation temperature, absorbed moisture content, etc can be traced with TGA. It determines the weight loss with respect to temperature, which in fact portrays the patterns of thermal response with raising temperature.

Thermogravimetric (TGA-DTG) and differential thermal (DTA) analyses were performed in a Shimadzu TGA-50 thermal analysis apparatus. Prior to the run, sample (typically 50 mg) was stabilized for 30 min at 15 °C and then the temperature was linearly increased from 15 to 800 °C with a ramp of 10 °C min^{-1} using dry nitrogen as a carrier gas.

2.2.6. Evaluation of optical and electrical properties

2.2.6.1. UV-vis spectroscopy

UV-vis absorption is a very first characterization method for the nanomaterials because the absorption features give information about the nanoparticle formation, the band gap and the size distribution of the nanoparticles. However, it is an indirect method for determining the particle size.

UV-vis absorption spectra of the samples were recorded in the range 250-900 nm using Shimadzu UV-2550 UV-visible spectrophotometer.

2.2.6.2. Photoluminescence (PL) spectroscopy

Photoluminescence spectroscopy is a contactless, nondestructive method of probing the electronic structure of materials. Light is directed onto a sample, where it is absorbed and imparts excess energy into the material in a process called photo-excitation. One way this excess energy can be dissipated by the sample is through the emission of light, or luminescence. In the case of photo-excitation, this luminescence is called photoluminescence. The intensity and spectral content of this photoluminescence is a direct measure of various important material properties.

PL spectra were recorded on a Hitachi F- 2500 Fluorescence spectrophotometer, by excitation of the samples at their absorption maximum.

2.2.6.3. I-V characteristics and DC electrical conductivity

The room temperature current-voltage (I-V) characteristics of PANI and metal/PANI nanocomposites were measured with a Keithley 2400 programmable current source meter by the two-probe method in the frequency range of 102-106 Hz.

The temperature dependent direct current (DC) conductivity was measured by the standard four-probe method over a temperature range from 30 up to 110 °C on pellets of approx. 1.5 cm diameter and 2 mm thickness compressed at 700 MPa with a compression-moulding machine with manual hydraulic press. The conductivity of the samples was calculated using the following formula (***Equation 2.2***):

$$\rho = (V/I)\, 2\pi S \qquad (2.2)$$

where ρ is the resistivity of the sample, V is the applied voltage, I is the measured current through the sample, S is the distance between probes.

2.3. Results and discussion

2.3.1. Metal nanoparticles

2.3.1.1. Synthesis of metal nanoparticles

The role of hydroxyl groups present in the polyphenolic compounds in the formation of nanoparticles was investigated earlier and results indicated that the molecule should have at least two hydroxyl groups at the ortho or para positions to each other to undergo two-electron oxidation to the corresponding quinone form for facile reduction of metal ions[70]. TA is a polyphenolic compound, which has great potential to act as a reductant in the formation of metallic nanoparticles. A representative structural formula of TA is shown in **Figure 2.1**. The structural formula of TA shows the presence of 25 phenolic OH groups; but only 10 pairs of o-dihydroxyphenyl groups are capable of taking part in redox reactions to form quinones and donate electrons, because of the chelating action of adjacent hydroxyl groups and constraints on carbon valency[71,72].

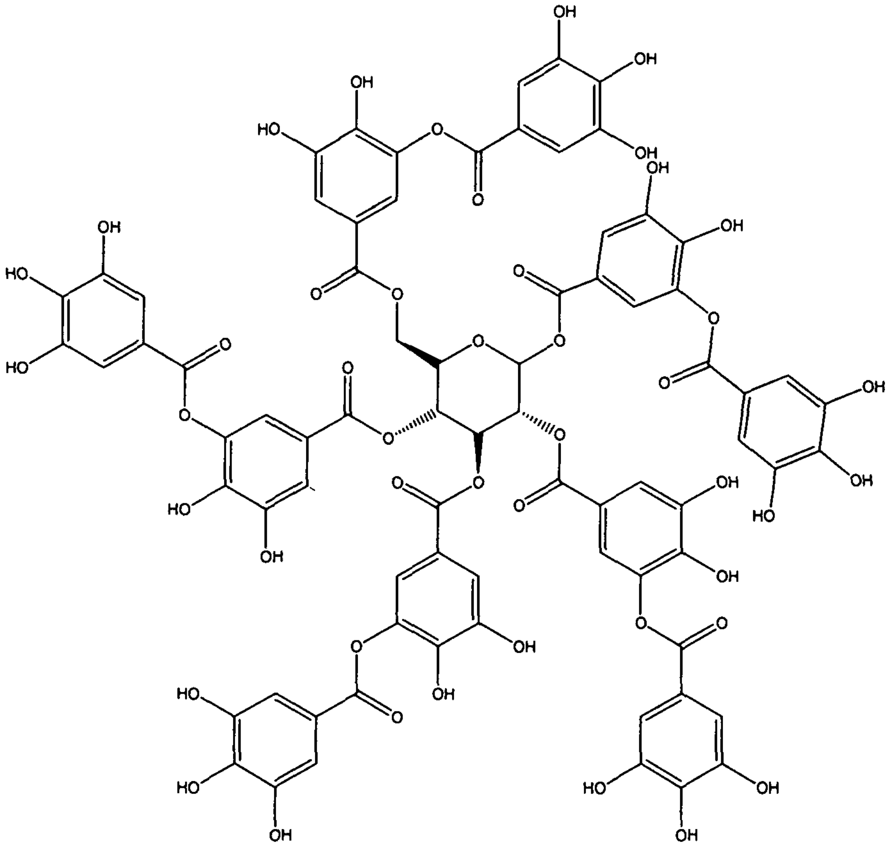

Figure 2.1. The representative structure of tannic acid ($C_{76}H_{52}O_{46}$).

Based on the properties of tannic acid, a possible reaction mechanism for the synthesis of Cu or Ni nanoprticles by TA reduction of CuAc or $NiCl_2$ in EG solution can be outlined in the next page[73].

Zhang *et al.* also reported the formation of Cu(II)-hydroxyl-EG complex as an intermediate in the run up of the reduction of Cu(II) by $NaBH_4$ in EG solvent while synthesizing Cu nanoparticles[74]. During synthesis of Cu nanoparticles, any white-blue precipitate for $Cu(OH)_2$ was not noticed instead the blue coloured solution turned into wine red indicating formation of pure Cu nanoparticles. Even in case of Ni nanoparticles synthesis, there was no formation of pale green precipitate for $Ni(OH)_2$. On the contrary, a yellow coloured dispersion of Ni nanoparticles was obtained. Further, it is well-known that EG is a mild reducing agent. To ascertain the role of EG as reducing agent, model experiments were performed without the aid of TA. However, there was no sign of the

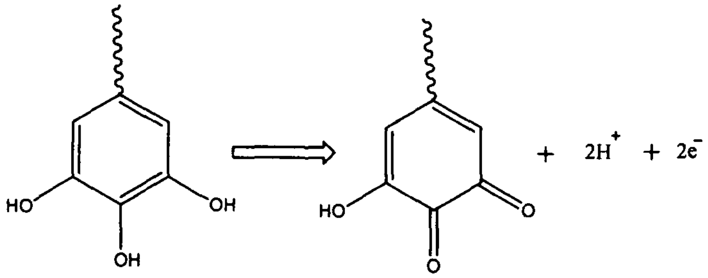

Phenolic form **Quinone form**

$Cu(CH_3COO)_2.H_2O \rightarrow Cu^{2+} + 2CH_3COO^- + H_2O$

CuAc **Copper(II) ion**

$NiCl_2.6H_2O \rightarrow Ni^{2+} + 2Cl^- + 6H_2O$

Nickel(II) ion

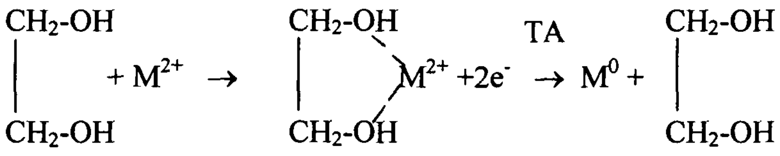

$$\begin{array}{l} CH_2\text{-}OH \\ | \\ CH_2\text{-}OH \end{array} + M^{2+} \rightarrow \begin{array}{l} CH_2\text{-}OH \\ | \\ CH_2\text{-}OH \end{array} M^{2+} + 2e^- \xrightarrow{TA} M^0 + \begin{array}{l} CH_2\text{-}OH \\ | \\ CH_2\text{-}OH \end{array}$$

EG **EG-Cu^{2+} complex** **EG**

where, M= Cu or Ni

formation of metal nanoparticles and this implies that TA is the real solitary reducing agent in the system.

2.3.1.2. XRD analysis of metal nanoparticles

Powder XRD patterns of Cu and Ni nanoparticles synthesized in EG with 0.04 M TA are shown in **Figures 2.2 and 2.3**, respectively. Bragg's reflections for Cu are observed in the XRD pattern at 2θ values of 43.6°, 50.7° and 74.45° representing Miller indices (111), (200) and (220) of face-centred-cubic (fcc) structure of copper with the space group of *Fm3m* (JCPDS No. 4-0836) (**Figure 2.2**). Interestingly, the spectrum has not displayed any other peak that attribute to possible impurities. The crystallite size of the Cu nanoparticles, *t*, was calculated from the major diffraction peaks of Cu(111) with the help of full-width at half maximum (FWHM) using ***Equation 2.1***. The diameter of the nanoparticles calculated by this formula is 8.7 ± 1 nm.

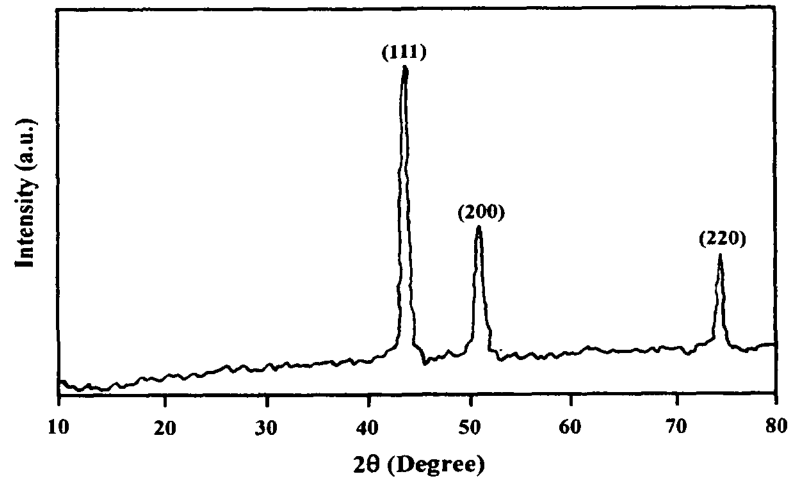

Figure 2.2. X- ray diffraction pattern of Cu nanoparticles synthesised with 0.04 M TA in EG.

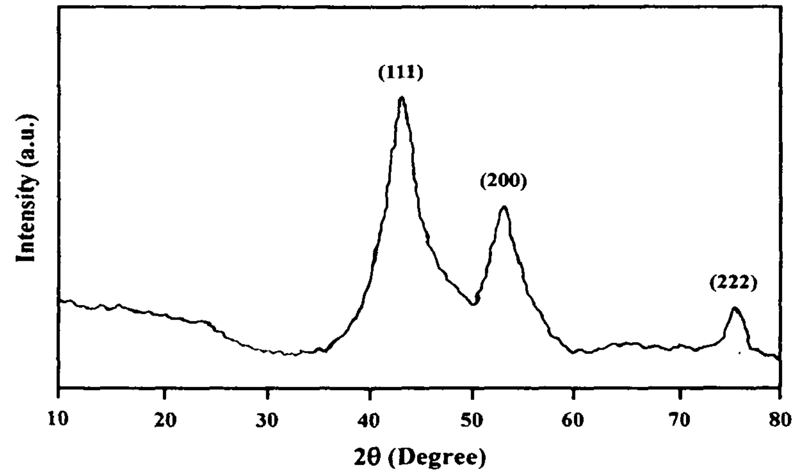

Figure 2.3. X- ray diffraction pattern of Ni nanoparticles synthesised with 0.04 M TA in EG.

For Ni nanoparticles, three characteristic peaks at 2θ values of 44.5°, 51.8°, and 76.4° are observed in diffraction pattern and can be indexed as (111), (200), and (222), respectively (**Figure 2.3**). These reflections reveal that the resultant particles are pure face-centered-cubic (fcc) nickel which is consistent with (PCPDF file no. 04-0850). No impurity peaks assigned to oxides or hydroxide such as NiO, Ni_2O_3, and $Ni(OH)_2$ are found in the experimental range. The crystallite size of the nickel nanoparticles was calculated from the major diffraction peaks of Ni(111) using ***Equation 2.1*** and found to be 5.1 ± 1 nm.

Both metal nanoparticles synthesised are pure. This could be substantiated to four facts: (i) the reaction was conducted in an organic solvent (EG) instead of in an aqueous medium, which might have prevented the formation of oxides or hydroxides; (ii) TA (being a capping agent) protects the resultant nanoparticles from oxidation; (iii) the experimental conditions like temperature and TA concentration were appropriate; and (iv) the reaction was performed by bubbling N_2 gas continuously, which created an inert atmosphere leading to the synthesis of pure metal nanoparticles.

2.3.1.3. FTIR analysis of metal nanoparticles

Figure 2.4 shows the FTIR spectra of Cu and Ni nanoparticles prepared in EG with 0.04 M TA along with pure TA to find out supportive evidence about the interaction of TA with the metal nanoparticles. The broad band at 3400 cm $^{-1}$ is attributed to the -OH stretching of the phenol group and methylol group of TA. This characteristic band of TA is also observed in the spectra of metal nanoparticles, but it became narrow. This could be due to the interaction of hydroxyl groups of TA with metal ions. An absorption band at 2926 cm $^{-1}$ is observed in the spectrum of TA and can be assigned to aromatic C-H stretching mode of vibration. Cu and Ni nanoparticles also posses this characteristic band, however, it shifted slightly to higher wavenumber region. The absorption bands at 1732 cm^{-1} and 1716 cm^{-1} noticed in the TA spectrum are attributed to C=O stretching frequency of ketone and carboxyl groups. These bands are observed in Cu nanoparticles also with slight change in position and intensity. But in case of Ni nanoparticles, these bands are merged and broadened in the range of 1500-1700 cm^{-1} [75]. These changes may be due to the interaction of above functional groups to the surface of the nanoparticles and the presence of the *o*-benzoquinone derivative arising from the oxidation of TA. Further, from **Figure 2.4**, it can be seen that intensities of the bands at 1540 and 1450 cm^{-1} for aromatic C=C bending, and 1323 and 1197 cm^{-1}

corresponding to phenolic C-O stretching vibrations of TA have been reduced in the spectrum of metal nanoparticles indicating that the majority of the TA is present in its oxidised form[70-72,75]. For comparison, the characteristic bands of TA and metal nanoparticles are compiled in **Table 2.1**. The above FTIR features of the nanoparticles indicate that TA acts as capping agent and hence, offers stability to the nanoparticles.

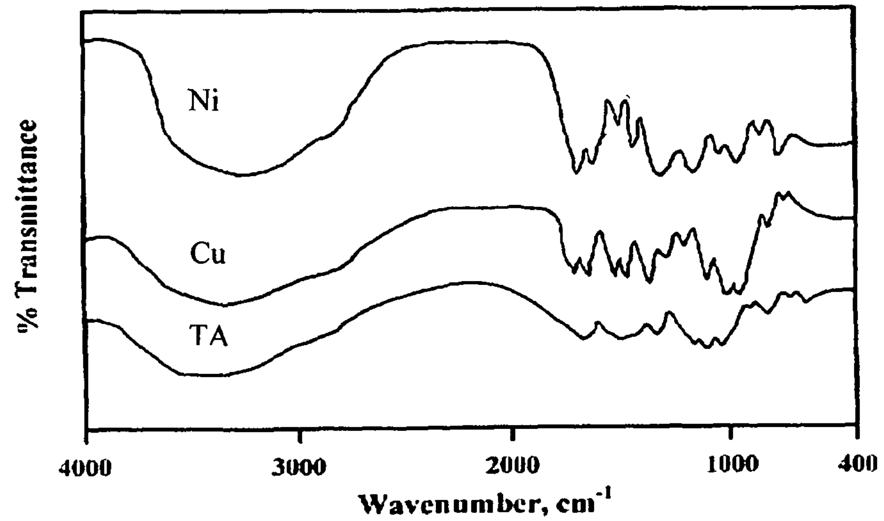

Figure 2.4. FTIR spectra of pure TA, and Cu and Ni nanparticles synthesised with 0.04 M TA in EG.

Table 2.1. Assignment of IR bands for TA and metal nanoparticles

IR band	Assignment	Peak position/Wavenumber cm^{-1}		
		TA	Cu	Ni
$\nu_{O\text{-}H}$ stretching	Phenol and methylol Groups	3400	3400	3400
$\nu_{C\text{-}H}$ stretching	Aromatic C-H bond	2926	2930	2937
$\nu_{C=O}$ stretching	Ketone and carboxyl Groups	1732 & 1716	1735 & 1721	1500-1700
$\nu_{C=C}$ bending	Aromatic C=C bond	1540 & 1450	1538 & 1453	1575
$\nu_{C\text{-}O}$ stretching	Phenolic C-O	1323 & 1197	1330 1187	1326 1192

2.3.1.4. XPS analysis of metal nanoparticles

XPS is a sensitive tool for the analysis of surface chemistry of materials and hence, it was used to analyse metal nanoparticles surface composition. **Figures 2.5 and 2.6** show typical survey spectra of Cu and Ni nanoparticles, respectively, synthesised in EG with 0.04 M TA. The elements detected in the survey spectra of both Cu and Ni are the same (C and O) except the metal.

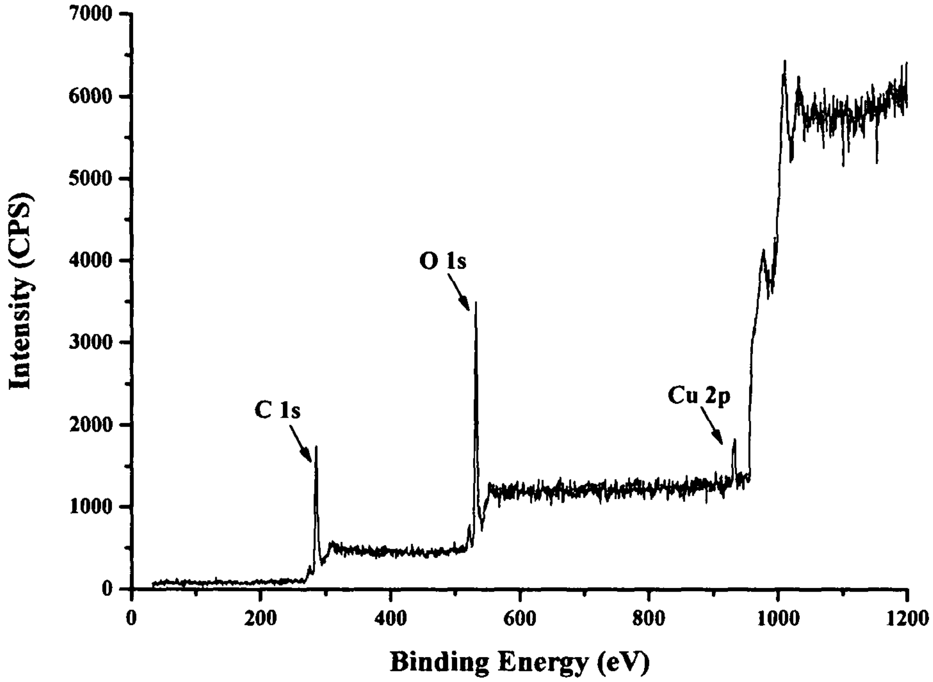

Figure 2.5. X-ray photoelectron survey spectrum of Cu nanoparticles synthesised with 0.04 M TA in EG.

The presence of Cu 2p peak at 932.6 eV in the survey spectrum (**Figure 2.5**) indicates that Cu is in elemental state[76]. The presence of O 1s peak at 532.1 eV and C 1s peak at 284.9 eV in the survey spectrum could be assigned to O=C-O linkage[77] and C_6H_5CO linkage[78], respectively. These moieties are most common in the complex structure of TA. This implies the adherence of TA to the surface of Cu nanoparticles.

The high resolution spectrum of Cu 2p exhibits the characteristic peak of Cu $2p_{3/2}$ at 932.6 eV with no detactable shake-up peak at ~ 934 eV[79], pointing to the absence of Cu(II) oxides (**Figure 2.7**). The amount of Cu quantitatively estimated from the Cu 2p peak area as 5.21%.

From **Figure 2.6**, the Ni $2p_{3/2}$ peak identified at 858.0 eV implies that Ni exists as Ni^0 state[80]. Wang *et al.* reported binding energies of Ni 2p3/2 at 855.61 and 852.97 eV for Ni^{3+} and Ni^{2+}, respectively[81]. The high resolution spectrum of Ni (2p) indicates the absence of prominent peaks for other oxidation states of Ni (**Figure 2.8**).

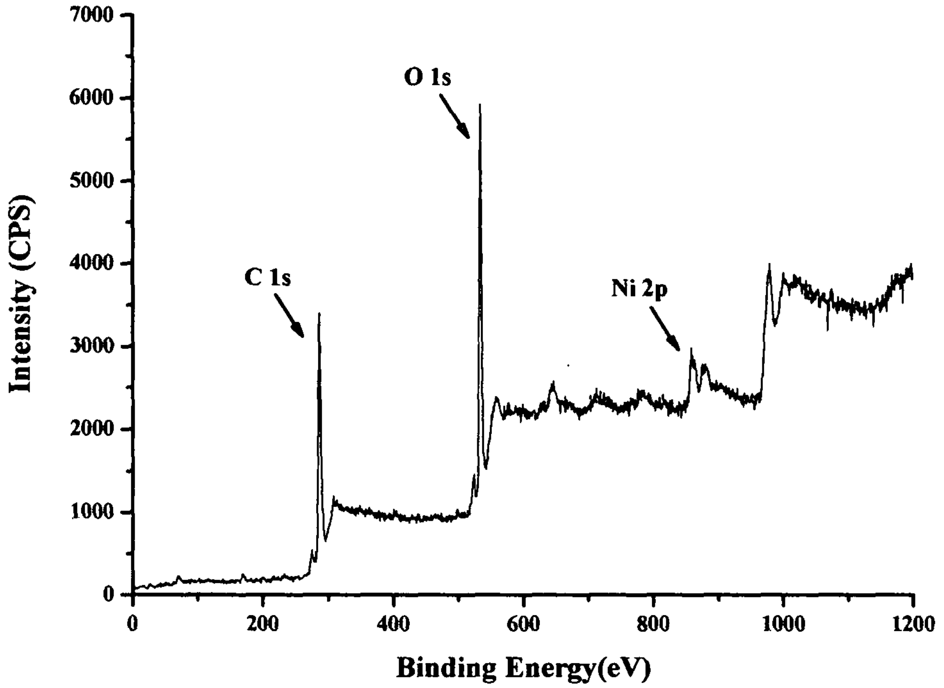

Figure 2.6. X-ray photoelectron survey spectrum of Ni nanoparticles synthesised with 0.04 M TA in EG.

This indicates that TA passivates the nanostructure surfaces against oxidation. Strong oxygen O 1s peak at 533.4 eV for O=C-O of acetate ligand[77] and C 1s peak at 285.5 eV for C_6H_5CO linkage[78] are also observed in survey spectrum of Ni sample. Thus, XPS results confirm the absence of impurities like NiO, Ni_2O_3, Ni $(OH)_2$ etc, which is in good agreement with XRD analysis. The amount of Ni was calculated from the XPS peak area and is found to be 4.47%, which is relatively low due to lower concentration of the precursor as compared to TA.

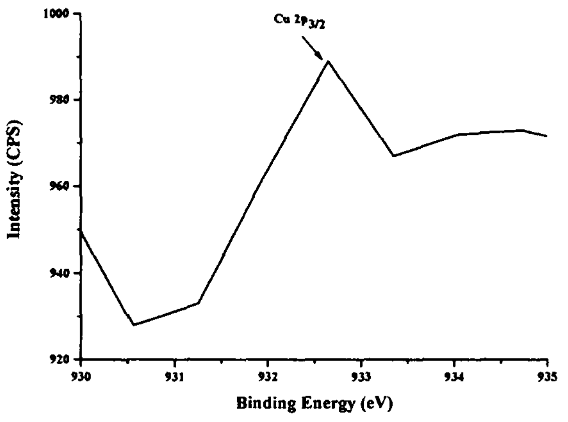

Figure 2.7. High resolution Cu 2p XPS spectrum of Cu nanoparticles synthesised with 0.04 M TA in EG.

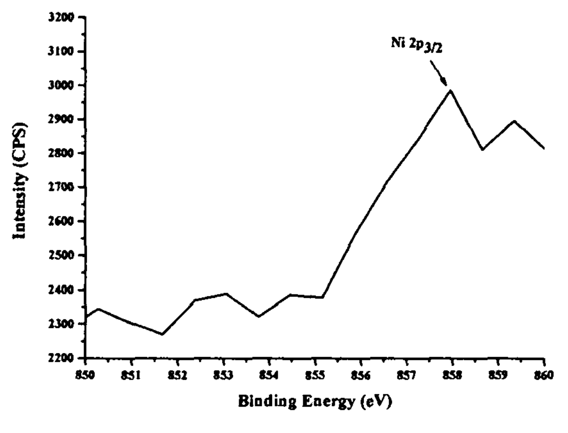

Figure 2.8. High resolution Ni 2p XPS spectrum of Ni nanoparticles synthesised with 0.04 M TA in EG.

2.3.1.5. TGA of metal nanoparticles

TGA was carried out to determine the desorption temperature of the materials (EG and TA) associated with the metal nanoparticles and the weight loss characteristics.

Figures 2.9 and 2.10 shows the TGA and DTG curves recorded in the temperature range of 25-800 °C under N_2 atmosphere of Cu and Ni nanoparticles, respectively, synthesized by 0.04 M TA reduction in EG medium. Both samples exhibited a first weight loss (6.5% for Cu and 5.5% for Ni) below 130 °C. This is due to the removal of adsorbed and pyrolysis water. The major weight loss region begins at 180 °C and witness a total weight loss of about 92.6% for Cu and 95.0% for Ni at 270 °C, which corresponds to the decomposition of EG and TA adhered to the metal nanoparticles. This is likely because the boiling point of the major component (EG) is 197 °C and the melting point of TA is 218 °C. DTGs of the two samples further substantiate the major weight loss region with sharp and symmetric peaks with a minimum at around 250 °C. Decomposition was complete at 270 °C. The differential thermoanalyses (DTA) curves were also recorded simultaneously (***not shown in the figures***), however, in both cases

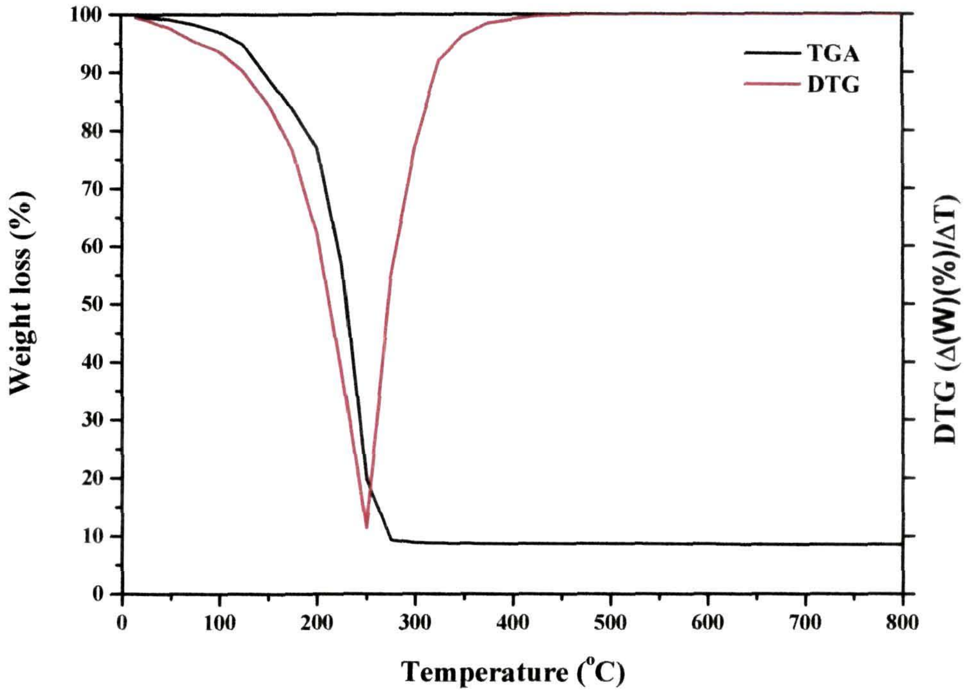

Figure 2.9. Thermal gravimetric analysis (TGA) and differential thermal gravimetry (DTG) curves of Cu nanoparticles synthesised with 0.04 M TA in EG.

they exhibited only one endotherm that superimposed with the DTG peak. The TGA trace reveals that less than 8% Cu and 5% Ni nanoparticles remain in the samples. The essential weight loss characteristics are summarized in **Table 2.2.** The percent amounts of metals are substantially low because the analyses were done with liquid samples. The organic components were lost almost completely before 300 °C as indicated by the almost horizontal nature of the TGA pattern to the abscissa.

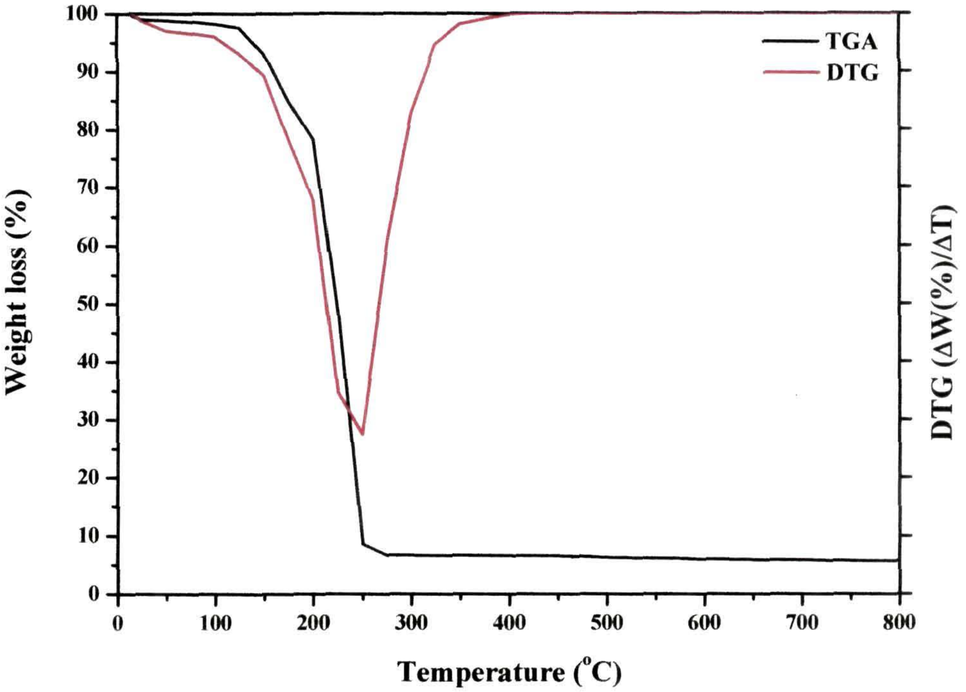

Figure 2.10. Thermal gravimetric analysis (TGA) and differential thermal gravimetry (DTG) curves of Ni nanoparticles synthesised with 0.04 M TA in EG.

Table 2.2. Essential weight loss characteristics of metal nanoparticles

Sample	**Weight loss (%) at**	
	130 °C	**270 °C**
Cu	6.5	92.6
Ni	5.5	95.0

2.3.1.6. Morphology of metal nanoparticles

2.3.1.6.1. Cu nanoparticles

Figure 2.11 represents the SEM images of Cu nanostructures prepared in EG with 0.04 M TA. The SEM image shown in **Figure 2.11a** reveals numerous flower-like architectures assembled in arrays. On going through the high-magnification images, it has been found that, the nanoflowers are approximately of 1 μm in size and constructed from the assembly of numerous laminar structures that are interpenetrated and behaved like a network in the flower. The SEM image of the individual flower provides more structural information, revealing rice-like features on the top of the laminar layer and is approximately 100 nm in length. The TEM image of Cu nanostructures shown in **Figure 2.11d**, divulging nanoflowers of about 1 μm in size, consistent with the SEM results. After six months, morphology of the Cu nanostructures has been changed to

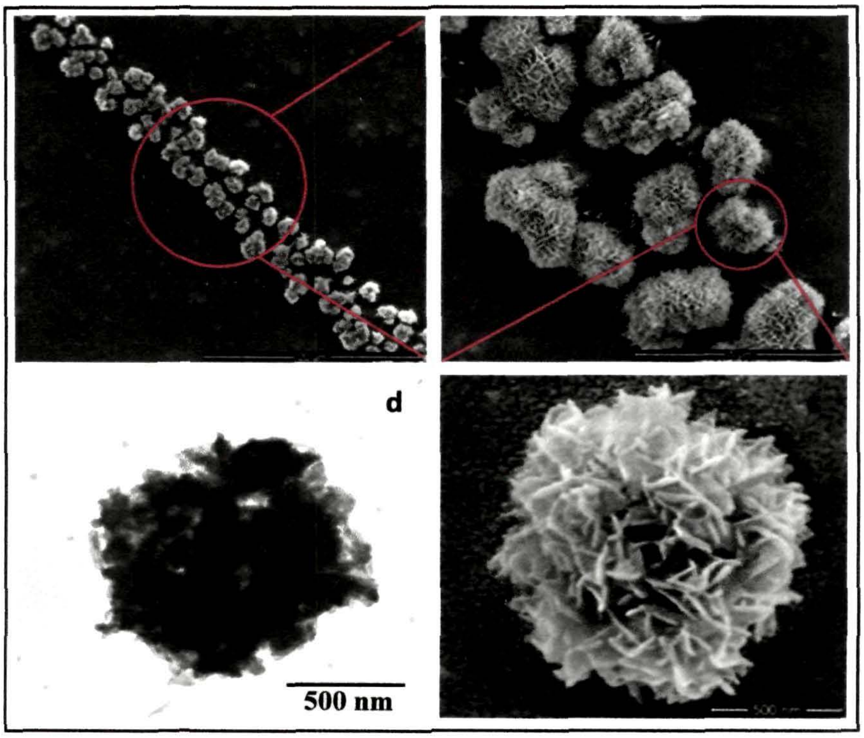

Figure 2.11. Top-down FE-SEM images of Cu nanostructures synthesised with 0.04 M TA in EG: (**a**) well ordered arrangement of flower-like structure at low magnification; (**b**) well ordered arrangement of flower-like structure at high magnification; (**c**) an individual flower; and (**d**) a TEM image of an individual flower.

rice- like features of average sizes 100 nm (**Figure 2.12**), distributed throughout the surface. From the magnified images, it is seen that the rice-like structures are nothing but the structures that have been seen on the top of the nanosheets in flower like architecture. The chelating nature of tannic acid helps in accommodating the metals into the cages bound by oxygen atoms and result is the flower like morphology. The interaction is not strong enough to hold the flower like structure prolong. This is due to the lone pair-lone pair repulsion of oxygen atoms and hence they get solvated resulting in the architectural break down from *3-D* to *1-D* rice-like morphology.

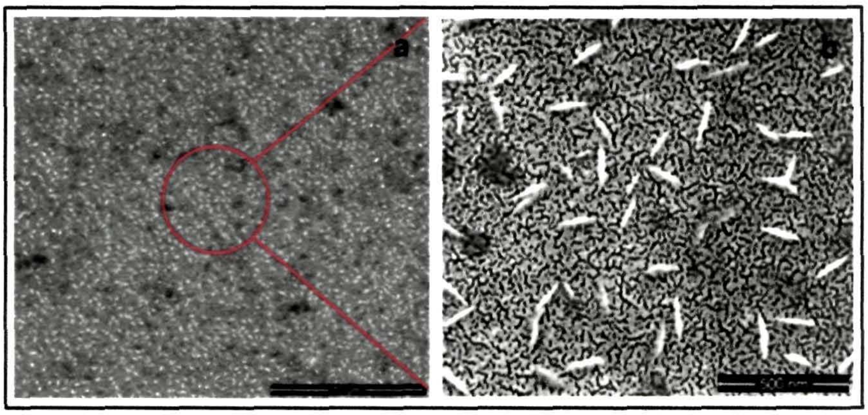

Figure 2.12. Top-down FE-SEM images of rice-like Cu nanoparticles synthesised with 0.04 M TA in EG, after 6 months at different magnifications (**a**) and (**b**).

The AFM tapping mode *2-D* topography and phase images (**Figure 2.13**) of the Cu nanostructures prepared by 0.04 M TA reduction were acquired simultaneously at the same sample location. The corresponding *3-D* images are also presented in **Figure 2.13**. Unlike SEM image, the topography image shows that the AFM tip was unable to trace the flower-like morphology clearly; however, from the *3-D* image, a partial view of a large feature can be noticed with uneven surface topography. This is further substantiated by the height profile of the topography image, which indicates a maximum height difference of *ca.* 450 nm. The same sample was scanned by AFM after 6 months in an effort to support the SEM result, and the images are presented in **Figure 2.14**. The rice-like features observed in SEM images are also found in the AFM scans. The height profile of the topography image points out a maximum height difference of *ca.* 1.3 nm and average size of *ca.* 65 nm.

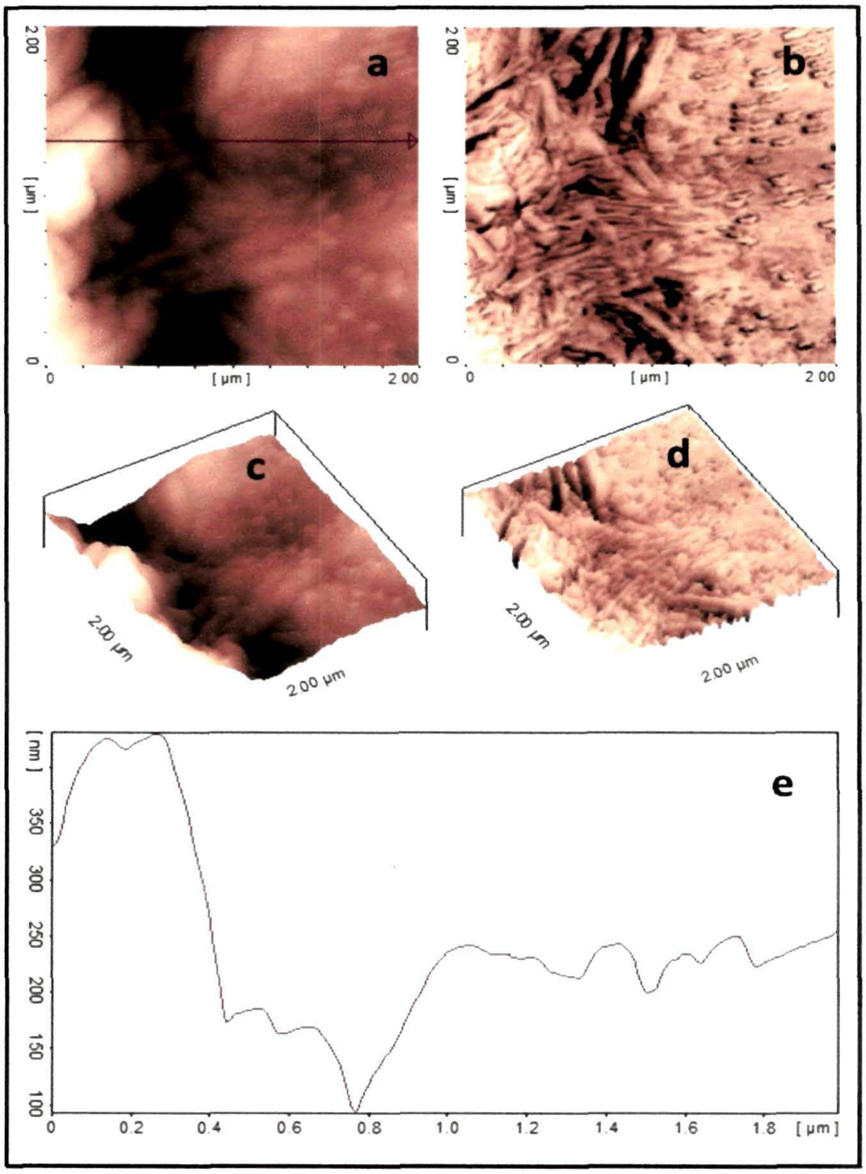

Figure 2.13. AFM tapping mode *2-D* topography (**a**) and phase (**b**) images of flower-like Cu nanostructures synthesised with 0.04 M TA in EG. (**c**) and (**d**) are the corresponding *3-D* images of (**a**) and (**b**); and (**e**) is the typical height cross section image of (**a**).

There is no agreement of the particle sizes obtained from SEM, TEM and AFM with XRD data. Debye-Scherrer equation is normally used to probe the structure of nanoparticles, however, the formula is unreliable at estimating particle size because the assumption of an underlying crystal structure is often invalid[82]. In addition, Patterson[83] found that this formula gives accurate particle size for spherical shape particles only. Thus, the calculation of non-spherical nanoparticles size using this formula is not proper.

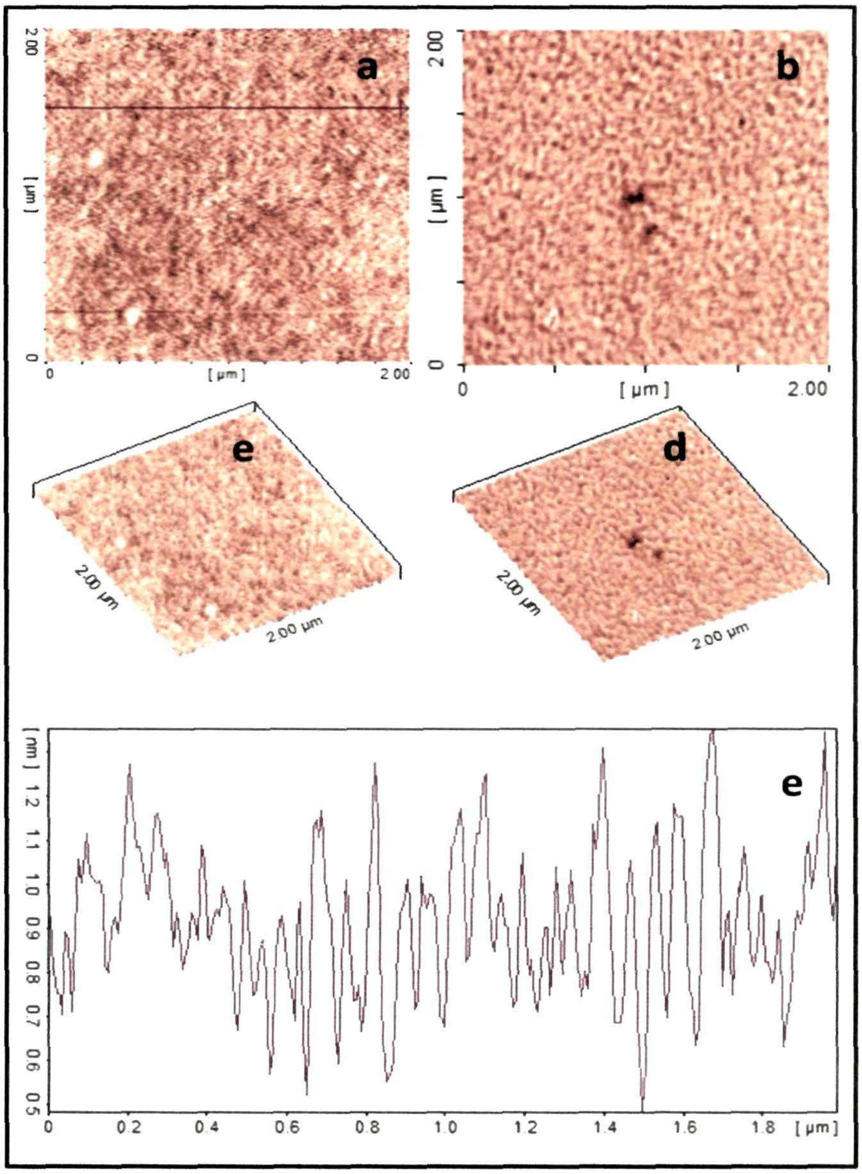

Figure 2.14. AFM tapping mode *2-D* topography (**a**) and phase (**b**) images of rice-like Cu nanostructures synthesised with 0.04 M TA in EG, after 6 months. (**c**) and (**d**) are the corresponding *3-D* images of (**a**) and (**b**); and (**e**) is the typical height cross section image of (**a**).

2.3.1.6.2. Ni nanoparticles

The SEM image of the Ni nanoparticles prepared by 0.04 M TA reduction shows flower-like morphology as shown in **Figure 2.15**. While trying to get insight into the flower, it divulges that the flower is composed of pollen grain like features at the centre with some cubic nanostructures in the periphery as revealed from the magnified image. The pollen grain region of the flower on further magnification shows evenly distributed Ni nanoparticles. Structural characters found in SEM images are revealed in TEM images (**Figure 2.15**) also. The TEM image of an individual flower-like structure gives a diameter of about 1 μm (**Figure 2.15d**). When this flowery structure is magnified, it is clearly differentiated that the nano flowers are not single crystalline but rather composed of some cubic nanostructures in which many well separated spherical shaped (faceted in some particles) nanoparticles of size 4 ± 1 nm (**Figure 2.15e**) are uniformly distributed. Several factors might be responsible for the formation of this type of structure. One factor is the dendrite structure of TA that has the ability to form supra molecular assemblies due to the high density of hydroxyl groups. This leads to extensive inter- and

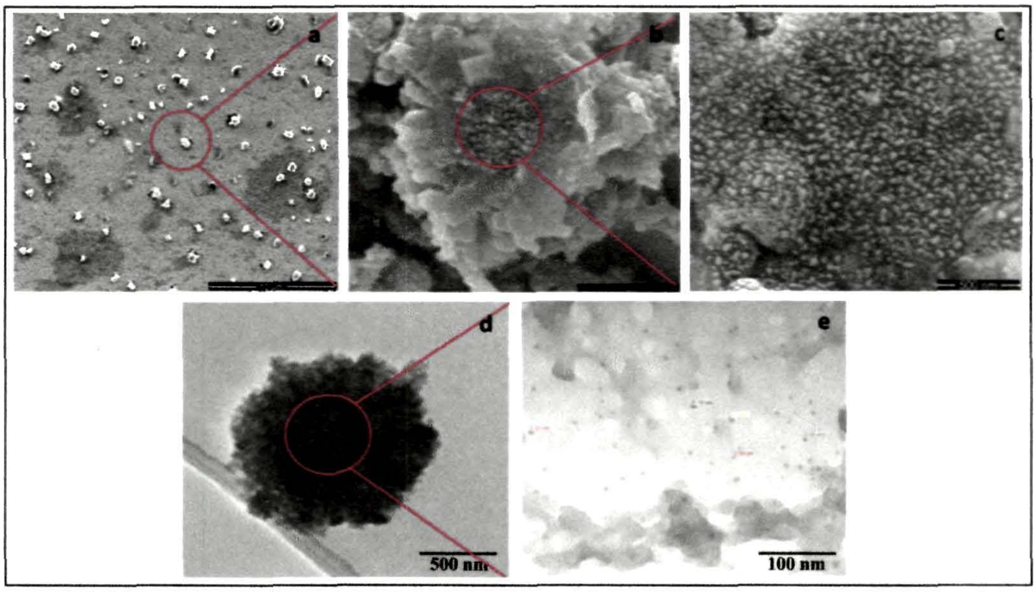

Figure 2.15. Top-down FE-SEM (a, b, c) and TEM (d, e) images of Ni nanostructures synthesised with 0.04 M TA in EG: (a) flowery structures at low magnification; (**b**) an individual flower; (**c**) magnified image of an individual flower.; (**d**) TEM image of an individual flower and (e) magnified image of an individual flower.

intra-molecular hydrogen bonded network resulting in molecular level capsules, which can act as templates for nanoparticle growth and help to passivate the surface of the nanoparticles[70,73]. Another factor is the strong magnetic attraction among the particles. Thus, the formation of flower-like morphology observed in SEM and TEM images is most probably the *3-D* Ni-TA complex hybrid nanostructures constructed by TA acid capped cubic Ni nanostructures through self-assembly process. This hybrid nanostructure serves as a glue to hold the spherical shaped smaller nanoparticles homogeneously. Proper TA concentration is important in this regards.

Similar to Cu nanostructures, a time dependent morphological changes study of the Ni nanoparticles synthesized by 0.04 M TA has been carried out after six months. There is no change in physical appearance of the dispersion; however, from SEM images (**Figure 2.16**), morphological changes have been observed. Cubic shaped particles, which are congregated in large scale, are now more prominent (**Figure 2.16a**)

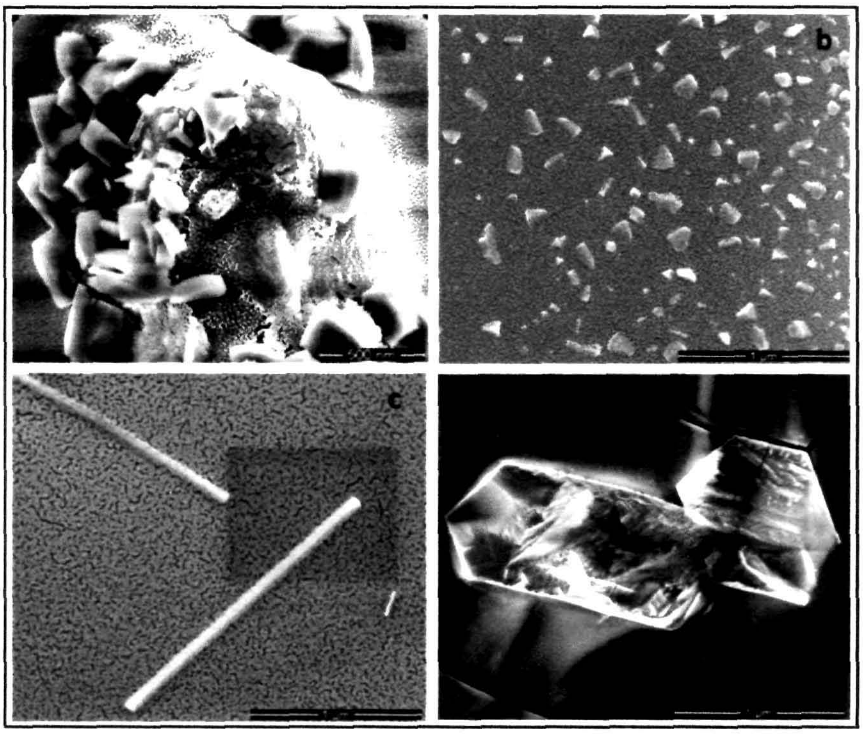

Figure 2.16. Top-down FE-SEM images of (a) congregated cubes, (b) discs, (c) rods and (d) scattered cubes of Ni nanoparticles synthesised with 0.04 M TA in EG, after 6 months.

as compared to the earlier flowery-like morphology (**Figure 2.15**). Besides, various shapes of nanostructures like disc-like (**Figure 2.16b**), rod shaped (**Figure 2.16c**) and large cubic (**Figure 2.16d**) morphologies, scattered all across the surface have been observed during SEM imaging. The reasons behind the morphological changes in Cu

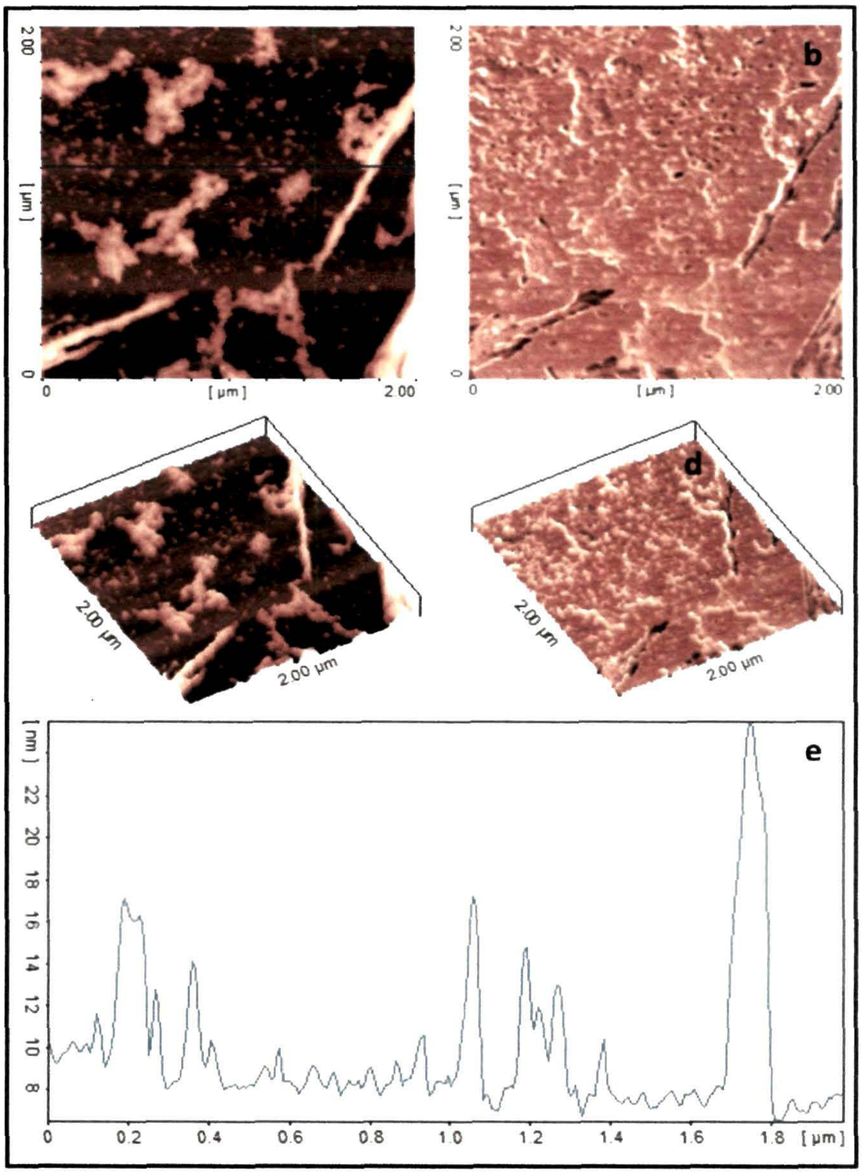

Figure 2.17. AFM tapping mode *2-D* topography (**a**) and phase (**b**) images of Ni nanostructures synthesised with 0.04 M TA in EG. (**c**) and (**d**) are the corresponding *3-D* images of (**a**) and (**b**); and (**e**) is the typical height cross section image of (**a**).

nanostructures could be carried forward to explain these morphological changes. These changes observed at room temperature are mainly kinetically driven process.

Figure 2.17 shows the AFM tapping mode *2-D* and *3-D* topography and phase images of the Ni nanoparticles prepared by 0.04 M TA reduction acquired

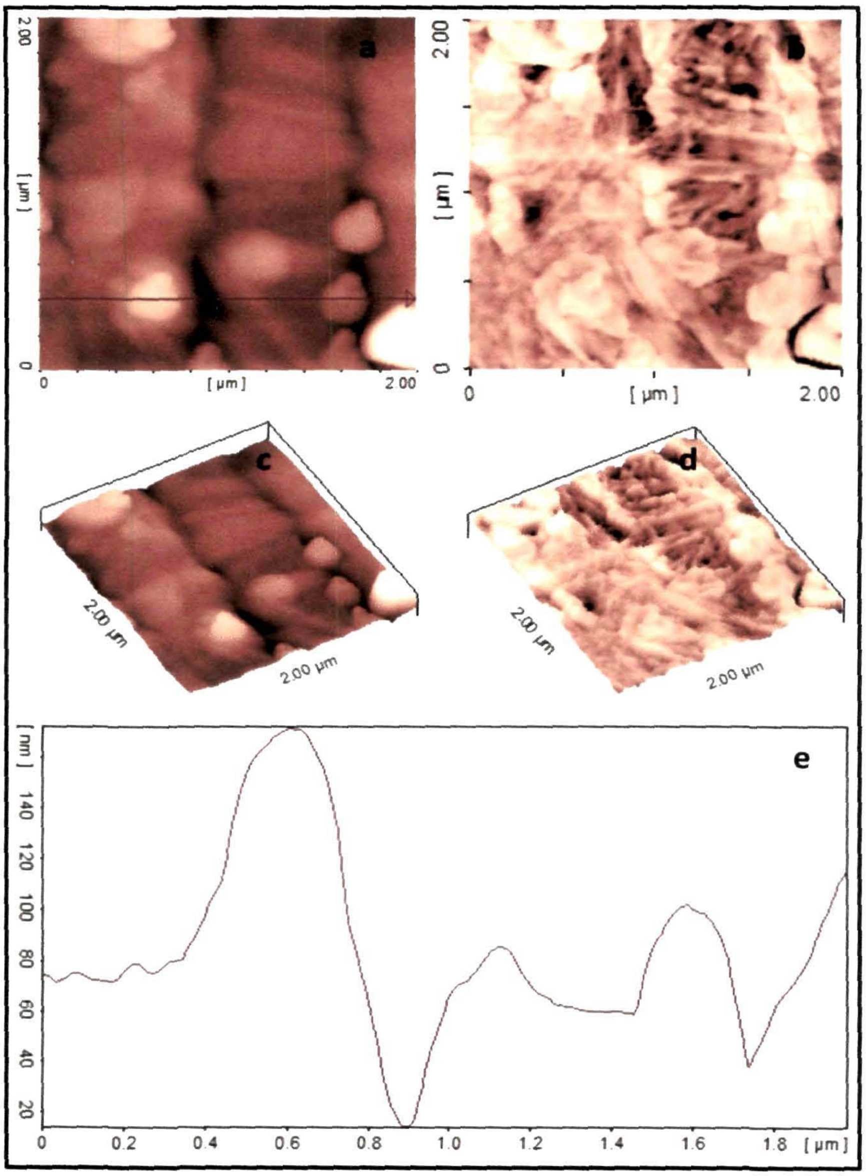

Figure 2.18. AFM tapping mode *2-D* topography (**a**) and phase (**b**) images of Ni nanostructures synthesised with 0.04 M TA in EG, after 6 months. (**c**) and (**d**) are the corresponding *3-D* images of (**a**) and (**b**); and (**e**) is the typical height cross section image of (**a**).

simultaneously at the same sample location. The topographic image shows brighter spherical (or near spherical) particles of sizes ranging from 10 to 30 nm. Typical height cross section of the topography image indicates a maximum height difference of *ca.* 26 nm (**Figure 2.17e**). In comparison, the topography and the phase images correspond well; besides, the brighter nanoparticles in the topography correspond to the relatively dark areas in the phase image. It appears that smaller nanoparticles are the primary particles, which might have aggregated to form the larger particles. AFM scans of the sample taken after 6 months are presented in **Figure 2.18**. From the topography and phase images, particles of various shape like cube, rod, etc., can be identified. A clear surface profile can be found from the *3-D* images. The height profile of the topography image gives a maximum height difference of *ca.* 155 nm.

2.3.1.7. Effect of TA concentration on morphology of metal nanoparticles

2.3.1.7.1. Cu nanoparticles

It has already been established that, in the formation of complex nanoarchitectures, capping ligands often play a driving role by binding selectively onto particular facets of the seed particles[84-86] and serve as a structure-directing coordination template. The well-ordered chain-arrangement of flower-like morphology of Cu nanostructures synthesized with 0.04 M TA, drives us to further researched the influence of TA concentrations on the morphology of Cu nanostructures by carrying out synthesis at two more different concentrations viz. 0.02 M and 0.06 M TA, keeping all other reaction parameters unchanged. At 0.02 M TA concentration, the Cu nanostructures formed are entirely different from 0.04 M TA mediated nanostructures (flower-like morphology, **Figure 2.11**) and appear to have wire-like morphology (**Figure 2.19a**). On the contrary, clusters are observed in the case of 0.06 M TA (**Figure 2.19b**). Unlike the changes observed in 0.04 M TA, we did not notice any such types of changes in morphology of the Cu nanostructures after 6 months with 0.02 M and 0.06 M TA. Based on the above results the formation of various Cu nanoarchitectures obtained by varying TA concentrations is schematically illustrated in **Scheme 2.1**. The capping agent

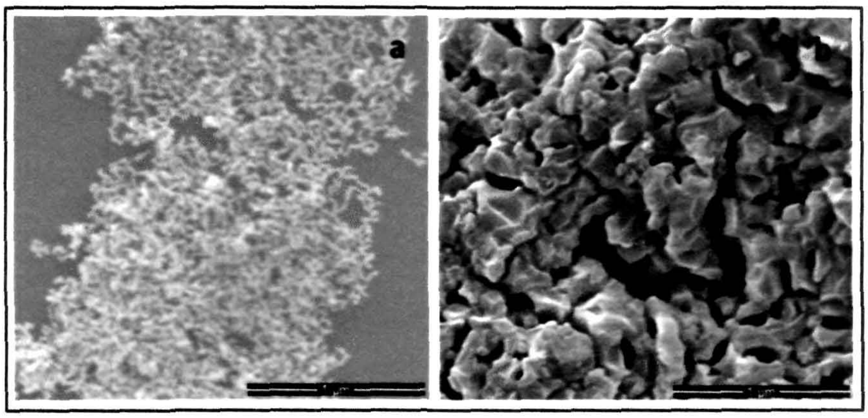

Figure 2.19. Top-down FE-SEM images of Cu nanoparticles synthesised with (a) 0.02 M TA and (b) 0.06 M TA in EG.

adhered to the nanoparticles drives the incipient nanoparticles to self-aggregates or self-assembles to form larger particles through hydrogen bonds and hence, minimize the

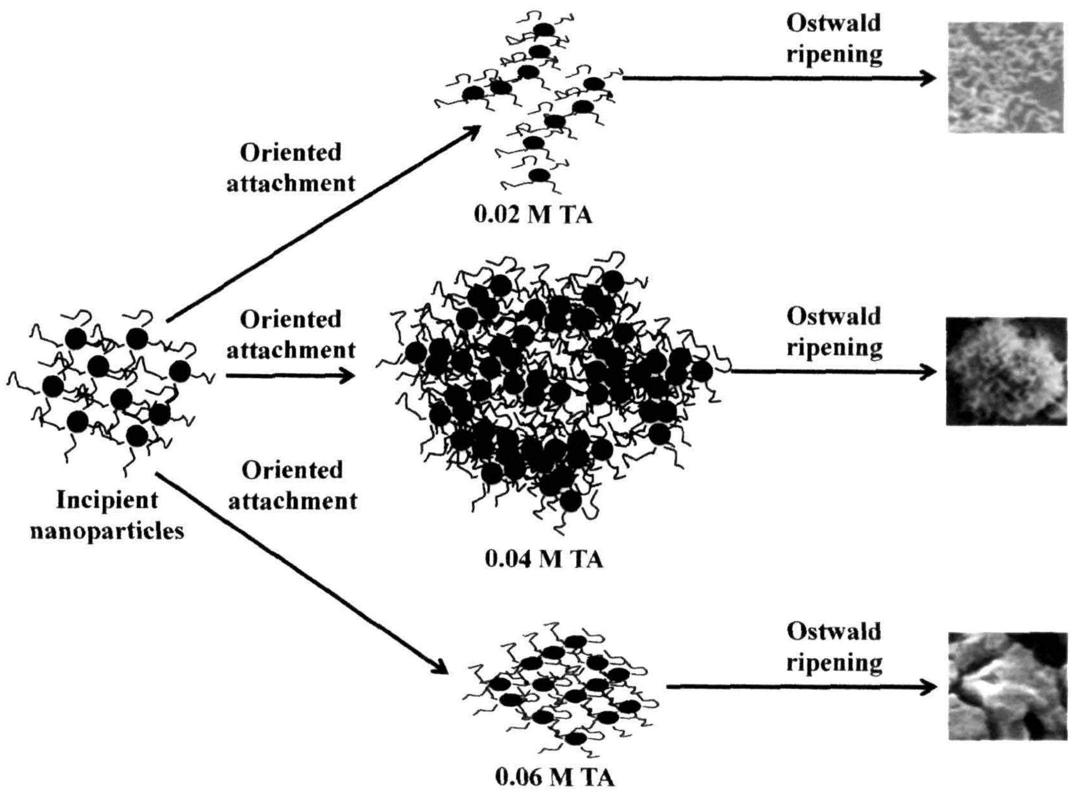

Scheme 2.1. Schematic illustration for the formation of various Cu nanostructures obtained by varying TA concentrations in EG solution.

interfacial energy. This continuous self-aggregation accompanying with Ostwald ripening results in the formation of various shaped structures built from a large number of nanoparticles.

2.3.1.7.2. Ni nanoparticles

SEM images of the Ni nanoparticles synthesised with 0.02 M and 0.06 M TA shown in **Figure 2.20** reveal different types of morphologies, thereby demonstrating the formation of different Ni nanostructures. **Figure 2.20a** shows the formation of micrometer-size lumps in case of nanoparticles synthesized with lower concentration of TA (0.02 M). Formation of lumps might be due to weak interaction between TA and surface of the Ni nanoparticles and hence magnetic interaction between the particles is more dominant in order to minimize the total surface energy of the system resulting agglomeration of nanoparticles. Ni nanoparticles synthesised with 0.06 M TA shows the formation of bigger particles partially exposed from wavy-like surface (**Figure 2.20b**). Excess TA could have formed such kind of surface and trapped the nanoparticles. For easy understanding, the formation of various Ni nanostructures is schematically illustrated in ***Scheme 2.2***.

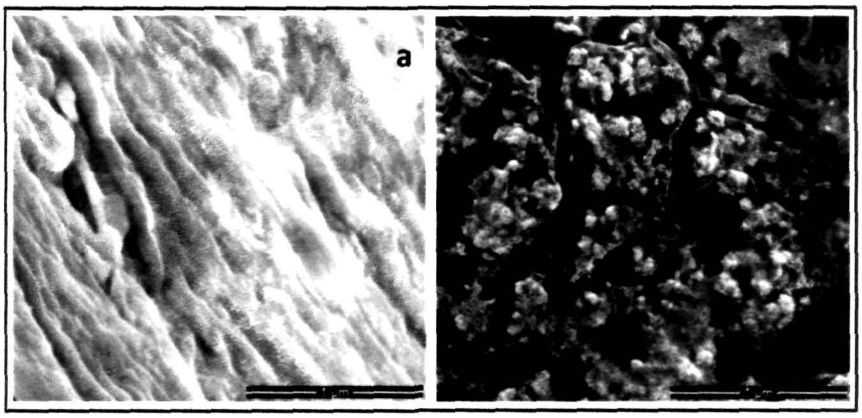

Figure 2.20. Top-down FE-SEM images of Ni nanoparticles synthesised with (a) 0.02 M TA and (b) 0.06 M TA in EG.

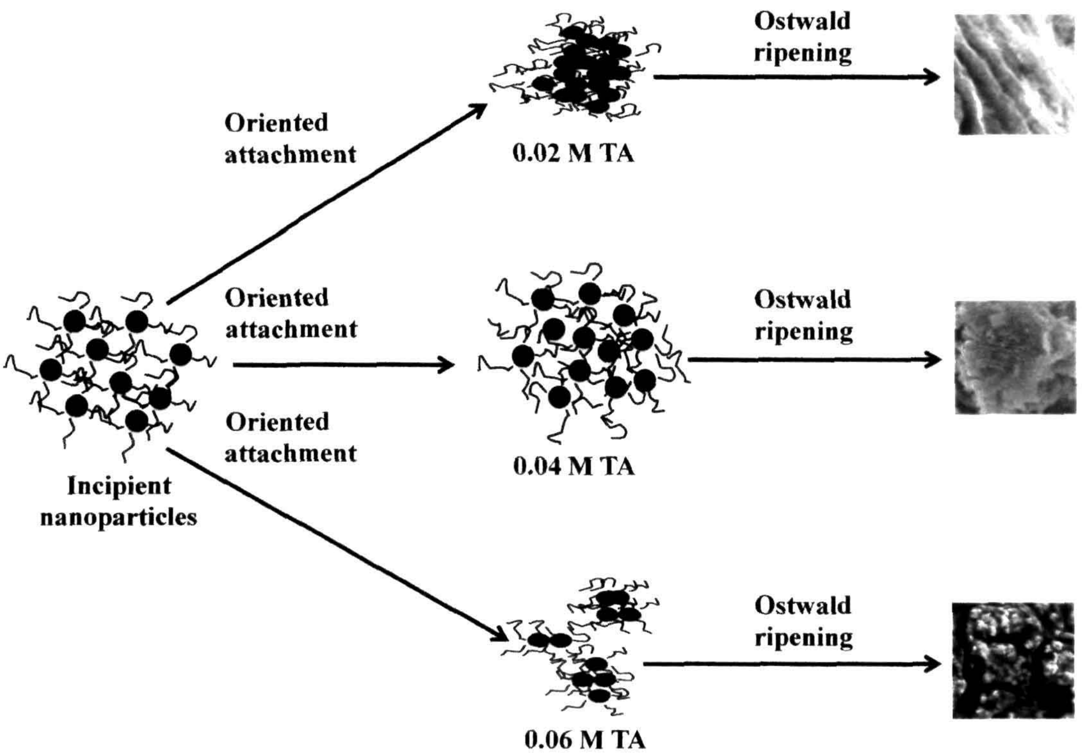

Scheme 2.2. Schematic illustration for the formation of various Ni nanostructures obtained by varying TA concentrations in EG solution.

2.3.1.8. Stability of metal nanoparticles

Stability of nanoparticles dispersion is difficult to achieve due to the strong intermolecular forces among the particles. These forces are due to the high electron affinity and the high surface tension arising from the partially filled d-orbital and van der Waals attraction among the polarizable metal particles. Magnetic dipole-dipole interaction makes this kind of attraction even stronger in magnetic nanoparticles such as Ni, Fe, etc. Hence, it is a very challenging task to get stable dispersion of magnetic nanoparticles. In our present investigation, highly stable colloidal dispersions of metal nanoparticles (Cu and Ni) were achieved by reducing the metal ions using 0.04 M TA and dispersion remained unchanged for six months under ambient conditions. The concentration of TA has profound influence on the stability of the nanoparticles dispersion. The dispersions of both nanoparticles were highly unstable and quickly precipitated out on standing at either end of TA concentrations (0.02 M and 0.06 M).

However, 0.04 M TA synthesized metal nanoparticles dispersion was highly stable even after 6 months under ambient conditions. Though we noticed architectural changes (**Figures 2.11 and 2.15**), yet the physical appearance of the dispersion remained unchanged.

2.3.2. Metal/PANI nanocomposites

2.3.2.1. Synthesis of metal/PANI nanocomposites

Both Cu and Ni nanoparticles were synthesised by identical procedure in EG medium using TA as reductant as stated before. The two metal nanoparticles were synthesised by varying the concentration of TA (0.02, 0.04 and 0.06 M) to investigate the effect of TA on stability, size distribution and morphology of the resultant nanoparticles. For convenience, the metal nanoparticles are designated as M-2, M-4 and M-6 (M = Cu or Ni) for 0.02, 0.04 and 0.06 M TA, respectively. The characteristic properties of the metal nanoparticles could influence the properties of the nanocomposites and therefore, all the metal nanoparticles were considered for

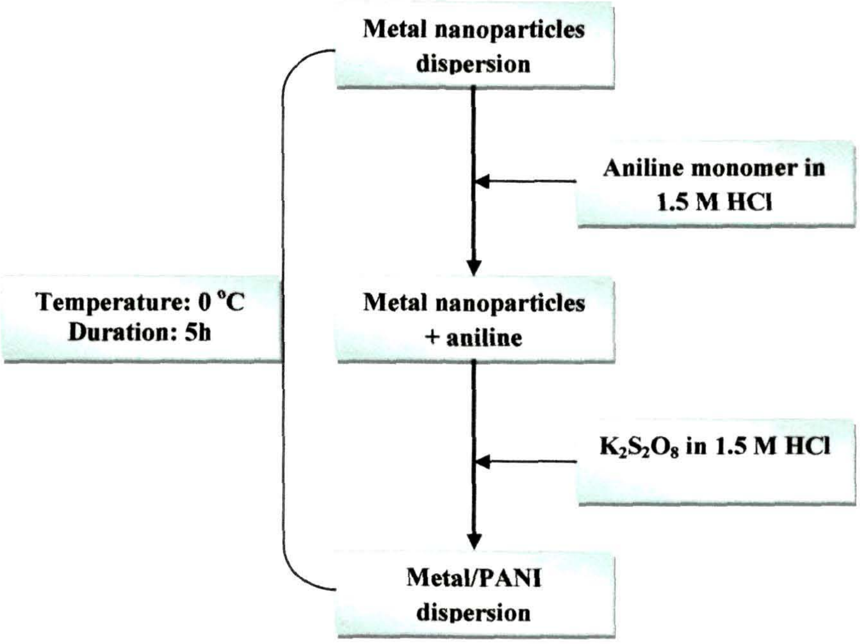

Scheme 2.3. Schematic illustration for the synthesis of metal/PANI nanocomposites.

subsequent synthesis of metal/PANI nanocomposites by *in-situ* polymerization technique. ***Scheme 2.3*** presents a systematic layout of the synthesis procedure. All the metal/PANI nanocomposites were characterised using various techniques, and their optical and electrical properties were evaluated as discussed below.

2.3.2.2. XRD analysis of metal/PANI nanocomposites

Figure 2.21 illustrates the powder XRD patterns of PANI and Cu/PANI nanocomposites. Bragg's diffraction peaks for PANI are observed at 2θ values of 15.2°, 20.3°, 25.1°, 27° and 30°, and can be indexed as (011), (020), (200), (121) and (022), respectively, crystalline plane classically observed for PANI in its emeraliadne form[87,88]. These peaks might have originated from the scattering of PANI chains at interplanar spacing[89] and suggest a significant crystalline fraction.

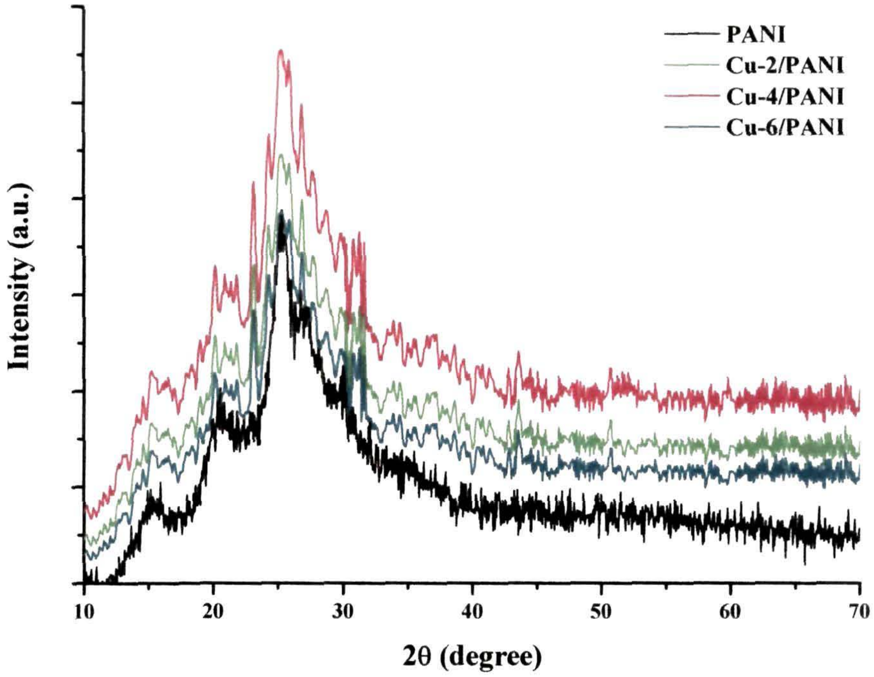

Figure 2.21. Powder X-ray diffraction patterns of pure PANI and Cu/PANI nancomposites.

For the Cu/PANI nanocomposites, the diffraction peaks are observed at 2θ values of 15.2°, 20.4°, 25.1°, 43.6°, 50.7° and 74.45°. The first three peaks are originated from PANI while the other peaks correspond to the peaks of Cu nanoparticles as discussed in ***Section 2.3.1.2***. It illustrates the existence of Cu nanoparticles in the resulting nanocomposites and the data matches well to face-centred-cubic (fcc) structure of copper (JCPDS No. 4-0836). Further, it indicates that the structures of the Cu nanoparticles in the resultant nanocomposites are not modified by PANI. The crystallite size of Cu nanoparticles calculated using Debye-Scherrer's formula (***Equation 2.1***) from the full width at half maximum (FWHM) of Cu(111) reflection are 7.4 ± 1 nm, 8.6 ± 1 nm and 10.8 ± 1 nm for Cu-2/PANI, Cu-4/PANI and Cu-6/PANI, respectively.

In Ni/PANI nanocomposites (**Figure 2.22**), the presence of Ni nanoparticles are evidenced in terms of peaks at 2θ ~20.16°, 23.25°, 33.0° and 39.0°. These data match

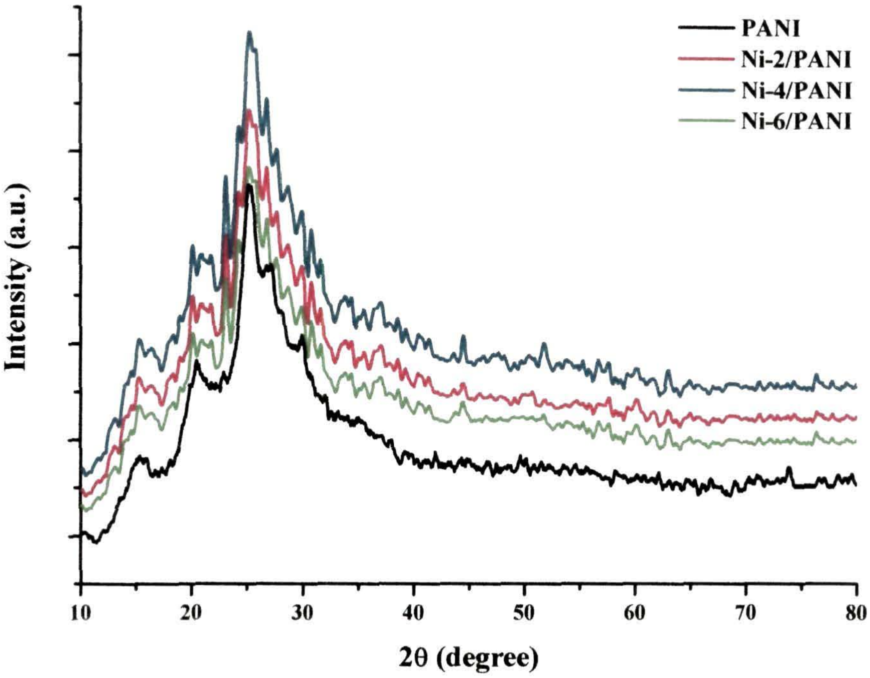

Figure 2.22. Powder X-ray diffraction patterns of pure PANI and Ni/PANI nancomposites.

well with the ASTM data for face-centered-cubic (fcc) nickel[90]. Like Cu, the structures of the Ni nanoparticles in the synthesised nanocomposites are not affected by PANI. The crystallite size of the nickel nanoparticles is calculated from the major diffraction peaks of Ni(111) using ***Equation 2.1*** and is found to be 6.3 ± 1 nm, 5.2 ± 1 nm and 8.7 ± 1 nm for Ni-2/PANI, Ni-4/PANI and Ni-6/PANI, respectively.

A comparison of the diffraction patterns of metal nanoparticles (***Section 2.3.1.2***) and metal/PANI nanocomposites (**Figures 2.21 and 2.22**) reveals the change in intensity and slight shifting in positions of diffraction peaks in the nanocomposites. These changes can be attributed to some structural change in the polymer caused by the close interaction with the disperse nanoparticles phase[91]. During the growth of crystals (nanocomposite), the growth of each plane of the components can be different due to the different adsorptions between each plane and organic or inorganic additives[92]. Further, compared to PANI diffraction pattern, the peaks corresponding to PANI in the nanocomposites are sharp, indicating higher crystallinty in composites. Thus, the XRD patterns of nanocomposites evidence reorganization in the structure of the polymer and the co-existence of the metal reflections suggesting its effective and stable incorporation in the nanocomposite structure.

2.3.2.3. FTIR analysis of metal/PANI nanocomposites

Figure 2.23 presents the typical FTIR spectra of pure PANI and its composites with Cu-4 and Ni-4 nanoparticles. This study was undertaken in order to find out any possible interaction of metal nanoparticle with PANI matrix. From the spectrum of pure PANI bands at 3282, 2920, 1567, 1466, 1296, 1243, 1106 and 876 cm^{-1} can be identified and can be attributed to the polyaniline emeraldine[93]. These bands can be assigned to different vibrational modes and these characteristics are compiled in **Table 2.3**. These characteristic bands of PANI can also be detected in the IR spectra of Cu-4/PANI and Ni-4/PANI which is a direct evidence of its formation in the nanocomposites. For comparison, all the characteristic IR bands of metal/PANI nanocomposites are also compiled in the **Table 2.3**. A careful examination of the table however, shows shifting in peak positions of the bands associated with C=C, C=N and C-N stretching of the quinoid ring. This strongly attributes to the existence of some degree of interaction

	in bipolaron			--
$\nu_{-C=C}$-stretching	Quinoid ring	1567	1570	1571
$\nu_{-C=C}$stretching	Benzoid ring	1466	1468	1468
ν_{-C-H} in- plane Bending	Benzoid ring	1106	1110	1110
ν_{-C-H} out- of- plane Bending	Benzoid ring	876	873	876
ν_{-C-H} stretching	C-H bond in phenyl ring	2920	2930	2930

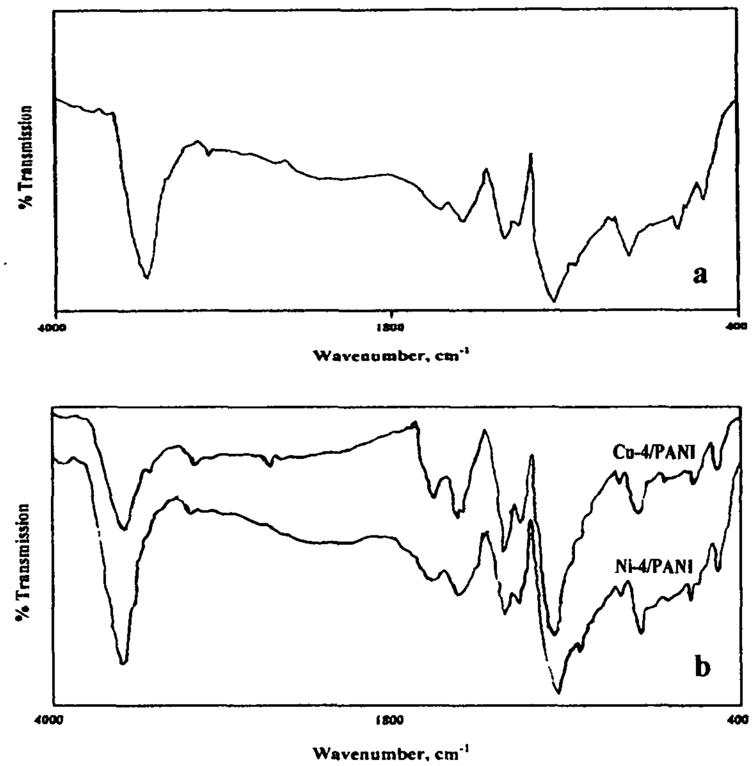

Figure 2.23. FTIR spectra of pure PANI (a), and Cu-4/PANI and Ni-4/PANI (b) nanocomposites.

Table 2.3. Assignment of IR bands for PANI and metal/PANI nanocomposites

IR band	Assignment	Peak position/Wavenumber cm^{-1}		
		PANI	Cu-4/PANI	Ni-4/PANI
$v_{\text{-N-H}}$ stretching	Amine -N-H	3282	3287	3287
$v_{\text{-C-N}}$ stretching	2° amine -C-N bond	1296	1301	1297
$v_{\text{-C=N}}$ stretching	-C=N bond in bipolaron	1243	1240	1248
$v_{\text{-C=C}}$-stretching	Quinoid ring	1567	1570	1571
$v_{\text{. C=C}}$stretching	Benzoid ring	1466	1468	1468
$v_{\text{-C-H}}$ in- plane Bending	Benzoid ring	1106	1110	1110
$v_{\text{-C-H}}$ out- of- plane Bending	Benzoid ring	876	873	876
$v_{\text{-C-H}}$ stretching	C-H bond in phenyl ring	2920	2930	2930

between metal nanoparticles and PANI and could have resulted from the presence of metal nanoparticles in close proximity of the imine nitrogen of PANI.

2.3.2.4. XPS analysis of metal/PANI nanocomposites

The surface compositions of the two metal/PANI nanocomposites are further investigated by XPS. Analysis is also carried out on pure PANI as a reference. The survey spectrum of pure PANI (**Figure 2.24**) shows clearly the presence of C, O and N. The high resolution C 1s, O 1s and N 1s spectra are presented in **Figure 2.25**. The highly intense and large C 1s peak at 285.5 eV is assigned to PANI backbones[94]. A sharp peak observed at 532.6 eV for O 1s. The presence of oxygen is attributed to the oxidant and to extra contaminating oxygen. The N 1s peak detected points out binding energy of 400.0 eV that corresponds to -NH- group of PANI. All the nanocomposits exhibit very similar survey spectra and therefore, the spectra of Cu-4/PANI (**Figures 2.26**) and Ni-4/PANI (**Figure 2.27**) are presented. The elements viz. C, O and N

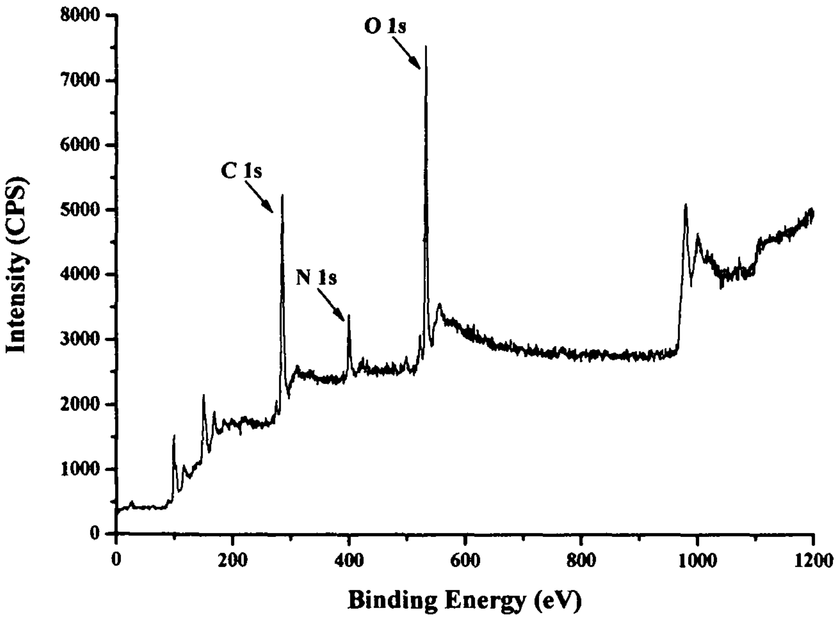

Figure 2.24. X-ray photoelectron survey spectrum of pure PANI.

detected in the spectrum of PANI can also be identified in the spectra of nanocomposites besides the respective metals. The peak positions of the essential elements identified the

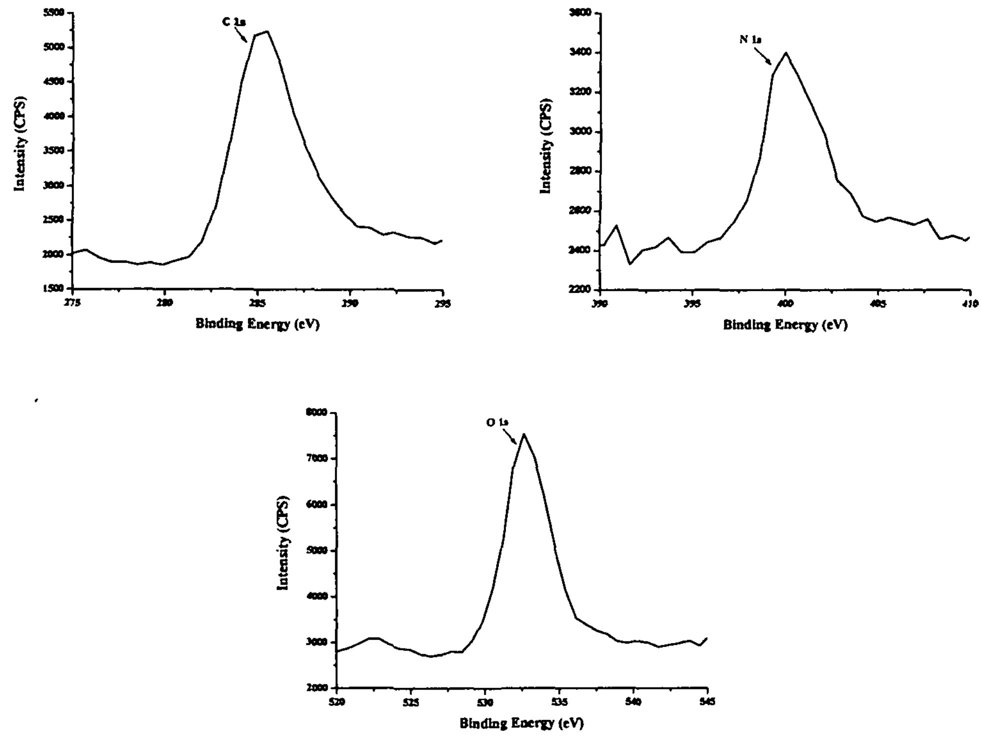

Figure 2.25. High resolution C 1s, N 1s and O 1s spectra of pure PANI.

XPS spectra of pure PANI, Cu-4/PANI and Ni-4/PANI are compiled in **Table 2.4**. The composites and the reference material exhibit similar C 1s, N 1s and O 1s peaks, however, their intensity and positions are slightly changed. These changes can be accounted for the change in the chemical environment of PANI in composites. Further,

Table 2.4. XPS peak positions of essential elements in pure PANI and metal/PANI nanocomposites

Compound	**Peak positions, eV**				
	C 1s	**O 1s**	**N 1s**	**Cu 2p**	**Ni 2p**
PANI	285.5	532.6	400.0	--	--
Cu-4/PANI	284.9	532.9	398.7	933.4	--
Ni-4/PANI	286.2	534.0	398.8	--	857.9

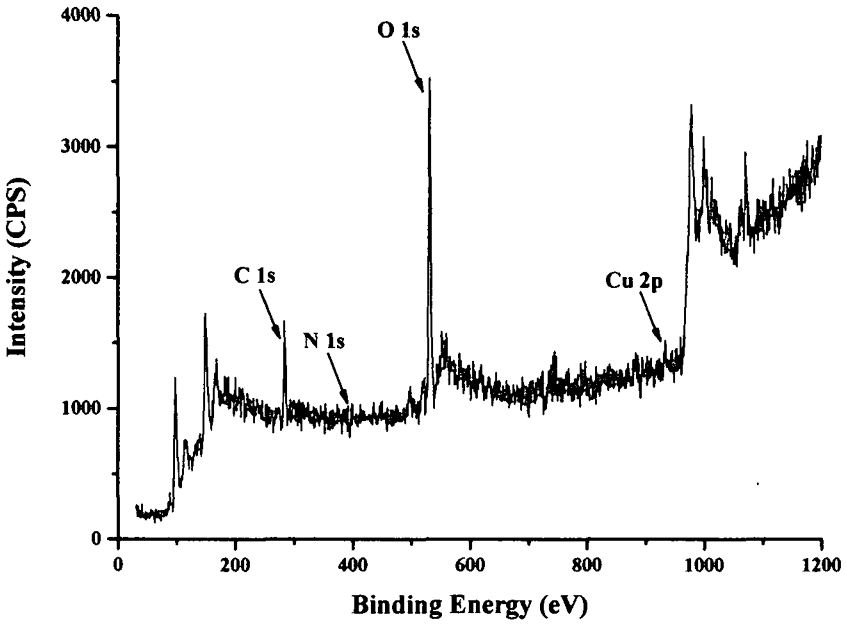

Figure 2.26. X-ray photoelectron survey spectrum of Cu-4/PANI nanocomposite.

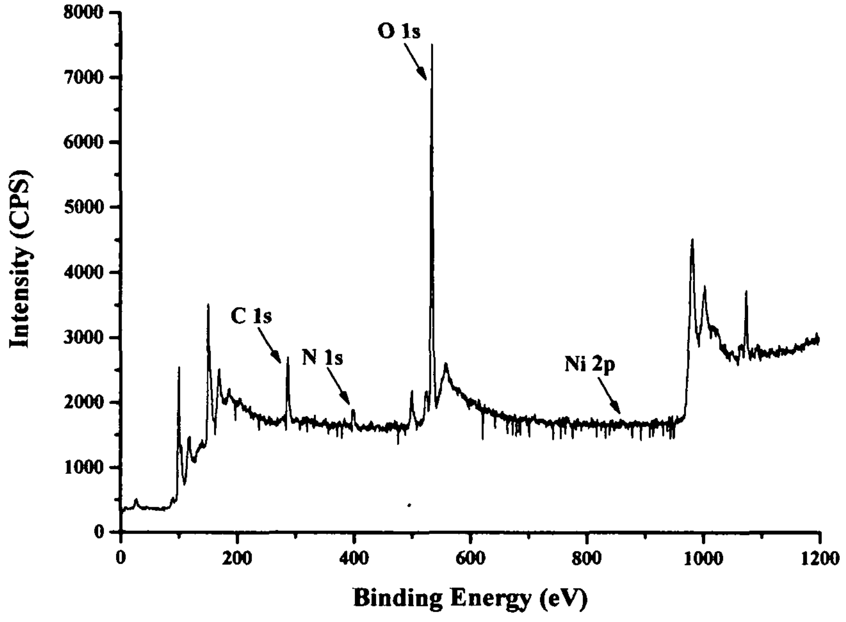

Figure 2.27. X-ray photoelectron survey spectrum of Ni-4/PANI nanocomposite.

the signals of Cu and Ni in their respective nanocomposites are very low. This is due to the lower amount of metal phase in the composite. The other reason is the limited probing depth of XPS technique to explore the core metal phase coated with PANI.

2.3.2.5. TGA of metal/PANI nanocomposites

TGA study of PANI and its composite with metal nanoparticles was carried out to understand the thermal property of the materilas. The TGA traces of pure PANI and Cu/PANI nanocomposites are displayed in **Figure 2.28**, and that of pure PANI and Ni/PANI nanocomposites in **Figure 2.29**. The thermograms were recorded in the temperature range of 25-800 °C at a heating rate of 10 °C/min in an inert environment. It is evident from **Figure 2.28 and 2.29** that the degradation behaviour of PANI and its metal nanocomposites is almost similar. This suggests the occurrence of similar thermal events and accompanying weight losses. Though the weight loss appears to be gradual in

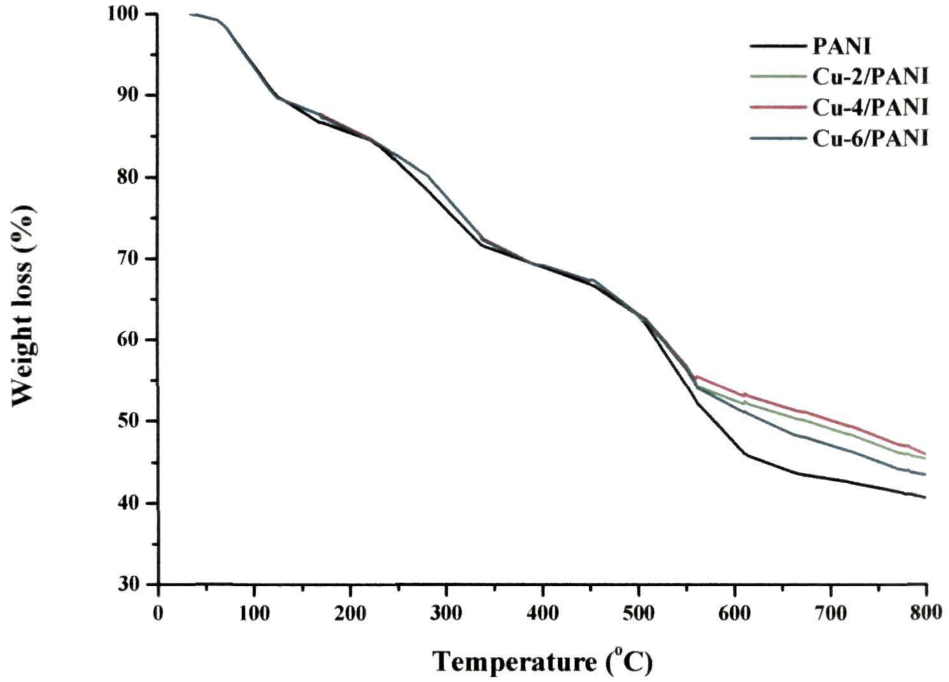

Figure 2.28. TGA thermographs for pure PANI and Cu/PANI nanocomposites.

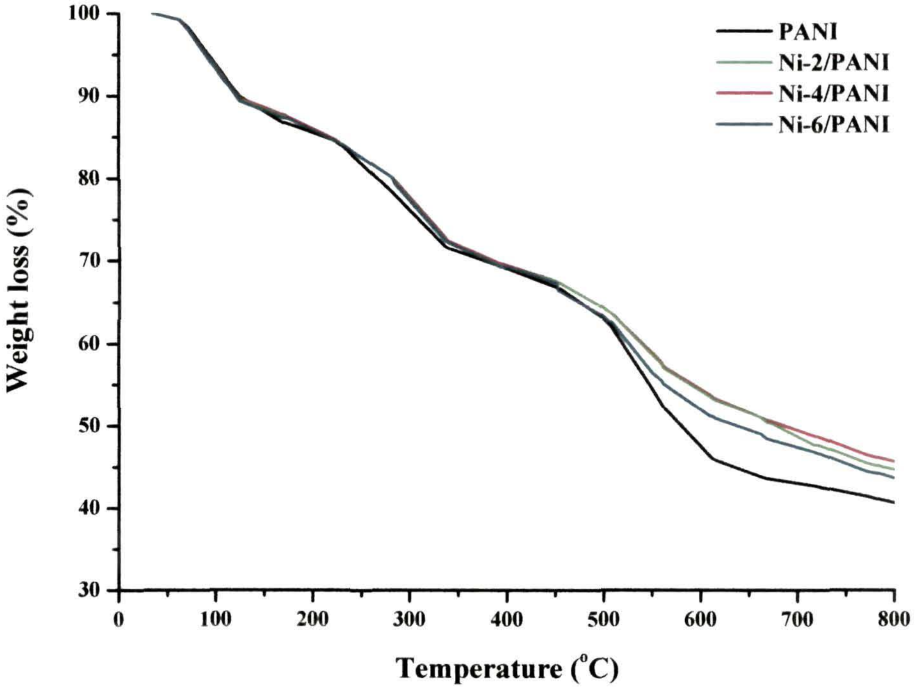

Figure 2.29. TGA thermographs for pure PANI and Ni/PANI nanocomposites.

Table 2.5. Essential weight loss characteristics of PANI and metal/PANI nanocomposites

Compound	**Weight loss (%) at**		
	115 °C	**340 °C**	**600 °C**
PANI	9.5	28.7	52.5
Cu-2/PANI	9.8	27.9	47.6
Cu-4/PANI	9.7	27.5	46.1
Cu-6/PANI	9.7	27.8	48.4
Ni-2/PANI	9.2	27.8	46.0
Ni-4/PANI	8.7	27.6	45.3
Ni-6/PANI	9.7	27.8	48.1

all the compounds during the course of the degradation process, yet a three step weight loss mechanism can be distinctly identified in the TGA profiles. The first weight loss in the temperature range of 25-120 °C is mainly contributed by the elimination of moisture and pyrolysis water. The second weight loss in the temperature range of 220-340 °C is accompanied by the removal of HCl bound to the PANI chain and low molecular weight oligomers[95]. The third step after 500 °C, which is considered as the major weight loss step indicates the structural decomposition of the polymer. The essential weight loss characteristics of pure PANI, Cu/PANI and Ni/PANI are presented in **Table 2.5**. The weight loss is relatively lower in the naocomposites below which indicates the improvement of thermal property of the polymer due to the presence of metal naoparticles. Thus, it strongly attributes the interaction of metal nanoparticles with PANI by stronger binding force between nanoparticles and the lone pair electrons of N atom in the polymer backbone[96].

2.3.2.6. Morphology of metal/PANI nanocomposites

The SEM image of pure PANI is shown in **Figure 2.30**. It appears that as-synthesised PANI has fibrous morphology. The morphology of PANI is further investigated by AFM. The AFM scans were performed in tapping mode to acquire simultaneously the topography and phase images in the same location. Scans were done in different areas of the same sample to check homogeneity and the same kind of results

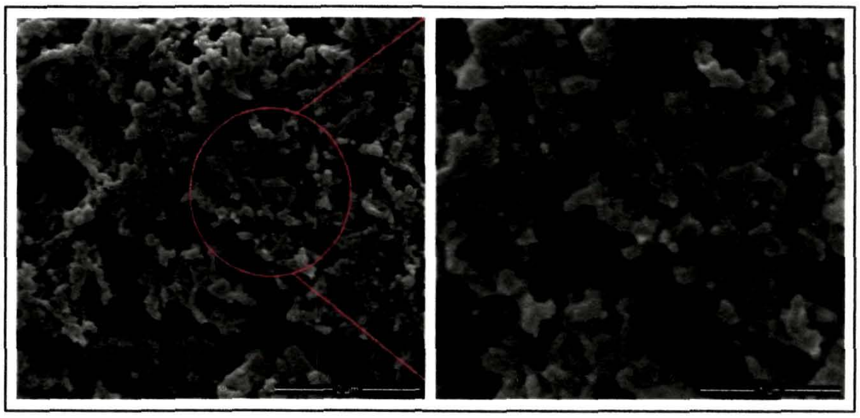

Figure 2.30. Top-down FE-SEM images of pure PANI.

were observed. **Figure 2.31** shows the *2-D* topography and phase images of PANI with fibrous morphology like SEM observation.

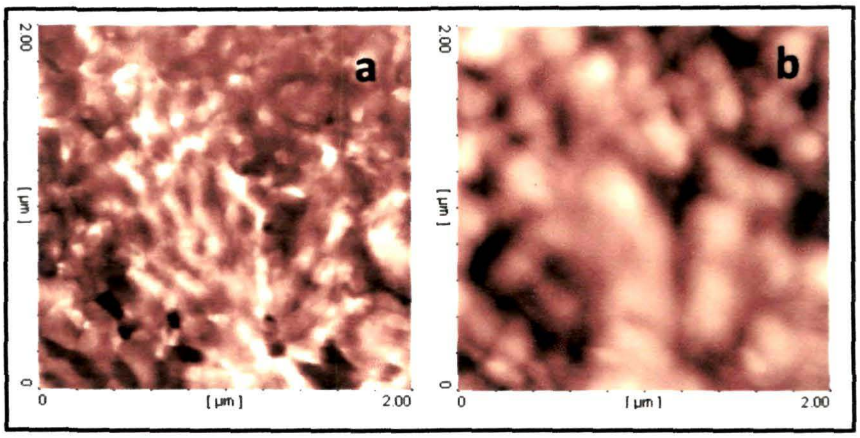

Figure 2.31. AFM tapping mode *2-D* topography (**a**) and phase (b) images of pure PANI.

However, the morphology of pure PANI has been changed in presence of metal nanoparticles. The morphologies of Cu/PANI and Ni/PANI nanocomposites are discussed separately in the following sections.

2.3.2.6.1. Cu/PANI nanocomposites

Three diverge morphologies are observed for three types of Cu/PANI nanocomposites as shown in **Figures 2.32, 2.33 and 2.34**. Bunch of thread-like features distributed uniformly in layer-by-layer fashion is observed in Cu-2/PANI nanocomposite (**Figure 2.32**). As discussed earlier, Cu nanoparticles synthesised with 0.02 M TA produced wire-like structures. These wires could have acted as template to guide the growth of PANI eventually ended up with thread-like morphology. The presence of Cu nanoparticles in the nanocomposite can be confirmed from the TEM image. On the other hand, **Figure 2.33** of Cu-4/PANI nanocomposite shows cypress-leaf-like dendrite morphology. Some brighter spherical shaped particles are also observed in the SEM image and could be the loosely bound metal nanoparticles with PANI. The TEM image further supports a similar dendritic structure, with branches of ~400 nm length. However, raspberry-like uneven surface along with wire-like morphology are observed in Cu-6/PANI as shown in **Figure 2.34**. Thus, wire-like, flower-like and clustered

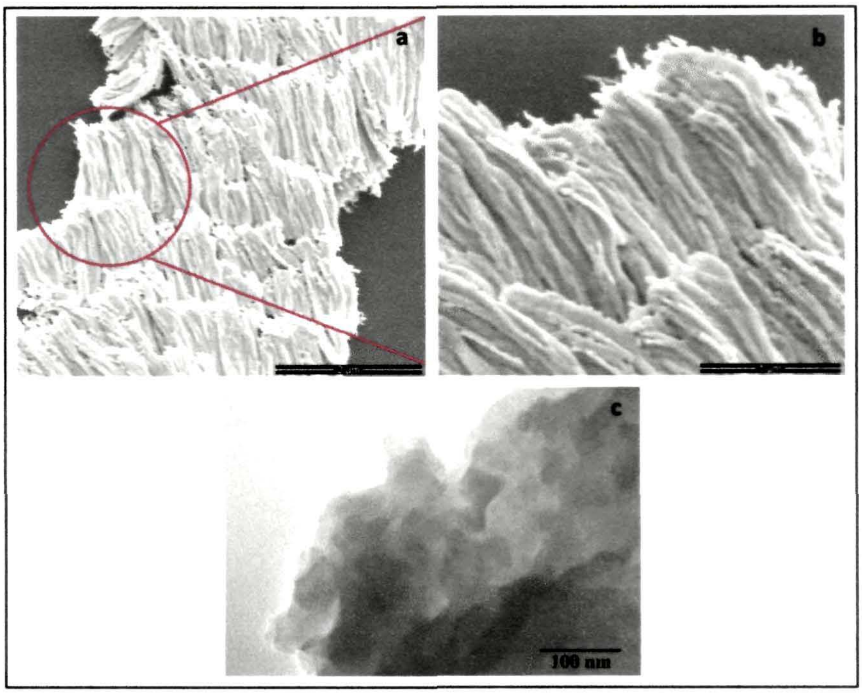

Figure 2.32. Top-down FE-SEM (**a**, **b**) and TEM (**c**) images of Cu-2/PANI nanocomposite.

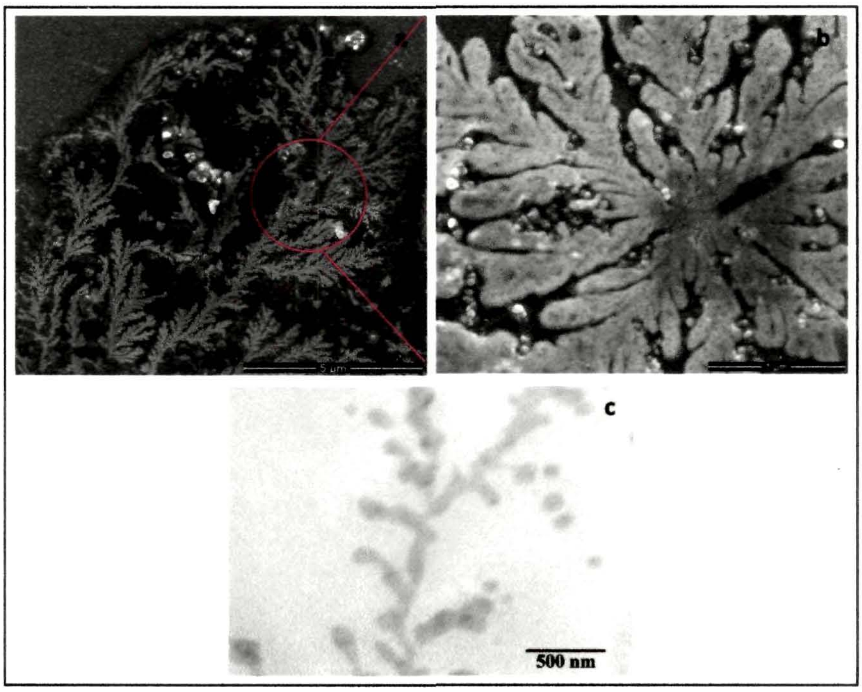

Figure 2.33. Top-down FE-SEM (**a**, **b**) and TEM (**c**) images of Cu-4/PANI nanocomposite.

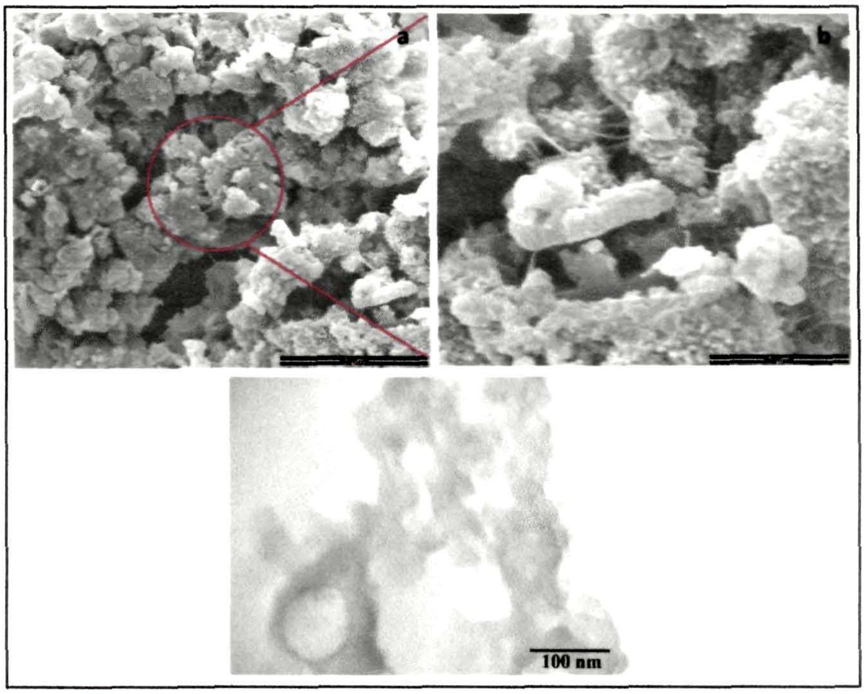

Figure 2.34. Top-down FE-SEM (**a**, **b**) and TEM (**c**) images of Cu-6/PANI nanocomposite.

morphologies of pristine Cu naoparticles transformed into layered threads, leaf and raspberry-like features after interaction with PANI.

The topography and phase images of Cu/PANI nanocomposites are presented in **Figures 2.35, 2.36 and 2.37** for Cu-2/PANI, Cu-4/PANI and Cu-6/PANI, respectively. Like SEM and TEM, the *2-D* and *3-D* topography and phase images (**Figure 2.35**) of Cu-2/PANI also show thread-like structures. The height profile of the topography image reveals very irregular size distribution with a maximum height difference of *ca.* 150 nm. The topography and phase images of Cu-4/PANI are however unable to identify the entire dendritic structure; instead reveal particles holding branch-like features (**Figure 2.36**). The scan area is not large enough to portray the entire leaf-like feature. The height profile of the topography image indicates a very rough surface with a maximum height difference of *ca.* 160 nm. In Cu-6/PANI nanocomposite, the topography and phase images (**Figure 2.37**) demonstrates the presence of raspberry-like features- an observation similar to SEM and TEM. The height profile of the topography image points out a maximum height difference of *ca.* 100 nm and average size of *ca.* 200 nm for these clusters.

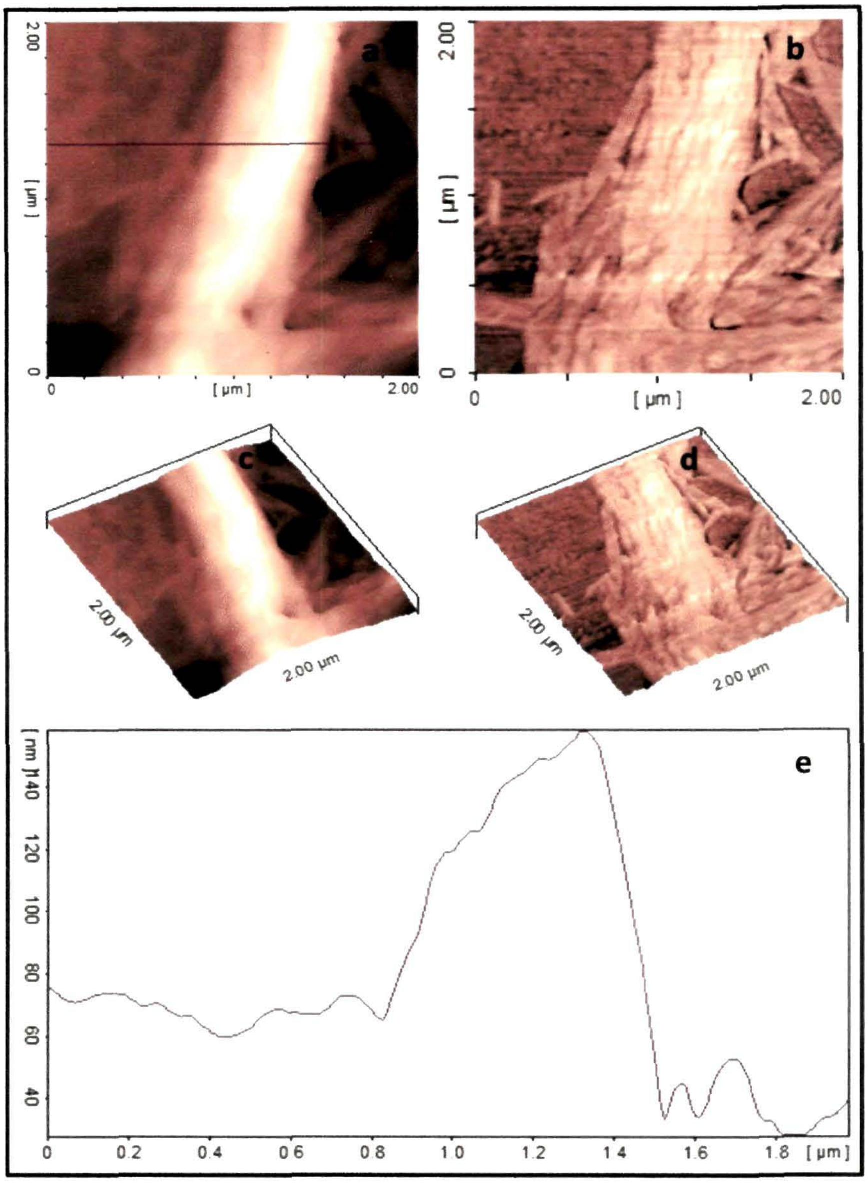

Figure 2.35. AFM tapping mode *2-D* topography (**a**) and phase (**b**) images of Cu-2/PANI nanocomposite. (**c**) and (**d**) are the corresponding *3-D* images of (**a**) and (**b**); and (**e**) is the typical height cross section image of (**a**).

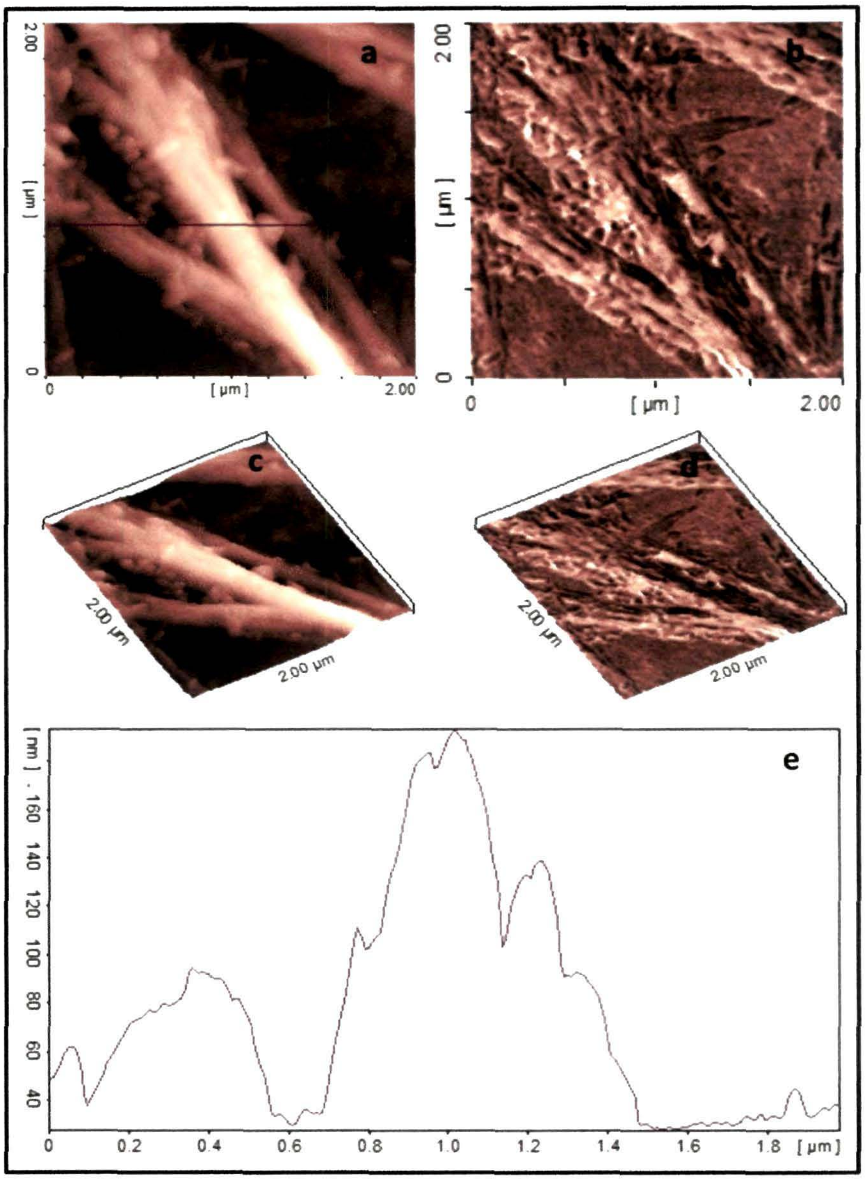

Figure 2.36. AFM tapping mode *2-D* topography (**a**) and phase (**b**) images of Cu-4/PANI nanocomposite. (**c**) and (**d**) are the corresponding *3-D* images of (**a**) and (**b**); and (**e**) is the typical height cross section image of (**a**).

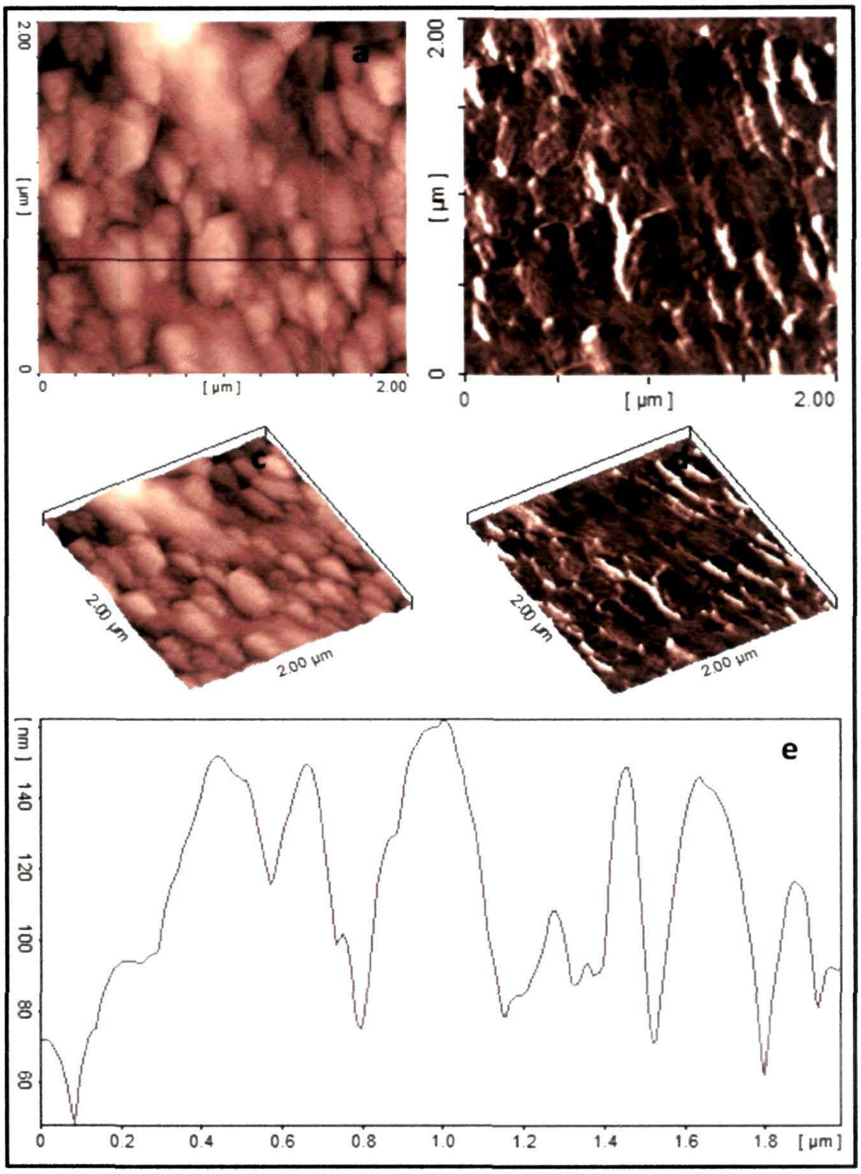

Figure 2.37. AFM tapping mode *2-D* topography (**a**) and phase (**b**) images of Cu-6/PANI nanocomposite. (**c**) and (**d**) are the corresponding *3-D* images of (**a**) and (**b**); and (**e**) is the typical height cross section image of (**a**).

2.3.2.6.2. Ni/PANI nanocomposites

Similar to Cu/PANI nanocomposites, Ni/PANI nanocomposites prepared from Ni-2, Ni-4 and Ni-6 nanoparticles also possess three different morphologies. For Ni-2/PANI, large agglomerates (**Figure 2.38**) ranging from nanometer to

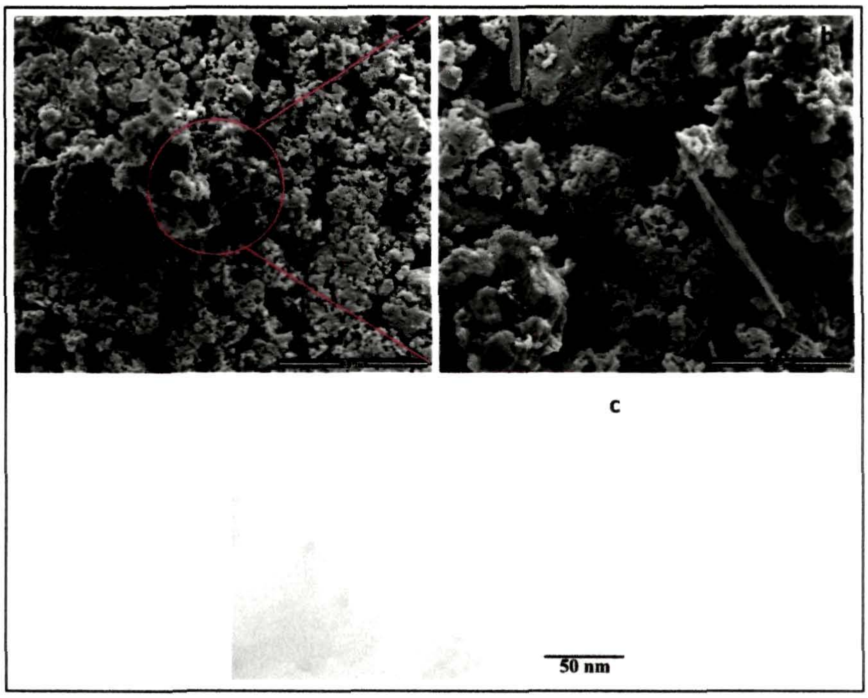

Figure 2.38. Top-down FE-SEM (**a**, **b**) and TEM (**c**) images of Ni-2/PANI nanocomposite.

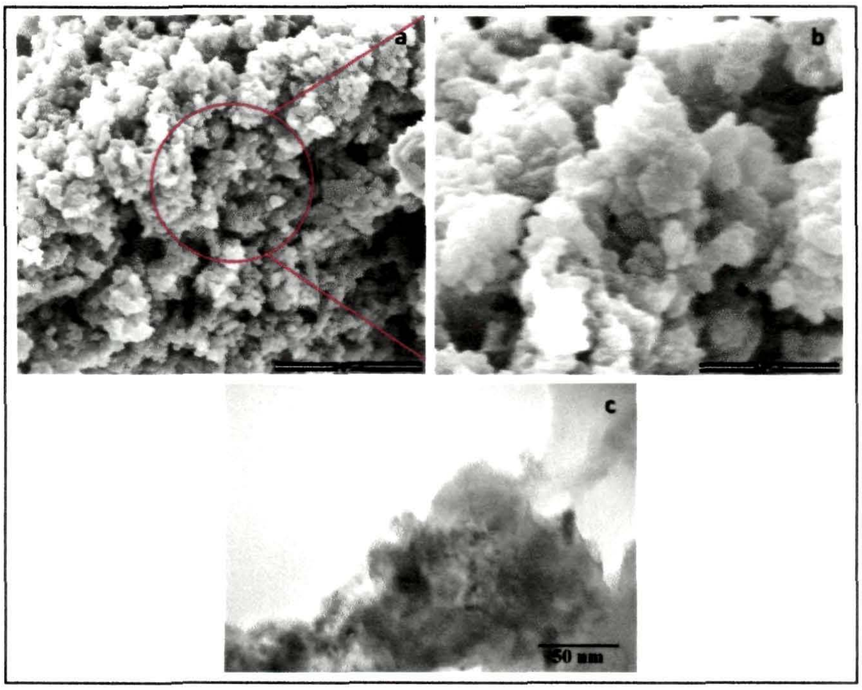

Figure 2.39. Top-down FE-SEM (**a**, **b**) and TEM (**c**) images of Ni-4/PANI nanocomposite.

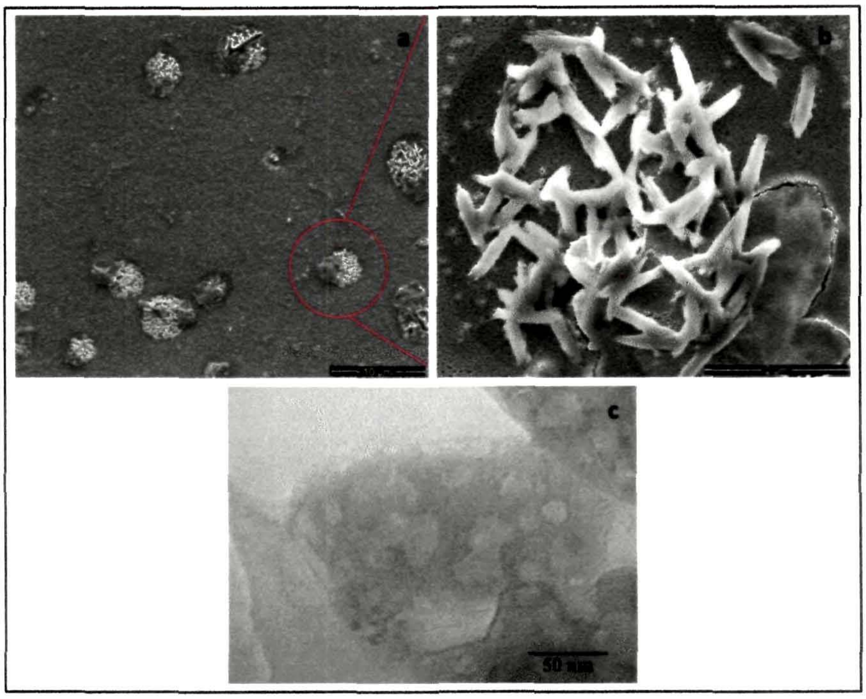

Figure 2.40. Top-down FE-SEM (**a**, **b**) and TEM (**c**) images of Ni-6/PANI nanocomposite.

micrometer sacle are observed in SEM images, whereas Ni-4/PANI comprises of globular clusters of 50 nm to 2 μm (**Figure 2.39**). Rod-like features (**Figure 2.40**) of almost uniform size (1.5 μm) are noticed in case of Ni-6/PANI composite. From TEM images, aggregates, thick particles and nanofoils are observed for Ni-2/PANI, Ni-4/PANI and Ni-6/PANI, respectively. Thus, it is evident that the interaction of nanoparticles with PANI accompanies morphological changes.

Like SEM and TEM, the AFM *2-D* and *3-D* topography and phase images of Ni-2/PANI Ni-4/PANI and Ni-6/PANI also show aggregates (**Figures 2.41**), clusters (**Figures 2.42**) and entangled rods (**Figures 2.43**), respectively. The height profile of the topography images show irregular surfaces in all nanocomposites and point out a maximum height difference of *ca.* 150 nm, 115 nm and 48 nm, respectively, for Ni-2/PANI, Ni-4/PANI and Ni-6/PANI.

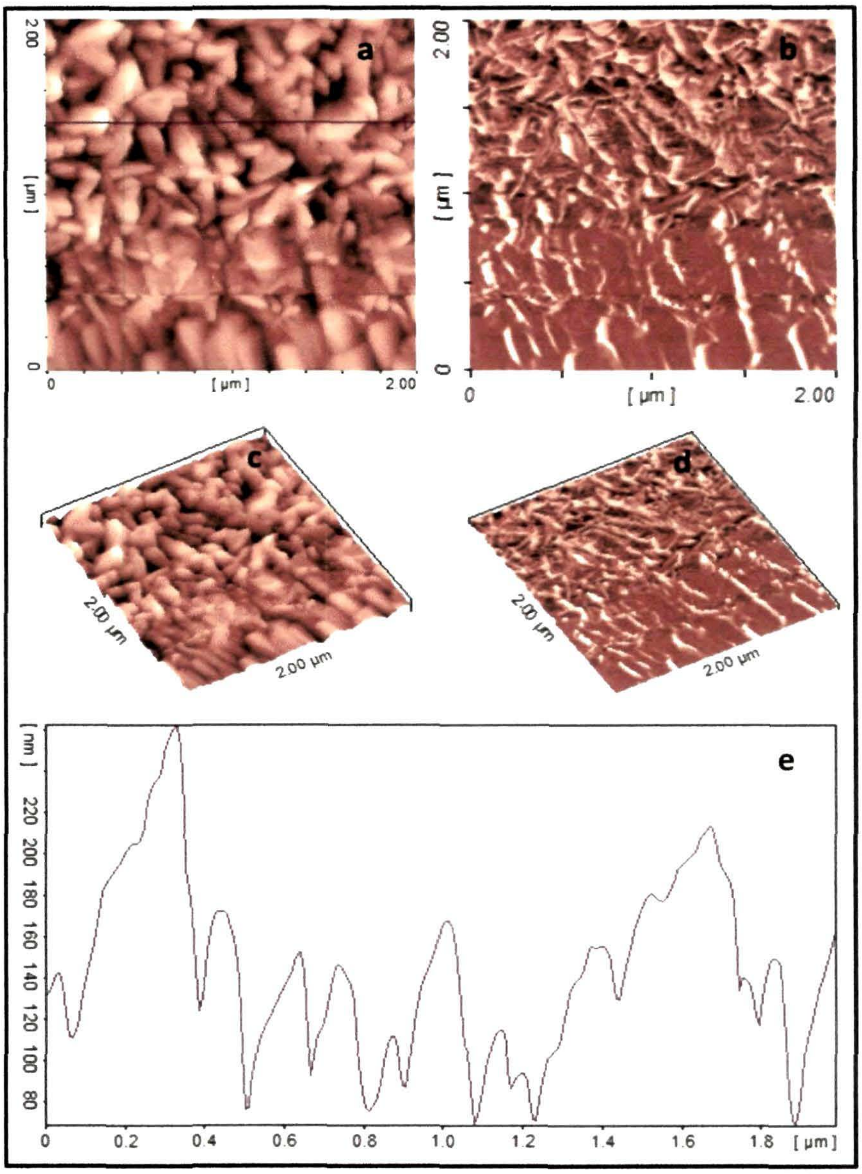

Figure 2.41. AFM tapping mode *2-D* topography (**a**) and phase (**b**) images of Ni-2/PANI nanocomposite. (**c**) and (**d**) are the corresponding *3-D* images of (**a**) and (**b**); and (**e**) is the typical height cross section image of (**a**).

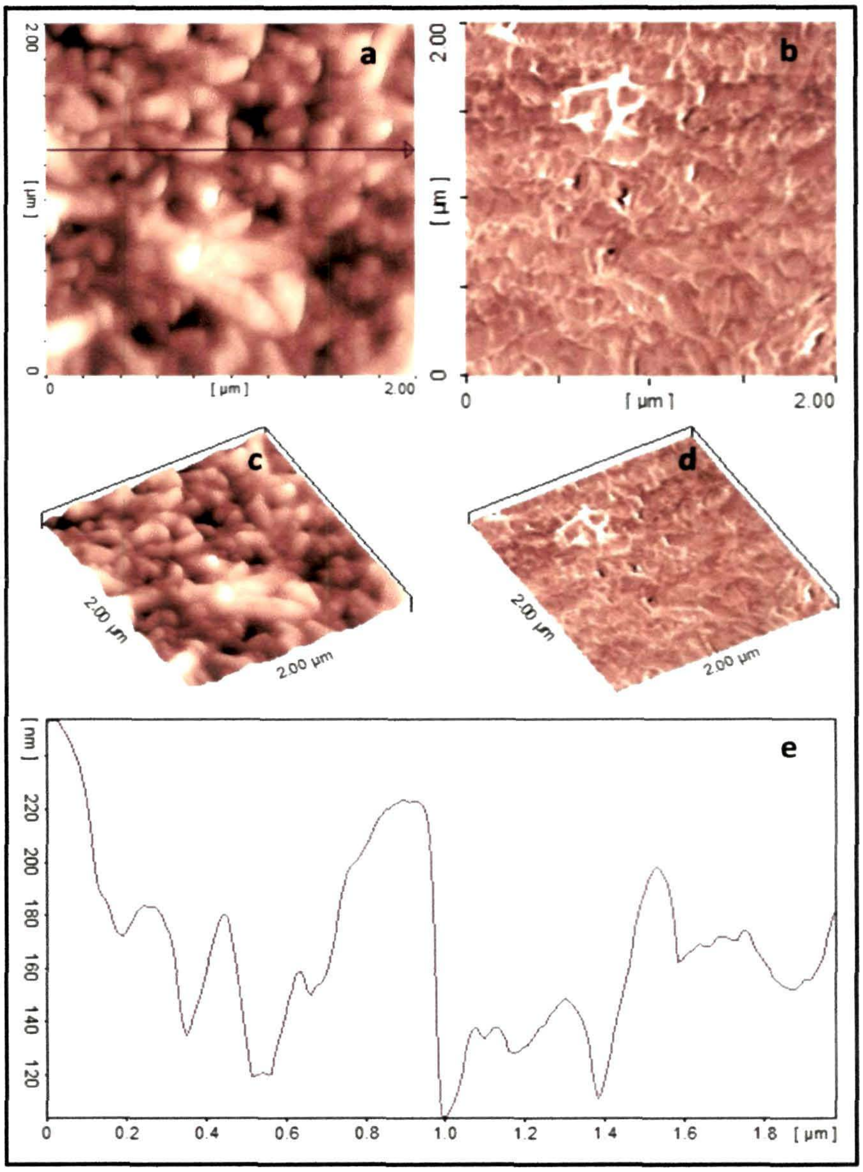

Figure 2.42. AFM tapping mode *2-D* topography (**a**) and phase (**b**) images of Ni-4/PANI nanocomposite. (**c**) and (**d**) are the corresponding *3-D* images of (**a**) and (**b**); and (**e**) is the typical height cross section image of (**a**).

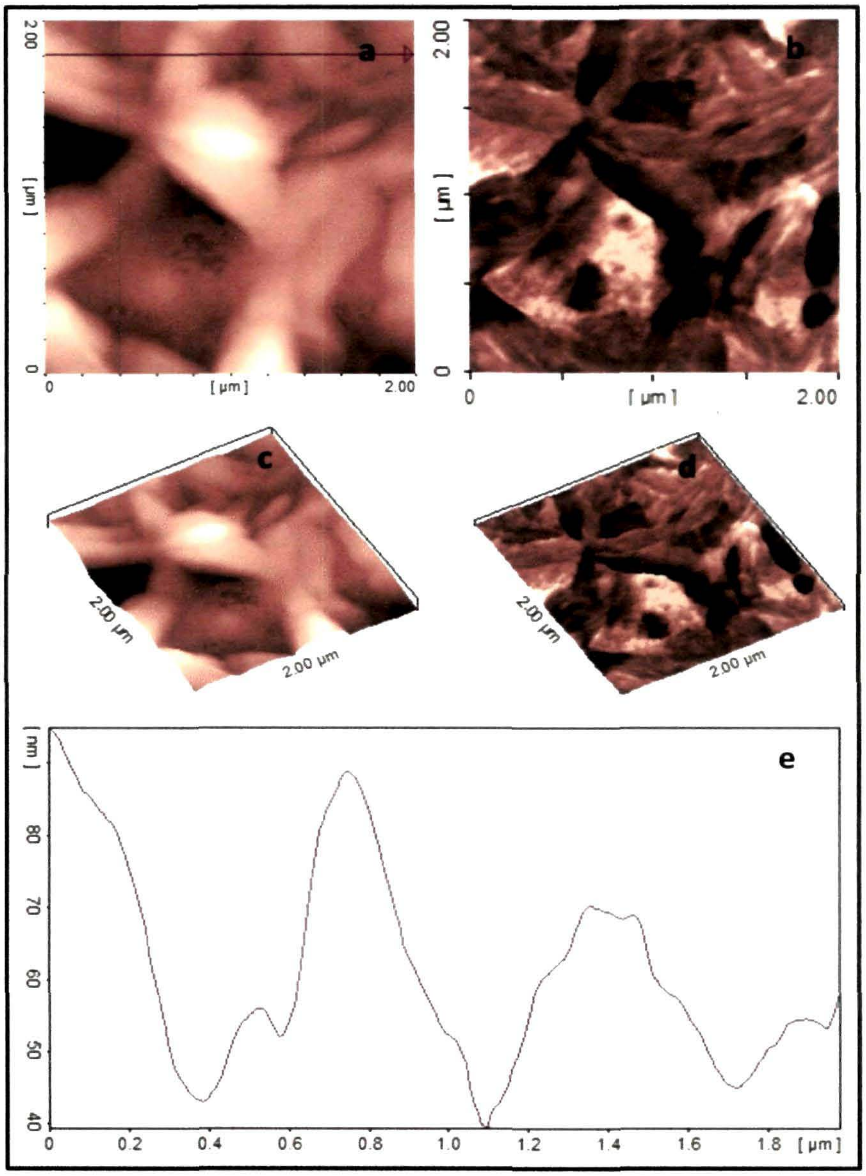

Figure 2.43. AFM tapping mode *2-D* topography (**a**) and phase (**b**) images of Ni-6/PANI nanocomposite. (**c**) and (**d**) are the corresponding *3-D* images of (**a**) and (**b**); and (**e**) is the typical height cross section image of (**a**).

2.3.3. Optical properties of metal nanoparticles and metal/PANI nanocomposites

UV-vis absorption spectra of Cu nanoparticles synthesized by varying TA concentrations are presented in **Figure 2.44**. The UV-vis absorption band for Cu nanoparticles is generally expected at around 570 nm[97,98] and this is due to the excitation of plasmon resonance or interband transition. However, from **Figure 2.44**, it is evident that irrespective of the concentration of TA used in the synthesis, the nanoparticles show absorption at around 370 nm without the appearance of surface plasmonic band at around 570 nm. Formation of smaller particles and the presence of high conformational surface ordering of TA on the surface of Cu nanoparticles might be the reasons of the disappreance of plasmon band. Foresti *et al.* observed this kind of phenomenon while synthesizing thiophene protected Cu nanoparticles [99]. In addition, according to Mie's theory, a UV-vis absorption profiles exhibiting an exponential decay Mie scattering with decreasing photon energy, without the surface-plasmon band, is a

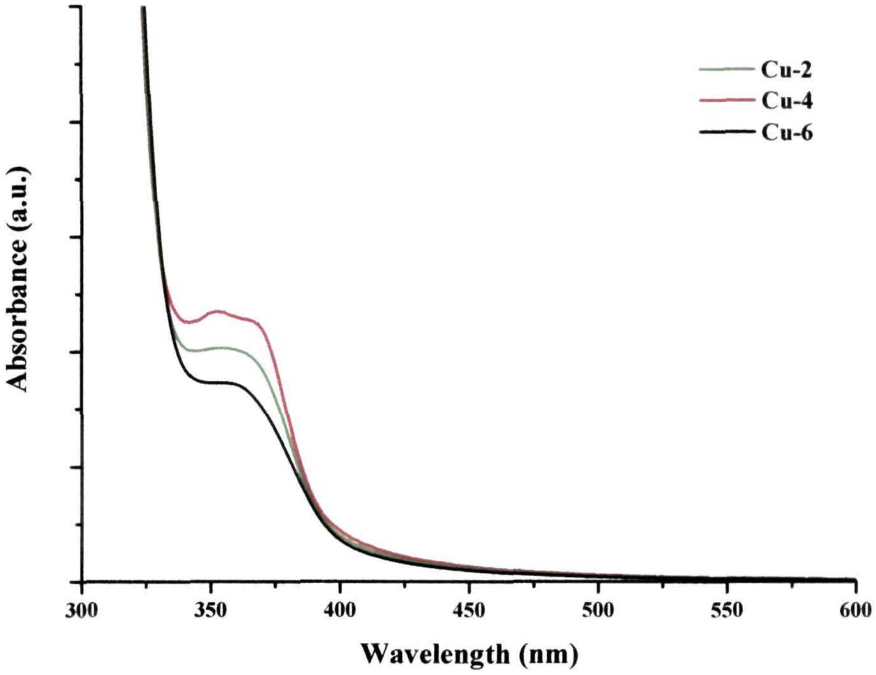

Figure 2.44. UV-visible absorption spectra of Cu nanoparticles.

characteristic of nanosized particles and this kind of profiles have been observed for smaller Cu nanoprticles[100,101].

The UV-visible absorption spectra of PANI and its composites with Cu nanoparticles were also recorded in order to study the influence of nanoparticles on the optical properties of PANI. **Figure 2.45** exhibits the UV-vis absorption spectra of PANI and Cu/PANI nanocomposites. The absorption spectrum of pure PANI shows two distinct characteristic peaks at 340 and 635 nm. The absorption peak at 340 nm arises from the highest occupied molecular orbital (HOMO) and lowest unoccupied molecular orbital (LUMO) in the benzenoid rings. The peak at 635 nm is associated with a benzenoid to quinoid excitonic transition[102]. The absorption bands for Cu/PANI nanocomposites are found almost in the same positions of that of PANI; however, the band intensities increase with respect to PANI. This could be attributed to the interaction

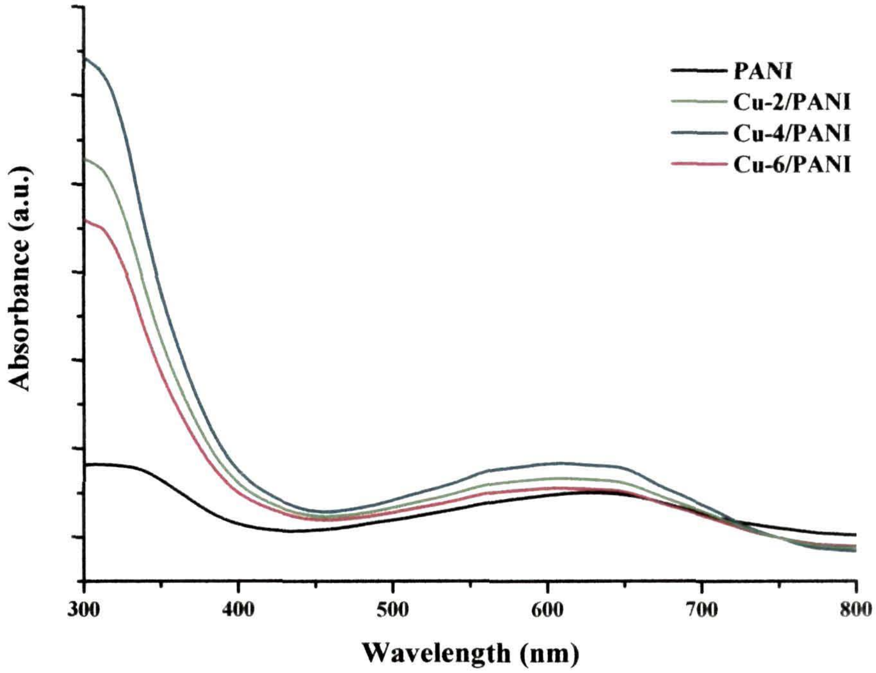

Figure 2.45. UV-visible absorption spectra of PANI and Cu/PANI nanocomposites.

between metal and polymer, which results in combined effect in increasing absorption ability of the nanocomposites.

PL measurements also provide important information about optical properties of Cu nanoparticles and their corresponding composites with PANI. **Figure 2.46** shows the PL spectra of Cu nanoparticles prepared with varying TA concentrations, and the spectra were recorded by exciting at their maximum absorption wavelength. Cu nanoparticles emit in the region of green light with a maximum intensity located at 513 nm irrespective of TA concentration used in the synthesis.

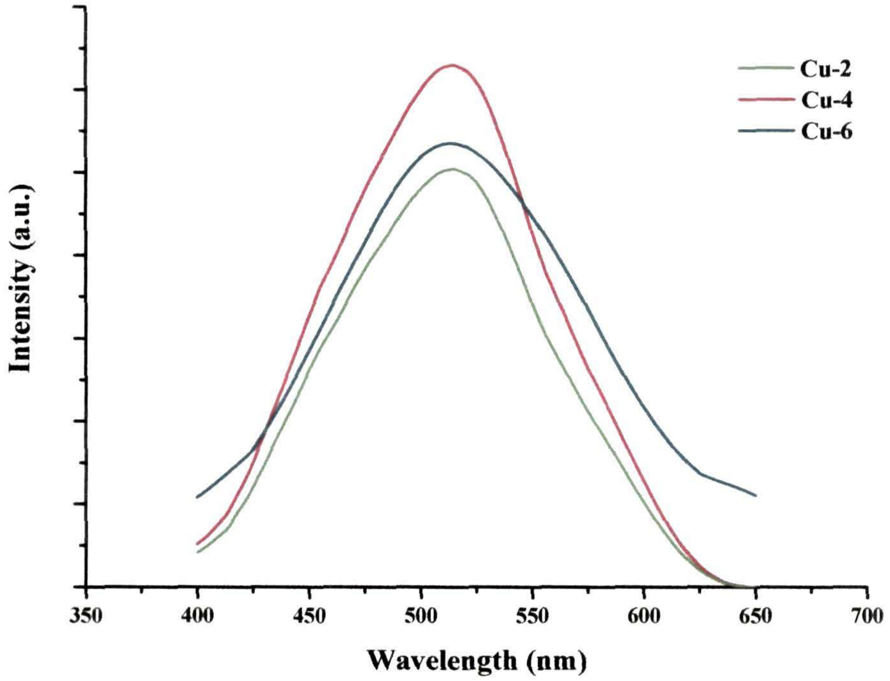

Figure 2.46. PL spectra of Cu nanoparticles.

As revealed in **Figure 2.47**, all Cu/PANI nanocomposites exhibit gratifying photoluminescence characteristics. Since PANI does not show photoluminescence property and therefore, the emission spectra found in the composites are mainly due to Cu nanoparticles. However, the luminescence maximum for Cu nanoparticles in presence of PANI is red shifted with band centre around 542 nm. Thus, hydrogen bonding and electrostatic interaction of carboxyl and hydroxyl groups of TA around Cu nanoparticles with PANI chain affected the PL emission of Cu nanoparticles.

For Ni nanoparticles, UV-vis absorption spectra are presented in **Figure 2.48**. The curves present broad and weak absorption spectra of nanoparticles, showing that the surface plasmon resonance absorption of all Ni nanoparticles is in the range 340-370 nm. This result is consistent with the earlier reports[103, 104]. The resulting broad and weak absorption band of the nanoparticles is probably due to the strong interaction between TA and Ni nanoparticles, resulting smaller nanoparticles.

The UV-vis absorption spectra of pure PANI and Ni/PANI are presented in **Figure 2.49**. Similar to Cu/PANI, the absorption bands for Ni/PANI are also found almost in the same positions of PANI. However, all Ni nanoparticles and their corresponding composites with PANI did not show PL emission spectra.

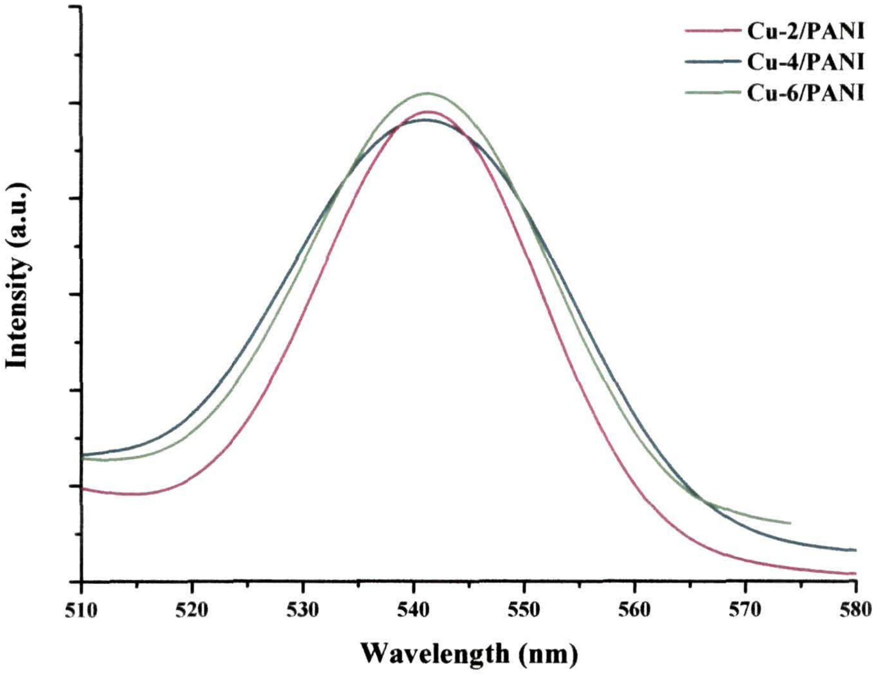

Figure 2.47. PL spectra of Cu/PANI nanocomposites.

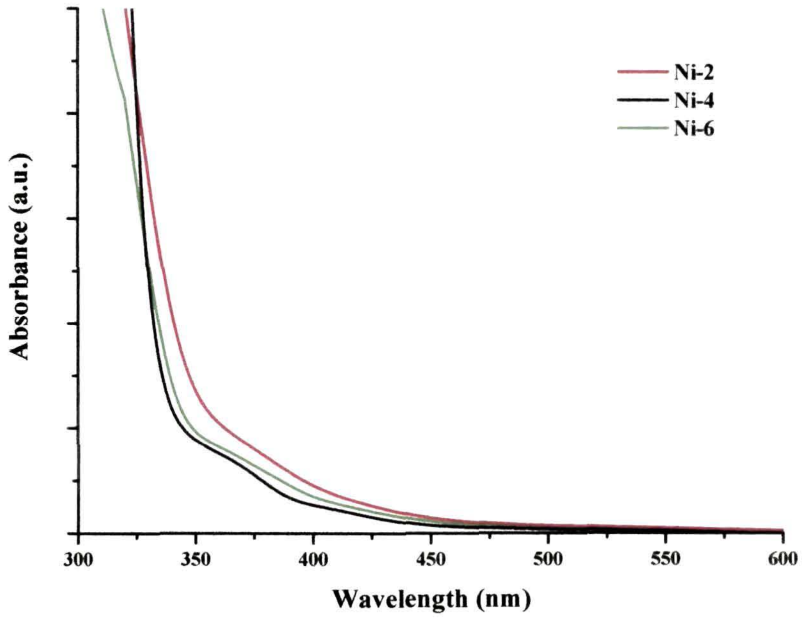

Figure 2.48. UV-visible absorption spectra of Ni nanoparticles.

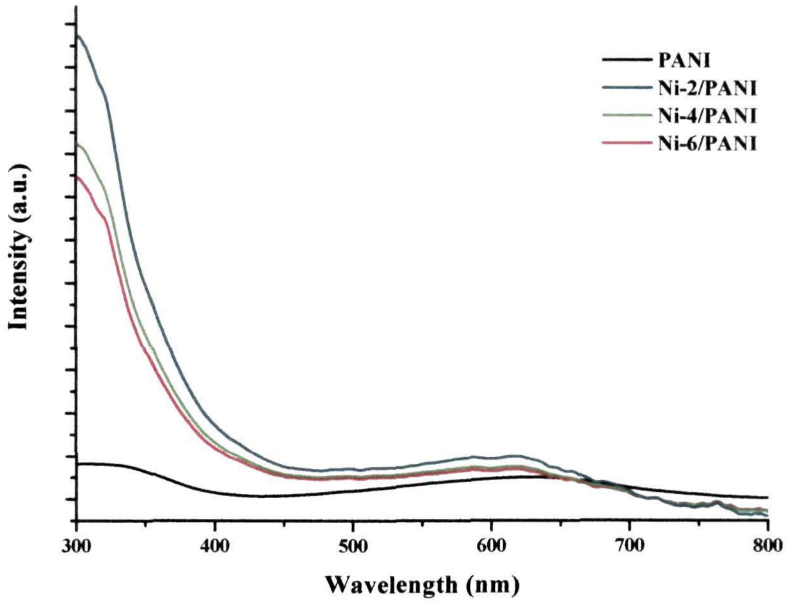

Figure 2.49. UV-visible absorption spectra of PANI and Ni/PANI nanocomposites.

2.3.4. Electrical properties of metal/PANI nanocomposites

Figures 2.50 and **2.51** show the I-V characteristics of Cu/PANI and Ni/PANI nanocomposites, respectively. The I-V characteristics are asymmetric and nonlinear for forward and reverse directions of applied voltage. This suggests the semiconducting behavior and the formation of Schottky barrier in the nanocomposites[105]. Thus, the diode like I-V characteristic of the nanocomposites is due to the modification of the metal nanoparticles with PANI and the formation of nanosize grains.

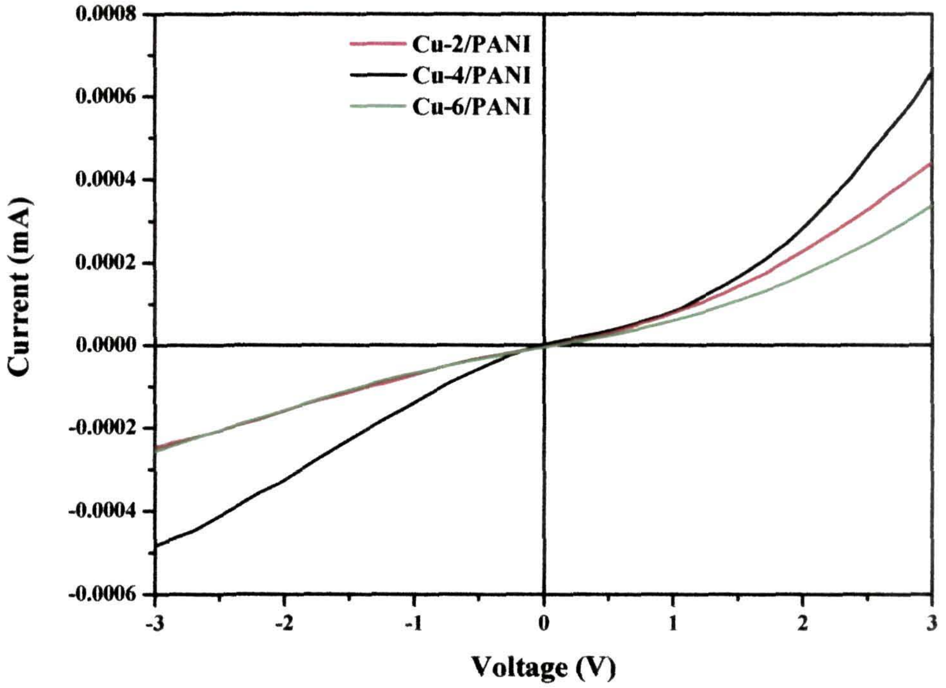

Figure 2.50. I-V characteristic curves of Cu/PANI nanocomposites at room temperature.

The temperature dependent DC conductivity of PANI and Cu/PANI nanocomposites are presented in **Table 2.6.** It is evident from the table that the conductivities of all Cu/PANI nanocomposites are found to be significantly higher than the pure polymer, PANI irrespective of the temperature and nature of the composites. Initially, DC conductivity of all nanocomposites decreased with increasing temperature up to 70 °C and then kept on rising with the increase of temperature. However, decrease in conductivity upto 50 °C and then gradual increase in conductivity was observed in case of pure PANI. In the initial state of heating, heat may be used up in molecular as

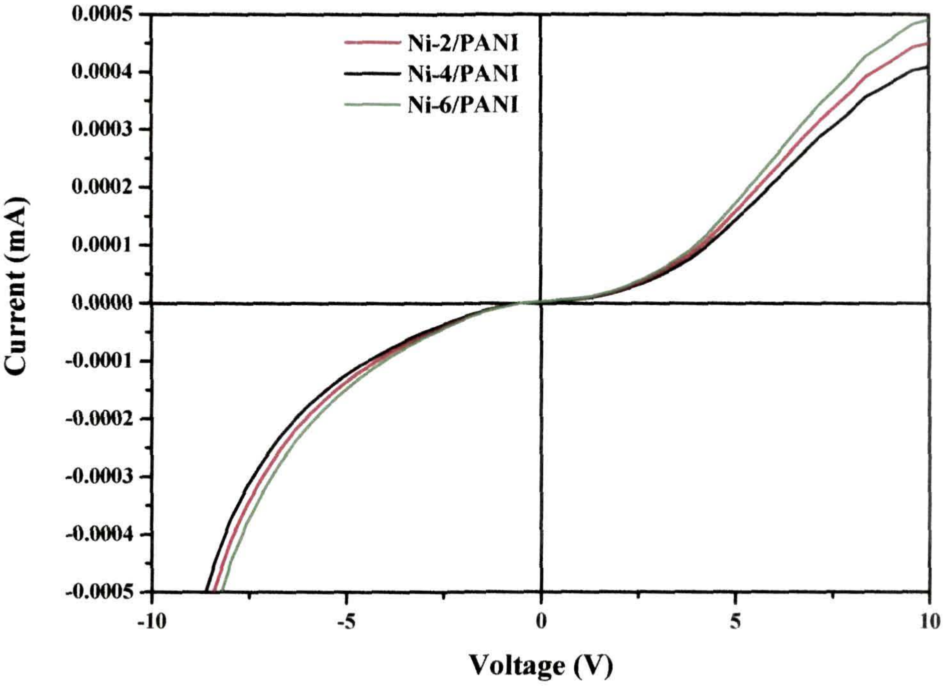

Figure 2.51. I-V characteristic curves of Ni/PANI nanocomposites at room temperature.

Table 2.6. DC electrical conductivities of pure PANI and Cu/PANI nanocomposites at different temperatures

Temperature (oC)	**Conductivity (S/cm)**			
	PANI	Cu-2/PANI	Cu-4/PANI	Cu-6/PANI
30	0.044	0.169	0.178	0.140
50	0.042	0.080	0.087	0.072
70	0.044	0.080	0.087	0.071
90	0.046	0.089	0.090	0.087
100	0.046	0.100	0.100	0.095

well as filler orientation instead of electron hopping from HOMO to LUMO and hence, the decreases in conductivity observed initially[95,106]. On the other hand, the increase in conductivities with the rise of temperature can be attributed to the increasing charge carrier mobility of electrons through the polymer backbone due to thermal activation. At elevated temperatures, kinetic energy of electrons increases, causing higher electron movement rate and hence, increase in electrical conduction. On the contrary, at low temperatures, charge carrier mobility is not enough for interchain and intrachain hopping for composite system. Number of charge carriers and degree of π-electron delocalization are also correlated with the conductivity. Insufficient level of π-electron delocalization and limited number of charge carriers could be the result of having low conductivity.

The DC electrical conductivities of Ni/PANI and PANI with respect to temperature are compiled in **Table 2.7**. The interaction of Ni with PANI did not show great enhancement of DC electrical conductivity upto 70 °C. This decrease in conductivity can be explained by the following two reasons: (1) non-formation of any charge transfer complex, and formation of some unwanted chemical reactions, and new unwanted chemical bonds between capping agent and nanoparticles; (2) having more crackings, reduced aggregations, and voids may origin to verify the lowest conductivity

Table 2.7. DC electrical conductivities of pure PANI and Ni/PANI nanocomposites at different temperatures

Temperature (°C)	**Conductivity (S/cm)**			
	PANI	**Ni-2/PANI**	**Ni-4/PANI**	**Ni-6/PANI**
30	0.044	0.014	0.014	0.011
50	0.042	0.013	0.013	0.010
70	0.044	0.014	0.015	0.013
90	0.046	0.128	0.147	0.127
100	0.046	0.128	0.147	0.128

of the composites. Decrease in conductivity in nanocomposites as compared to bare polymer has been observed by Flitton *et al.*[107]. They justified their findings as a direct consequence of increase in resistive interparticle contacts within the material. However, in the present investigation, the slight increase in conductivity was observed after 70 °C and this could be attributed to the increase in conjugation and number of charge carriers at higher temperature.

2.4. Conclusions

The important findings of this investigation on Cu and Ni nanoparticles, and their corresponding PANI composites are given below:

- A one-step synthesis procedure has been achieved successfully for synthesis of stable colloidal dispersion of Cu and Ni nanoparticles. TA, a green reagent is used as reducing as well as capping agent. It has been observed that particle size and morphology of metal nanostructures could be controlled by varying TA concentrations. Growth mechanism based on oriented attachment and Ostwald ripening is proposed. This method opens a new way for shape- and size- controlled synthesis of other metallic nanoparticles.
- XRD analysis reveals face-centred-cubic (fcc) structure for both Cu and Ni naoparticles. Average particle sizes calculated by Scherrer formula are 8.7 ± 1 nm and 5.1 ± 1 nm, respectively, for Cu and Ni nanoparticles synthesized with 0.04 M TA.
- FTIR analysis reveals that TA adheres to the metal nanoparticles and hence, offers stability to the naoparticles. This capping role of TA is further supported by XPS study.
- Weight loss characteristic studied by TGA reveals that less than 8% Cu and 5% Ni nanoparticles synthesized with 0.04 M TA remain in the samples at 800 °C.
- Wire-like, flower-like and cluster-like morphologies are observed for Cu nanostructures synthesized with 0.02, 0.04 and 0.06 M TA, respectively. This

implies structure-directing nature of TA.

- PANI and its metal-based nanocomposites of different morphologies have been synthesized utilizing the synthesized metal nanostructures by *in-situ* polymerization technique. FTIR and XPS results indicate sufficient interaction of metal nanoparticles with PANI. From TGA data, it has been found that the thermal stability of bare polymer is enhanced after interaction with metal nanoparticles.
- UV-vis absorption study reveals the absence of surface plasmon resonance band in Cu nanoparticles because of smaller particles and the presence of high conformational surface ordering of TA on the surface of Cu nanoparticles. These Cu nanoparticles are photoluminescent and emit in green light region. In case of all nanocomposites, the PL maximum of Cu nanoparticles is red-shifted.
- For Ni nanoparticles, broad and weak surface plasmon resonance bands are observed in the UV-vis spectra. The two characteristics peaks of PANI at 340 and 635 nm remain unchanged after interaction with Ni nanoparticles. All Ni nanoparticles and their corresponding composites with PANI do not exhibit any photoluminescence property.
- The I-V characteristics of metal and PANI based nanocomposites are asymmetric and nonlinear for forward and reverse directions of applied voltage suggesting the semiconducting behavior and the formation of Schottky barrier in the nanocomposites.
- The temperature dependent DC conductivities of Cu/PANI nanocomposites are found to be significantly higher than that of pure PANI. On the other hand, decrease in conductivity up to 70 °C with respect to bare PANI are observed in case of Ni/PANI composites. However, after rising temperature, the conductivity of the Ni/PANI composites increases as compared to pure PANI.

References

1. Milliron, D. J. *et al.* Colloidal nanocrystal heterostructures with linear and branched topology, *Nature* **430**, 190-195 (2004)
2. Colfen, H.; Antonietti, M. Mesocrystals: inorganic superstructures made by highly parallel crystallization and controlled alignment, *Angew. Chem. Int. Ed.* **44**, 5576-5591 (2005)
3. Biswas, A.; Eilers, H.; Hidden, F.; Aktas, O. C.; Kiran, C. V. S. Large broadband visible to infrared plasmonic absorption from Ag nanoparticles with a fractal structure embedded in a teflon AF® matrix, *Appl. Phys. Lett.* **88**, 013103-013105 (2006)
4. Yu, X.; Cao, C. Photoresponse and field-emission properties of bismuth sulfide nanoflowers, *Cryst. Growth Des.* **8**, 3951-3955 (2008)
5. Xiong, S.; Zhang, X.; Qian, Y. CdS with various novel hierarchical nanostructures by nanobelts/nanowires self-assembly: controllable preparation and their optical properties, *Cryst. Growth Des.* **9**, 5259-5265 (2009)
6. Xu, L.; Lu, C.; Zhang, Z.; Yang, X.; Hou, W. Various self-assembled three-dimensional hierarchical architectures of $La_2(MoO_4)_3$: controlled synthesis, growth mechanisms, luminescence properties and adsorption activities, *Nanoscale* **2**, 995-1005 (2010)
7. Whitesides, G. M.; Grzybowski, B. Self-assembly at all scales, *Science* **295**, 2418-2421 (2002)
8. Chen, H.; Lesnyak, V.; Bigall, N. C.; Gaponik, N.; Eychmuller, A. Self-assembly of TGA-capped CdTe nanocrystals into three-dimensional luminescent nanostructures, *Chem. Mater.* **22**, 2309-2314 (2010)
9. Wang, X.; Zhuang, J.; Peng, Q.; Li, Y. Liquid-solid-solution synthesis of biomedical hydroxyapatite nanorods, *Adv. Mater.* **18**, 2031-2034 (2006)
10. Qian, L. Self-assembled heavy lanthanide orthovanadate architecture with controlled dimensionality and morphology, *Chem. Eur. J.* **15**, 1233-1240 (2009)

11. Watt, J. Ultrafast growth of highly branched palladium nanostructures for catalysis, *ACS Nano* **4**, 396-402 (2010)
12. Kuo, C. H.; Huang, M. H. Synthesis of branched gold nanocrystals by a seeding growth approach, *Langmuir* **21**, 2012-2016 (2005)
13. Liu, X.; Liang, X.; Zhang, N.; Qiu, G.; Yi, R. Selective synthesis and characterization of sea urchin-like metallic nickel nanocrystals, *Mater. Sci. Eng. B* **132**, 272-277 (2006)
14. Sun, Y.; Xia, Y. Shape-controlled synthesis of gold and silver nanoparticles, *Science* **298**, 2176-2179 (2002)
15. Kilin, D. S.; Prezhdo, O. V.; Xia, Y. N. Shape-controlled synthesis of silver nanoparticles: Ab initio study of preferential surface coordination with citric acid, *Chem. Phys. Lett.* **458**, 113-116 (2008)
16. Suber, L.; Sondi, I.; Matijevic, E.; Goia, D. V. Preparation and the mechanisms of formation of silver particles of different morphologies in homogeneous solutions, *J. Colloid Interface Sci.* **288**, 489-495 (2005)
17. Mirkin, C. A. Programming the assembly of two- and three- dimensional architectures with DNA and nanoscale inorganic building blocks, *Inorg. Chem.* **39**, 2258-2272 (2000)
18. Waley, S. R.; English, D. S.; Hu, E. L.; Barbara, P. F.; Belcher, A. M. Selection of peptides with semiconductor binding specificity for directed nanocrystal assembly, *Nature* **405**, 665-668 (2000)
19. Mamedova, N. N.; Kotov, N. A.; Rogach, A. L.; Studer, J. Albumin-CdTe nanoparticle bioconjugates: preparation, structure, and interunit energy transfer with antenna effect, *Nano Lett.* **1**, 281-286 (2001)
20. Zhong, Z. *et al.* Controlled organizations of Au colloids into linear assemblies, *J. Phys. Chem. B* **108**, 18119-18123 (2004)
21. Fowler, C. E.; Shenton, W.; Stubbs, G.; Mann, S. Tobacco mosaic virus liquid crystals as templates for the interior design of silica mesophases and nanoparticles, *Adv. Mater.* **13**, 1266-1269 (2001)

22. Rosi, N. L.; Thaxton, C. S.; Mirkin, C. A. Control of nanoparticle assembly using DNA-modified diatom templates, *Angew. Chem. Int. Edn.* **43**, 5500-5503 (2004)

23. Yoosaf, K.; Ipe, B. I.; Suresh, C. H.; Thomas, K. G. In situ synthesis of metal nanoparticles and selective naked-eye detection of lead ions from aqueous media, *J. Phys. Chem. C* **111**, 12839-12847 (2007)

24. Dujardin, E.; Peet, C.; Stubbs, G.; Culver, J. N.; Mann, S. Organization of metallic nanoparticles using tobacco mosaic virus templates, *Nano Lett.* **3**, 413-417 (2003)

25. Taton, T. A.; Mirkin, C. A.; Letsinger, R. L. Scanometric DNA array detection with nanoparticle probes, *Science* **289**, 1757-1760 (2000)

26. Liu, J.; Lu, Y. A colorimetric lead biosensor using DNAzyme-directed assembly of gold nanoparticles, *J. Am. Chem. Soc.* **125**, 6642-6643 (2003)

27. Keren, K.; Berman, R. S.; Buchstab, E.; Sivan, U.; Braun, E. DNA-templated carbon nanotube field-effect transistor, *Science* **302**, 1380-1382 (2003)

28. Eastman, J. A.; Choi, S. U. S.; Li, S.; Yu, W.; Thompson, L. J. Anomalously increased effective thermal conductivities of ethylene glycol-based nanofluids containing copper nanoparticles, *Appl. Phys. Lett.* **78**, 718-720 (2001)

29. Lu, L.; Sui, M. L.; Lu, K. Superplastic extensibility of nanocrystalline copper at room temperature, *Science* **287**, 1463-1466 (2000)

30. Anyaogu, K. C.; Fedorov, A. V.; Neckers, D. C. Synthesis, characterization, and antifouling potential of functionalized copper nanoparticles, *Langmuir* **24**, 4340-4346 (2008)

31. Zhou, W. Copper catalyzing growth of single-walled carbon nanotubes on substrates, *Nano Lett.* **6**, 2987-2990 (2006)

32. Ressler, T.; Kniep, B. L.; Kasatkin, I.; Schögl, R. The microstructure of copper zinc oxide catalysts: bridging the materials gap, *Angew. Chem. Int. Ed.* **44**, 4704-4707 (2005)

33. Vukojević, S.; Trapp, O.; Grunwaldt, J.; Kiener, C.; Schüth, F. Quasi-homogeneous methanol synthesis over highly active copper nanoparticles, *Angew. Chem. Int. Ed.* **44**, 7978-7981 (2005)

34. Reetz, M. T.; Helbig, W. J. Size-selective synthesis of nanostructured transition metal clusters, *J. Am. Chem. Soc.* **116**, 7401-7402 (1994)

35. Iglesias, J.; García De Saldaña, E.; Jaén, J. A. On the tannic acid interaction with metallic iron, *Hyperfine Interact.* **134**, 109-114 (2001)

36. Lee, Y.; Choi, J.; Lee, K. J.; Stott, N. E.; Kim, D. Large-scale synthesis of copper nanoparticles by chemically controlled reduction for applications of inkjet-printed electronics, *Nanotechnology* **19**, 415604-415610 (2008)

37. Peng, X. G. *et al.* Shape control of CdSe nanocrystals, *Nature* **404**, 59-61 (2000)

38. Ogawa, T.; Ootani, M.; Asai, T.; Hasegawa, M.; Ito, O. Effect of inorganic binders on the properties of thick film copper conductor, *IEEE Trans. Compon. Packag. Manuf. Technol. A* **17**, 625-630 (1994)

39. Esteban-Cubillo, A.; Pecharroma'n, C.; Aguilar, E.; Santare'n, J.; Moya, J. S. Antibacterial activity of copper monodispersed nanoparticles into sepiolite, *J. Mater. Sci.* **41**, 5208-5212 (2006)

40. Ohde, H.; Hunt, F.; Wai, C. M. Synthesis of silver and copper nanoparticles in a water-in-supercritical-carbon dioxide microemulsion, *Chem. Mater.* **13**, 4130-4135 (2001)

41. Crouse, C.; Barron, A. R. Reagent control over the size, uniformity, and composition of Co-Fe-O nanoparticles, *J. Mater. Chem.* **18**, 4146-4153 (2008)

42. Pileni, M. P. Ferrite magnetic fluids: a new fabrication method and magnetic properties of nanocrystals differing by their size and composition, *Adv. Funct. Mater.* **11**, 323-333 (2001)

43. Wang, S. F.; Xie, F.; Hu, R. F. Carbon-coated nickel magnetic nanoparticles modified electrodes as a sensor for determination of acetaminophen, *Sensors and Actuators B* **123**, 495-500 (2007)

44. Speliotis, D. E. Magnetic recording beyond the first 100 years, *J. Magn. Magn. Mater.* **193**, 29-35 (1999)

45. Matasushita, N.; Chong, C. P.; Mizutani, T.; Abe, M. Ni-Zn ferrite films with high permeability (μ'= ~30, μ''= ~30) at 1 GHz prepared at 90 °C, *J. Appl. Phys.* **91**, 7376-7378 (2002)

46. Deliyanni, E. A.; Bakoyannakis, D. N.; Zouboulis, A. I.; Matis, K. A. Sorption of As(V) ions by akaganeite-type nanocrystals, *Chemosphere* **50** 155-163 (2003)

47. Trivedi, P.; Axe, L. Modeling Cd and Zn sorption to hydrous metal oxides, *Environ. Sci. Technol.* **34**, 2215-2223 (2000)

48. Jendelova, P. *et al.* Magnetic resonance tracking of transplanted bone marrow and embryonic stem cells labelled by iron oxide nanoparticles in rat brain and spinal cord, *J. Neurosci. Res.* **76**, 232-243 (2004)

49. Wiltshire, M. C. K. *et al.* Microstructured magnetic materials for RF flux guides in magnetic resonance imaging, *Science* **291**, 849-851 (2001)

50. Loubeyre, P. *et al.* Comparison of iron oxide particles (AMI 227) with a gadolinium complex (Gd-DOTA) in dynamic susceptibility contrast MR imaging's (FLASH and EPI) for both phantom and rat brain at 1.5 Tesla, *J. Mag. Reson. Imaging* **9**, 447-453 (1999)

51. Bucak, S.; Jones, D. A.; Laibinis, P. E.; Hatton, T. A. Protein separations using colloidal magnetic nanoparticles, *Biotechnol. Prog.* **19**, 477-484 (2003)

52. Hatch, G. P.; Steler, R. E. Magnetic design considerations for devices and particles used for biological high-gradient magnetic separation (HGMS) systems, *J. Magn. Magn. Mater.* **225**, 262-276 (2001)

53. Shinkai, M.; Ito, A. Functional magnetic particles for medical application, *Adv. Biochem. Eng. Biotechnol.* **91**, 191-220 (2004)

54. Chan, D. C. F.; Kirpotin, D. B.; Bunn, P. A. Synthesis and evaluation of colloidal magnetic iron oxides for the site-specific radio frequency-induced hyperthermia of cancer, *J. Magn. Magn. Mater.* **122**, 374-378 (1993)

55. Heracleous, E.; Lee, A. F.; Wilson, K.; Lemonidou, A. A. Investigation of Ni-based alumina supported catalysts for the oxidative dehydrogenation of ethane to ethylene: structural characterization and reactivity studies, *J. Catal.* **231**, 159-171 (2005)

56. Li, X. K.; Ji, W. J.; Zhao, J.; Wang, S. J.; Au, C. T. Ammonia decomposition over Ru and Ni catalysts supported on fumed SiO_2, MCM-41, and SBA-15, *J. Catal.* **236**, 181-189 (2005)

57. Molina, A. I. *et al.* Nickel supported on porous silica as catalysts for the gas-phase hydrogenation of acetonitrile, *J. Catal.* **225**, 479-488 (2004)

58. Li, Y. *et al.* Novel Ni catalysts for methane decomposition to hydrogen and carbon nanofibers, *J. Catal.* **238**, 412-424 (2006)

59. Li, Y. D.; Li, C. W.; Wang, H. R.; Li, L. Q.; Qian, Y. T. Preparation of nickel ultrafine powder and crystalline film by chemical control reduction, *Mater. Chem. & Phys.* **59**, 88-90 (1999)

60. Ni, X. *et al.* A novel chemical reduction route towards the synthesis of crystalline nickel nanoflowers from a mixed source, *Eur. J. Inorg. Chem.* **23**, 4788-4793 (2005)

61. Hou, Y.; Kondoh, H.; Ohta, T.; Gao, S. Size-controlled Synthesis of nickel nanoparticles, *Appl. Surf. Sci.* **241**, 218-222 (2005)

62. Balal, T. *et al.* Block copolymer mediated stabilization of sub-5 nm superparamagnetic nickel nanoparticles in an aqueous medium, *Nanotechnology* **20**, 415603-415613 (2009)

63. Athawale, A. A.; Bhagawat, S. V. Synthesis and characterization of novel copper/polyaniline nanocomposite and application as a catalyst in the Wacker oxidation reaction. *J. Appl. Polym. Sci.* **89**, 2412-2417(2003)

64. Houdayer, A.; Schneider, R.; Billaud, D.; Ghanbaja, J.; Lambert, J. New polyaniline/Ni(0) nanocomposites: synthesis, characterization and evaluation of their catalytic activity in Heck couplings, *Synth. Met.* **151**, 165-174 (2005)

65. Sih, B. C.; Wolf, M. O. Metalnanoparticle-conjugated polymer nanocomposites. *Chem. Commun.* 3375-3384 (2005)

66. Chen, H. M.; Hsin, C. F.; Liu, R. S.; Lee, J. F.; Jang, L. Y. Synthesis and characterizaiton of multi-pod-shaped gold/silver nanostructures, *J. Phys. Chem. C* **111**, 5909-5914 (2007)

67. Han, J.; Dai, J.; Li, L.; Fang, P.; Guo, R. Highly uniform self-assembled conducting polymer/gold fibrous nanocomposites: additive-free controllable synthesis and application as efficient recyclable catalysts, *Langmuir* **27**, 2181-2187 (2011)

68. Amaya, T.; Saio, D.; Hirao, T. Template synthesis of polyaniline/Pd nanoparticle and its catalytic application, *Tetrahedron Lett.* **48**, 2729-2732 (2007)

69. Palmero, S. Layer-by-layer electrosynthesis of Pt-polyaniline nanocomposites for the catalytic oxidation of methanol, *Electrochem. Commun.* **11**, 122-125 (2009)

70. Yoosaf, K.; Ipe, B. I.; Suresh, C. H.; Thomas, K. G. In situ synthesis of metal nanoparticles and selective naked-eye detection of lead ions from aqueous media, *J. Phys. Chem. C* **111**, 12839-12847 (2007)

71. McDonald, M.; Mila, I.; Scalbert, A. Precipitation of metal ions by plant polyphenols: optimal conditions and origin of precipitation, *J. Agric. Food Chem.* **44**, 599-606 (1996)

72. Sivaraman, S. K.; Elango, I.; Kumar, S.; Santhanam, V. A green protocol for room temperature synthesis of silver nanoparticles in seconds, *Cur. Sci.* **97**, 1055-1059 (2009)

73. Bulut, E.; Özacar, M. Rapid, facile synthesis of silver nanostructure using hydrolyzable tannin, *Ind. Eng. Chem. Res.* **48**, 5686-5690 (2009)

74. Zhang, H. X.; Siegert, U.; Liu, R.; Cai, W. B. Facile fabrication of ultrafine copper nanoparticles in organic solvent, *Nanoscale Res. Lett.* **4**, 705-708 (2009)

75. Aelenei, N.; Popa, M. I.; Novac, O.; Lisa, G.; Balaita, L. Tannic acid incorporation in chitosan-based microparticles and in vitro controlled release, *J. Mater. Sci: Mater. Med.* **20**, 1095-1102 (2009)

76. Park, B. K.; Jeong, S.; Kim, D.; Moon, J.; Lim, S.; Kim, J. S. Synthesis and size control of monodisperse copper nanoparticles by polyol method, *J. Colloid Interface Sci.* **311**, 417-424 (2007)

77. Poleunis, C.; Weng, L. T.; Sclavons, M.; Bertrand, P.; Franquinet, P.; Legras, R.; Carlier, V. Sizing removal and functionalization of carbon fiber surface studied by combined TOF SIMS and XPS, *J. Adhes. Sci. Technol.* **9**, 859-871 (1995)

78. Sundberg, P.; Larsson, R.; Folkesson, B. On the core electron binding energy of carbon and the effective charge of the carbon atom, *J. Electron. Spectrosc. Relat. Phenom.* **46**, 19-29 (1988)

79. Toshima, N.; Wang, Y. Preparation and catalysis of novel colloidal dispersions of copper/noble metal bimetallic clusters, *Langmuir* **10**, 4574-4580 (1994)

80. Kim, K. S.; Davis, R. E. Electron spectroscopy of the nickel-oxygen system, *J. Electron. Spectrosc. Relat. Phenom.* **1**, 251-258 (1972/73)

81. Wang, H.; Kou, X.; Zhang, L.; Li, J. Size-controlled synthesis, microstructure and magnetic properties of Ni nanoparticles, *Mater. Res. Bull.* **43**, 3529-3536 (2008)

82. Hall, B. D.; Zanchet, D.; Ugarte, D. Estimating nanoparticle size from diffraction measurements, *J. Appl. Cryst.* **33**, 1335-1341 (2000)

83. Patterson, A. L. The scherrer formula for X-ray particle size determination, *Phys. Rev.* **56**, 978-982 (1939)

84. Peng, X. G.; Manna, L.; Yang, W. D.; Wickham, J.; Scher, E.; Kadavanich, A.; Alivisatos, A. P. Shape control of CdSe nanocrystals, *Nature* **404**, 59-61 (2000)

85. Cordente, N.; Respaud, M.; Senocq, F.; Casanove, M. J.; Amiens, C.; Chaudret, B. Synthesis and magnetic properties of nickel nanorods, *Nano. Lett.* **1**, 565-568 (2001)

86. Jun, Y. W.; Lee, S. M.; Kang, N. J.; Cheon, J. Controlled synthesis of multi-armed CdS nanorod architectures using monosurfactant system, *J. Am. Chem. Soc.* **123**, 5150-5151 (2001)

87. Karatchevtseva, I.; Zhang, Z. M.; Hanna, J.; Luca, V. Electrosynthesis of macroporous polyaniline-V_2O_5 nanocomposites and their unusual magnetic properties, *Chem. Mater.* **18**, 4908-4916 (2006)

88. Angelopoulos, M.; Ray, A.; MacDiarmid, A. G.; Epstein, A. J. Polyaniline: processability from aqueous solutions and effect of water vapor on conductivity, *Synth. Met.* **21**, 21-30 (1987)

89. Feng, W.; Sun, E.; Fujii, A.; Wu, H.; Nihara, K.; Yoshina, K. Synthesis and characterization of photoconducting polyaniline- TiO_2 nanocomposite, *Bull. Chem. Soc. Jpn.* **72**, 2627-2633 (2000)

90. Sun, Y. P.; Rollins, H. W.; Guduru, R. Preparation of nickel, cobalt, and iron nanoparticles through the rapid expansion of supercritical fluid solutions (RESS) and chemical reduction, *Chem. Mater.* **11**, 7-9 (1999)

91. Yavuz, Ö.; Ram, M. K.; Aldissi, M.; Poddar, P.; Hariharan, S. Synthesis and the physical properties of MnZn ferrite and NiMnZn ferrite- polyaniline nanocomposite particles, *J. Mater. Chem.* **15**, 810-817 (2005)

92. Siegfried, M. J.; Choi, K. S. Electrochemical crystallization of cuprous oxide with systematic shape evolution, *Adv. Mater.* **16**, 1743-1746 (2004)

93. Jing, S.; Xing, S.; Yu, L.; Wu, Y.; Zhao, C. Synthesis and characterization of Ag/polyaniline core-shell nanocomposites based on silver nanoparticles colloid, *Mater. Lett.* **61**, 2794-2797 (2007)

94. Li, J.; Tang, S. B.; Lu, L.; Zeng, H. C. Preparation of nanocomposites of metals, metal oxides, and carbon nanotubes vis self-assembly, *J. Am. Chem. Soc.* **129**, 9401-9409 (2007)

95. Konwer, S.; Pokhrel, B.; Dolui, S. K. Synthesis and characterization of polyaniline/graphite composites and study of their electrical and electrochemical properties, *J. Appl. Polym. Sci.* **116**, 1138-1145 (2010)

96. Kim, B. J.; Oh, S. G.; Han, M. G.; Im, S. S. Synthesis and characterization of polyaniline nanoparticles in SDS micellar solutions, *Synth. Met.* **122**, 297-304 (2001)

97. Creighton, J. A.; Eadon, D. G. Ultraviolet-visible absorption spectra of the colloidal metallic elements, *J. Chem. Soc. Faraday Trans.* **87**, 3881-3891 (1991)

98. Sandhyarani, N.; Pradeep, T. An investigation of the structure and properties of layered copper thiolates, *J. Mater. Chem.* **11**, 1294-1299 (2001)

99. Foresti, E.; Fracasso, G.; Lanzi, M.; Lesci, I. G.; Paganin, L.; Zuccheri, T.; Roveri, N. New thiophene monolayer-protected copper nanoparticles: synthesis and chemical-physical characterization, *J. Nanomater.* **2008**, 1-6 (2008)

100. Samim, M.; Kaushik, N. K.; Maitra, A. Effect of size of copper nanoparticles on its catalytic behaviour in Ullman reaction, Bull. Mater. Sci. **30**, 535-540 (2007)

101. Brege, J. J.; Hamilton, C. E.; Crouse, C. A.; Barron, A. R. Ultrasmall copper nanoparticles from a hydrophobically immobilized surfactant template, *Nano. Lett.* **9**, 2239-2242 (2009)

102. Lu, X.; Gao, H.; Chen, J.; Chao, D.; Zhang, W.; Wei, Y. Poly(acrylic acid)-guided synthesis of helical polyaniline/CdS composite microwires, *Nanotechnology* **16**, 113-117 (2005)

103. Johnson, P. B.; Christy, R. W. Optical constants of transition metals: Ti, V, Cr, Mn, Fe, Co, Ni, and Pd, *Phys. Rev. B* **9**, 5056-5070 (1974)

104. Li, D.; Komarneni, S. Microwave-assisted polyol process for synthesis of Ni nanoparticles, *J. Am. Ceram. Soc.* **89**, 1510-1517 (2006)

105. Dey, A.; De, S.; De, A.; De, S. K. Characterization and dielectric properties of polyaniline-TiO_2 nanocomposites, *Nanotechnology* **15**, 1277-1283 (2004)

106. Leeuw, D. M.; Simenon, M. J.; Brown, A. R.; Einerhand, R. E. F. Stability of n-type doped conducting polymers and consequences for polymeric microelectronic devices, *Synth. Met.* **87**, 53-59 (1997)

107. Flitton, R.; Johal, J.; Maeda, S.; Armes, S. P. Synthesis of colloidal dispersions of polypyrrole-silica nanocomposites using "stringy" silica particles, *J. Colloid Interface Sci.* **173**, 135-142 (1995)

CHAPTER 3

Synthesis of Cadmium Sulphide (CdS) Nanoparticles and Their Interaction with Polyaniline (PANI)

3.1: Introduction

Semiconductor nanostructures have been investigated from the experimental and theoretical standpoint due to their excellent prospective in the fabrication of novel electronic devices. The most versatile system in this context is cadmium sulphide (CdS), a p-type semiconductor. This material possesses a wide band gap with Bohr radius of 2.4 nm and direct band gap of 2.40 eV[1]. Recent researches on CdS have revealed its relatively large nonlinear response[2], photocatalytic activity[3], etc. These findings are noteworthy due to possible applications for photoelectronic conversion in solar cells[4], light-emitting diodes (LEDs) for flat-panel displays[5], single electron transistors[6] and biosensing devices[7].

A simple approach to comprehend the practical solid-state device fabrication, the nanoparticles are typically integrated into a processable polymer matrix which should meet the mechanical and functional requirements determined by the application[8]. Nanoparticle impregnated polymer based devices have advantages over the fully organic counterparts in many respects. They have long-term stability over the simply organic-based devices making them especially attractive in a range of applications. Further, there is the possibility of obtaining p-n nanojunctions in polymer-nanocrystal based devices, which is otherwise impossible in polymer-polymer systems. Polymer nanocomposites also enjoy the opportunity to tailor the band gap of the inorganic component simply by changing the size of the nanoparticles that enables manipulation of the LED photodiode characteristics[9]. The inclusion of nanocrystals into conducting polymers improve charge separation and also broadens the photoconductivity response[10,11]. Broadening the photoconductivity response allows solar cells to capture a greater portion of the solar spectrum and possibly have higher white light power conversion efficiencies[8]. These spectacular properties have given new dimensions to material scientists to explore novel nanocomposite materials in recent times.

Among all the useful polymeric materials, polyaniline (PANI) has attracted much attention as it offers high conductivity, environmental stability and flexible processibility[12,13], coupled with versatility for design and fabrication of nanostructures materials including nanotubes[14], nanoscale conducting cylinders[15], and hybrid nanocomposites[16].

Voluminous literature is available on the synthesis of CdS/PANI nanocomposite. Seoudia *et al.* synthesised spherical shaped core-shell nanocomposites of CdS nanoparticles incorporated in polyaniline[17]. Khiew *et al.* synthesised polyaniline coated CdS nanocomposite employing microemulsion processing technique[18]. Poly (acrylic acid)- guided synthesis of helical CdS/PANI composite microwires were reported by Lu *et al* [19]. Dutta *et al.* obtained aligned CdS nanorods by dispersing CdS in the conducting polymer matrix[20]. But there is little discussion on the post nucleation and growth mechanism of both nanoparticles and their corresponding composites as the PANI based processes leads to complicated architecture. Further shape of CdS plays an important role in determining properties of host-guest matrix.

The present investigation describes a one step simple synthesis route for the preparation of stable colloidal dispersion of CdS nanoparticles in water using cadmium acetate and sodium thiosulphate as cadmium and sulphur sources, respectively, in presence of 3-mercaptopropionic acid as capping agent. The synthesized nanoparticles have been integrated with PANI using *in-situ* polymerization technique to study the effect of nanoparticles on the optical and electrical behaviour of the nanocomposites.

3.2. Materials and method

3.2.1. Materials

Cadmium acetate dihydrate (CdAc) ($Cd(CH_3COO)_2).2H_2O$, sodium thiosulphate (STS) ($Na_2S_2O_3.\ 5H_2O$), potassium peroxydisulphate (KPS) ($K_2S_2O_8$) and sodium hydroxide (NaOH) were purchased from Merck. Aniline (99%, monomer) and 3-mercaptopropionic acid (MPA) were obtained from Fluka. Ethanol and hydrochloric acid were of the highest purity commercially available and used without further purification. Double distilled water was used in all reactions.

3.2.2. Synthesis of CdS nanoparticles

CdS nanoparticles were prepared in aqueous dispersion by using MPA as capping agent. 0.001 mole of CdAc was dissolved in 30 ml double distilled water, taken in a 100 ml three-necked round bottom flask equipped with a condenser. The whole system was placed over a magnetic stirrer. Then 0.004 mole of MPA was dropped slowly into the above solution with constant stirring. The pH of the final solution was adjusted to 10.5 by the addition of 1 M NaOH solution. The temperature was raised slowly up to 60 °C and mixing was continued until the solution became optically clear. Next, 0.001 mole STS in 30 ml water was added dropwise to the above solution under vigorously stirred condition. The whole reaction was continuously purged with nitrogen. The colour of the initial solution turned slightly green after addition of STS dropwise. A yellowish aqueous dispersion of CdS nanoparticles was obtained within 1h. Following the similar procedure, CdS nanoparticles were synthesized by varying the CdAc: STS: MPA molar ratios as described below in **Table 3.1**.

Table 3.1. Summary of the reaction conditions for CdS synthesis.

Sample code	CdAc: STS: MPA molar ratio	Temperature (°C)	Duration (h)	Appearance
CdS-1	1: 1: 6	80	6	Yellow dispersion
CdS-2	1: 2: 2	80	6	Yellow dispersion
CdS-3	1: 3: 4	80	6	Yellow dispersion

3.2.3. Synthesis of polyaniline (PANI)

For the synthesis of PANI, 1 ml (0.01 mole) of aniline was dissolved in 10 ml of 1.5 M HCl solution in a 50 ml conical flask and cooled down to 0 °C. The oxidizing agent was prepared by dissolving 0.0166 g (0.0125 mole) of KPS in 5 ml 1.5 M HCl solution. KPS solution was added drop wise to the aniline solution while stirring and continued to add for 1 h keeping the reaction temperature at 0 °C. The reaction mixture was then left to warm up to room temperature. Afterwards the reaction mixture was filtered under gravity, washed with 1.5 M HCl and double distilled water until the washing liquid become colourless and finally dried at 60 °C for 24 h under vacuum to obtain a fine tint green powder.

3.2.4. Synthesis of CdS/PANI nanocomposites

CdS/PANI nanocomposites have been synthesized by *in-situ* polymerization technique. The polymerization was carried out by injecting 1 ml aniline into 10 ml of 1.5 M HCl with 0.1 g of synthesized CdS nanoparticles under constant stirring. After 2 h, 0.0166 g KPS (dissolved in 5 ml water) was then dropped into the solution with constant stirring. The polymerization was allowed to proceed for 5 h. The reaction mixture was then filtered under gravity, washed repeatedly with 1.5 M HCl followed by double distilled water, and finally dried at 60 °C for 24 h under vacuum. The final product was obtained in powdery form with green tint.

3.2.5. Characterization of CdS nanoparticles and CdS/PANI nanocomposites

3.2.5.1. Scanning electron microscope (SEM)

Top-down SEM images of the samples were conducted in a high resolution field emission scanning electron microscope (FEI INSPECT F, model no. FP 2031/11) operating at a voltage of 5 kV. Samples were gold coated (Bio-rad Polaron E5000 gold coater) prior to SEM analysis for 10 s at a voltage of 2.5 kV and a current of 18 mA.

3.2.5.2. Transmission electron microscope (TEM)

Transmission electron microscopy (TEM) images were taken on JEOL-JEM-2000FX transmission electron microscope. The samples were prepared by sonication in appropriate solvents for 10 min prior to transfer to copper grids. To obtain an accurate estimation of the average particle size, at least 100 particles were manually counted.

3.2.5.3. Atomic force microscope (AFM)

AFM provides images of structural details without any chemical treatment (etching or staining) of the specimens. The AFM used was a DME 2452 DualScope Scanner DS Atomic Force Microscope. Scans were carried out in AC mode under ambient conditions with a silicon microcantilever probe tips, using the parameters: force constant: 60,000 N/m; force: 0.15 nN; loop gain: 1,000 loop filter: 3 Hz.

3.2.5.4. Fourier transform infrared spectrometer (FTIR)

Spectra were recorded from pressed KBr pellets using a Perkin Elmer FT-IR spectrometer in the range of 4000-400 cm^{-1} at room temperature.

3.2.5.5. Powder X-ray diffraction (XRD)

XRD data were collected on a Rigaku Miniflex X-ray diffractometer with Cu K_α radiation (λ= 0.15418 nm) at 30 kV and 15 mA using a scan rate of 0.05° s^{-1} in 2θ ranges from 10° to 70°.

3.2.5.6. X-ray photoelectron spectrometer (XPS)

Spectra were acquired on a PHI Quantum 2000 spectrometer with monochromated AlK_α 1486.6 eV X-ray radiation. Samples were loaded into the vacuum chamber within 1 h after being prepared and were subjected to XPS analysis. The analysis area was 1200 μm x 400 μm on each sample. The take off angle in the instrument was set at 90°.

3.2.5.7. Thermogravimetric analysis (TGA)

Thermogravimetric (TGA-DTG) and differential thermal (DTA) analyses were performed in a Shimadzu TGA-50 thermal analysis apparatus. Prior to the run, sample (typically 50 mg) was stabilized for 30 min at 25 °C and then the temperature was linearly increased from 25 to 800 °C with a ramp of 10 °C min^{-1} using dry nitrogen as a carrier gas.

3.2.6. Evaluation of optical and electrical properties

3.2.6.1. UV-vis spectroscopy

UV-vis absorption spectra of the samples were recorded in the range 250-900 nm using Shimadzu UV-2550 UV-visible spectrophotometer.

3.2.6.2. Photoluminescence (PL) spectroscopy

PL spectra were recorded on a Hitachi F- 2500 Fluorescence spectrophotometer, by excitation of the samples at their absorption maximum.

3.2.6.3. I-V characteristics and DC electrical conductivity

The room temperature current-voltage (I-V) characteristics of PANI and CdS/PANI nanocomposites were measured with a Keithley 2400 programmable current source meter by the two probe method in the frequency range of 102-106 Hz.

The temperature dependent direct current (DC) conductivity was measured by the standard four probe method over a temperature range from 30 up to 110 °C on pellets of approx. 1.5 cm diameter and 2 mm thickness compressed at 700 MPa with a compression-moulding machine with manual hydraulic press. The conductivity of the samples was calculated using ***Equation 2.1*** as discussed in ***Chapter 2.***

3.3. Results and discussion

3.3.1. CdS nanoparticles

3.3.1.1. Synthesis of CdS nanoparticles

CdS nanoparticles have been synthesized using CdAc, STS and MPA in the molar ratios of 1: 1: 6, 1: 2: 2, and 1: 3: 4 for CdS-1, CdS-2, and CdS-3, respectively, at pH 10.5. The clear solution of CdAc turned cloudy upon addition of MPA and became optically clear when heated to 80 °C. Formation of the complex intermediate $[Cd\text{-}MPA]^{2+}$ could be the reason behind it. Based on these observations, a possible reaction mechanism can be outlined as

$$Cd(CH_3COO)_2.2H_2O \rightarrow Cu^{2+} + 2CH_3COO^- + 2H_2O$$

$$Cd^{2+} + MPA \rightarrow \textbf{Cloudy dispersion}\ (\textit{immessible}) \xrightarrow{\Delta} [Cd\text{-}MPA]^{2+}$$

Clear solution

The optically clear solution turned light green and immediately became yellow at the addition of STS dropwise. The possible reactions leading to CdS formation are given below:

$$Na_2S_2O_3 + H_2O \xrightarrow{\Delta} 2Na^+ + SO_4^{2-} + H_2S$$

$$H_2S \rightarrow 2H^+ + S^{2-}$$

$$2Cd^{2+} + 2S^{2-} \rightarrow CdS$$

Yellow dispersion

3.3.1.2. XRD analysis of CdS nanoparticles

The XRD patterns of CdS-1, CdS-2 and CdS-3 nanoparticles are compiled in **Figure 3.1**. The diffraction peaks of the synthesised nanoparticles are observed at 2θ values of ~26.5°, 43.5° and 51.5° can be indexed to scattering from (111), (220), and (311) planes respectively, of cubic CdS phase, irrespective of the variations brought in the synthesis procedure. The data are compared with the JCPDS file No. 10-454 and is in good agreement with that of cubic phase. The absence of peaks at 28.3° (101 planes) and 48.1° (103 planes) referring to the hexagonal CdS indicates the purity of the product[21]. The broadness of the peaks indicates that the dimensions of the CdS nanoparticles are very small. The average particles size calculated from the full width at half maximum of the most intense peak of the XRD patterns using ***Equation 2.1*** (as discussed in ***Chapter 2***) are found to be ~4.1 ± 1, 6.8 ± 1 and 9.7 ± 1 nm for CdS-1,

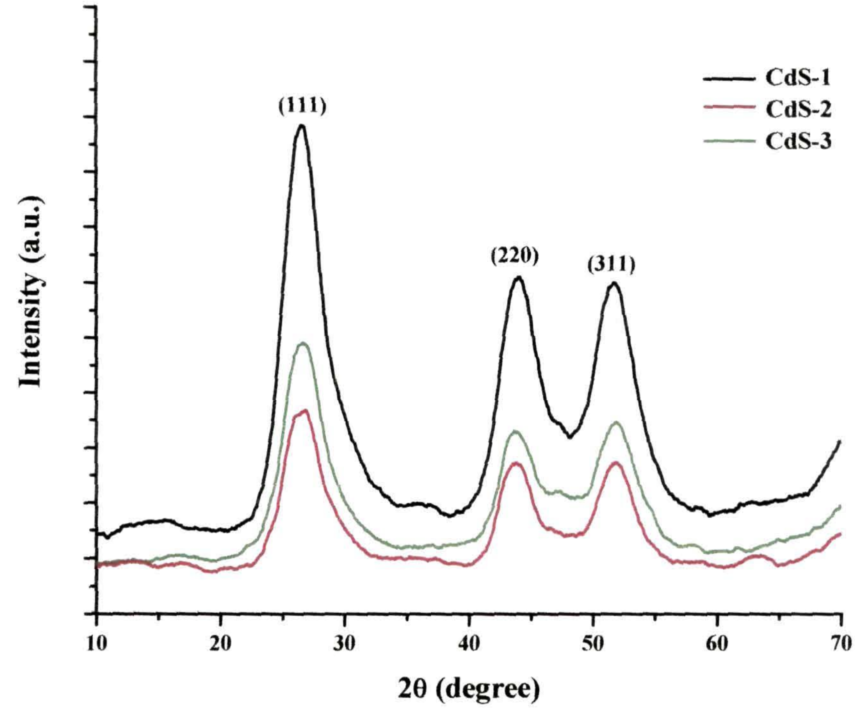

Figure 3.1. Powder X-ray diffraction patterns of the CdS nanoparticles.

CdS-2 and CdS-3, respectively. The CdS nanoparticles synthesized by CdAc: STS: MPA molar ratio of 1: 1: 6 give small particles size.

3.3.1.3. XPS analysis of CdS nanoparticles

Figure 3.2 shows the XPS survey spectrum of CdS nanoparticles prepared in CdAc: STS: MPA molar ratio 1: 1: 6. The survey spectrum reveals the presence of Cd, S, C, O and Na elements in the nanoparticles sample. The C 1s core level peak at 286.1 eV could be assigned to the MPA CH_2 groups remained with the nanoparticles[22]. The presence of a relatively stronger O 1s peak at 533.1 eV could be due to (i) the presence of O=C-O of acetate ligand[23], (ii) water, and (iii) the exposure to the atmosphere since nanocrystalline material exhibits a high surface-to-volume ratio. The Na 1s peak at 1072.9 eV in the spectrum evolved from STS used as sulphur source in the synthesis. The high-resolution XPS spectra of Cd 3d and S 2p shown in **Figure 3.3**

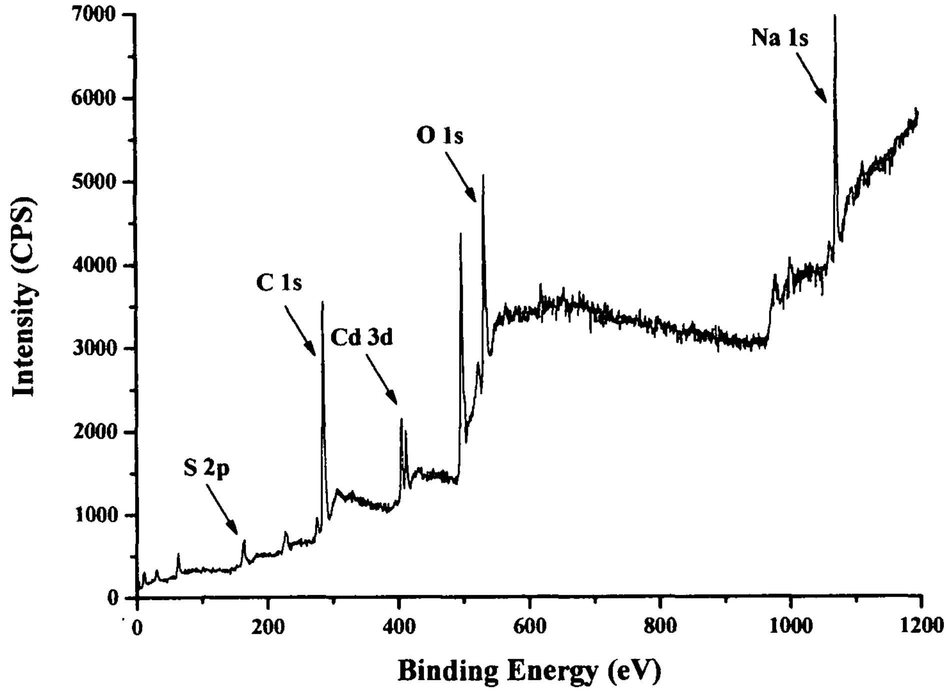

Figure 3.2. X-ray photoelectron survey spectrum of CdS-1 nanoparticles prepared with CdAc: STS: MPA molar ratio of 1: 1: 6.

in several reports[25-27]. This mechanism of crystal growth views the formation of bigger indicate doublet peaks at 404.2 eV and 412.3 eV are assigned to Cd 3d$_{5/2}$ and Cd 3d$_{3/2}$, and the one at 163.8 eV is attributed to the S 2p core-electrons, consistent with that observed in CdS^{24}. The quantification of peaks Cd 3d and S 2p cores gives the Cd: S atomic ratio as 1: 0.98, which is almost consistent with the stoichiometry of CdS. Similar kind of results are observed with other CdS samples and therefore, omitted for the sake of brevity.

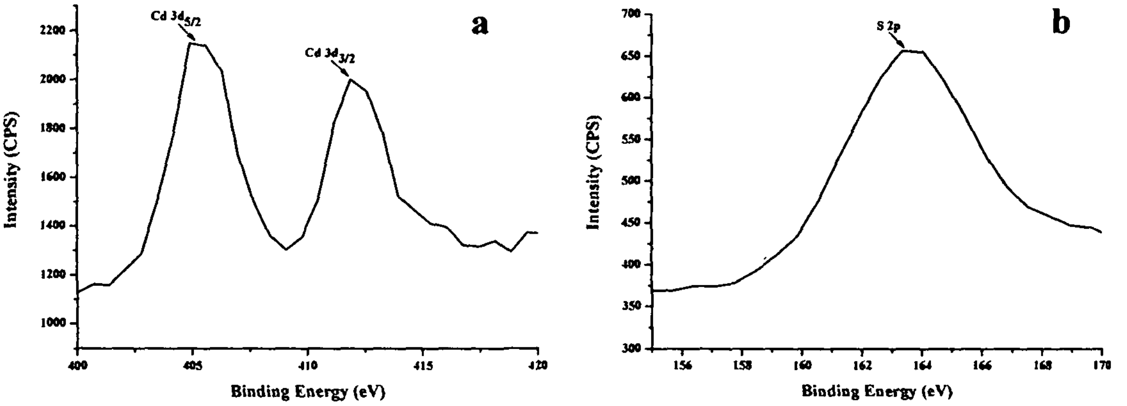

Figure 3.3. High resolution (a) Cd 3d and (b) S 2p XPS spectra of CdS-1 nanoparticles prepared with CdAc: STS: MPA molar ratio of 1: 1: 6.

3.3.1.4. SEM and TEM analysis of CdS nanoparticles

Figure 3.4 presents the SEM and TEM images of CdS-1 sample, and shows the distribution of spherical shaped nanoparticles in large areas. The magnified SEM image (**Figure 3.4b**) reveals well ordered arrangement of the nanoparticles. TEM image further supports the formation of spherical CdS nanoparticles with a narrow size distribution (**Figure 3.4c**). The particle size (5 ± 1 nm) obtained from the TEM image is consistent with the XRD data.

SEM and TEM images of CdS-2 nanoparticles are displayed in **Figure 3.5**. The micrographs give an overview of the sample in which evenly distributed cubic structures of CdS of two distinct categories of sizes (with the lower size dominating) are observed. The growth of bigger cubic nanocrystal may be due to the oriented attachment suggested in several reports$^{25-27}$. This mechanism of crystal growth views the formation of bigger crystals as a result of pileup and coalescence of smaller particles with sizes of a few nanometers rather than the adhesion of individual monomers such as ions. The average size of the bigger cubic nanocrystal is 30 ± 1 nm that might have been formed from the pileup of smaller nanocrystal of about 5 ± 1 nm in size. Formation of cubic CdS is also supported by XRD analysis.

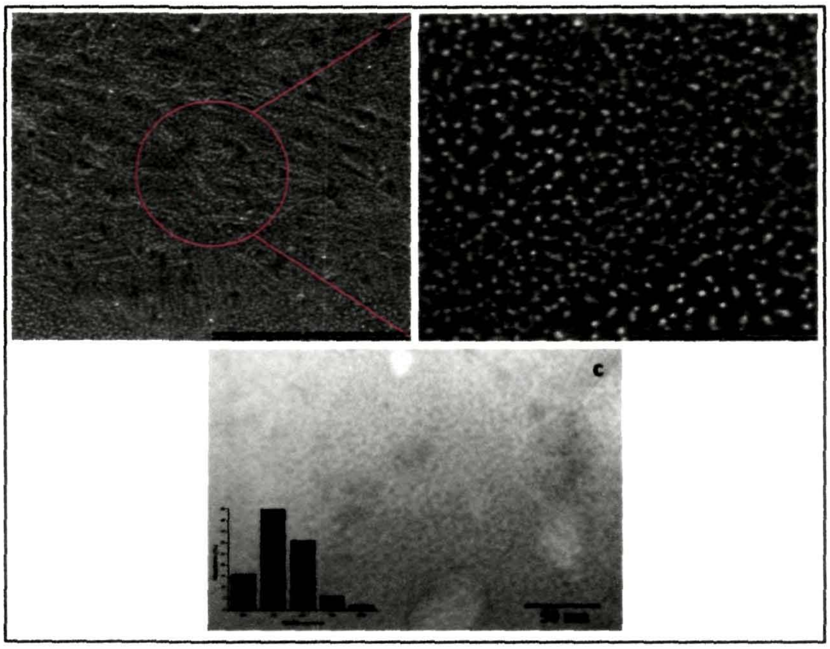

Figure 3.4. Top-down FE-SEM (a, b) and TEM (c) images of CdS-1 nanoparticles (inset of TEM is the statistical size distribution).

Formation of CdS nanocubes accumulated into bunch of flowers-like clusters are observed in the SEM micrographs of CdS-3 sample as shown in **Figure 3.6**. The enlarged SEM image further reveals that the nanocubes are supported on a sheet-like material. Niu and Gao reported that thioglycolic acid (TGA) reacts with Cd^{2+} ions to form wire-like structures[28]. This interaction between TGA and Cd^{2+} occurs through the carboxylic group of TGA. The capping agent MPA used in this study has the potential to form similar [Cd^{2+}-MPA] complex nanostructures. The stem-like features observed in **Figure 3.6** could be this amorphous coordinated complex that acts as glue to assemble the nanocubes. Further, the growth and accumulation of nanocrystal can be described based on the combined mechanism of 'Ostwald Ripening' and oriented attachment. The

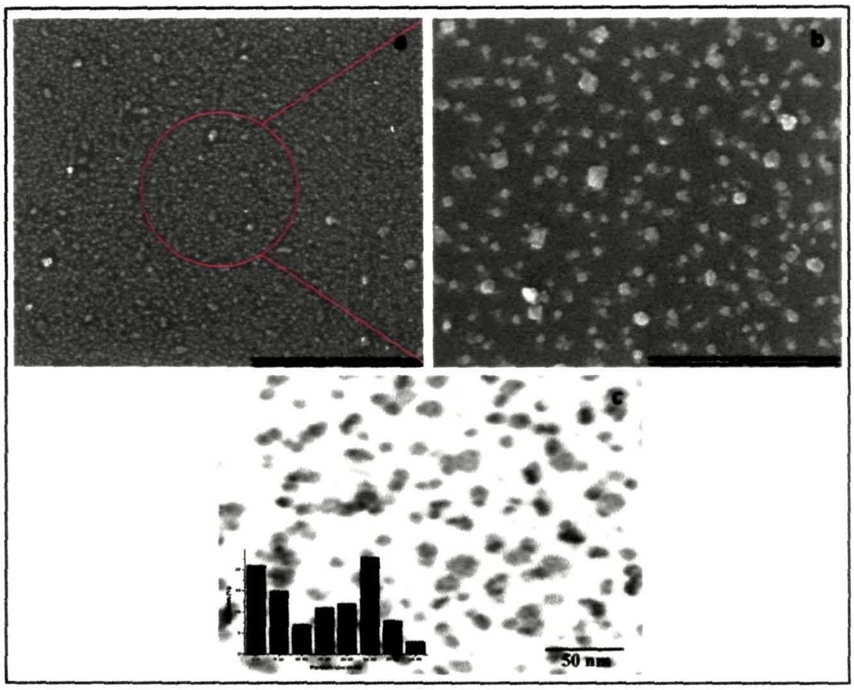

Figure 3.5. Top-down FE-SEM (a, b) and TEM (c) images of CdS-2 nanoparticles (inset of TEM is the statistical size distribution).

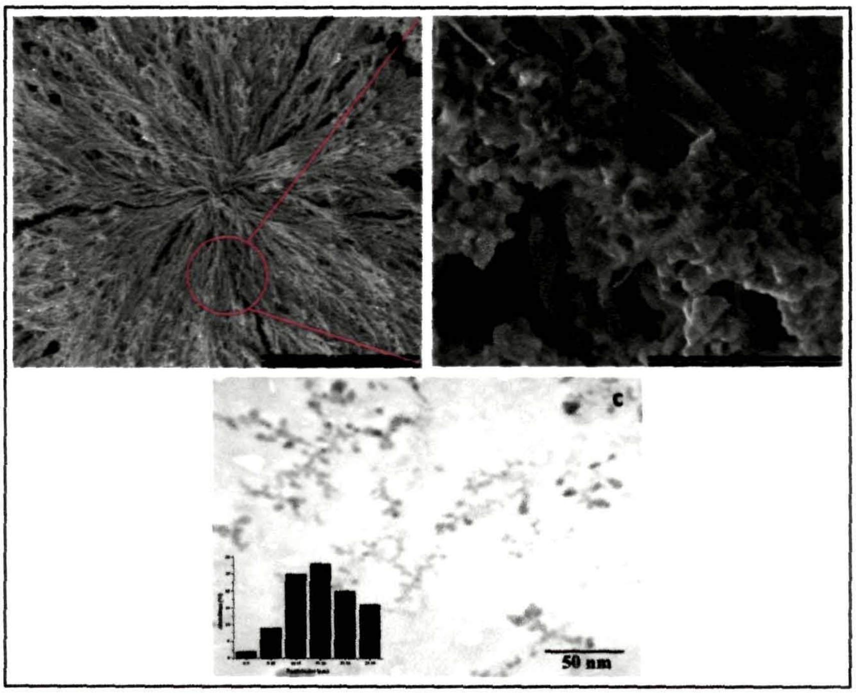

Figure 3.6. Top-down FE-SEM (a, b) and TEM (c) images of CdS-3 nanoparticles (inset of TEM is the statistical size distribution).

'Ostwald Ripening mechanism explains the formation of particles larger than the average size resulting from the shrinking and disappearance of smaller nanocrystal while larger ones are still growing. It is well-known that nanoparticles have the tendency to get accumulate to clusters in some ordered fashions under certain experimental conditions[29]. Thus, it appears that nanomaterials growth is sensitive to the experimental conditions and through the adjustment of these conditions, nanostructures with different morphologies and sizes can be controllably synthesised.

3.3.1.5. AFM analysis of CdS nanoparticles

The AFM tapping mode *2-D*, and *3-D* topography and phase images, and height profile of CdS-1 nanoparticles are shown in **Figure 3.7**. Homogeneity was checked by taking AFM scans on different areas of the same sample and same kind of results have been found in all cases. The *2-D* topography and phase images show near spherical CdS nanoparticles. It is even clearer from the *3-D* images. The height profile of the topography image reveals homogeneous size distribution and points out a maximum height difference of *ca.* 14 nm.

Figure 3.8 reports the topography, phase and height profile images of CdS-2 sample. Cubic nanostructures of CdS are revealed from the *2-D* and *3-D* topography and phase images. Consistent with SEM results, nanocubes of two distinct size categories can be seen in the AFM images. The height profile of the topography image further supports this observation and indicates a maximum height difference of *ca.* 95 nm.

The *2-D* topography and phase images of CdS-3 sample (**Figure 3.9**) clearly reveal the presence of spherical shape particles accumulated on top of sheet-like material- a result consistent with the SEM and TEM analysis. A better view of the surface can be obtained from the corresponding *3-D* images. The height profile of the topography image is inhomogeneous and indicates a maximum height difference of *ca.* 34 nm. The sheet-like material makes the surface rough resulting in inhomogeneous height profile. From the height profile images, it is very difficult to estimate the average particle sizes of the CdS samples because of wider size distribution.

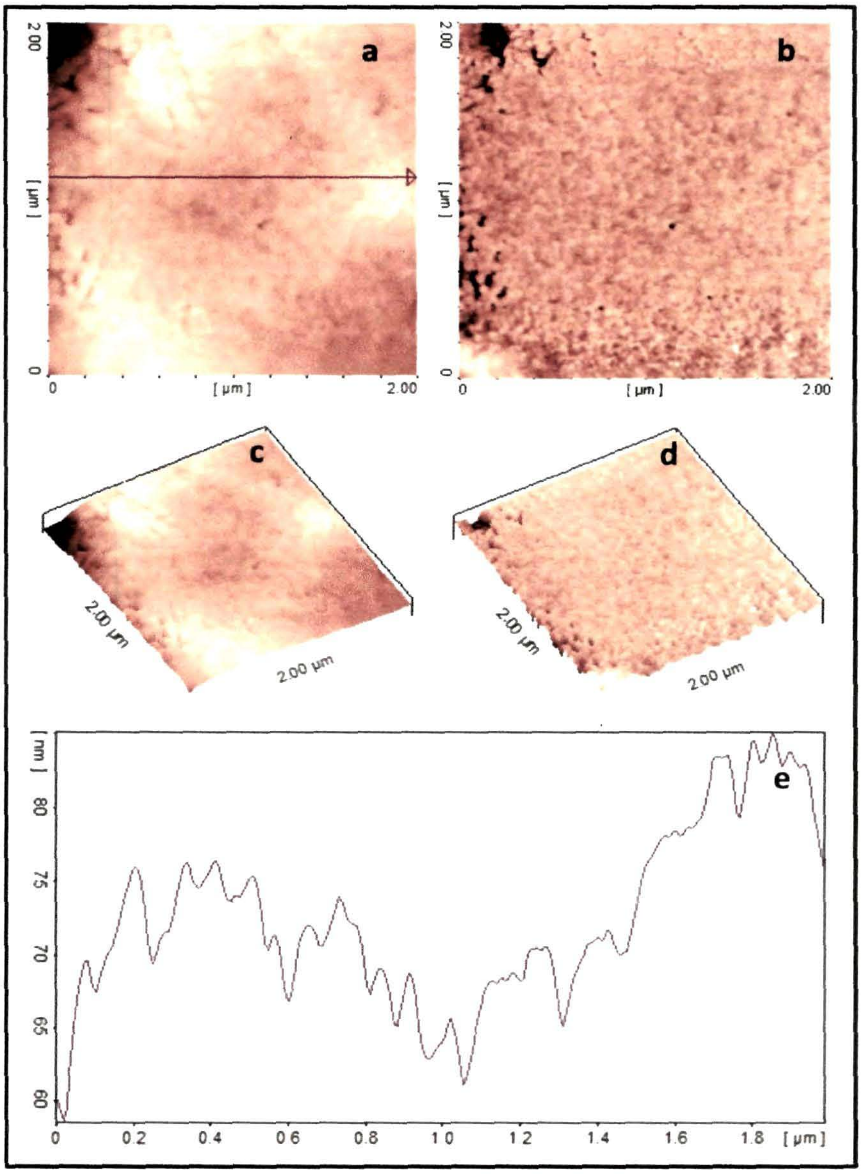

Figure 3.7. AFM tapping mode *2-D* topography (**a**) and phase (**b**) images of CdS-1 nanoparticles prepared with CdAc: STS: MPA molar ratio of 1: 1: 6. (**c**) and (**d**) are the corresponding *3-D* images of (**a**) and (**b**); and (**e**) is the typical height cross section image of (**a**).

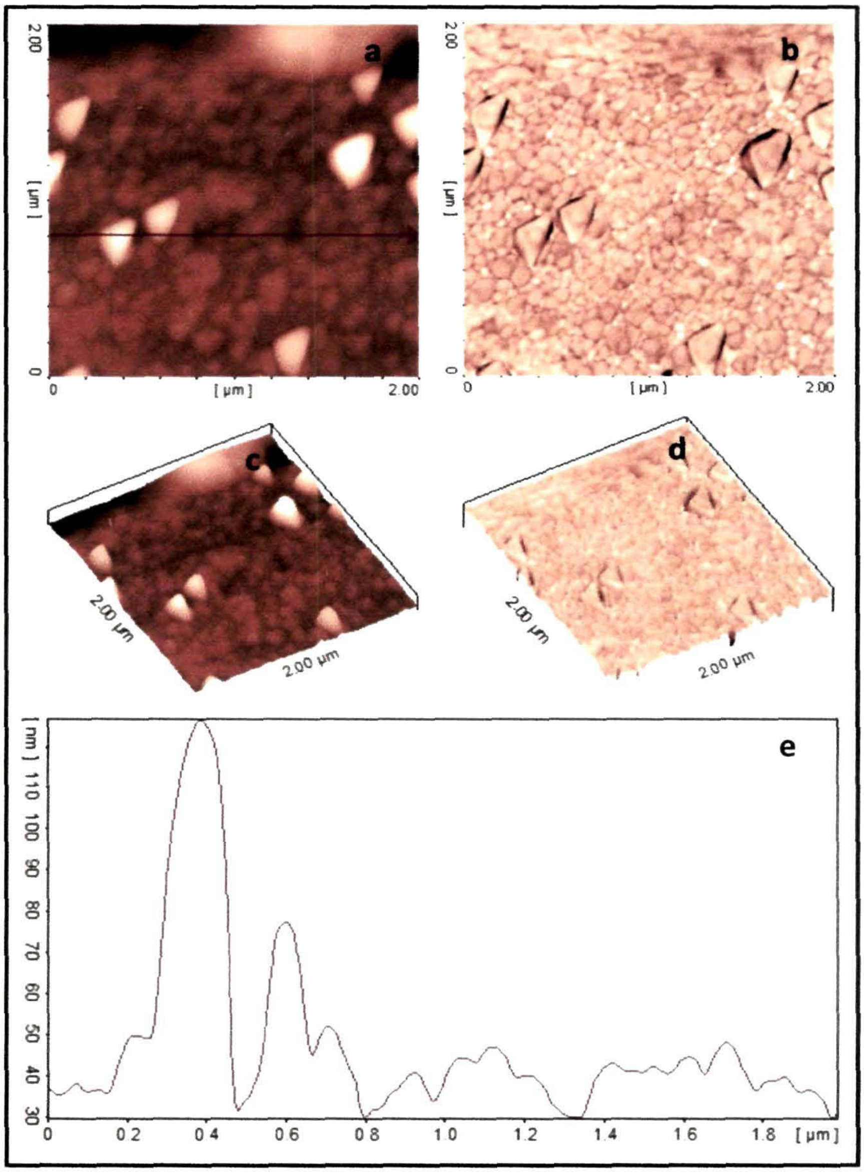

Figure 3.8. AFM tapping mode *2-D* topography (**a**) and phase (**b**) images of CdS -2 nanoparticles prepared with CdAc: STS: MPA molar ratio of 1: 2: 2. (**c**) and (**d**) are the corresponding *3-D* images of (**a**) and (**b**); and (**e**) is the typical height cross section image of (**a**).

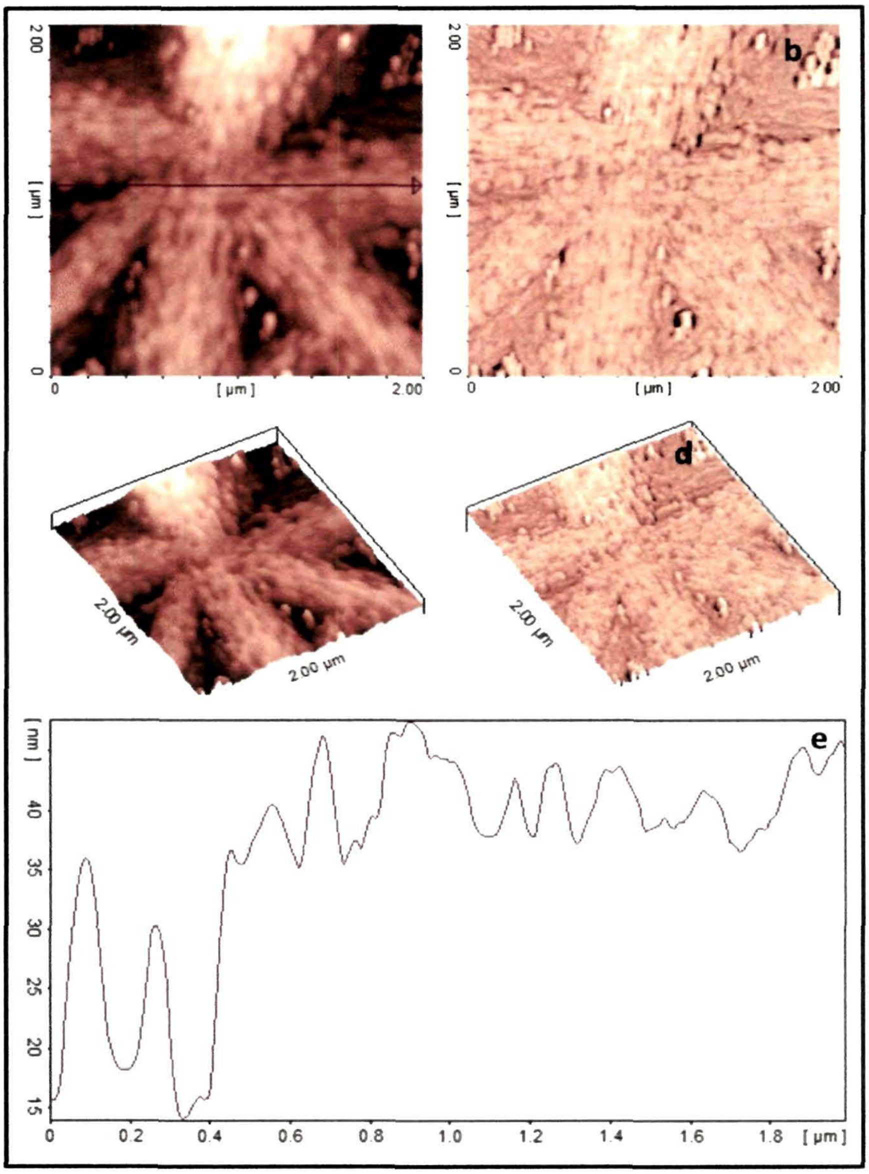

Figure 3.9. AFM tapping mode *2-D* topography (**a**) and phase (**b**) images of CdS-3 nanoparticles prepared with CdAc: STS: MPA molar ratio of 1: 3: 4. (**c**) and (**d**) are the corresponding *3-D* images of (**a**) and (**b**); and (**e**) is the typical height cross section image of (**a**).

3.3.2. CdS/PANI nanocomposites

3.3.2.1. Synthesis of CdS/PANI nanocomposites

CdS nanoparticles synthesised by three different molar ratios of CdAc: STS: MPA show variation of particle size and morphology. All three dispersions of nanoparticles demonstrated good stability and narrow size distribution. They were subsequently used in the synthesis of CdS/PANI nanocomposites by *in-situ* polymerization technique. The objective is to understand the effect of CdS nanoparticles size and morphology on the morphology, and optical and electrical behaviour of the resultant nanocomposites. ***Scheme 3.1*** presented below gives a schematic layout of the synthesis procedure.

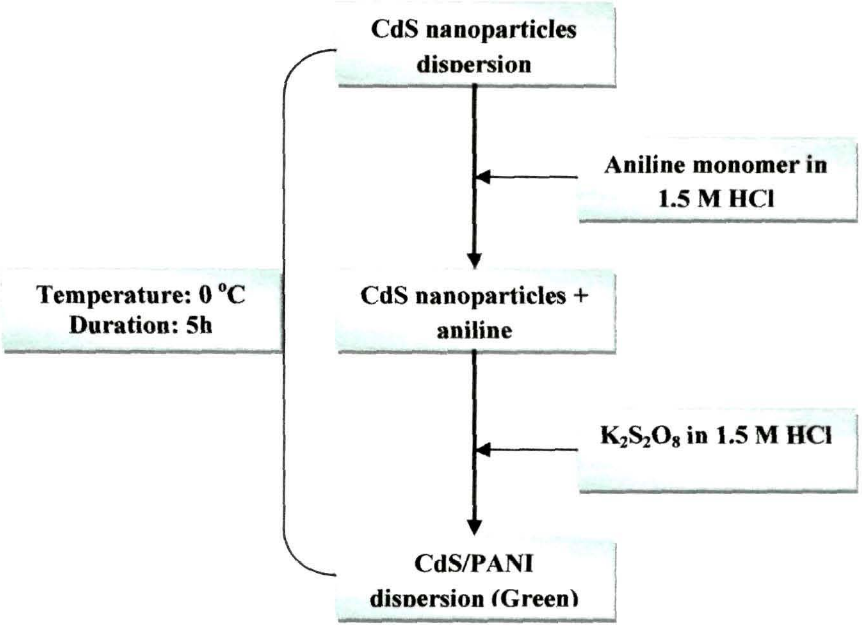

Scheme 3.1. Schematic illustration of the synthesis of CdS/PANI nanocomposites.

3.3.2.2. XRD analysis of CdS/PANI nanocomposites

Figure 3.10 displays the powder XRD profiles of pure PANI and CdS/PANI nanocomposites. The diffraction peaks of PANI are observed at 2θ values of 15.2°, 20.3°, 25.1°, 27° and 30°, and can be assigned to (011), (020), (200), (121) and (022), respectively, crystalline plane diffraction peaks of PANI in its emeraliadne form[30,31].

These peaks might have originated from the scattering of PANI chains at interplanar spacing[32] and suggests a significant crystalline fraction.

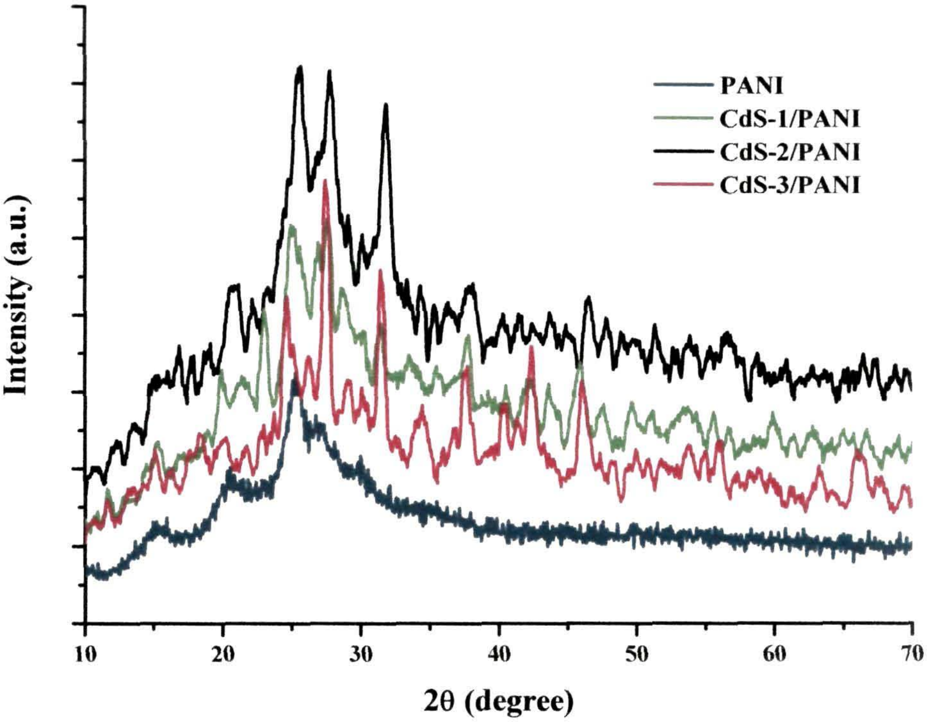

Figure 3.10. Powder X-ray diffraction patterns of pure PANI and CdS/PANI nancomposites.

For CdS/PANI nanocomposites, the diffraction peaks are observed at 2θ ~ 15.2°, 20.3°, 25.2°, 27°, 30°, 36.9° and 44.3°. It is clearly seen that the characteristic peaks of both PANI and CdS (***Section 3.3.1.2***) appear in the XRD patterns of CdS/PANI nanocomposites. The first three and the fifth peaks are originated from PANI while the other peaks correspond to the peaks of CdS nanoparticles as discussed in ***Section 3.3.1.2***. However, with respect to the diffraction patterns of the CdS nanoparticles, change in intensity and slight shifting in positions are observed in the diffraction patterns of nanocomposites. Further, a new peak appeared at 36.9° and the peak at 51.5° disappeared in the XRD patterns of the nanocomposites. These changes can be related to some structural change in the polymer caused by the close interaction with the disperse nanoparticles phase[33]. During the growth of crystals (nanocomposite), the growth of each plane of the components can be different due to the different adsorptions between each plane and organic or inorganic additives[34]. Further, compared to PANI diffraction pattern, the peaks corresponding to PANI in the nanocomposites, are sharp, indicating higher crystallinty in composites. Thus, the XRD patterns of nanocomposites evidence reorganization in the structure of the polymer and the co-existence of the CdS reflections suggesting its effective and stable incorporation in the nanocomposite structure.

3.3.2.3. FTIR analysis of CdS/PANI nanocomposites

Interaction between CdS nanoparticles and PANI matrix could be possible, and to investigate this, FTIR spectra of pure PANI and CdS/PANI were recorded. FTIR spectra of CdS/PANI nanocomposites are presented in **Figure 3.11**. A detail about the FTIR spectrum of pure PANI is discussed in ***Section 2.3.2.3, Chapter 2***, and found to be in emeraldine form[35]. The different vibrational bands found in PANI are compiled in **Table 3.2**. These characteristic bands of PANI can also be identified in the IR spectra of the nanocomposites confirming the presence of PANI in the composites. The infrared

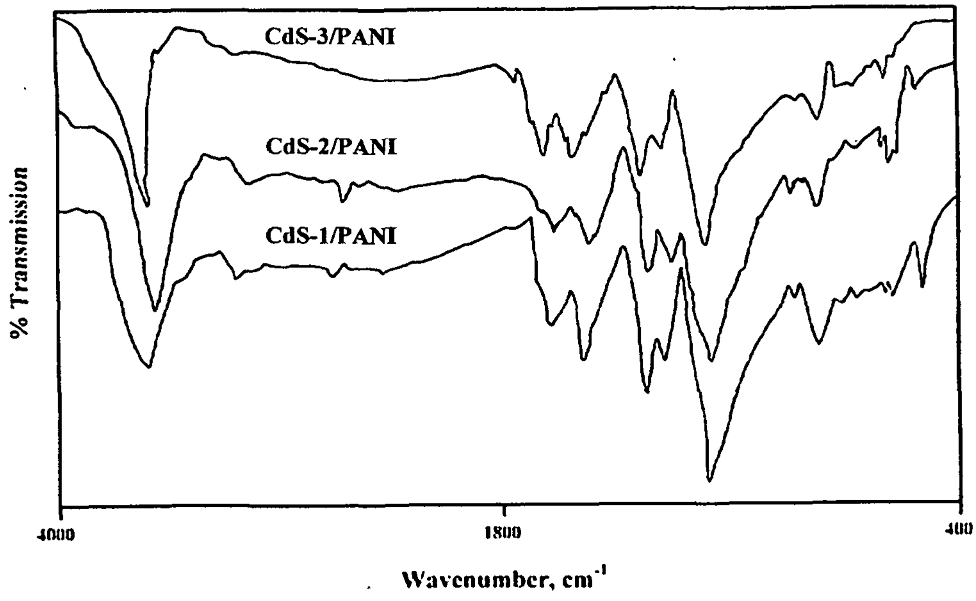

Figure 3.11. FTIR spectra of pure PANI, and CdS/PANI nanocomposites.

bands of CdS/PANI nanocomposites are also compiled in the Table for ease of comparison. However, shifting in peak positions associated with C=C and C=N stretching of the quinoid ring has been observed. This can be attributed to the interaction between CdS and PANI by virtue of the presence of CdS nanoparticles in close proximity of the imine nitrogen of PANI.

Table 3.2. Assignment of IR bands for PANI and CdS/PANI nanocomposites

IR band	**Assignment**	**Peak position/Wavenumber cm^{-1}**			
		PANI	**CdS-1/PANI**	**CdS-2/PANI**	**CdS-3/PANI**
ν_{-N-H} stretching	Amine -N-H	3282	3206	3209	3207
ν_{-C-N} stretching	2° amine -C-N bond	1296	1299	1299	1300
$\nu_{-C=N}$ stretching	-C=N bond in bipolaron	1243	1240	1238	1240
$\nu_{-C=C}$-stretching	Quinoid ring	1567	1564	1563	1556
$\nu_{-C=C}$stretching	Benzoid ring	1466	1470	1473	1474
ν_{-C-H} in- plane Bending	Benzoid ring	1106	1119	1112	1110
ν_{-C-H} out- of- plane Bending	Benzoid ring	876	882	885	876
ν_{-C-H} stretching	C-H bond in phenyl ring	2920	2925	2924	2927

3.3.2.4. XPS analysis of CdS/PANI nanocomposites

The nanocomposites are further characterised by XPS and the survey spectrum of CdS-1/PANI is reported in **Figure 3.12**. The survey spectra of CdS-2/PANI and CdS-3/PANI are very similar and therefore, omitted for the sake of brevity. The spectrum of pure PANI was also recorded as a reference material and a detailed discussion can be found in ***Section 2.3.2.4, Chapter 2***. All the essential elements (Cd, S, O and C) of the nanocomposite can be identified in the survey spectrum. Peaks for C and O are originated from PANI and that implies PANI formation in the nanocomposites. The intense C 1s peak at 284.5 eV. is assigned to PANI backbones[36]. A sharp peak observed at 531.6 eV for O 1s. The presence of oxygen is attributed to the oxidant and to extra contaminating oxygen. The N 1s peak could not be detected which is usually found at 398.6 eV. This could be due to the interaction of CdS nanoparticles with the -NH- group of PANI. From the XPS spectrum, Cd 3d and S 2p peaks are located at 408.5 eV and 163.6 eV, respectively. The peak positions of the essential elements identified the XPS spectra of pure PANI and CdS-1/PANI nanocomposites are compiled in **Table 3.3**. The composites and the reference material exhibit similar C 1s,

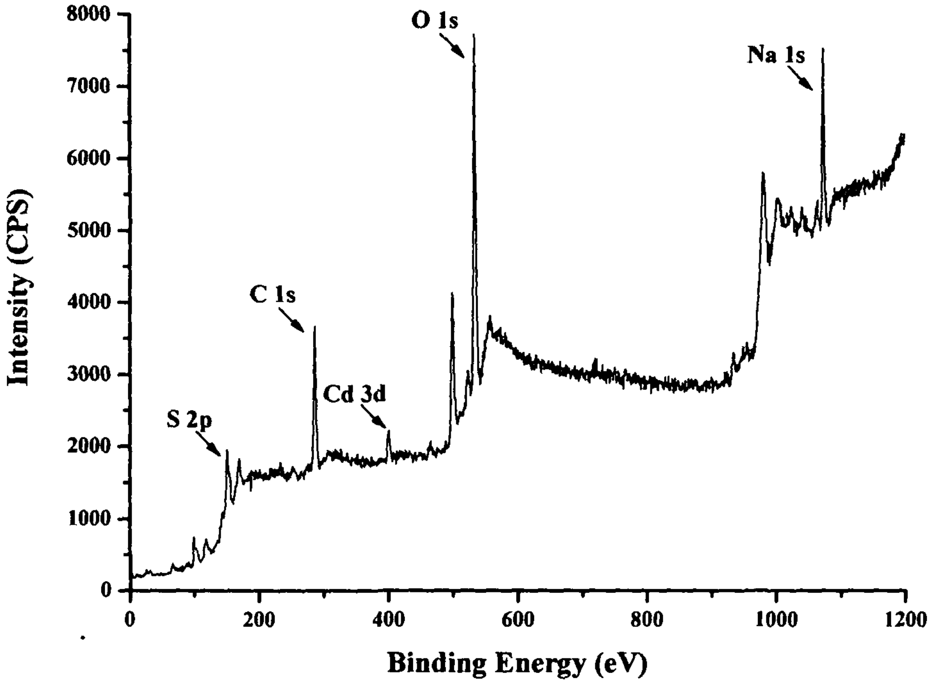

Figure 3.12. X-ray photoelectron survey spectrum of CdS-1/PANI nanocomposite.

Table 3.3. XPS peak positions of essential elements in pure PANI and CdS-1/PANI nanocomposites

Compound	Peak positions, eV				
	C 1s	O 1s	N 1s	Cd 3d	S 2p
PANI	285.5	532.6	400.0	--	--
CdS-1/PANI	284.9	532.9	--	408.5	163.6

N 1s and O 1s peaks, however, their intensity and positions are slightly changed. These changes can be accounted for the change in the chemical environment of PANI in composites.

3.3.2.5. TGA of CdS/PANI nanocomposites

The thermal behaviour of the polymer before and after introducing CdS nanoparticles was investigated by thermo gravimetric (TG) analysis. The TGA profiles of PANI and CdS/PANI are shown in **Figure 3.13**. The TGA patterns were recorded up to 800 °C at a heating rate of 10 °C/min under nitrogen flow. The thermal events accompanying weight losses lead to similar kind of degradation profiles for both pure PANI and CdS/PANI **(Figure 3.13)**. Though all the compounds experience gradual weight loss throughout the thermal process, yet a three step weight loss steps can be distinctly identified in the TGA profiles. The first weight loss up to 120 °C is mainly contributed by the elimination of moisture. The second weight loss in the temperature

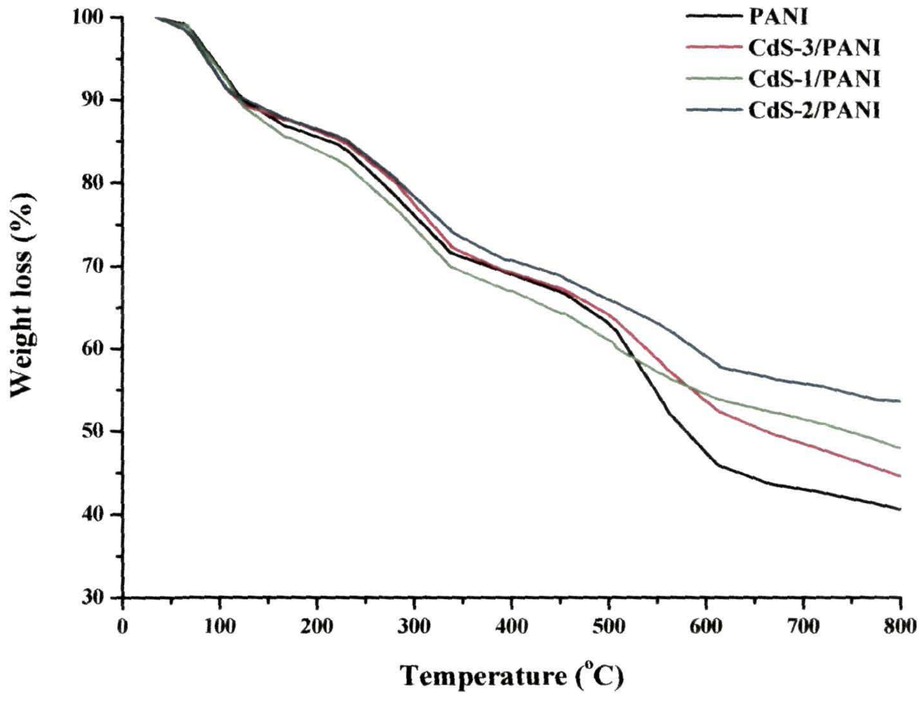

Figure 3.13. TGA thermographs of pure PANI and CdS/PANI nanocomposites.

range of 220-340 °C is accompanied by the removal of HCl bound to the PANI chain and low molecular weight oligomers[37]. The third step after 500 °C experiences the major weight loss and indicates the structural decomposition of the polymer. The essential weight loss characteristics are summarized in **Table 3.4.**

Table 3.4. Essential weight loss characteristics of PANI and CdS/PANI nanocomposites

Compound	**Characteristics**		
	Weight loss (%) at		
	115 °C	**340 °C**	**600 °C**
PANI	8.5	28.7	52.5
CdS-1/PANI	11.2	31.8	45.4
CdS-2/PANI	9.5	26.9	41.7
CdS-3/PANI	10.3	28.6	46.7

Even though both the two compounds experience heavy weight loss after 500 °C, the loss is relatively lower in CdS/PANI which indicates that the thermal property of the polymer is improved due to the presence of CdS nano fillers. Thus, it strongly attributes the interaction between CdS and PANI through stronger binding forces between nanoparticles and the lone pair electrons of N atom in the polymer backbone[38].

3.3.2.6. SEM and TEM analysis of CdS/PANI nanocomposites

The morphology of CdS/PANI nanocomposites and pure PANI are studied by SEM, TEM and AFM. Fibrous morphology was observed for pure PANI as discussed in ***Section 2.3.2.6, Chapter 2.*** Introduction of CdS nanoparticles into PANI matrix, however, resulted in morphologies different from PANI. **Figure 3.14** shows the SEM and TEM micrographs of CdS-1/PANI nanocomposite. SEM image reveals the

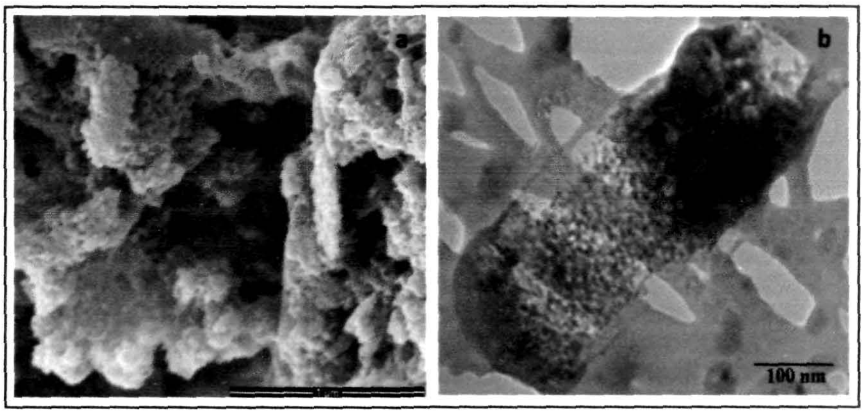

Figure 3.14. Top-down FE-SEM (**a**) and TEM (**b**) images of CdS-1/PANI nanocomposite.

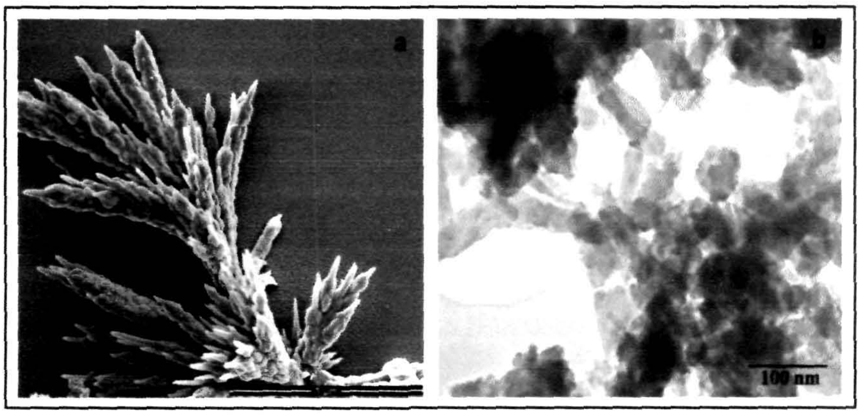

Figure 3.15. Top-down FE-SEM (**a**) and TEM (**b**) images of CdS-2/PANI nanocomposite.

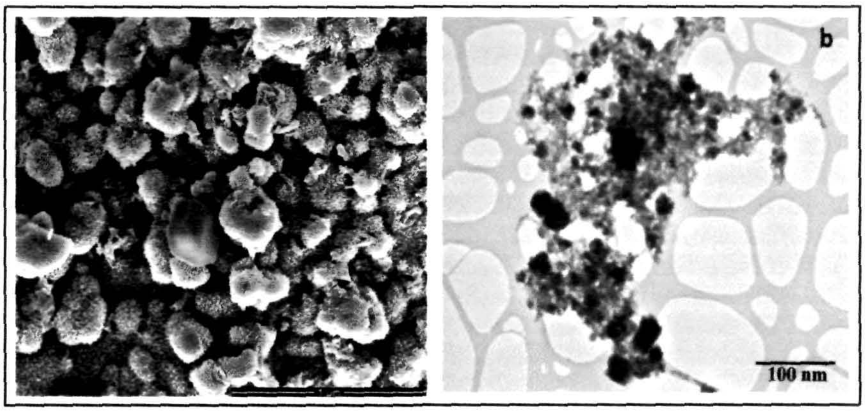

Figure 3.16. Top-down FE-SEM (**a**) and TEM (**b**) images of CdS-3/PANI nanocomposite.

formation of bee-hive like morphology of the composite material. The TEM image of the nanocomposites revels that the CdS nanoparticles are well combined and distributed within the polymer matrix. The morphology of CdS-2/PANI is interesting. The SEM image of **Figure 3.15** shows the growth of spike-paddy like features. The TEM image reveals the existence of CdS nanoparticles into the polymer matrix- a result consistent with XRD analysis (***Section 3.3.2.2***).

Unlike fibrous morphology of PANI, the SEM image of CdS-3/PANI nanocomposite shows the formation of raspberry-like features (**Figure 3.16**). TEM further reveals the incorporation of CdS nanoparticles into the polymer matrix. Existence of CdS nanopartilces in the PANI matrix is also confirmed by XRD analysis as discuss in the ***Section 3.3.2.2***.

3.3.2.7. AFM analysis of CdS/PANI nanocomposites

The AFM tapping mode topography and phase images of CdS-1/PANI are shown in **Figure 3.17**. Similar to SEM and TEM results, growth of micrometer size lumps can be seen in the *2-D* and *3-D* topography and phase images. The height profile of the topography image points out a maximum height difference of *ca.* 150 nm and average size of the lump > 1 μm.

Figure 3.18 reports the AFM scans of CdS-2/PANI nanocomposite along with the height profile image. The *2-D* topography and phase images demonstrate the formation of nanocomposites in the form of tree-branch- a result consistent with the SEM and TEM study. The height profile of the topography image indicates a maximum height difference of *ca.* 13 nm. Growth of raspberry-like features can also be identified in the *2-D* and *3-D* topography and phase images of CdS-3/PANI sample presented in **Figure 3.19**. The height profile of the topography image reveals almost irregular size distribution of the composite particles with a maximum height difference of *ca.* 110 nm and average particle size of ~400 nm.

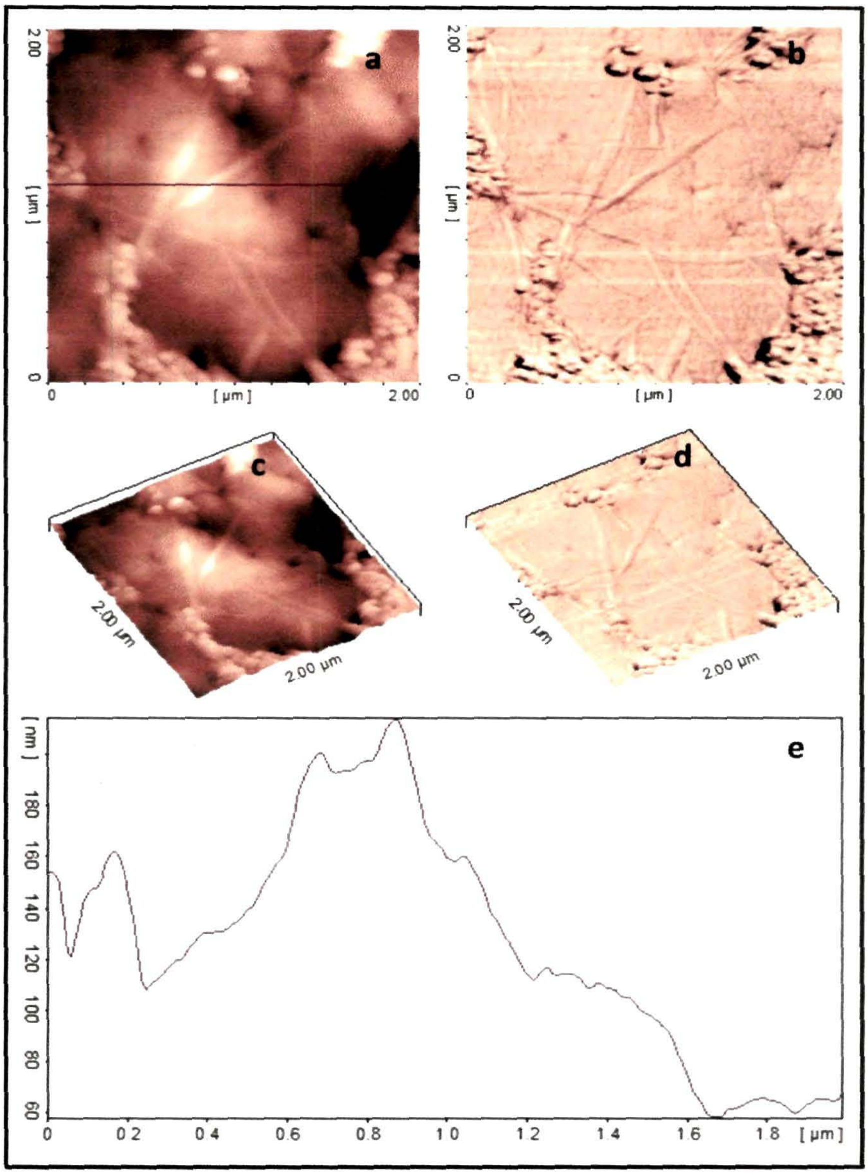

Figure 3.17. AFM tapping mode *2-D* topography (**a**) and phase (**b**) images of CdS-1/PANI nanocomposite. (**c**) and (**d**) are the corresponding *3-D* images of (**a**) and (**b**); and (**e**) is the typical height cross section image of (**a**).

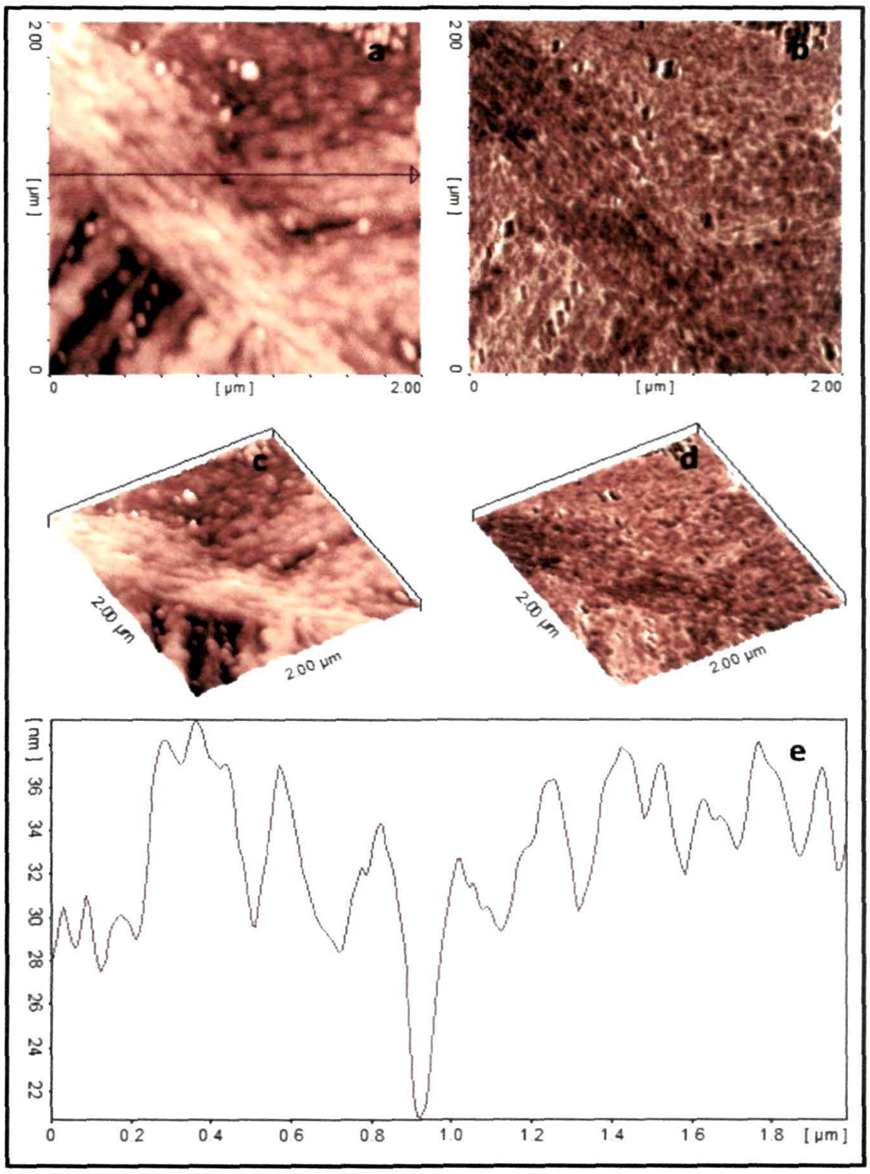

Figure 3.18. AFM tapping mode *2-D* topography (**a**) and phase (**b**) images of CdS-2/PANI nanocomposite. (**c**) and (**d**) are the corresponding *3-D* images of (**a**) and (**b**); and (**e**) is the typical height cross section image of (**a**).

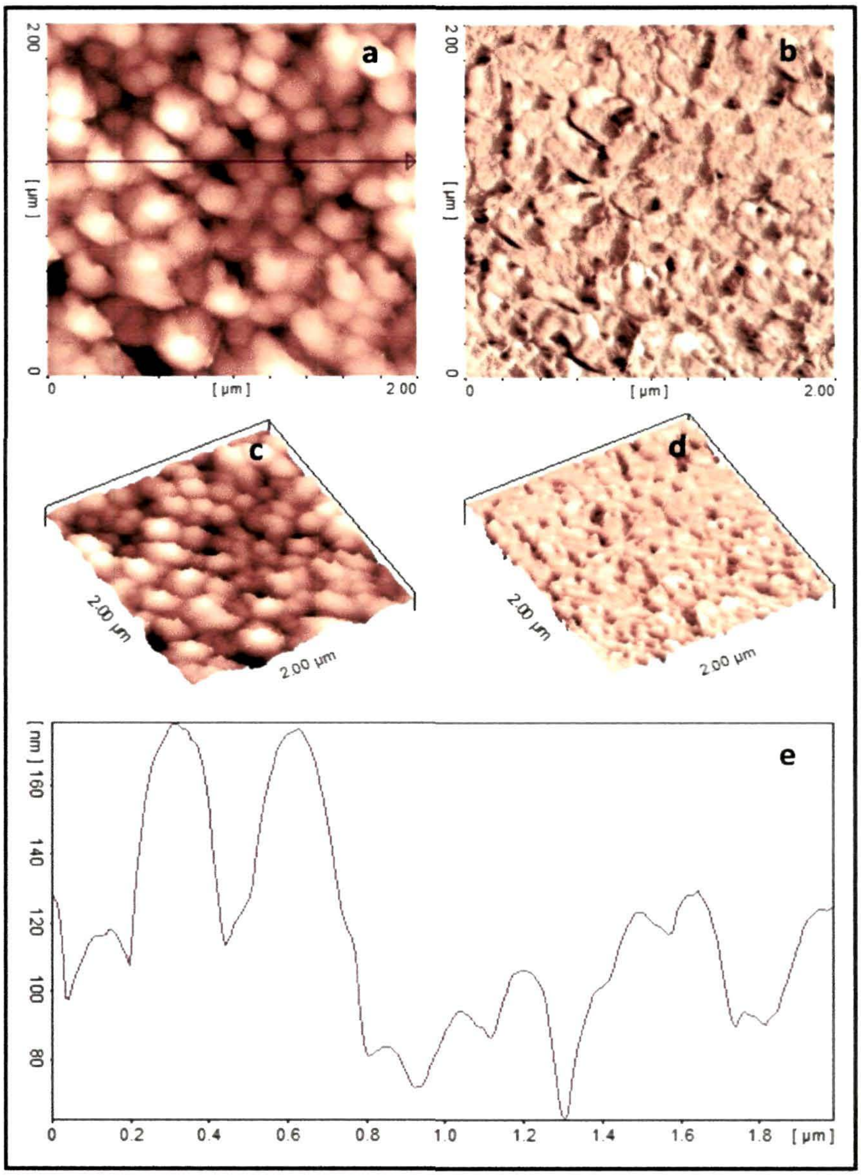

Figure 3.19. AFM tapping mode *2-D* topography (**a**) and phase (**b**) images of CdS-3/PANI nanocomposite. (**c**) and (**d**) are the corresponding *3-D* images of (**a**) and (**b**); and (**e**) is the typical height cross section image of (**a**).

3.3.3. Optical properties of CdS nanoparticles and CdS/PANI nanocomposites

UV-vis absorption spectra of CdS nanoparticles synthesised with different molar ratios of CdAc: STS: MPA are presented in **Figures 3.20**. The spectra of CdS nanoparticles exhibit absorption maxima at 340, 400 and 410 nm for CdS-1, CdS-2 and CdS-3, respectively. The absorption maxima are blue-shifted with respect to bulk CdS (~515 nm) arising from quantum confinement effect in the nanoparticles[39].

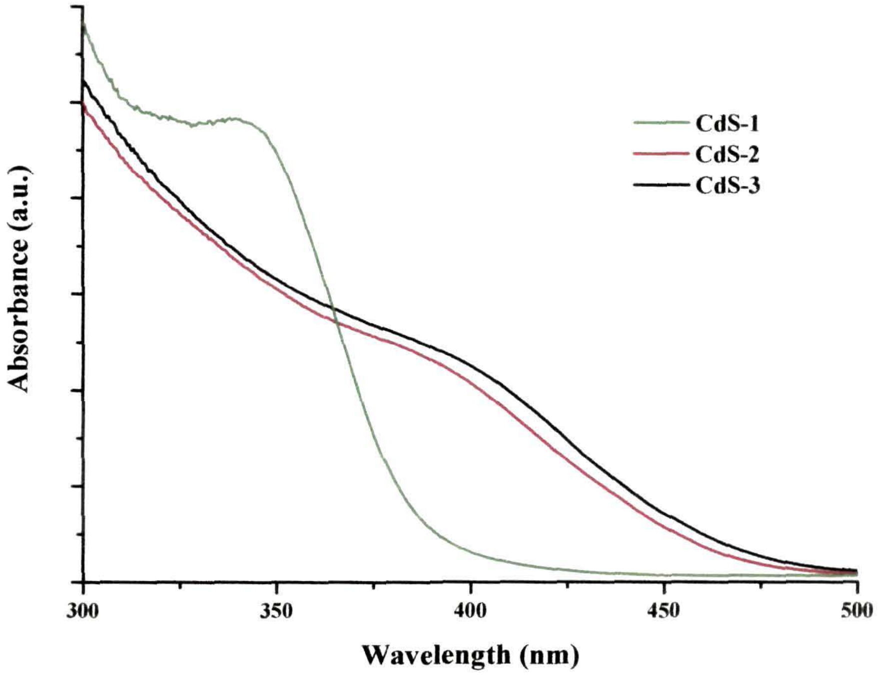

Figure 3.20. UV-vis absorption spectrum of CdS nanoparticles.

Figure 3.21 displays the UV-vis absorption spectra of PANI and CdS/PANI nanocomposites. As discussed in ***Section 2.3.3, Chapter 2***, pure PANI shows two distinct characteristic peaks at 340 and 635 nm. Both bands of PANI are blue-shifted after the CdS/PANI nanocomposites are formed implying decrease in conjugation.

The PL emission spectra of CdS nanoparticles excited at absorption maximum are reported in **Figure 3.22**. One strong emission peak is observed in each of the CdS samples. When the precursor molar ratio of CdAc: STS: MPA was 1: 1: 6 (CdS-1), the resultant nanoparticles show PL characteristic in the range of orange colour (peak: 595 nm). CdS nanoparticles synthesised with 1: 2: 2 molar ratio of CdAc: STS: MPA (CdS-2), emit in green region (peak: 520 nm), and when the molar ratio was 1: 3: 4 (CdS-3), the as-prepared nanoparticles show emission in the red region (peak: 635 nm).

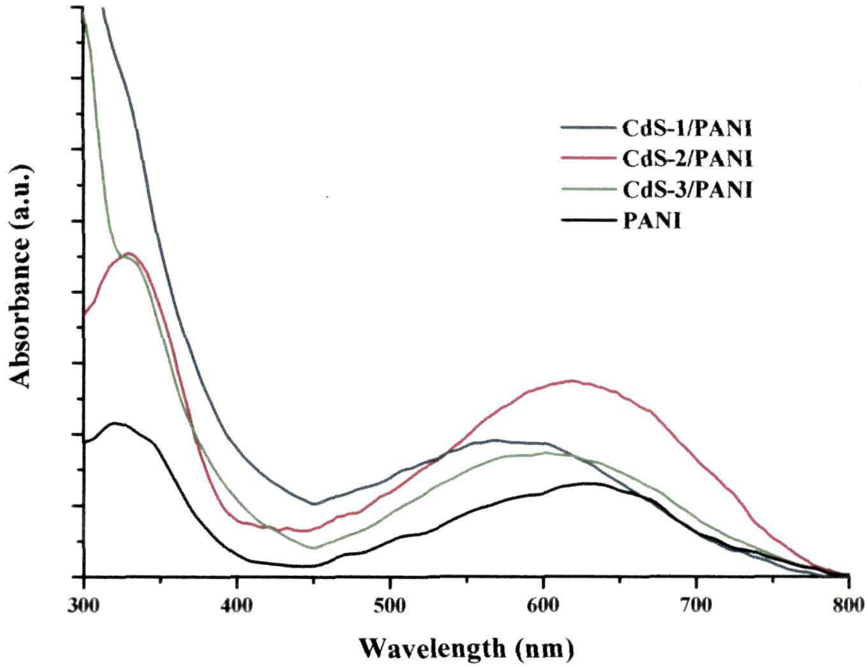

Figure 3.21. UV-visible absorption spectra of PANI, CdS/PANI nanocomposites.

All CdS/PANI nanocomposites are found to be photoluminescent (**Figure 3.23**). As stated earlier, PANI does not possess photoluminescence property and therefore, the emission spectra found in the composites are mainly due to CdS nanoparticles. However, the PL maximum for CdS-1 nanoparticles in presence of PANI is blue-shifted with band centre at 400 nm. In case of CdS-2/PANI, two emission peaks centred at 622 nm and 670 nm are observed and found to be red-shifted as compared to CdS-2. CdS-3/PANI nanocomposite also shows emission spectra at 645 nm that is red-shifted.

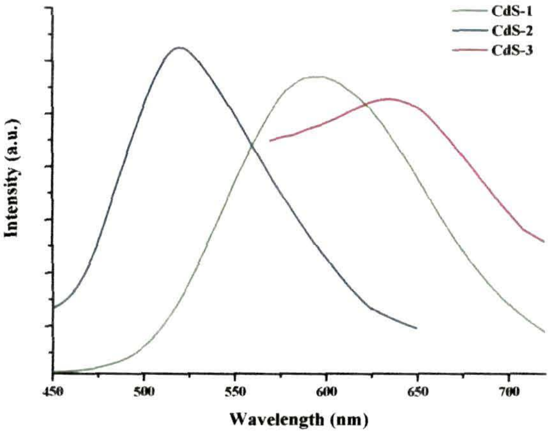

Figure 3.22. PL spectra of CdS nanoparticles.

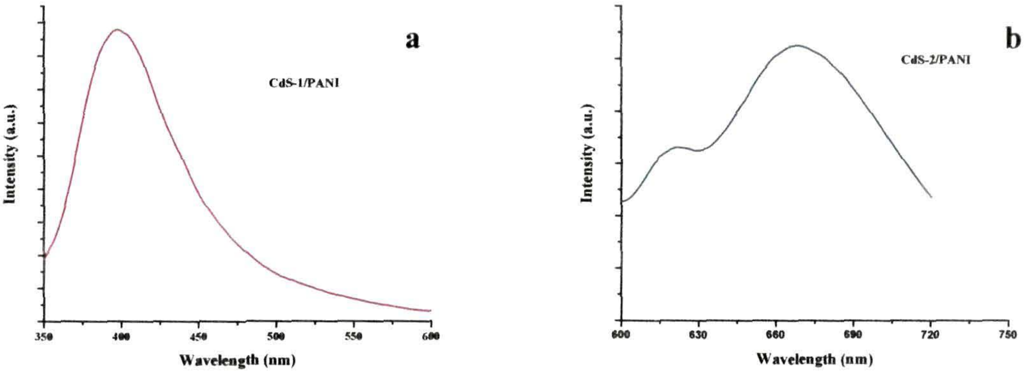

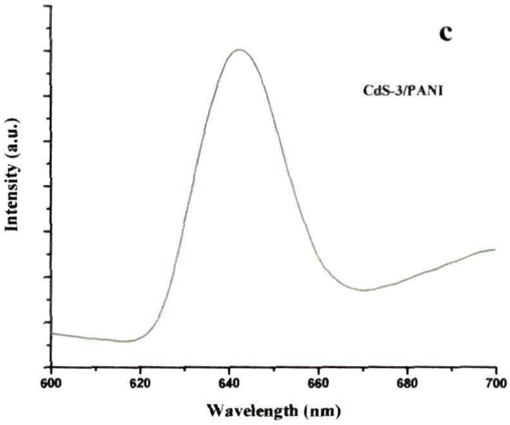

Figure 3.23. PL spectra of CdS-1/PANI (**a**), CdS-2/PANI (**b**) and CdS-3/PANI (c) nanocomposites.

3.3.4. Electrical properties of CdS/PANI nanocomposites

The I-V plots of three types of CdS/PANI nanocomposits at room temperature are shown in **Figure 3.24**. The plots show asymmetric and nonlinear characteristics for forward and reverse directions of applied voltage. Thus, the nanocomposites are semiconducting in nature and implies the formation of Schottky barrier[40]. The diode like I-V characteristic of the nanocomposites is due to the interaction of CdS nanoparticles with PANI and the formation of nanosize grains.

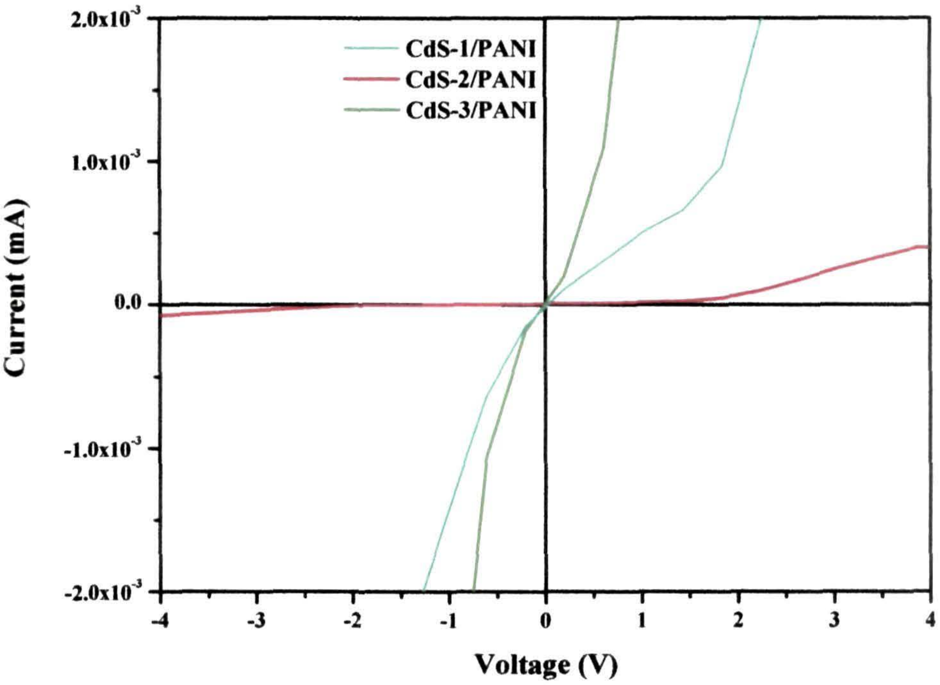

Figure 3.24. I-V characteristic curves of CdS/PANI nanocomposites at room temperature.

The DC conductivity, one of the most important properties of nanocomposites gives information on the conduction phenomenon and interaction of nanoparticles with polymer. The enhancement in DC conductivity of PANI has been observed due to the interaction PANI with CdS nanoparticles in the temperature range of 30-100 °C. All the data are summerized in the **Table 3.5**. From the table, an abrupt increase in conductivity

Table 3.5. DC electrical conductivities of pure PANI and CdS/PANI nanocomposites at different temperatures

Temperature (°C)	Conductivity (S/cm)			
	PANI	CdS-1/PANI	CdS-2/PANI	CdS-3/PANI
30	0.044	1.95	6.60	0.127
50	0.042	0.052	5.35	0.119
70	0.044	0.159	5.43	0.317
90	0.046	2.26	3.88	4.60
100	0.046	3.37	3.78	3.37

of 6.60 S/cm at room temperature is observed in case of CdS-2/PANI nanocomposite. From room temperature (30 °C) to 50 °C, the conductivity decreases in all samples. In the initial state of heating, heat may be used up in molecular as well as filler orientation resulting in the decrease in conductivity. The Table clearly shows that in PANI and CdS-1/PANI, conductivities continuously increase upto 100 °C, whereas it decreases at that temperature for CdS-2/PANI and CdS-3/PANI. This increase in conductivity is due to the increase interchain and intrachain hopping that results in high charge carrier mobility within the nanocomposite. The decrease in conductivity of CdS-2/PANI and CdS-3/PANI at 100 °C could be the consequence of increase in resistive interparticle contacts within the composite material.

3.4. Conclusions

The following important conclusions can be extracted from this investigation:

- CdS nanoparticles have been successfully synthesized using CdAc, STS and MPA in three different CdAc: STS: MPA proportionate ratios following a simple colloidal dispersion synthetic route.
- XRD patterns indicate the formation of cubic CdS nanoparticles irrespective of the precursor molar ratios used in the synthesis. CdS nanoparticles synthesized with

CdAc: STS: MPA molar ratio of 1: 1: 6 give smaller nanoparticles of average particle size 4.1 ± 1 nm.

- Formation of CdS nanoparticles was confirmed by XPS analysis and further quantification of Cd and S peak areas gives the Cd: S atomic ratio as 1: 0.98 that is almost consistent with the stoichiometry of CdS.
- Morphology (SEM, TEM and AFM) studies reveal well ordered near spherical-shape, cube-shape and nanocubes in bunch of flower-like clusters of CdS nanoparticles synthesized with CdAc: STS: MPA molar ratio of 1: 1: 6 (CdS-1), 1: 2: 2 (CdS-2) and 1: 3: 4, (CdS-3), :respectively.
- All three CdS samples were utilised in the synthesis of PANI based nanocomposites via *in-situ* polymerization technique.
- XRD reveals the presence of CdS and PANI in the nanocomposites. However, some changes in peak positions from the original CdS and PANI diffraction peaks are observed.
- FTIR and XPS reveal the interaction of CdS with PANI matrix.
- The thermal property of PANI was improved in the presence of CdS nanoparticles as revealed from TGA analysis.
- SEM, TEM and AFM images reveal bee-hive-like, spike-paddy-like and raspberry-like morphologies for CdS-1/PANI, CdS-2/PANI and CdS-3/PANI, respectively.
- The UV-vis absorption bands for CdS nanoparticles are all blue-shifted with respect to bulk CdS. In CdS/PANI nanocomposites, bands are also blue-shifted with respect to PANI suggesting decrease in conjugation in composites.
- Both CdS nanoparticles and their corresponding PANI composites are photoluninescent.
- The I-V characteristic curves are asymmetric and nonlinear for forward and reverse directions of applied voltage for all CdS/PANI nanocomposites. This

suggests semiconducting behavior and the formation of Schottky barrier in the nanocomposites.

- Among all the CdS/PANI nanocomposites, CdS-2/PANI nanocomposite possesses highest DC electrical conductivity value of 6.60 S/cm at room temperature.

References

1. Shen, G.; Cho, J. H.; Yoo, Y. K.; Yi, G. C.; Lee, C. J. Synthesis of single-crystal CdS microbelts using a modified thermal evaporation method and their photoluminescence, *J. Phys. Chem. B.* **109**, 9294-9298 (2005)
2. Wang, Y. Nonlinear optical properties of nanometer-sized semiconductor clusters, *Acc. Chem. Res.* **24**, 133-139 (1991)
3. Han, M. Y.; Gan, L. M.; Huang, W.; Chew, C. H.; Zou, B. S. Enhancement of photocatalytic oxidation activity by surface-modified CdS nanoparticles of high photostability, *Chem. Lett.* **8**, 751-752 (1997)
4. Morkel, M. *et al.* Flat conduction-band alignment at the CdS/CuInSe2 thin-film solar-cell heterojunction, *Appl. Phys. Lett.* **79**, 4482-4484 (2001)
5. Coe, S.; Woo, W.; Bawendi, M. G.; Bulovic, V. Electroluminescence from single monolayers of nanocrystals in molecular organic devices, *Nature* **420**, 800-803 (2002)
6. Alivisatos, A. P. Semiconductor clusters, nanocrystals, and quantum dots, *Science* **271**, 933-937 (1996)
7. Chan, W. C. W.; Nie, S. Quantum dot bioconjugates for ultrasensitive nonisotopic detection, *Science* **281**, 2016-2018 (1998)
8. Beecroft, L. L.; Ober, C. K. Nanocomposite materials for optical applications, *Chem. Mater.* **9**, 1302-1317 (1997)
9. Nair, P. S.; Radhakrishnan, T.; Revaprasadu, N.; Kolawole, G. A.; O'Brien, P. *NanoTech 2002- "At the Edge of Revolution"*, 9-12 September **2002**, Houston, Texas.
10. Greenham, N. C.; Peng, X.; Alivisatos, A. P. Charge separation and transport in conjugated-polymer/semiconductor-nanocrystal composites studied by photoluminescence quenching and photoconductivity, *Phys. Rev. B* **54**, 17628-17637 (1996)
11. McDonald, A. A. *et al.* Solution-processed PbS quantum dot infrared photodetectors and photovoltaics, *Nat. Mater.* **4**, 138-142 (2005)

12. Stejskal, J. *et al.* Solid-state protonation and electrical conductivity of polyaniline, *Macromolecules* **31**, 2218-2222 (1998)

13. MacDiarmid, A. G.; Epstein, A. J. The concept of secondary doping as applied to polyaniline, *Synth. Met.* **65**, 103-116 (1994)

14. Qiu, H.; Wan, M.; Matthews, B.; Dai, L. Conducting polyaniline nanotubes by template-free polymerization, *Macromolecules* **34**, 675-677 (2001)

15. Kosonen, H. *et al.* Nanoscale conducting cylinders based on self-organization of hydrogen-bonded polyaniline supramolecules, *Macromolecules* **33**, 8671-8675 (2000)

16. Mehrotra, V.; Giannelis, E. P. Metal-insulator molecular multilayers of electroactive polymers: intercalation of polyaniline in mica-type layered silicates, *Solid State Commun.* **77**, 155-158 (1991)

17. Seoudi, R.; Kamal M.; Shabaka, A. A.; Abdelrazek E. M.; Eisa W. Synthesis, characterization and spectroscopic studies of CdS/polyaniline core/shell nanocomposite, *Synth. Met.* **160**, 479-484 (2010)

18. Khiew, P. S.; Huang, N. M.; Radiman, S.; Ahmad M. S. Synthesis and characterization of conducting polyaniline-coated cadmium sulphide nanocomposites in reverse microemulsion, *Mater. Lett.* **58**, 516-521 (2004)

19. Lu, X. *et al.* Poly (acrylic acid)- guided synthesis of helical polyaniline/CdS composite microwires, *Nanotechnology* **16**, 113-117 (2005)

20. Dutta, K.; De, S.; De, S. K. Optical and electrical characterizations of self-assembled CdS nanorods-polyaniline composites, *J. Appl. Phys.* **101**, 093711-093716 (2007)

21. Tong, H.; Zhu, Y. -J. Synthesis of CdS nanocrystals based on low-temperature thermolysis of one single-source organometallic precursor, *Nanotechnology* **17**, 845-851 (2006).

22. Hota, G.; Idage, S. B.; Khilar, K. C. Characterization of nano-sized CdS-Ag_2S core-shell nanoparticles using XPS technique, *Colloids Surf. A* **293**, 5-12 (2007)

23. Poleunis, C.; Weng, L. T.; Sclavons, M.; Bertrand, P.; Franquinet, P.; Legras, R.; Carlier, V. Sizing removal and functionalization of carbon fiber surface studied by combined TOF SIMS and XPS, *J. Adhes. Sci. Technol.* **9**, 859-871 (1995)

24. Wanger, C. D.; Riggs, W. M.; Davis, L. E.; Moulder, J. E.; Muilenber, G. E. *Handbook of X-ray Photoelectron Spectroscopy* (Perkin Elmer, Physical Electronics Division, USA, 1979)

25. Lu, L.; Kobayashi, A.; Kikkawa, Y.; Tawa, K.; Ozaki, Y. Oriented attachment-based assembly of dendritic silver nanostructures at room temperature, *J. Phys. Chem. B* **110**, 23234-23241 (2006)

26. Zhang, D. F.; Sun, L. D.; Yin, J. L.; Yan, C. H.; Wang, R. M. Attachment driven morphology evolvement of rectangular ZnO nanowires, *J. Phys. Chem. B* **109**, 8786-8790 (2005)

27. Pacholski, C.; Kornowski, A.; Weller, H. Self-assembly of ZnO: from nanodots to nanorods, *Angew. Chem., Int. Ed.* **41**, 1188-1191 (2002)

28. Niu, H.; Gao, M. Diameter-tunable CdTe nanotubes template by 1D nanowires of cadmium thiolate polymer, *Angew. Chem., Int. Ed.* **45**, 6462-6466 (2006)

29. Chen, H.; Lesnyak, V.; Bigall, N. C.; Gaponik, N.; Eychmuller, A. Self-assembly of TGA-capped CdTe nanocrystals into three-dimensional luminescent nanostructures, *Chem. Mater.* **22**, 2309-2314 **(2010)**.

30. Karatchevtseva, I.; Zhang, Z. M.; Hanna, J.; Luca, V. Electrosynthesis of macroporous polyaniline-V_2O_5 nanocomposites and their unusual magnetic properties, *Chem. Mater.* **18**, 4908-4916 (2006)

31. Angelopoulos, M.; Ray, A.; MacDiarmid, A. G.; Epstein, A. J. Polyaniline: processability from aqueous solutions and effect of water vapor on conductivity, *Synth. Met.* **21**, 21-30 (1987)

32. Feng, W.; Sun, E.; Fujii, A.; Wu, H.; Nihara, K.; Yoshina, K. Synthesis and characterization of photoconducting polyaniline- TiO_2 nanocomposite, *Bull. Chem. Soc. Jpn.* **72**, 2627-2633 (2000)

33. Yavuz, Ö.; Ram, M. K.; Aldissi, M.; Poddar, P.; Hariharan, S. Synthesis and the physical properties of MnZn ferrite and NiMnZn ferrite- polyaniline nanocomposite particles, *J. Mater. Chem.* **15**, 810-817 (2005)

34. Siegfried, M. J.; Choi, K. S. Electrochemical crystallization of cuprous oxide with systematic shape evolution, *Adv. Mater.* **16**, 1743-1746 (2004)

35. Jing, S.; Xing, S.; Yu, L.; Wu, Y.; Zhao, C. Synthesis and characterization of Ag/polyaniline core-shell nanocomposites based on silver nanoparticles colloid, *Mater. Lett.* **61**, 2794-2797 (2007)

36. Li, J.; Tang, S. B.; Lu, L.; Zeng, H. C. Preparation of nanocomposites of metals, metal oxides, and carbon nanotubes vis self-assembly, *J. Am. Chem. Soc.* **129**, 9401-9409 (2007)

37. Konwer, S.; Pokhrel, B.; Dolui, S. K. Synthesis and characterization of polyaniline/graphite composites and study of their electrical and electrochemical properties, *J. Appl. Polym. Sci.* **116**, 1138-1145 (2010)

38. Kim, B. J.; Oh, S. G.; Han, M. G.; Im, S. S. Synthesis and characterization of polyaniline nanoparticles in SDS micellar solutions, *Synth. Met.* **122**, 297-304 (2001)

39. Berger, L. I. *Semiconductor Materials* (CRC Press, Boca Raton, FL, 1997)

40. Dey, A.; De, S.; De, A.; De, S. K. Characterization and dielectric properties of polyaniline-TiO_2 nanocomposites, *Nanotechnology* **15**, 1277-1283 (2004)

CHAPTER 4

Synthesis of Copper Sulphide (CuS) Nanoparticles and Their Interaction with Polyaniline (PANI)

4.1. Introduction

The recent trend of nanoscience research is to design and fabricate functional nanoscale devices such as organic solar cells, light emitting diodes, biosensor, etc. Semconducting nanoparticles or quantum dots show unique size dependant electronic[1], photonic[2], and catalytic[3] properties arising from quantum confinement and surface effects, and have been recognized as promising building blocks for nanoscale devices. Owing to this, synthesis and characterization of semiconducting metal chalcogenides have drawn more and more attention.

Amongst copper monosulphide (CuS) has gain considerable attention in material science due to its excellent prospective in catalysis[4], optical functionality[5], electronic functionality[6] and so on. In addition, copper monosulphide shows metallic conductivity and transform into superconductor at 1.6K, and exhibits fast-ion conduction at high temperature[7].

Therefore, a flexible synthetic route is indispensable to exploit these properties in materials. So far, a number of physical and chemical routes have been applied to produce nanoscale semiconductor materials including sonochemistry[8], solid state reaction[9], spray pyrolysis[10], etc. However, these techniques generally show disadvantages as poor size tuning and limited control on concentration. In recent years, to produce semiconductor nanoparticles via decomposition of organometallic precursors is extensively used[11]. Wang and Yang reported surfactant-assisted route to fabricate crystalline copper sulphide nanowires arrays from rough oxidized copper surfaces under hydrogen sulphide atmosphere[12]. Dong *et al.* used water-in-carbon dioxide microemulsion to prepare CuS nanocrystals[13]. However, copper sulphide has a number of stable, metastable and intermediate compositions and structures occurring between the two common sulphide end members, Cu_2S (the mineral chalcocite) and CuS (the mineral covellite)[14] and hence, the synthesis of CuS particles by a simple method is still a challenge. A simple colloidal synthesis route can be implemented to obtain nanosize semiconductor particles. Usually the particles in the dispersion adhere to one another and form aggregates of successively increasing size that may settle out under the influence of gravity[15]. In order to overcome this problem, different types of stabilizing agent are used during the colloidal synthesis. Gautam and Mukherjee used poly (*N*-vinyl-2-pyrrolidone) (PVP) and sodium (bis-2-ethylhexyl) sulfosuccinate (Na-AOT) as stabilizers to synthesize the CuS nanocrystal[16]. Triethylenediamine (TEDA), tetramethylenethylenediamine (TEMA) were used as stabilizers by Lu and co-workers during the synthesis of CuS nanorods[17].

Composite materials based on conducting polymers and inorganic semiconductors have shown synergistic enhancement in properties. In this context, a special attention has been paid to polymers like polyaniline (PANI)[18], polypyrrole (PPY)[19], etc. The combination of nanoparticles with conducting polymers offers an attractive route to reinforce the polymer as well as to introduce electronic properties based on morphological modification or electronic interaction between the two components. Chandrakanthi and Careem reported the synthesis of Cu_2S/PANI nanocomposite[20]. However, there is no report on the synthesis of CuS/PANI nanocomposite.

This present investigation focuses on the synthesis of CuS nanoparticles using two different procedures. Stabilizing agents like SDS, PVP, Na-AOT and MPA are used in the synthesis processes. The synthesized nanoparticles are used in the preparation of PANI based nanocomposites. The effects of nanoparticles on optical and electrical properties of polymer have also been studied systematically.

4.2. Materials and methods

4.2.1. Materials

Copper acetate monohydrate (CuAc) ($Cu(CH_3COO)_2$). H_2O, aniline (99%, monomer), 3-mercaptopropionic acid (MPA) and sodium (bis-2-ethylhexyl) sulfosuccinate (Na-AOT) were obtained from Fluka. Thiourea (THU) (NH_2CSNH_2), and potassium peroxydisulfate (KPS) ($K_2S_2O_8$), sodium dodecyl sulphate (SDS), poly (*N*-vinyl-2-pyrrolidone) (PVP) ($M_w = 44{,}000$), and sodium thiosulphate (STS)

($Na_2S_2O_3$ $5H_2O$) were purchased from Merck. Ethanol and hydrochloric acid were of the highest purity commercially available and were used without further purification. Double distilled water was used in all reactions.

4.2.2. Synthesis of CuS nanoparticles

4.2.2.1. Synthesis of CuS nanoparticles (CuS(THU)) using THU as sulphur source: Procedure I

CuS nanoparticles were prepared in aqueous dispersion by using PVP, Na-AOT and SDS as stabilizers. The procedure employed was as follows: 0.2 g of SDS in 10 ml water was taken in a 100 ml three-necked round bottom flask equipped with a condenser and the whole system was placed over a magnetic stirrer. 0.099 g (0.0005mol) CuAc was dissolved in 10ml of double distilled water and added slowly to the aqueous solution of the stabilizer. The temperature was raised slowly to 80 °C and mixing was continued for 1 h. Then 0.076 g (0.001 mol) of THU in 10 ml of double distilled water was added drop wise to the above solution under vigorously stirred condition. During the process the colour changes from blue to white then colourless, followed by green was observed over a period of 24 h indicating the formation of CuS nanoparticles. Following the similar procedure, CuS nanoparticles were synthesized by using different concentrations of CuAc, THU and different types of stabilizers.

4.2.2.2. Synthesis of CuS nanoparticles (CuS(STS)) using STS as sulphur source: Procedure II

CuS nanoparticles were prepared in aqueous dispersion by using MPA as capping agent. CuAc of 0.001 mole was dissolved in 30 ml double distilled water, taken in a 100 ml three-necked round bottom flask equipped with a condenser. The whole system was placed over a magnetic stirrer. Then 0.006 mole of MPA was dropped slowly into the above solution with constant stirring. The solution became white. The temperature was raised slowly up to 80 °C and mixing was continued until the solution became optically clear. Next, 0.003 mole STS in 30 ml water was added dropwise to the above solution under vigorously stirred condition. The reaction mixture was continuously purged with nitrogen. The colour of the initial solution turned slightly brown after addition of STS dropwise, and then became dark brown followed by green to dark green. The reaction was completed in 6 h and the green precipitate was finally dried at 60 °C under vacuum for 24 h.

4.2.3. Synthesis of polyaniline (PANI)

Aniline of 1 ml (0.01 mole) was dissolved in 10 ml of 1.5 M HCl solution in a 50 ml conical flask and cooled down to 0 °C. The oxidizing agent was prepared by dissolving 0.0166 g (0.0125 mole) of KPS in 5 ml 1.5 M HCl solution. KPS solution was added dropwise to the aniline solution while stirring and continued to add for 1 h keeping the reaction temperature at 0 °C. The reaction mixture was then left to warm up to room temperature. Afterwards the reaction mixture was filtered under gravity, washed with 1.5 M HCl and double distilled water until the washing liquid become colourless and finally dried at 60 °C for 24 h under vacuum to obtain a fine tint green powder.

4.2.4. Synthesis of CuS/PANI nanocomposites

CuS/PANI nanocomposites have been synthesized by *in-situ* polymerization technique. The polymerization was carried out by injecting 1 ml aniline into 10 ml of 1.5 M HCl with 0.1 g of synthesized CuS nanoparticles under constant stirring to reduce the aggregation of nanoparticles. After 2 h, 0.0166 g KPS (dissolved in 5 ml water) was then dropped into the solution with constant stirring. The polymerization was allowed to proceed for 5 h. The reaction mixture was then filtered under gravity, washed repeatedly with 1.5 M HCl followed by double distilled water, and finally dried at 60 °C for 24 h under vacuum. The final product was obtained in powdery form with green tint.

4.2.5. Characterization of CuS nanoparticles and CuS/PANI nanocomposites

4.2.5.1. Scanning electron microscope (SEM)

Top-down SEM images of the samples were conducted in a high resolution field emission scanning electron microscope (FEI INSPECT F, model no. FP 2031/11) operating at a voltage of 5 kV. Samples were gold coated (Bio-rad Polaron E5000 gold coater) prior to SEM analysis for 10 s at a voltage of 2.5 kV and a current of 18 mA.

4.2.5.2. Transmission electron microscope (TEM)

Transmission electron microscopy (TEM) images were taken on JEOL-JEM-2000FX transmission electron microscope. The samples were prepared by sonication in appropriate solvents for 10 min prior to transfer to copper grids. To obtain an accurate estimation of the average particle size, at least 100 particles were manually counted.

4.2.5.3. Atomic force microscope (AFM)

AFM provides images of structural details without any chemical treatment (etching or staining) of the specimens. The AFM used was a DME 2452 DualScope Scanner DS Atomic Force Microscope. Scans were carried out in AC mode under ambient conditions with a silicon microcantilever probe tips, using the parameters: force constant: 60,000 N/m; force: 0.15 nN; loop gain: 1,000 loop filter: 3 Hz.

4.2.5.4. Fourier transform infrared spectrometer (FTIR)

Spectra were recorded from pressed KBr pellets using a Perkin Elmer FT-IR spectrometer in the range of 4000-400 cm^{-1} at room temperature.

4.2.5.5. Powder X-ray diffraction (XRD)

XRD data were collected on a Rigaku Miniflex X-ray diffractometer with Cu K$_\alpha$ radiation (λ = 0.15418 nm) at 30 kV and 15 mA using a scan rate of 0.05° s^{-1} in 2θ ranges from 10° to 70°.

4.2.5.6. X-ray photoelectron spectrometer (XPS)

Spectra were acquired on a PHI Quantum 2000 spectrometer with monochromated AlK$_\alpha$ 1486.6 eV X-ray radiation. Samples were loaded into the vacuum chamber within 1 h after being prepared and were subjected to XPS analysis. The analysis area was 1200 μm x 400 μm on each sample. The take off angle in the instrument was set at 90°.

4.2.5.7. Thermogravimetric analysis (TGA)

Thermogravimetric (TGA-DTG) and differential thermal (DTA) analyses were performed in a Shimadzu TGA-50 thermal analysis apparatus. Prior to the run, sample (typically 50 mg) was stabilized for 30 min at 25 °C and then the temperature was linearly increased from 25 to 800 °C with a ramp of 10 °C min^{-1} using dry nitrogen as a carrier gas.

4.2.6. Evaluation of optical and electrical properties

4.2.6.1. UV-vis spectroscopy

UV-vis absorption spectra of the samples were recorded in the range 250-900 nm using Shimadzu UV-2550 UV-visible spectrophotometer.

4.2.6.2. Photoluminescence (PL) spectroscopy

PL spectra were recorded on a Hitachi F- 2500 Fluorescence spectrophotometer, by excitation of the samples at their absorption maximum.

4.2.6.3. I-V characteristics and DC electrical conductivity

The room temperature current-voltage (I-V) characteristics of PANI and CuS/PANI nanocomposites were measured with a Keithley 2400 programmable current source meter by the two probe method in the frequency range of 102-106 Hz.

The temperature dependent direct current (DC) conductivity was measured by the standard four probe method over a temperature range from 30 up to 110 °C on pellets of approx. 1.5 cm diameter and 2 mm thickness compressed at 700 MPa with a compression-moulding machine with manual hydraulic press. The conductivity of the samples was calculated using ***Equation 2.1*** as discussed in ***Chapter 2***.

4.3. Results and discussion

4.3.1. CuS nanoparticles

4.3.1.1. *CuS nanoparticles (CuS(THU)): Procedure I*

4.3.1.1.1. Synthesis of CuS(THU) nanoparticles

The formation of CuS(*THU*) nanocrystal from CuAc and THU involves formation of many intermediates. However, reason is not known yet why CuS formation could not take place directly. In the present investigation, the formation of intermediates can be noticed by gradual change of colour of the reaction mixture (***Scheme 4.1***). The reaction carried out with equimolar amount of CuAc and THU, the blue colour of CuAc solution became white. With further addition of THU, the white solution turned light brown after 2-3 h followed by golden brown after 24 h. On further keeping the reaction for almost 7 days golden brown sol produced brown sol with a greenish tint. Silvester and his co-workers reported that the golden brown solution is a poorly crystalline form of covellite (the green form) and has been assigned the general form $Cu_{1+x}S$, i.e. a copper-rich covellite, of a stoichiometry approaching that of Cu_2S also named chalcocite[21]. It has been reported that the white coloration of the solution is due to the formation of [THU-Cu(II)] complex in the solution and the formation of golden brown dispersion is due to the formation of Cu_2S. This Cu_2S is assumed to stay associated with some elemental sulphur[21,22]. Thus, the possible reaction can be written as

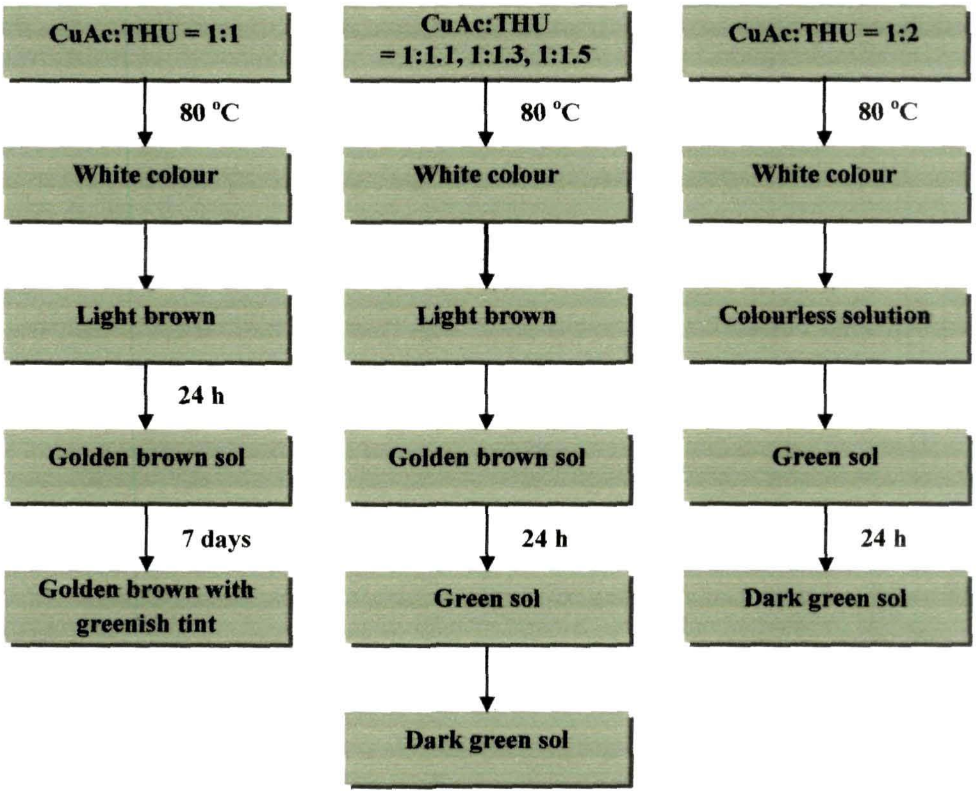

Scheme 4.1. Schematic illustration of the colour changes during the formation of CuS(*THU*) nanoparticles.

$$[Cu\,(THU)_x\,(H_2O)_y]^{2+} \rightarrow Cu^{2+} + THU_x + (H_2O)_y$$

White colour

$$THU + H_2O \rightarrow NH_3 + CO_2 + S^{2-}$$

$2Cu^{2+} + 2S^{2-} \rightarrow Cu_2SS^0$

Golden brown

By using CuAc: THU in the molar ratios of 1: 1.1, 1: 1.3 and 1: 1.5 after 2-3 drops addition of THU in to the CuAc solution, the blue colour of the solution turned white. With passage of time, white solution became brown, and then converted into dark green over a period of 24 h. The conversion of golden brown sol to green is presumed to the conversion from Cu(I) to Cu(II) *via* direct oxidation of dissolved oxygen. The probable reactions are given below:

$Cu^{+} + 2H^{+} + 1/2O_2 \rightarrow Cu^{2+} + H_2O$

$S^{2-} + Cu^{2+} \rightarrow CuS$

Green sol

Thus, at a little excess of THU, complete conversion of golden brown sol to green takes place. However, in case of equimolar amount of THU, golden brown sol with greenish tint has been obtained. In addition, in this case conversion process is less time consuming.

At CuAc: THU molar ratio of 1: 2, after addition of THU the blue solution of CuAc first turned white became colourless then green and became increasingly dark green over a period of 24 h. Thus, CuAc: THU molar ratio of 1: 2 results in formation of new intermediate other than golden brown Cu_2S. Colourless dispersion has not been observed, when the reaction was carried out with CuAc: THU molar ratios of 1: 1, 1: 1.1, 1: 1.3 and 1: 1.5, and instead of getting colourless dispersion, golden brown Cu_2S has developed. The formation of colourless intermediate is presumed to be the formation of [THU-Cu(I)] complex, which is colourless[21-25]. It implies that redox process happened to occur owing to the excess of THU. The probable reactions are given below:

$[Cu(THU)_x(H_2O)_y]^{2+} \rightarrow [Cu(THU)_x(H_2O)_y]^{+}$

White colour ***Colourless***

$[Cu\,(THU)_x(H_2O)_y]^{+} \rightarrow Cu^{+} + THU_x + (H_2O)_y$

$Cu^{+} \rightarrow Cu^{2+}$

$Cu^{2+} + S^{2-} \rightarrow CuS$

Green sol

The most important factor concerning the synthesis of nanoparticles is their stability. It is well known that strong intermolecular forces, such as van der Waals attraction, π–π interaction etc contributes to the aggregation of nanoparticles. Thus, it is a challenge to obtain stable dispersion. Therefore during the synthesis of CuS(*THU*), different types of stabilizers have been used to get stable dispersion. The concentration of the stabilizer influences the stability of the dispersion. To study the stability of the dispersion, the reaction was carried out with different experimental conditions

Table 4.1. Experimental summary of the synthesis of CuS(*THU*) nanoparticles under different reaction conditions

CuAc:THU molar ratio	Surfactant Used	Amount of surfactant used (g/l)	Stability of the dispersion	Result
1:1	SDS	-	Precipitate out	Golden brown Cu_2S sol
1:1	SDS	10	Precipitate out	Golden brown Cu_2S sol
1:1	SDS	20	Some portion precipitate out	Golden brown Cu_2S sol
1:1.2	SDS	20	Some portion precipitate out	Golden brown Cu_2S sol
1:1.5	SDS	20	One day stability	CuS green sol
1:2	SDS	-	Precipitate out	CuS green sol
1:2	SDS	10	30days stability	CuS green sol
1:2	SDS	20	210days stability	CuS green sol
1:2	PVP	20	210days stability	CuS green sol
1:2	Na-AOT	20	210days stability	CuS green sol

CuAc: Copper acetate monohydrate; THU: Thiourea; SDS: Sodium docecyl sulphate; PVP: polyN-vinylpyrrolidone; Na-AOT: Sodium (bis-2ethylhexyl) sulphosuccinate

4.3.1.1.3. XPS analysis of CuS(THU) nanoparticles

The as-prepared CuS(*THU*) nanoparticles were further characterized by XPS for the evaluation of their composition and purity, and a typical survey spectrum is presented in **Figure 4.2**. The XPS survey spectra indicate the presence of Cu, S, C, O, N and Na elements. Stronger oxygen peak in the sample is likely due to (i) the presence of O=C-O of acetate ligand[26] and (ii) exposure to the atmosphere since nanocrystalline material exhibits a high surface-to-volume ratio. The Na 1s peak at 1072.9 eV in the spectrum evolved from SDS used as stabilizer in the synthesis. Peaks of any impurities such as oxide or metallic copper are not detected in the XPS spectra, indicating a relatively pure product. This result is in good agreement with XRD analysis. The high-resolution XPS spectra of Cu 2p and S 2p are shown in **Figure 4.3.**, indicate

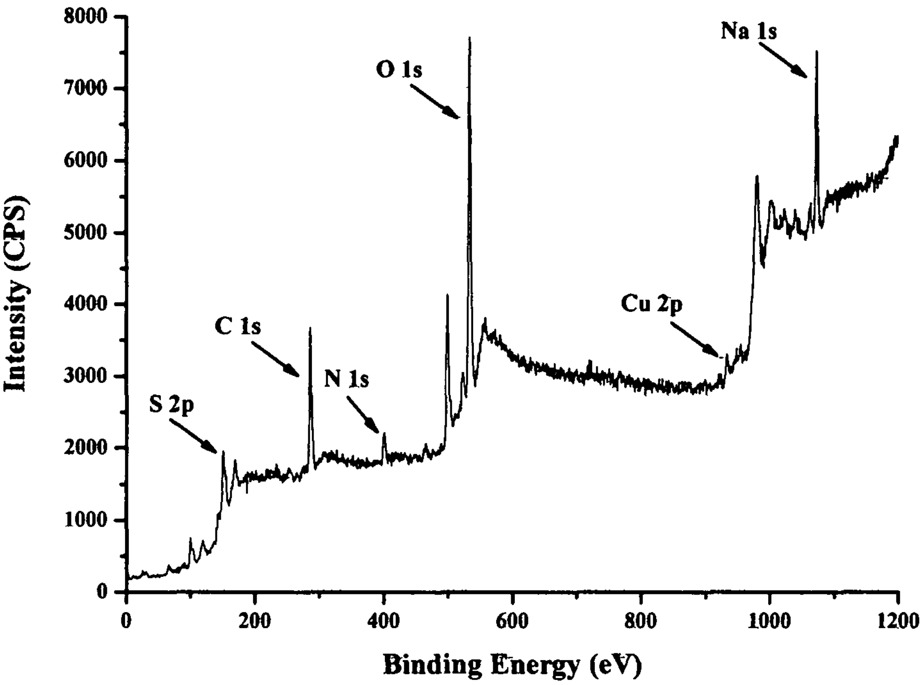

Figure 4.2. X-ray photoelectron survey spectrum of CuS(*THU*) nanoparticles prepared with CuAc: THU molar ratio of 1: 2 and 0.2g SDS.

the presence of two strong peaks located at 932.2 and 952.1 eV (**Figure 4.3a**) are assigned to Cu 2p binding energy and the one at 162.8 eV (**Figure 4.3b**) is attributed to the S 2p core-electrons. Peak area of Cu and S cores is measured and quantification of the peaks gives an atomic ratio of Cu to S as 1: 0.96, which is close to the stoichiometry of CuS.

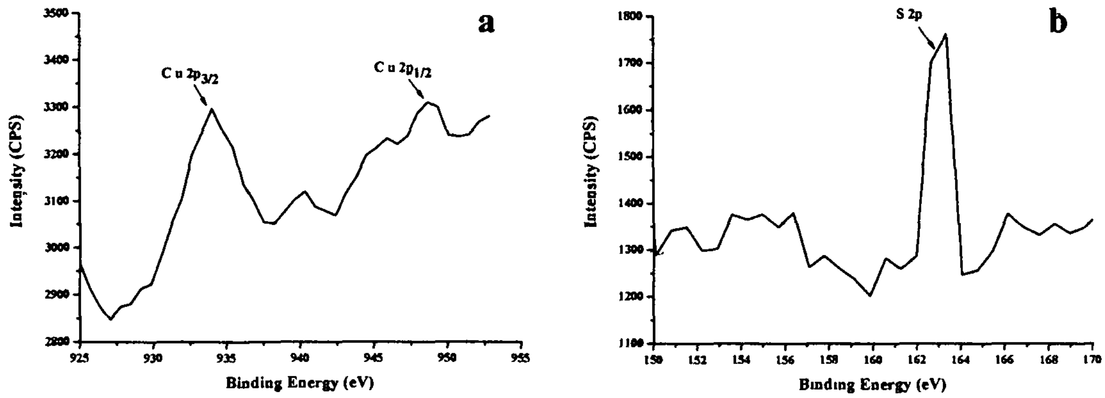

Figure 4.3. High resolution (a) Cu 2p and (b) S 2p XPS spectra of the CuS(*THU*) nanoparticles prepared with CuAc: THU molar ratio of 1: 2 and 0.2g SDS.

4.3.1.1.4. SEM and TEM analysis of CuS(THU) nanoparticles

The morphology of the CuS(*THU*) nanoparticles prepared in different molar ratios of CuAc: THU are investigated by SEM and TEM. **Figure 4.4** shows the SEM and TEM images of CuS(*THU*) nanoparticles prepared in 1: 2 (**a, d**), 1: 1.5 (**b, e**) and 1: 1 (**c, f**) CuAc: THU molar ratios and 0.2 g SDS. From the images, it is clearly seen that the particles prepared in CuAc: THU molar ratios 1: 1 and 1: 1.5 with 0.2 g SDS adhere and have formed bigger particles with almost spherical in shape. On the other hand, the sample prepared in CuAc: THU molar ratio of 1: 2 with 0.2 g SDS consists of well-spherical structures and disperses uniformly as compared to the other two samples. The average particles sizes are calculated from the statistical size distribution diagrams and are plotted against the molar ratios of the precursors used in the synthesis (**Figure 4.5**). Thus, particle size increases with decreasing the concentration of THU.

CuS(*THU*) nanoparticles prepared with CuAc: THU molar ratio of 1: 2 gives the lowest particle size (76 ± 1 nm).

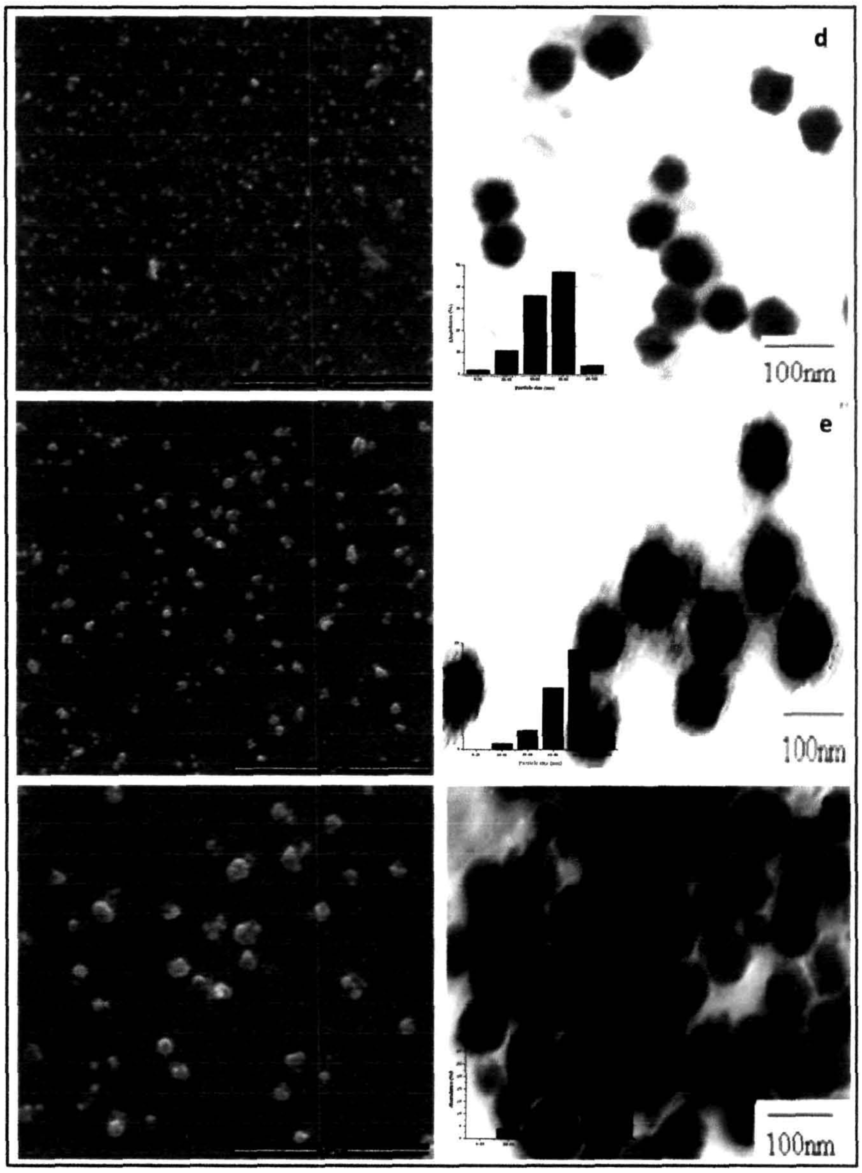

Figure 4.4. Top down FE-SEM images of CuS(*THU*) nanoparticles prepared with CuAc: THU molar ratios of: **a**, 1: 2, **b**, 1: 1.5 and **c**, 1: 1; and **d, e** and **f** are the corresponding TEM images (insets are the statistical size distribution).

Figure 4.6 shows the SEM and TEM micrographs of the sample prepared by 1: 2 CuAc: THU molar ratio with 0.2 g SDS after 210 days of preparation. The image reveals that particles tend to agglomerate to some extent.

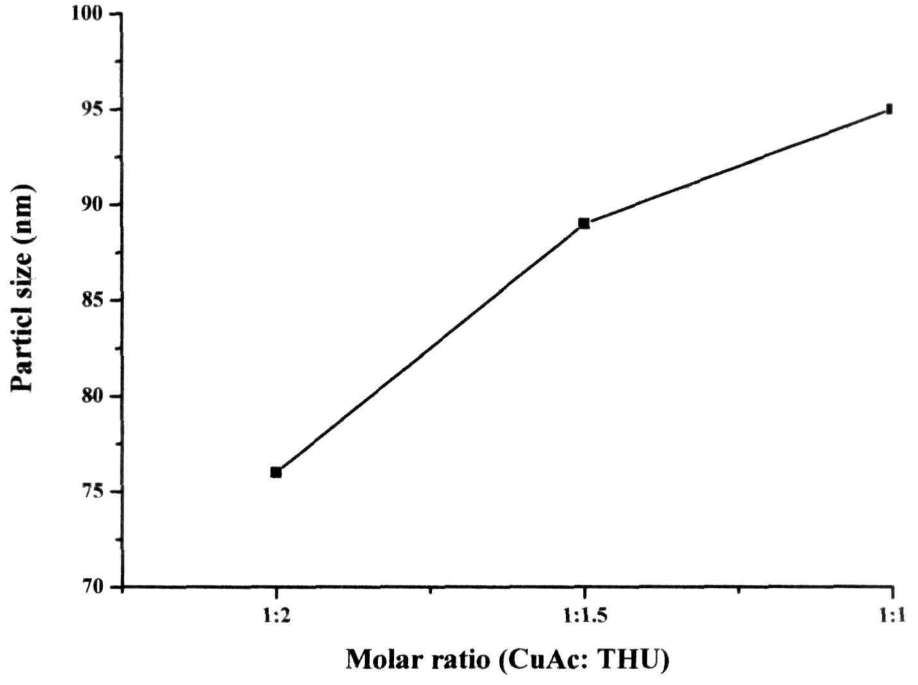

Figure 4.5. Plot of particle size against CuAc: THU molar ratios used for CuS(*THU*) synthesis.

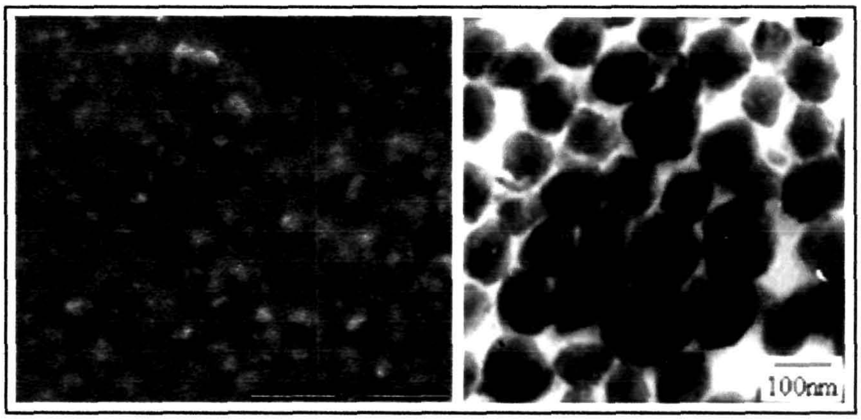

Figure 4.6. Top down FE-SEM (a) and TEM (b) images of CuS(*THU*) nanoparticles prepared with CuAc: THU molar ratios of 1: 2 imaged after 210 days.

4.3.1.1.5. AFM analysis of CuS(THU) nanoparticles

The AFM tapping mode topography and phase images acquired simultaneously for CuS(*THU*) nanoparticles prepared with CuAc: THU molar ratios of 1: 2, 1: 1.5 and

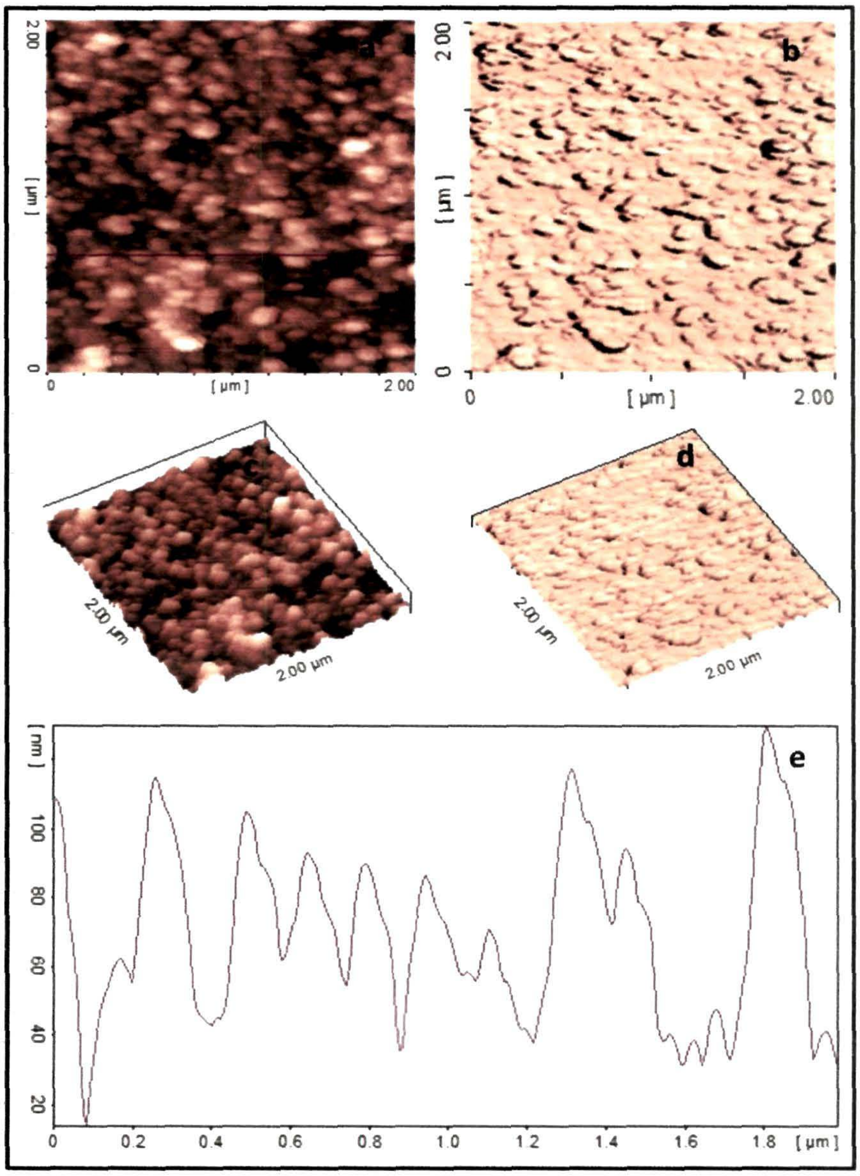

Figure 4.7. AFM tapping mode *2-D* topography (**a**) and phase (**b**) images of CuS(*THU*) nanoparticles prepared with CuAc: THU molar ratio of 1: 2 and 0.2 g SDS. (**c**) and (**d**) are the corresponding *3-D* images of (**a**) and (**b**); and (**e**) is the typical height cross section image of (**a**).

1: 1, and 0.2 g SDS, are presented in **Figures 4.7, 4.8 and 4.9**, respectively. AFM scans were performed on different areas of the same sample to check homogeneity and in all samples, the same kind of results has been found. Like SEM and TEM, near spherical shape of the particles are clearly visible from the topography images, which are even

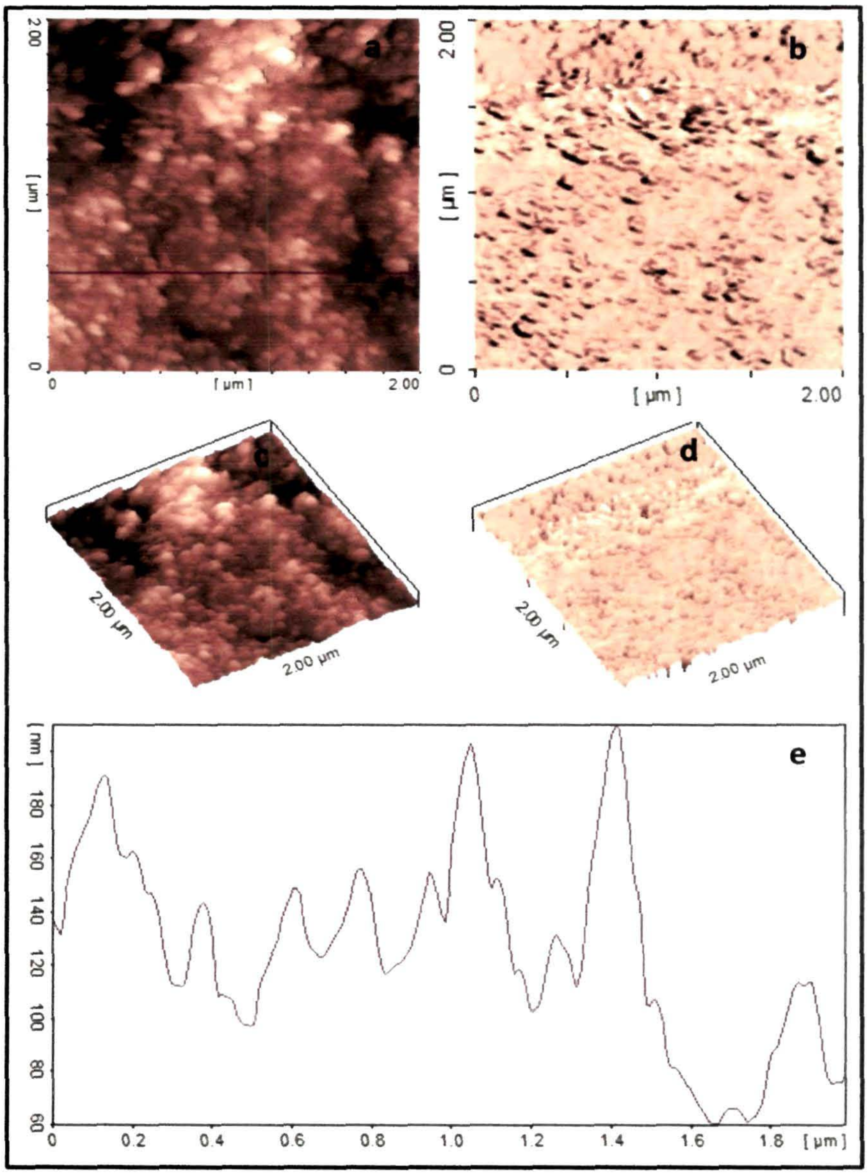

Figure 4.8. AFM tapping mode *2-D* topography (**a**) and phase (**b**) images of CuS(*THU*) nanoparticles prepared with CuAc: THU molar ratio of 1: 1.5 and 0.2 g SDS. (**c**) and (**d**) are the corresponding *3-D* images of (**a**) and (**b**); and (**e**) is the typical height cross section image of (**a**).

clearer from the *3-D* images. A comparison of the height profiles of the topography images of all the samples reveals very inhomogeneous size distribution in case of

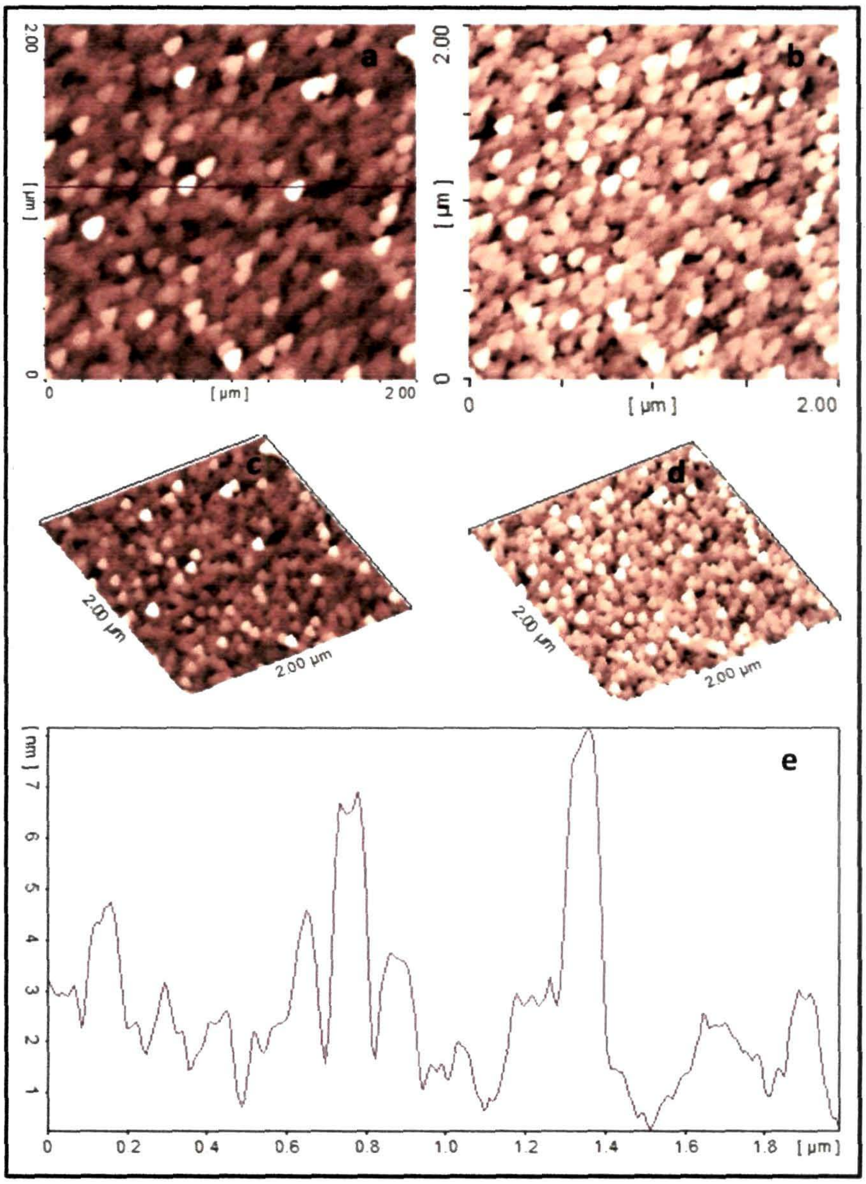

Figure 4.9. AFM tapping mode *2-D* topography (**a**) and phase (**b**) images of CuS(*THU*) nanoparticles prepared with CuAc: THU molar ratio of 1: 1 and 0.2 g SDS. (**c**) and (**d**) are the corresponding *3-D* images of (**a**) and (**b**); and (**e**) is the typical height cross section image of (**a**).

CuS(*THU*) nanoparticles prepared with CuAc: THU molar ratios of 1: 1.5 and 1: 1. CuS(*THU*) nanoparticles prepared with CuAc: THU molar ratio of 1: 2 produced near homogeneous particles as is evident from the height profile image, and indicates a maximum height difference of *ca.* 95 nm and average size of *ca.* 140 nm. The average particle sizes of other samples are very difficult to calculate from the height profile images because of wider size distribution. The average particle sizes calculated from AFM are higher than TEM data and are due to the AFM tip used is not small enough and traces all the materials associated with the nanoparticles apparently giving a larger particle.

4.3.1.2. *CuS nanoparticles (CuS(STS)): Procedure II*

4.3.1.2.1. Synthesis of CuS(STS) nanoparticles

Synthesis of CuS(*STS*) nanoparticles involves the use of CuAc, STS and MPA in the molar ratio of 1: 3: 6. As described in ***Section 4.2.2.2***, the blue coloured CuAc solution turned cloudy upon addition of MPA. The mixture became optically clear when heated to 80 °C. This could be due to the formation of the complex intermediate [Cu-MPA]$^{2+}$. Thus, the possible reactions can be outlined as

$$Cu(CH_3COO)_2.H_2O \rightarrow Cu^{2+} + 2CH_3COO^- + H_2O$$

$$Cu^{2+} + MPA \rightarrow \textbf{Cloudy dispersion } (\textit{immessible}) \xrightarrow{\Delta} [Cu\text{-}MPA]^{2+}$$

Clear solution

This optically clear solution turned brown after the addition of STS dropwise and then became dark green after 6 h. Appearance of brown colour is due to the formation of Cu_2S. Literature reveals that this Cu_2S is associated with some elemental sulphur[21,22]. The possible reaction mechanism for the formation of Cu_2S is given below:

$$Na_2S_2O_3 + H_2O \rightarrow 2Na^+ + SO_4^{2-} + H_2S$$

$$H_2S \rightarrow 2H^+ + S^{2-}$$

$$2Cu^{2+} + 2S^{2-} \rightarrow Cu_2SS^0$$

Brown colouration (unstable)

The brown coloured sol (Cu(I)) is converted to green (Cu(II)) via a direct oxidation of dissolved oxygen.

$Cu^+ + 2H^+ + 1/2O_2 \rightarrow Cu^{2+} + H_2O$

$S^{2-} + Cu^{2+} \rightarrow CuS$

Green precipitate

4.3.1.2.2. XRD analysis of CuS(STS) nanoparticles

The powder XRD pattern of CuS(*STS*) nanoparticles prepared with CuAc: STS: MPA molar ratio of 1: 3: 6 is presented in **Figure 4.10**. Bragg's diffraction peaks for CuS(*STS*) are observed in the XRD pattern at 2θ values of 27.5°, 29.6°, 32.3°, 48.4°, 52.9° and 59.5° representing Miller indices (100), (102), (103), (107), (108), and (203)

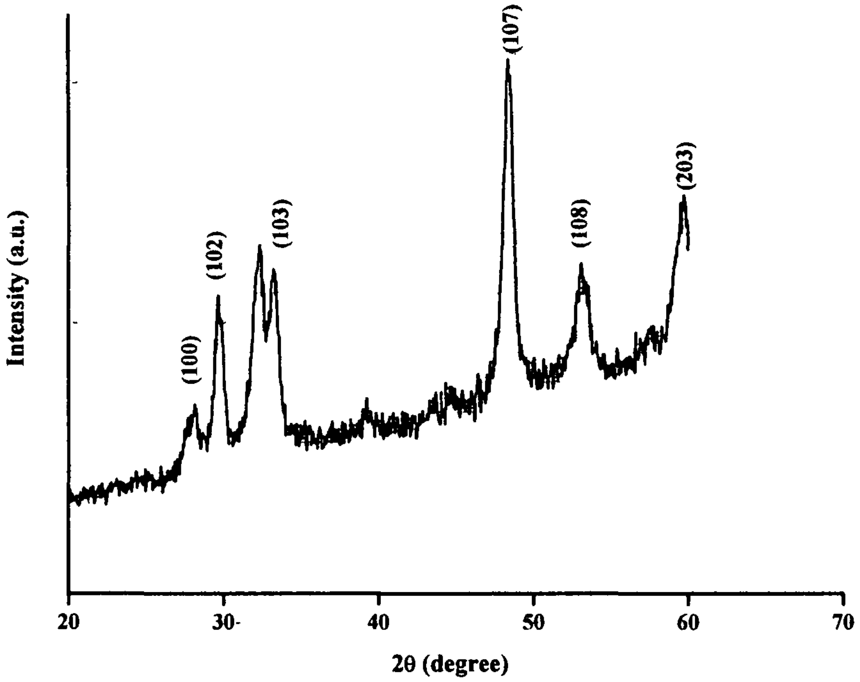

Figure 4.10. Powder X-ray diffraction pattern of the CuS(*STS*) nanoparticles prepared with CuAc: STS: MPA molar ratio of 1:3:6.

of hexagonal primitive CuS [PCPDFWIN 78-0880] and indicate the formation of CuS(*STS*). Peaks corresponding to impurities are not observed in the product synthesized by this approach. The average particles size calculated from the XRD data using the Scherrer's formula (***Equation 2.1, Chapter 2***) has been found to be 3 ± 1 nm in diameter, far smaller than CuS(*THU*) nanoparticles.

4.3.1.2.3. XPS analysis of CuS(STS) nanoparticles

Figure 4.11 shows the XPS survey spectrum of the synthesised CuS(*STS*) nanoparticles. This investigation was done with the aim of evaluating the composition and purity of the product. The survey spectrum indicates the presence of Cu, S, C and O elements in the sample. A strong oxygen peak is identified in the spectrum and is likely to originate from (i) the presence of O=C-O of acetate ligand[26] and (ii) exposure of the sample to the atmosphere. Even though STS was used as the sulphur source in the synthesis, lack of Na 1s peak in the spectrum is a fair indication of the complete elimination of Na during purification. The high-resolution XPS spectrum of Cu 2p and S 2p shown in **Figure 4.12** indicates the presence of two strong peaks

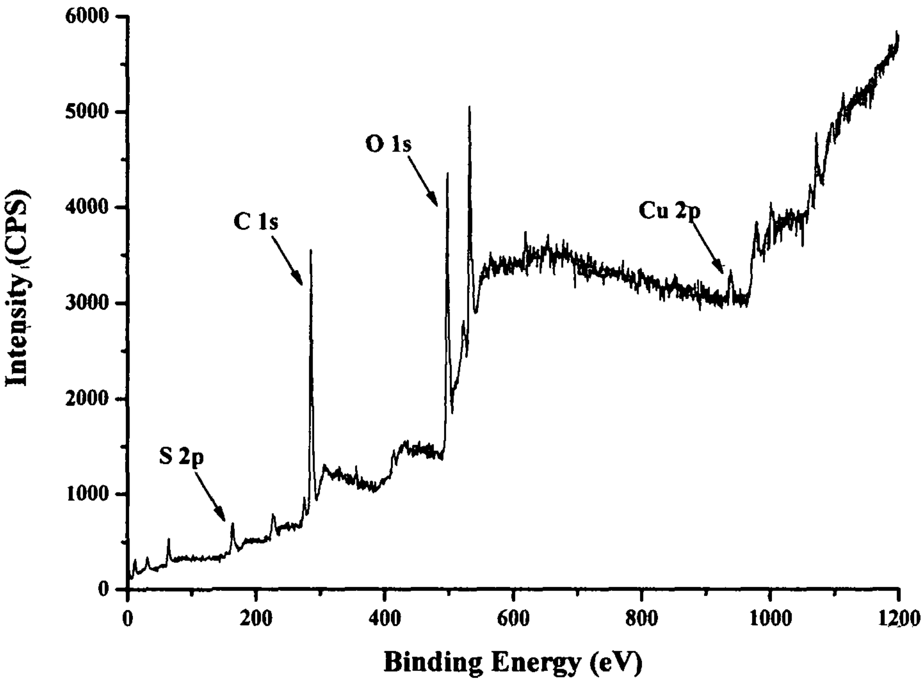

Figure 4.11. X-ray photoelectron survey spectrum of CuS(*STS*) nanoparticles prepared with CuAc: STS: MPA molar ratio of 1: 3: 6.

located at 932.9 and 952.2 eV, and are assigned to Cu $2p_{3/2}$ and Cu $2p_{1/2}$ transitions, respectively, and the one at 163.8 eV is attributed to the S 2p core-electrons. Further, the peak areas of Cu and S cores were measured and quantified to determine the stoichiometric ratio and found to be 1: 0.98, a close stoichiometry to CuS.

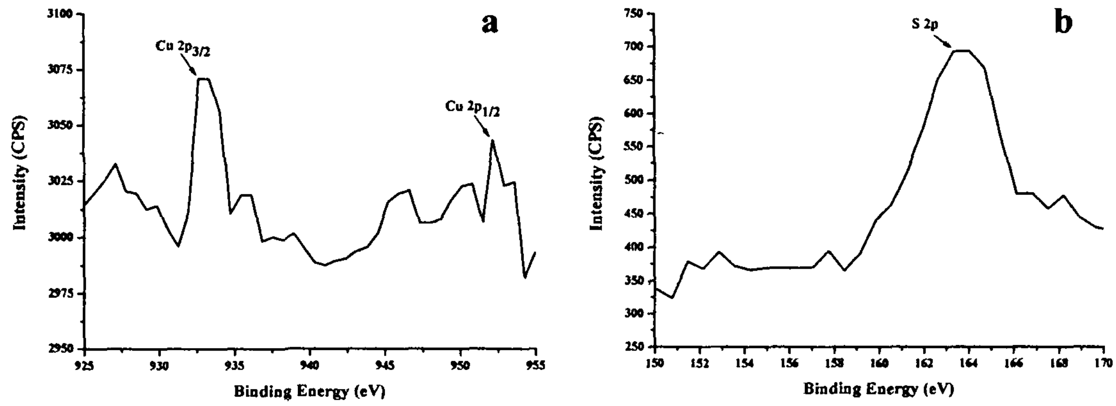

Figure 4.12. High resolution (a) Cu 2p and (b) S 2p XPS spectra of the CuS(*STS*) nanoparticles prepared with CuAc: STS: MPA molar ratio of 1: 3: 6.

4.3.1.2.4. SEM and TEM analysis of CuS(STS) nanoparticles

Similar to CuS(*THU*) nanoparticles, CuS(*STS*) particles were also imaged by SEM and TEM to investigate morphology and particle size distribution. The SEM and TEM images of the CuS(*STS*) nanoparticles are compiled in **Figure 4.13**. The SEM image shows that CuS(*STS*) nanoparticles of spherical shape are distributed over a sheet-like material. Some of the particles were aggregated in the edges of the sheet-like material. The sheet-like material could possibly be the complex [Cu(II)-MPA] formed from the interaction between Cu(II) and MPA. Niu and Gao reported that carboxylic acid groups of thioglycolic acid (TGA) reacts with Cd^{2+} ions to form Cd-TGA complex resulting in amorphous wire like structures[27]. The sheet-like material observed in the SEM image could be this amorphous coordinated complex that acts as glue for the CuS(*STS*) nanoparticles distributed over the material surface. This is further substantiated by the TEM image which shows a similar particle distribution. The average particle size measured from the statistical size distribution diagram is about 4 ± 1 nm- a value very close to the XRD data.

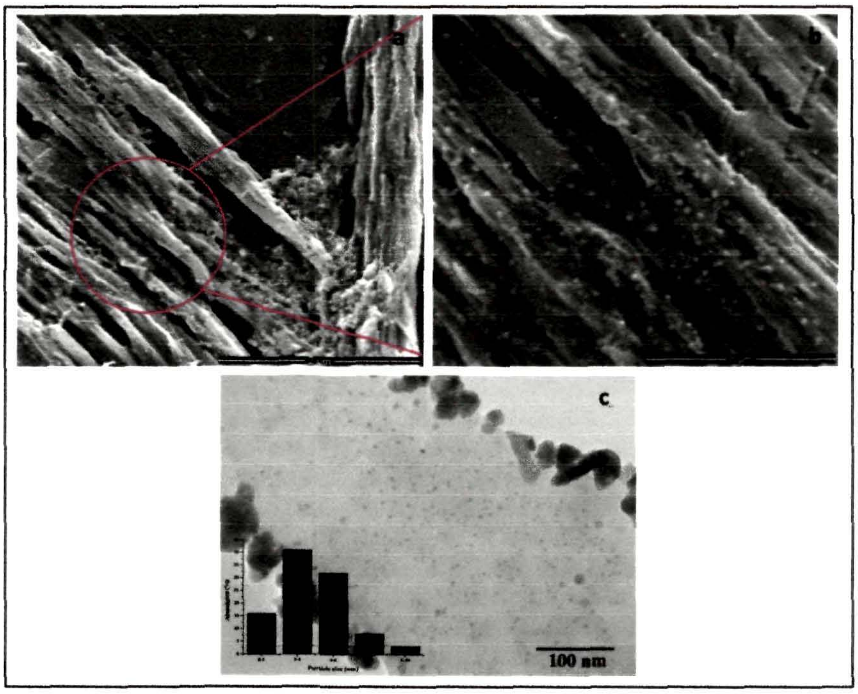

Figure 4.13. Top down FE-SEM (**a**, **b**) and TEM (**c**) (inset is the statistical size distribution) images of CuS(*STS*) nanoparticles prepared with CuAc: STS: MPA molar ratio of 1: 3: 6.

4.3.1.2.5. AFM analysis of CuS(STS) nanoparticles

Figure 4.14 shows the AFM tapping mode topography and phase images of CuS(*STS*) nanoparticles. The topography and phase images clearly reveal the presence of spherical shape particles evenly distributed on top of sheet-like material- a result consistent with the SEM and TEM analysis. The corresponding *3-D* images give even better view of the surface. The height profile of the topography image indicates a maximum height difference of *ca.* 37.5 nm and average size of *ca.* 45 nm for nanoparticles. Further, the width of the sheets are also calculated from the height profile and found to be of *ca.* 400 nm. The inhomogeneous nature of the height profile is due to the surface roughness created by the sheet-like material. Relatively larger particle size calculated from AFM could be due to (i) the AFM tip used is not small enough having insufficient lateral resolution, and (ii) tracing of all the materials associated with the nanoparticles.

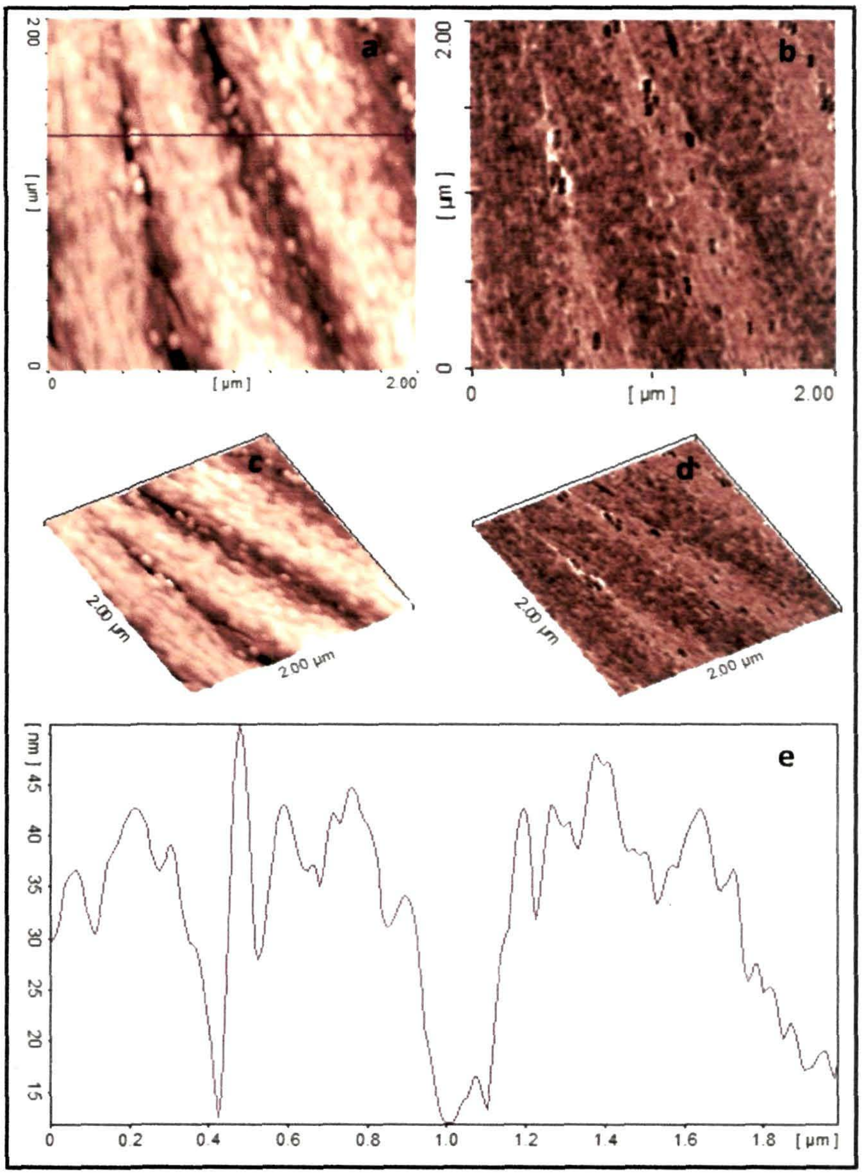

Figure 4.14. AFM tapping mode *2-D* topography (**a**) and phase (**b**) images of CuS(*STS*) nanoparticles prepared with CuAc: STS: MPA molar ratio of 1: 3: 6. (**c**) and (**d**) are the corresponding *3-D* images of (**a**) and (**b**); and (**e**) is the typical height cross section image of (**a**).

4.3.2. *CuS/PANI nanocomposites*

4.3.2.1. Synthesis of CuS/PANI nanocomposites

Two types of CuS/PANI nanocomposites have been synthesized by *in-situ* polymerization technique. The principle variable considered for the synthesis of nanocomposites is the CuS nanoparticles synthesized in two different pathways as stated before. CuS nanoparticles synthesized with CuAc: THU molar ratio of 1: 2 and 0.2g SDS (***Procedure I***: CuS(*THU*)) and CuAc: STS: MPA molar ratios of 1: 3: 6 (***Procedure II***: CuS(*STS*)) gave better stability and narrow size distribution among the CuS naoparticles synthesized. Therefore, these two nanoparticles were picked up to synthesize CuS/PANI nanocomposites. A schematic layout of the synthesis procedure is given in ***Scheme 4.2***:

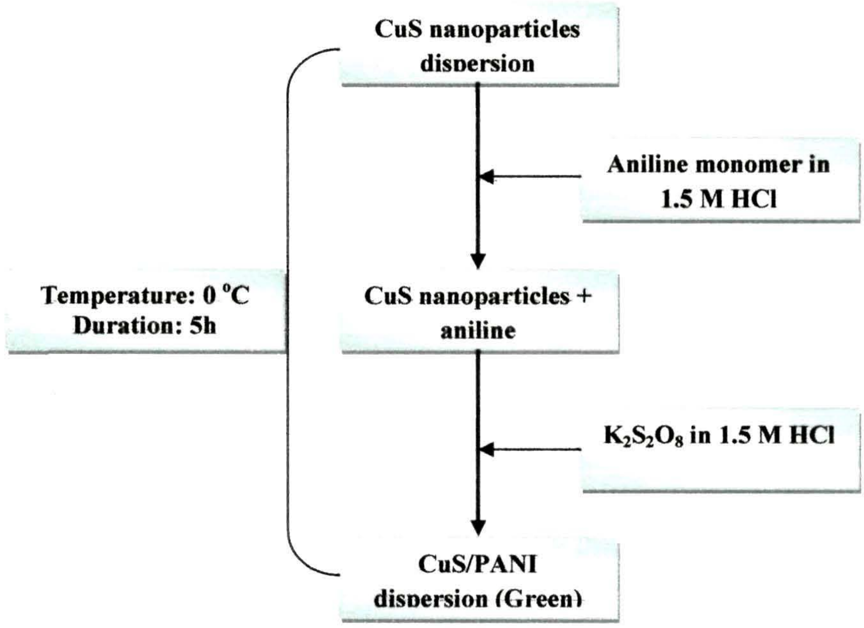

Scheme 4.2. Schematic illustration for the synthesis of CuS/PANI nanocomposites.

4.3.2.2. XRD analysis of CuS/PANI nanocomposites

The powder XRD patterns of PANI and its composites with CuS(*THU*) and CuS(*STS*) nanoparticles are presented in **Figure 4.15**. The diffraction peaks for PANI are observed at 2θ values of 15.2°, 20.3°, 25.1°, 27° and 30°, and can be assigned to

(011), (020), (200), (121) and (022), respectively, crystalline plane diffraction peaks of PANI in its emeraliadne form[28,29]. These peaks might have originated from the scattering of PANI chains at interplanar spacing[30], and suggests a significant crystalline fraction. For the CuS(*THU*)/PANI nanocomposite, the diffraction peaks are observed at 2θ values of 15.2°, 20.4°, 25.1°, 27.5°, 32°, 38°, 46.1° and 56.9°. The first three peaks are originated from PANI while the other peaks correspond to the peaks of CuS(*THU*) nanoparticles as discussed in ***Section 4.3.1.1.2***. In CuS(*STS*)/PANI, the diffraction peaks are observed at 2θ values of 15.2°, 20.4°, 25.1°, 27.5°, 31.9°, 38.0°, 48.0°, 52.9°, 59.5°. It is clearly seen that the characteristic peaks of both PANI (as mentioned above) and CuS(*STS*) (***Section 4.3.1.2.2***) appear in the XRD pattern of CuS(*STS*)/PANI nanocomposite. However, with respect to the diffraction patterns of the CuS nanoparticles as stated in ***Sections 4.3.1.1.2 and 4.3.1.2.2***, change in intensity and slight

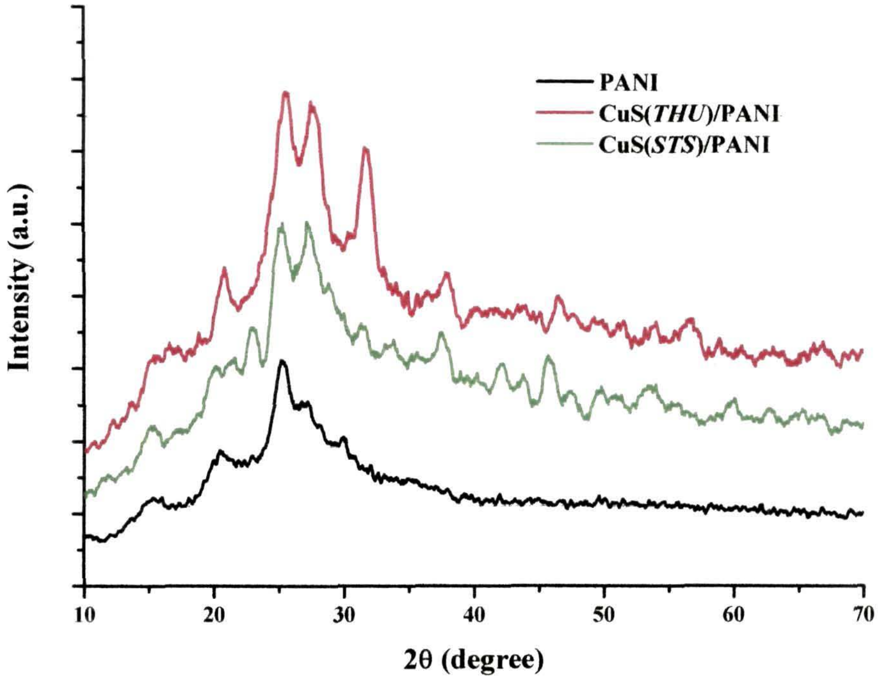

Figure 4.15. Powder X-ray diffraction patterns of pure PANI and CuS/PANI nancomposites.

shifting in positions are observed in the diffraction patterns of nanocomposites. Besides, the diffraction peaks at 2θ value of 29.9° for CuS(*THU*) and 29.6° for CuS(*STS*) nanoparticles are missing, instead a new peak appears at 2θ value of 38.0° in both composites. These changes can be related to some structural change in the polymer caused by the close interaction with the disperse nanoparticles phase[31]. During the growth of crystals (nanocomposite), the growth of each plane of the components can be different due to the different adsorptions between each plane and organic or inorganic additives[32]. Further, compared to PANI diffraction pattern, the peaks corresponding to PANI in the nanocomposites, are sharp, indicating higher crystallinty in composites. Thus, the XRD patterns of nanocomposites evidence reorganization in the structure of the polymer and the co-existence of the CuS reflections suggesting its effective and stable incorporation in the nanocomposite structure.

4.3.2.3. FTIR analysis of CuS/PANI nanocomposites

FTIR spectroscopy of pure PANI and its composites with CuS nanoparticles was performed in order to investigate the possibility of any interaction between CuS nanoparticles and PANI matrix. **Figure 4.16** displays the FTIR spectra of both CuS(*THU*)/PANI and CuS(*STS*)/PANI. Details about the FTIR spectrum of pure PANI

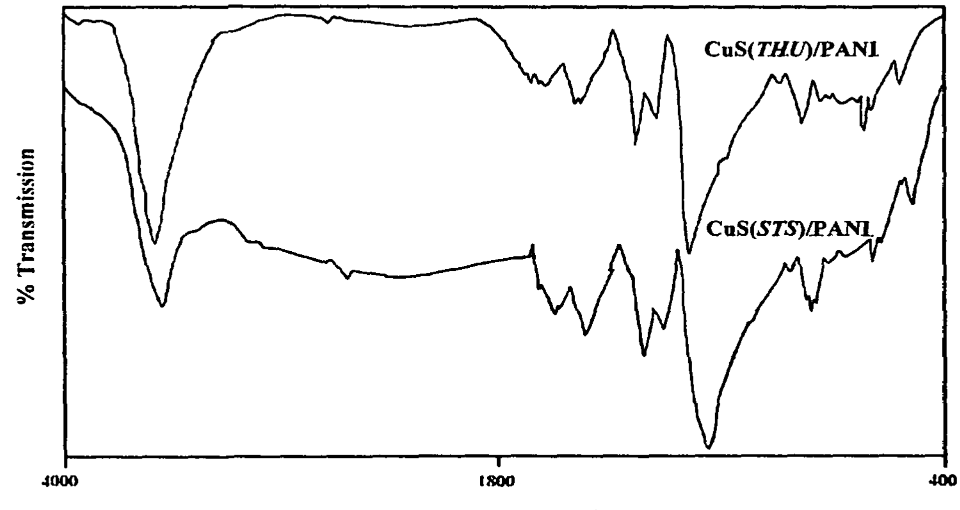

Figure 4.16. FTIR spectra of pure PANI, and CuS/PANI nanocomposites.

are discussed in ***Section 2.3.2.3, Chapter 2***, and found to be in emeraldine form[33]. The bands found in PANI are assigned to different vibrational modes as presented in **Table 4.2.** These characteristic bands of PANI can also be identified in the IR spectra of the two nanocomposites confirming its formation in the composites. For comparison, the infrared bands of CuS/PANI nanocomposites are also compiled in the **Table 4.2.**

Table 4.2. Assignment of IR bands for PANI and CuS/PANI nanocomposites

IR band	**Assignment**	**Peak position/Wavenumber cm^{-1}**		
		PANI	**CuS(*THU*)/PANI**	**CuS(*STS*)/PANI**
ν_{N-H} stretching	Amine –N-H	3282	3206	3207
ν_{C-N} stretching	2° amine –C-N bond	1296	1299	1300
$\nu_{C=N}$ stretching	-C=N bond in bipolaron	1243	1240	1240
$\nu_{C=C}$-stretching	Quinoid ring	1567	1564	1556
ν_{C-C}stretching	Benzoid ring	1466	1470	1474
ν_{C-H} in- plane Bending	Benzoid ring	1106	1119	1110
ν_{C-H} out- of- plane Bending	Benzoid ring	876	882	876
ν_{C-H} stretching	C-H bond in phenyl ring	2920	2925	2927

However, shifting in peak positions associated with C=C, C=N and C-N stretching of the quinoid ring are observed. This can be attributed to the interaction between CuS and PANI by virtue of the presence of CuS nanoparticles in close proximity of the imine nitrogen of PANI.

4.3.2.4. XPS analysis of CuS/PANI nanocomposites

The nanocomposites are further characterised by XPS and the survey spectra of CuS(*THU*)/PANI and CuS(*STS*)/PANI are reported in **Figures 4.17 and 4.18**, respectively. The spectrum of pure PANI was also recorded as a reference material and a detailed discussion can be found in ***Section 2.3.2.4, Chapter 2.*** All the essential elements (Cu, S, O, C and N) of the nanocomposite can be identified in the survey spectrum. Peaks for C, O and N are originated from PANI and that implies the formation of PANI in the nanocomposites. In both nanocomposites, the intense C 1s peak found at ~284.5 eV is assigned to PANI backbones[34]. The sharp peak observed at ~531.5 eV in the spectra of CuS(*THU*)/PANI and CuS(*STS*)/PANI is for O 1s. The presence of oxygen is attributed to the oxidant and to extra contaminating oxygen. The N 1s peak detected in the spectra points out binding energy of ~398.5 eV that corresponds to -NH- group of PANI. Further, the peaks at ~933.2 eV and ~163.5 eV are assigned to Cu 2p and S 2p, respectively. The peak positions of the essential elements identified the XPS spectra of pure PANI, CuS(*THU*)/PANI and CuS(*STS*)/PANI are compiled in **Table 4.3**. The nanocomposites and the reference material exhibit similar C 1s, N 1s and O 1s

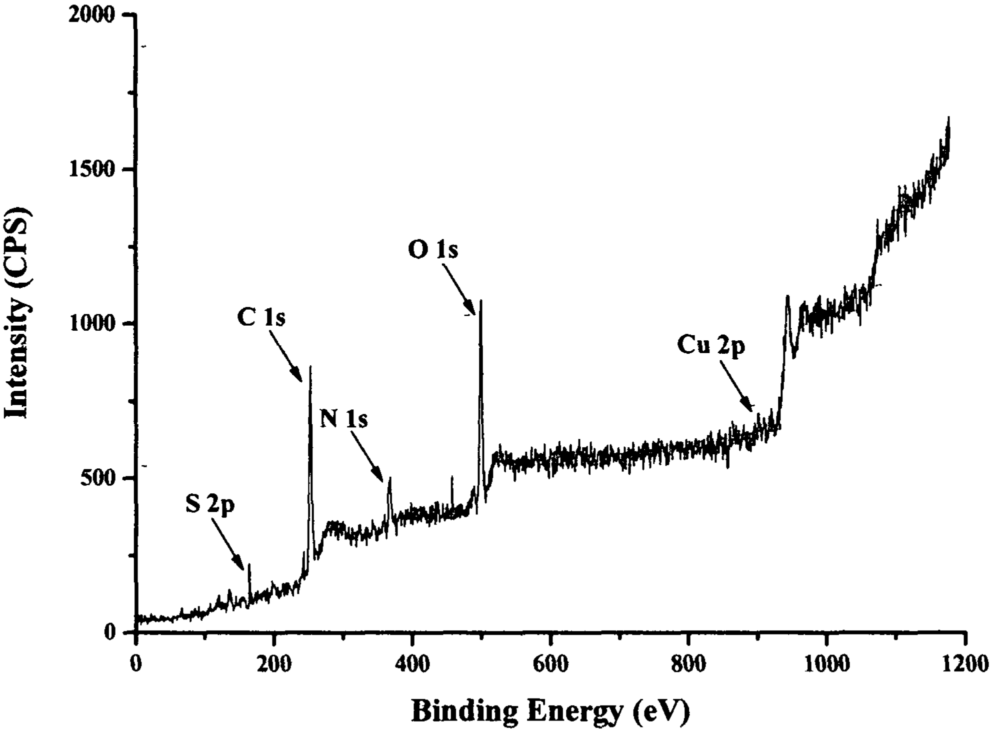

Figure 4.17. X-ray photoelectron survey spectrum of CuS(*THU*)/PANI nanocomposite.

peaks, however, their intensities and positions are slightly changed. These changes can be accounted for the change in the chemical environment of PANI in composites.

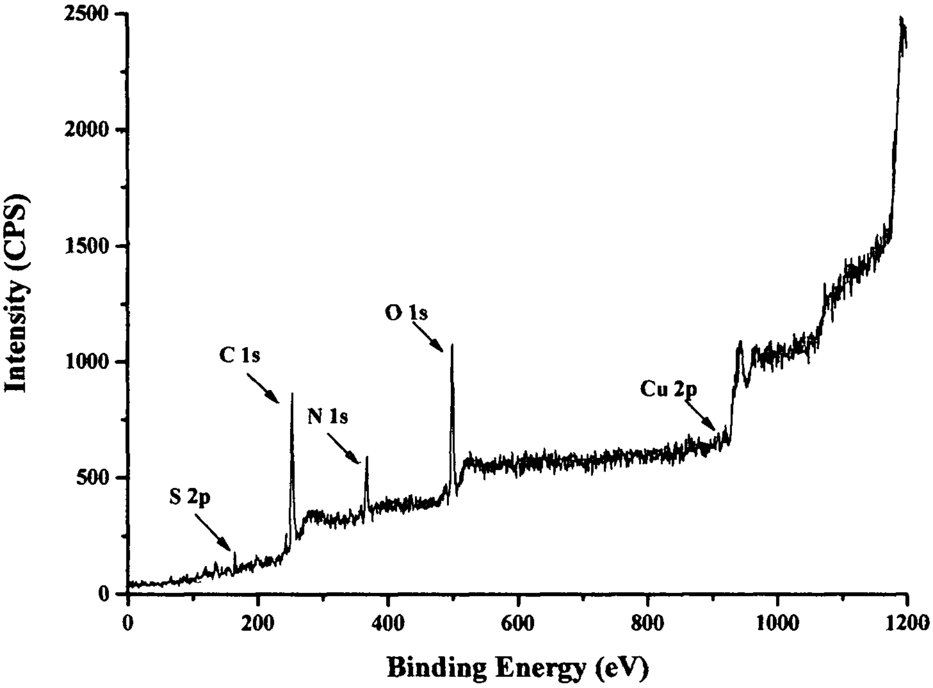

Figure 4.18. X-ray photoelectron survey spectrum of CuS(*STS*)/PANI nanocomposite.

Table 4.3. XPS peak positions of essential elements in pure PANI and CuS/PANI nanocomposites

Compound	**Peak positions, eV**				
	C 1s	**O 1s**	**N 1s**	**Cu 2p**	**S 2p**
PANI	285.5	532.6	400.0	--	--
CuS(*THU*)/PANI	284.9	532.9	398.7	933.4	163.7
CuS(*STS*)/PANI	286.2	534 0	398.8	933.2	163.5

4.3.2.5. TGA of CuS/PANI nanocomposites

The thermal property of the PANI before and after introducing CuS nanoparticles was investigated by thermo gravimetric (TG) analysis. The TGA profiles of PANI, CuS(*THU*)/PANI and CuS(*STS*)/PANI nanocomposites are shown in **Figure 4.19**. The TGA traces were recorded upto 800 °C at a heating rate of 10 °C/min under nitrogen flow. It is evident from **Figure 4.19** that the thermal events accompanying weight losses lead to similar kind of degradation profiles for both pristine PANI and its CuS nanocomposites. Though all the compounds experience gradual weight loss throughout the thermal process, yet a three step weight loss process can be distinctly identified in the TGA profiles. The first weight loss upto 120 °C is mainly contributed by the elimination of moisture. The second weight loss in the temperature range of 220-340 °C is accompanied by the removal of HCl bound to the PANI chain and low molecular weight oligomers[35]. The third step after 500 °C which is considered as the major weight loss step indicates the structural decomposition of the polymer. The essential weight loss characteristics of PANI, CuS(*THU*)/PANI and CuS(*STS*)/PANI are summarized in **Table 4.4**. It appears that the weight loss is relatively higher in both nanocomposites

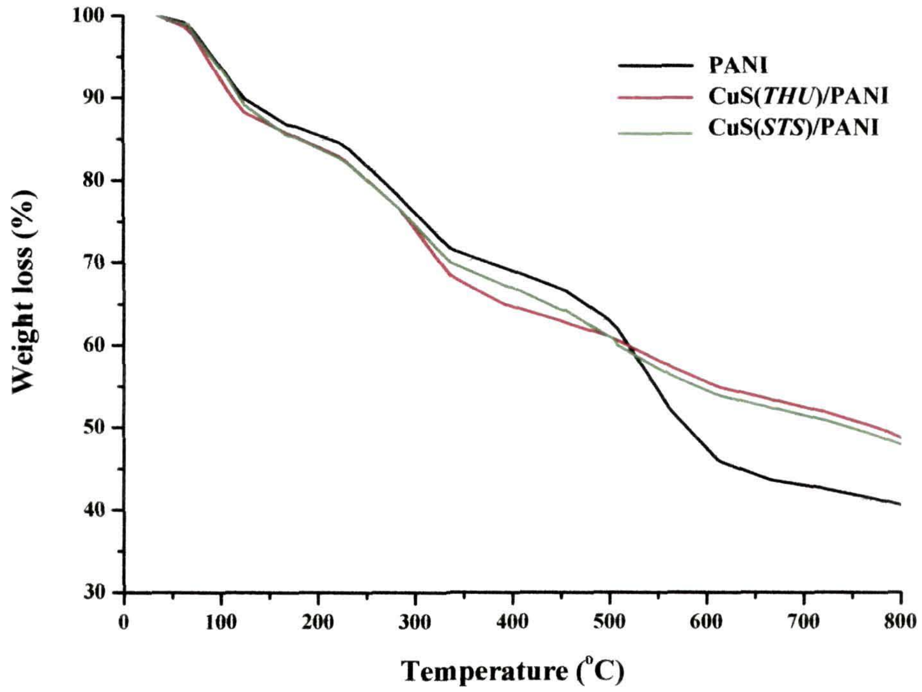

Figure 4.19. TGA thermographs of pure PANI and CuS/PANI nanocomposites.

below 500 °C and could be accounted for the presence of allied substances associated with the as-synthesized nanoparticles. However, the weight loss is relatively lower in the two composites after 500 °C, which indicates that the thermal property of the polymer is improved due to the presence of CuS nano fillers. Thus, it strongly attributes the interaction of CuS nanoparticles with PANI through stronger binding force between nanoparticles and the lone pair electrons of N atom in the polymer backbone[36].

Table 4.4. Essential weight loss characteristics of PANI and CuS/PANI nanocomposites

Compound	Weight loss (%) at		
	115 °C	340 °C	600 °C
PANI	8.5	28.7	52.5
CuS(*THU*)/PANI	11.2	31.8	44.5
CuS(*STS*)/PANI	9.5	30.6	45.7

4.3.2.6. SEM and TEM analysis of CuS/PANI nanocomposites

Morphologies of CuS(*THU*)PANI and CuS(*STS*)PANI nanocomposites are studied using SEM and TEM. As discussed earlier (***Section 2.3.2.6, Chapter 2***), pure PANI has fibrous morphology. However, with the introduction of CuS nanoparticles into PANI matrix, the morphology of the resulting composites has been changed. The morphological changes are expected because of possible coating of CuS with PANI. Two distinct morphologies are observed in the two nanocomposites prepared from CuS(*THU*) and CuS(*STS*) nanoparticles (**Figures 4.20 and 4.21**). It can be seen from the SEM images of **Figure 4.20**, the nanocomposite prepared from CuS(*THU*) and PANI has worm-like features. In some areas, the particles are agglomerated forming bigger particles. On the other hand, shuttle-like features are observed in the SEM images (**Figure 4.21**) of the nanocomposite prepared from CuS(*STS*) and PANI. The same experimental conditions were applied for the synthesis of CuS(*THU*)/PANI and

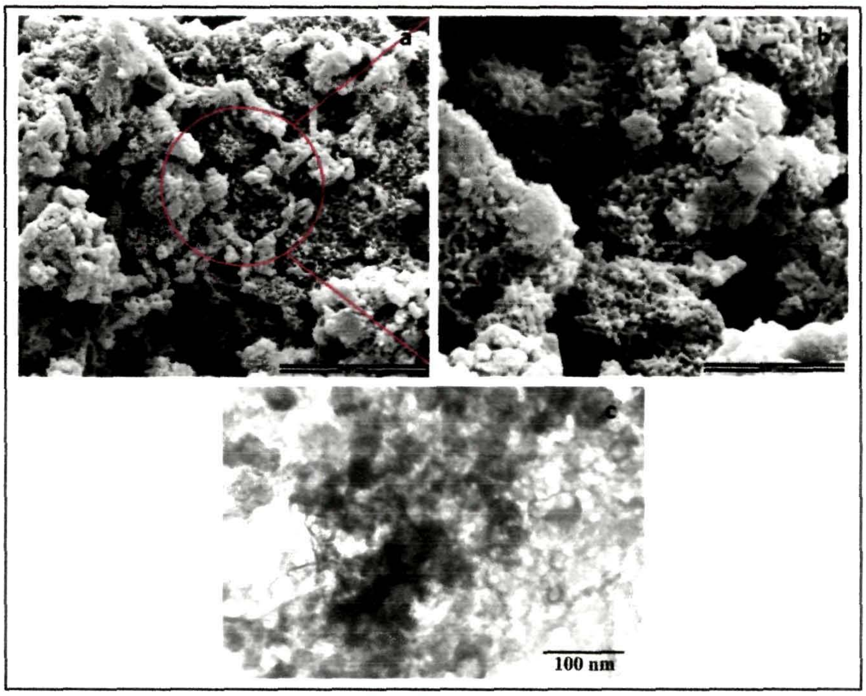

Figure 4.20. Top down FE-SEM (**a**, **b**) and TEM (**c**) images of CuS(*THU*)/PANI nanocomposite.

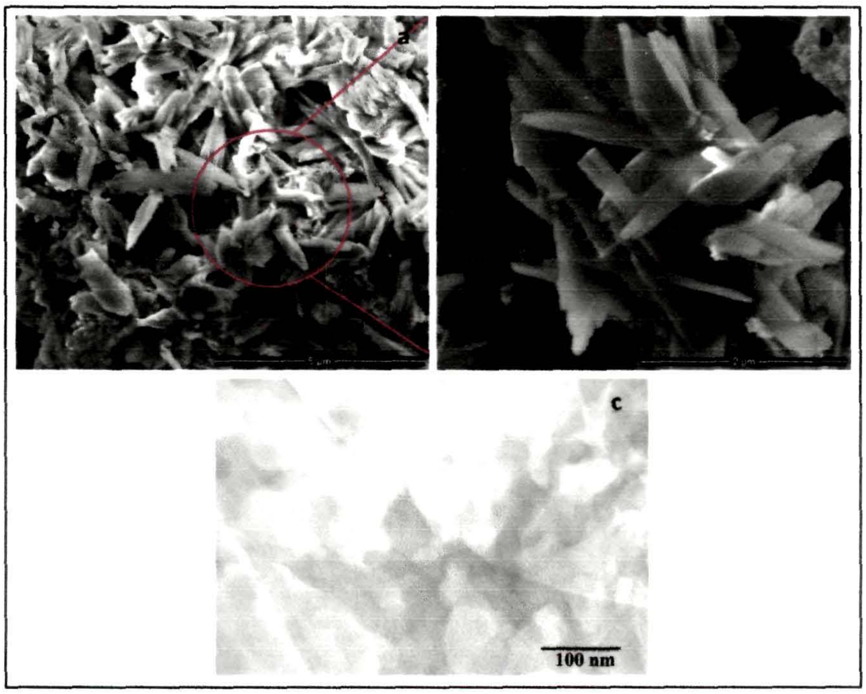

Figure 4.21. Top down FE-SEM (**a**, **b**) and TEM (**c**) images of CuS(*STS*)/PANI nanocomposite.

CuS(*STS*)/PANI, except CuS nanoparticles incorporated in PANI were produced from two different synthesis procedures. Thus, the difference in morphology observed in the two nanocomposites is the direct result of incorporation of CuS nanoparticles coming from two different environments. The presence of sheet-like structure resulting from the complex formation between Cu(II) and MPA during CuS(*STS*) nanoparticles synthesis also influence the formation of shuttle-like morphology in CuS(*STS*)/PANI nanocomposite. The TEM images (**Figures 4.20 and 4.21**) of both composites revel that CuS nanoparticles are well combined and distributed within the polymer matrix. Existence of CuS nanoparticles in the PANI matrix is also confirmed by XRD and XPS analyses as discuss earlier. Thus, the morphology of nanocomposites can be modified simply by tailoring the size and shape of nanoparticles.

4.3.2.7. AFM analysis of CuS/PANI nanocomposites

Figures 4.22 and 4.23 display the AFM tapping mode topography, phase and height profile images of CuS(*THU*)/PANI and CuS(*STS*)/PANI nanocomposites, respectively. The topography and phase images were acquired simultaneously in the same location of the samples. Further, to check homogeneity AFM scans were performed on different areas of the same sample and the same kind of results were observed in all cases. The *2-D* topography image of CuS(*THU*)/PANI composite shows worm-like features (**Figures 4.22**)- a result similar to SEM and TEM analyses as discussed above. The *3-D* image gives a better view of the topography. The height profile of the topography image reveals a rough surface and indicates a maximum height difference of *ca.* 400 nm. Like SEM, the *2-D* topography and phase images of CuS(*STS*)/PANI clearly reveal the presence of shuttle-like material, which is even clearer from the corresponding *3-D* images (**Figure 4.23**). The height profile of the topography image indicates a rough surface with a maximum height difference of *ca.* 110 nm.

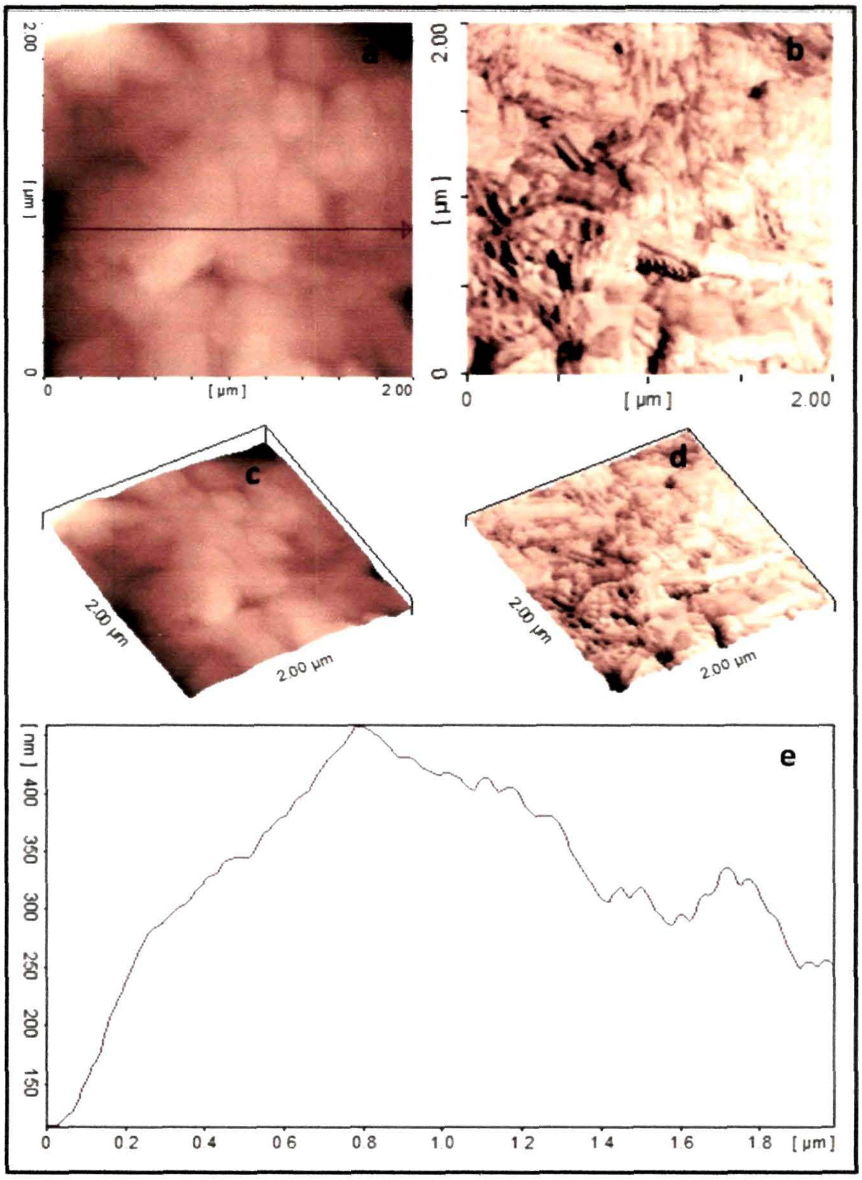

Figure 4.22. AFM tapping mode *2-D* topography (**a**) and phase (**b**) images of CuS(*THU*)/PANI nanocomposite. (**c**) and (**d**) are the corresponding *3-D* images of (**a**) and (**b**); and (**e**) is the typical height cross section image of (**a**).

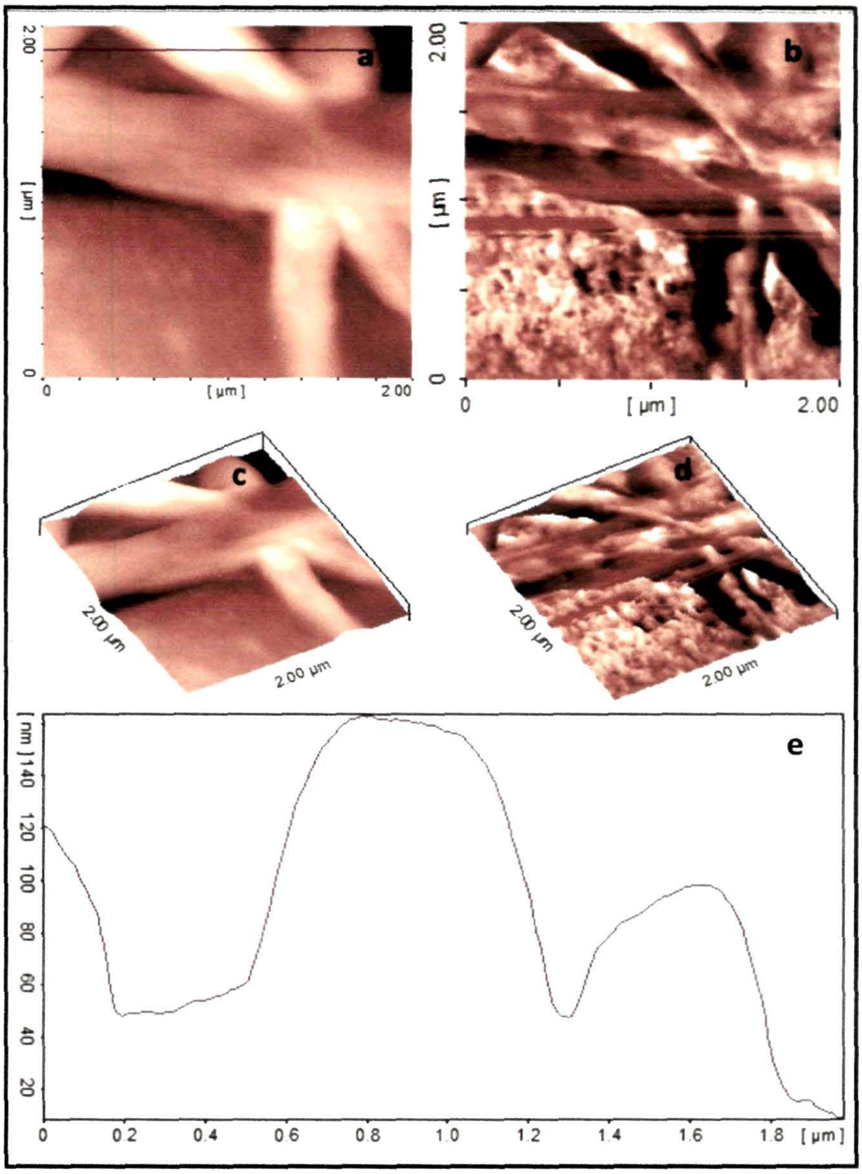

Figure 4.23. AFM tapping mode *2-D* topography (**a**) and phase (**b**) images of CuS(*STS*)/PANI nanocomposite. (**c**) and (**d**) are the corresponding *3-D* images of (**a**) and (**b**); and (**e**) is the typical height cross section image of (**a**).

4.3.3. Optical properties of CuS nanoparticles and CuS/PANI nanocomposites

Figures 4.24 and 4.25 present the UV-vis absorption spectra of the two CuS nanoparticles synthesised with THU and STS as sulphur source using **Procedure I** and **Procedure II**, respectively. Even though copper sulphide has the ability to form various stoichiometric products including covellite (CuS), anilite (Cu_7S_4), chalcocite (Cu_2S), djurleite ($Cu_{1.95}S$) each phase has its distinct optical absorption spectrum. However, it is evident from the figures that both CuS show broad absorption peaks in the near-IR region that correspond to the pure covellite phase[17,37,38]. Absence of any peak at 450 nm in the UV-vis spectra corresponding to the Cu_2S phase[39] strongly supports the formation of purely green covellite.

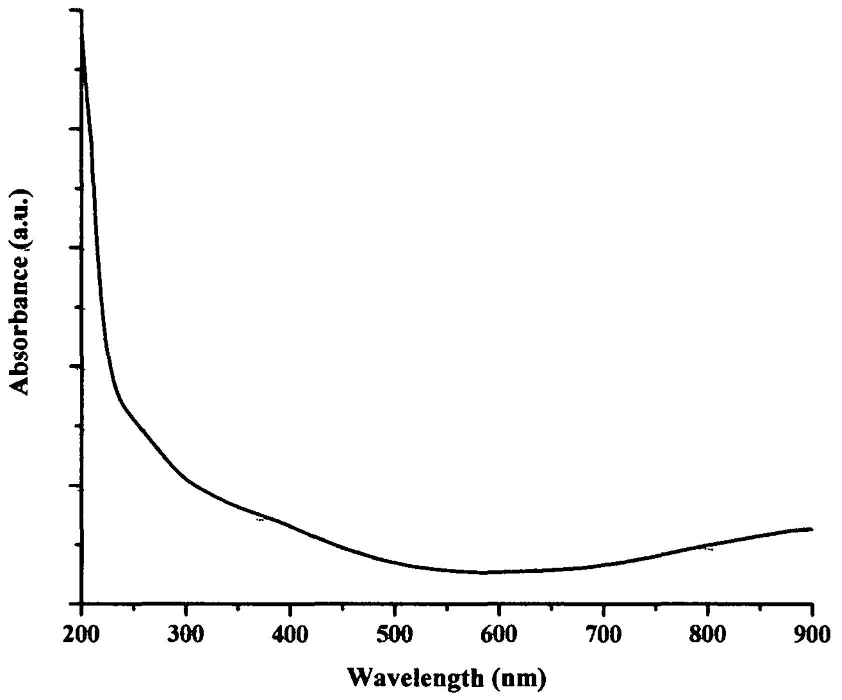

Figure 4.24. UV-vis absorption spectrum of CuS(*THU*) nanoparticles synthesised with **Procedure I**.

PL measurements also give important information about optical properties of nanoparticles. However, both CuS nanoparticles are unable to display any PL spectrum.

Jiang *et al.* also reported the absence of emission peak for CuS in the range of 400-800 nm[40], a result consistent with this study.

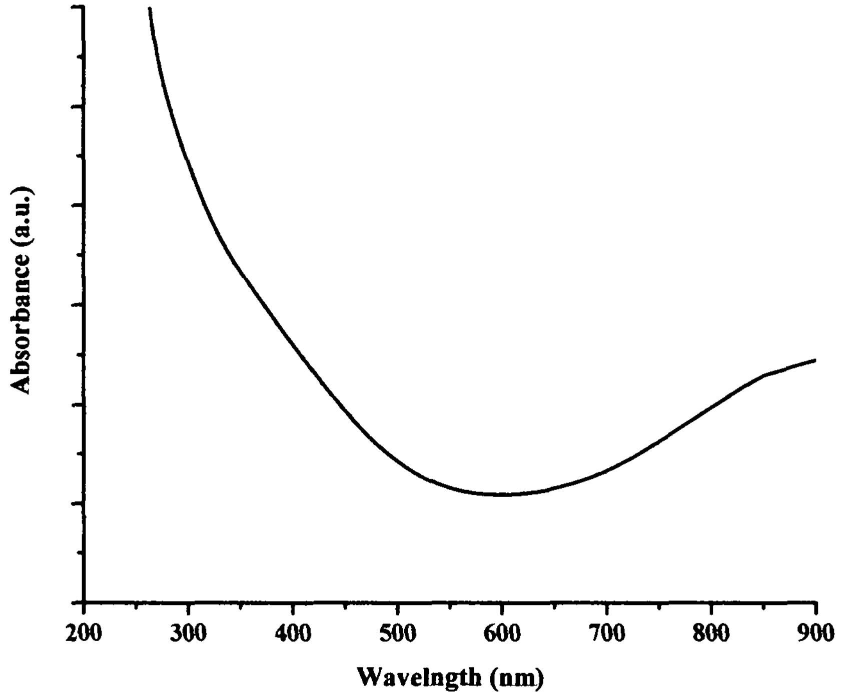

Figure 4.25. UV-vis absorption spectrum of CuS(*STS*) nanoparticles synthesised with **Procedure II**.

The UV-visible absorption and PL spectra of PANI and its composites with CuS(*THU*) and CuS(*STS*) nanoparticles were recorded in order to study the influence of nanoparticles on the optical properties of PANI. **Figure 4.26** shows the UV-vis absorption spectra of PANI and CuS/PANI nanocomposites. The absorption spectrum of pure PANI shows two distinct characteristics peaks at 340 and 635 nm. The absorption peak at 340 nm arises from the highest occupied molecular orbital (HOMO) and lowest unoccupied molecular orbital (LUMO) in the benzenoid rings. The peak at 635 nm is associated with a benzenoid to quinoid excitonic transition[41]. The absorption bands for CuS(*THU*)/PANI are found almost in the same positions of PANI; however, the band centred around 635 nm becomes broadened. In case of CuS(*STS*)/PANI, the bands are slightly shifted towards higher energies as compared to that of PANI. Such shift indicates minor reduction in conjugation.

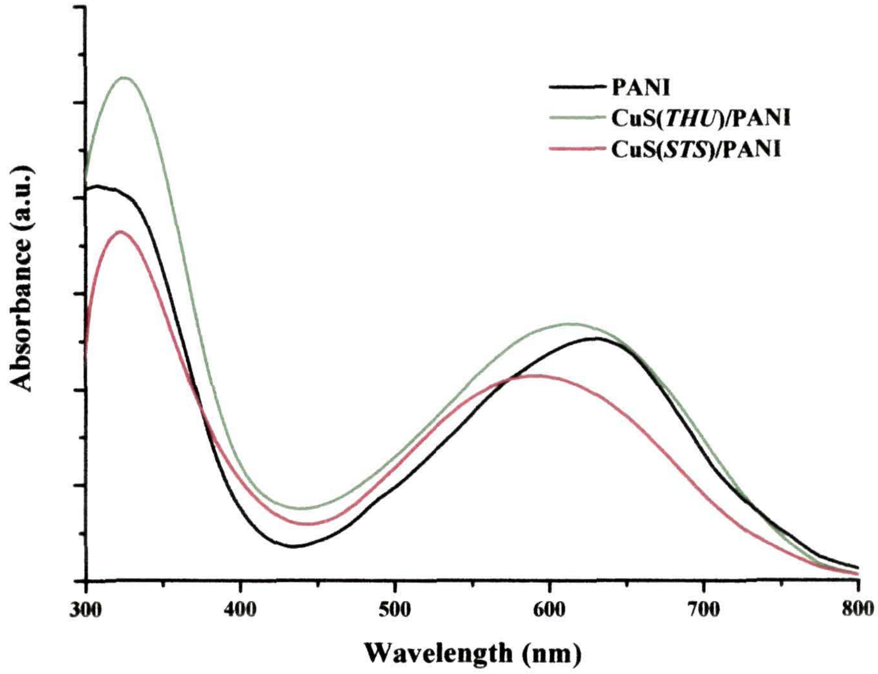

Figure 4.26. UV-visible absorption spectra of PANI, CuS(*THU*)/PANI and CuS(*STS*)/PANI.

Similar to CuS nanoparticles, their corresponding composites with PANI are also unable to display PL spectrum.

4.3.4. Electrical properties of CuS/PANI nanocomposites

The I-V characteristics of CuS/PANI nanocomposites at room temperature are shown in **Figure 4.27**. It is evident from the figure that the I-V characteristics are asymmetric and nonlinear for forward and reverse directions of applied voltage suggesting the semiconducting behavior and the formation of Schottky barrier in the nanocomposites[42]. Thus, the diode like I-V characteristic of the nanocomposites is due to the modification of the CuS nanoparticles with PANI and the formation of nanosize grains.

Variation of DC conductivities of PANI and CuS/PANI nanocomposites with respect to temperature has been studied over a temperature range of 30-100 °C. The data compiled in **Table 4.5** reveals that both CuS(*THU*)/PANI and CuS(*STS*)/PANI nanocomposites show higher conductivities as compared to pure PANI at all temperatures. However, decrease in conductivities up to 50 °C and gradual increase afterwards was observed in both nanocomposites. The decrease in conductivities in the initial stage of heating is due to the loss of solvent and trapped HCl. On the other hand, increased interchain and intrachain hopping results in high charge carrier mobility within the composite leading to increase in conductivities. Besides, the conductivities of CuS(*THU*)/PANI is higher than that of CuS(*STS*)/PANI. The interaction of different shape and size of CuS nanoparticles (as discussed in ***Sections 4.3.1.1.4 and 4.3.1.2.4***) with PANI results this kind of behaviour. The highest DC conductivity of

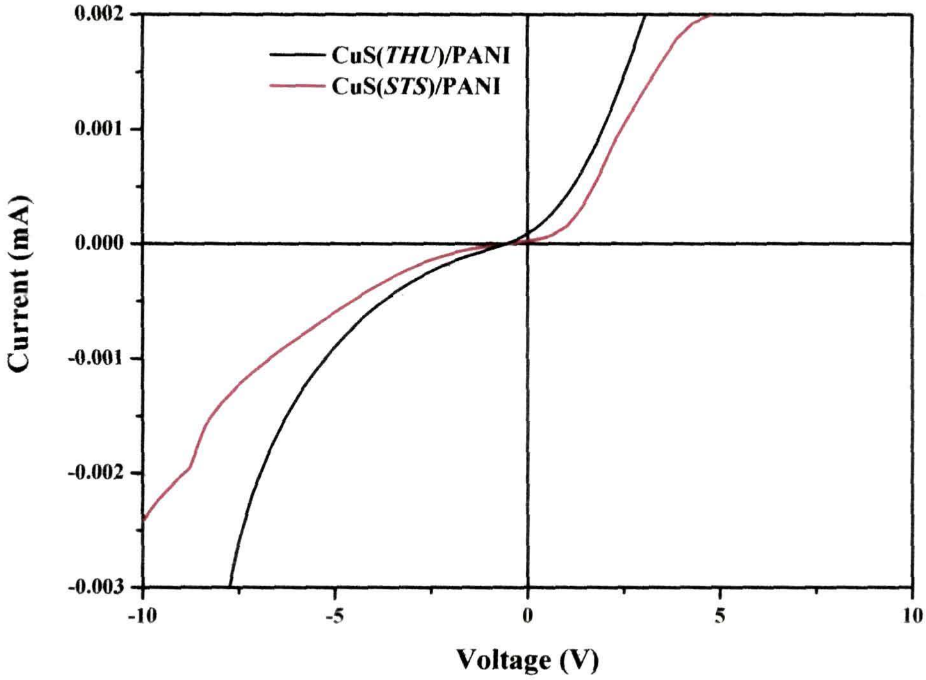

Figure 4.27. I-V characteristic curves of CuS/PANI nanocomposites at room temperature.

CuS(*THU*)/PANI and CuS(*STS*)/PANI were observed at 100 °C and found to be 0.520 S/cm and 0.496 S/cm, respectively (**Table 4.5**).

Table 4.5. DC electrical conductivities of pure PANI and CuS/PANI nanocomposites at different temperatures

Temperature (°C)	**Conductivity (S/cm)**		
	PANI	**CuS(*THU*)/PANI**	**CuS(*STS*)/PANI**
30	0.044	0.357	0.301
50	0.042	0.238	0.230
70	0.044	0.430	0.398
90	0.046	0.437	0.434
100	0.046	0.520	0.496

4.4. Conclusions

The important conclusions drawn from the above study are compiled below:

- Nanosized CuS were synthesized following two different approaches. In one approach, near spherical CuS nanoparticles have been prepared *via* a simple colloidal synthesis route, employing CuAc and THU as copper and sulphur sources, respectively. The CuS dispersion with CuAc: THU molar ratio of 1: 2 and 0.2 g SDS gives the lowest particle size (76 ± 1 nm) and is found stable for 210 days.
- Further study shows that, CuAc: THU molar ratio greatly influences the conversion of golden brown copper sulphide sol to green covellite.
- In the second approach, spherical shaped CuS nanoparticles have been obtained using CuAc and STS as copper and sulphur sources, respectively, in the presence MPA. The average particle size obtained from TEM is 4 ± 1 nm. The second method is advantageous in terms of simplicity and time effective.

- Both types of CuS nanoparticles have been found to be in hexagonal CuS phase. The formation of the covellite CuS phase appears to be concurrent with the development of strong absorption band in the near-IR region of UV-vis absorption spectra.
- These two types of CuS nanoparticles were used in the synthesis of CuS/PANI nanocomposites by *in-situ* polymerization technique. FTIR and XPS results confirm significant interaction of PANI with CuS in the two nanocomposites. Comparison of the thermal properties of pure PANI and the nanocomposites show that the thermal stability of the polymer is improved in the composites.
- Two distinct morphologies of worm-like and shuttle-like are observed for nanocomposites CuS(*THU*)/PANI and CuS(*STS*)/PANI, respectively.
- In both the nanocomposites, the absorption bands of PANI are blue-shifted indicating reduction in conjugation. Both nanoparticles and their corresponding composites do not display photoluminescence property.
- I-V characteristic CuS/PANI nanocomposites suggest semiconducting behaviour and the formation of Schottky barrier in the nanocomposites.
- The electrical conductivity of CuS(*THU*)/PANI nanocomposite is 0.520 S/cm at 100 °C, almost eleven and two times higher than that of pure PANI and CuS(*STS*)/PANI.

References

1. Hicks, J. F.; Miles, D. T.; Murray, R. W. Quantized double-layer charging of highly monodisperse metal nanoparticles, *J. Am. Chem. Soc.* **124**, 13322-13328 (2002)
2. Stroyuk, A. L.; Kryukov, A. I.; Kuchmii S. Ya.; Pokhodenko, V. D. Quantum size effects in the photonics of semiconductor nanoparticles, *Theor. Exp. Chem.* **46**, 273-278 (2010)
3. Wang, Y.; Zhang, L.; Liang, C.; Wang, G.; Peng, X. Catalytic growth and photoluminescence properties of semiconductor single-crystal ZnS nanowires, *Chem. Phys. Lett.* **357**, 314-318 (2002)
4. Mallik, K.; Witcomb, M. J.; Scurrell, M. S. Redox catalytic property of gold nanoclusters: evidence of an electron relay effect, *Appl. Phys. A* **80**, 797-801 (2005)
5. Liz-Marz'an, L. M. Tailoring surface plasmons through the morphology and assembly of metal nanoparticles, *Langmuir* **22**, 32-4 (2006)
6. Kamat, P. V. Photophysical, photochemical and photocatalytic aspects of metal nanoparticles, *J. Phys. Chem. B* **106**, 7729-7744 (2002)
7. Yang, Y. J.; Xiang, J. W. Template-free synthesis of CuS nanorods with a simple aqueous reaction at ambient conditions, *Appl. Phys. A* **81**, 1351-1353 (2005)
8. Wang, H.; Zhang, J. R.; Zhao, X. N.; Xu, S.; Zhu, J. J. Preparation of copper monosulphide and nickel monosulphide nanoparticles by sonochemical method, *Mater. Lett.* **55**, 253-258 (2002)
9. Parkin, I. P. Solid state metathesis reaction for metal borides, silicides, pnictides and chalcogenides: ionic or elemental pathways, *Chem. Soc. Rev.* **25**, 199-207 (1996)
10. Nascu, C.; Pop, I.; Ionescu, V.; Indrea, E.; Bratu, I. Spray pyrolysis deposition of CuS thin films, *Mater. Lett.* **32**, 73-77 (1997)
11. Talapin, D. V.; Regach, A. L.; Kornowski, A.; Hasse, M.; Weller, H. Highly luminescent monodisperse CdSe and CdSe/ZnS nanocrystals synthesized in a

hexadecylamine-trioctylphosphine oxide-trioctylphospine mixture, *Nano Lett.* **1**, 207-211 (2001)

12. Wang, S.; Yang, S. Surfactant-assisted growth of crystalline copper sulphide nanowire arrays, *Chem. Phys. Lett.* **322**, 567-571 (2000)
13. Dong, X.; Potter, D., Erkey, C. Synthesis of CuS nanoparticles in water-in-carbon dioxide microemulsions, *Ind. Eng. Chem. Res.* **41**, 4489-4493 (2002)
14. Pattrick, R. A. D. *et al.* The structure of amorphous copper sulphide precipitates: an X-ray absorption study, *Geochim. Cosmochim. Acta* **61**, 2023-2036 (1997)
15. Rong, M.; Zhang, M.; Liu, H.; Zeng, H. Synthesis of silver nanoparticles and their self-organization behavior in epoxy resin, *Polymer* **40**, 6169-6178 (1999)
16. Gautam, U. K.; Mukherjee, B. A simple synthesis and characterization of CuS nanocrystals, *Bull. Mater. Sci.* **29**, 1-5 (2006)
17. Lu, Q.; Gao, F.; Zhao, D. The assembly of semiconductor sulphide nanocrystallites with organic reagents as templates, *Nanotechnology* **13**, 741-745 (2002)
18. Afzal, A. B.; Akhtar, M. J.; Nadeem, M.; Hassan, M. M. Investigation of structural and electrical properties of polyaniline/gold nanocomposites, *J. Phys. Chem. C* **113**, 17560-17565 (2009)
19. Gangopadhyay, R.; De, A. Polypyrrole-ferric oxide conducting nanocomposites I. Synthesis and characterization, *Eur. Polym. J.* **35**, 1985-1992 (1999)
20. Chandrakanthi, R. L. N.; Careem, M. A. Preparation and characterization of CdS and Cu_2S nanoparticle/polyaniline composite films, *Thin Solid Films* **417**, 51-56 (2002)
21. Silvester, E. J.; Grieser, F.; Sexton, B. A.; Healy, T. W. Spectroscopic studies on copper sulphide sols, *Langmuir* 7(**12**), 2917-2922 (1991)
22. Liu, X. *et al.* Selected synthesis of CuS nanotubes and hollow nanospheres at room temperature, *J. Nanosci. Nanotechnol.* 7, 4501-4507 (2007)

23. Bott, R. C.; Bowmaker, G. A.; Devis, C. A.; Hope, G. A.; Jones, B. E. Crystal structure of $[Cu_4(tu)_7](SO_4)_2].H_2O$ and vibrational spectroscopic studies of some copper(I) thiourea complexes, *Inorg. Chem.* **37**, 651-657 (1998)

24. Bombicz, P.; Mutikainen, I.; Krunks, M.; Leskela, T.; Madarász J.; Niinisto, L. Synthesis, vibrational spectra and X-ray structures of copper(I) thiourea complexes, *Inorg. Chim. Acta* **357**, 513-525 (2004)

25. Qin, A. M.; Fang, Y. P.; Ou, H. D.; Liu, H. Q.; Su, C. Y. Formation of various morphologies of covellite copper sulphide submicron crystals by a hydrothermal method without surfactant, *Cryst. Growth Des.* **5**, 855-860 (2005)

26. Poleunis, C.; Weng, L. T.; Sclavons, M.; Bertrand, P.; Franquinet, P.; Legras, R.; Carlier, V. Sizing removal and functionalization of carbon fiber surface studied by combined TOF SIMS and XPS, *J. Adhes. Sci. Technol.* **9**, 859-871 (1995)

27. Niu, H.; Gao, M. Diameter-tunable CdTe nanotubes template by 1D nanowires of cadmium thiolate polymer, *Angew. Chem., Int. Ed.* **45**, 6462-6466 (2006)

28. Karatchevtseva, I.; Zhang, Z. M.; Hanna, J.; Luca, V. Electrosynthesis of macroporous polyaniline-V_2O_5 nanocomposites and their unusual magnetic properties, *Chem. Mater.* **18**, 4908-4916 (2006)

29. Angelopoulos, M.; Ray, A.; MacDiarmid, A. G.; Epstein, A. J. Polyaniline: processability from aqueous solutions and effect of water vapor on conductivity, *Synth. Met.* **21**, 21-30 (1987)

30. Feng, W.; Sun, E.; Fujii, A.; Wu, H.; Nihara, K.; Yoshina, K. Synthesis and characterization of photoconducting polyaniline- TiO_2 nanocomposite, *Bull. Chem. Soc. Jpn.* **72**, 2627-2633 (2000)

31. Yavuz, Ö.; Ram, M. K.; Aldissi, M.; Poddar, P.; Hariharan, S. Synthesis and the physical properties of MnZn ferrite and NiMnZn ferrite- polyaniline nanocomposite particles, *J. Mater. Chem.* **15**, 810-817 (2005)

32. Siegfried, M. J.; Choi, K. S. Electrochemical crystallization of cuprous oxide with systematic shape evolution, *Adv. Mater.* **16**, 1743-1746 (2004)

33. Jing, S.; Xing, S.; Yu, L.; Wu, Y.; Zhao, C. Synthesis and characterization of Ag/polyaniline core-shell nanocomposites based on silver nanoparticles colloid, *Mater. Lett.* **61**, 2794-2797 (2007)
34. Li, J.; Tang, S. B.; Lu, L.; Zeng, H. C. Preparation of nanocomposites of metals, metal oxides, and carbon nanotubes vis self-assembly, *J. Am. Chem. Soc.* **129**, 9401-9409 (2007)
35. Konwer, S.; Pokhrel, B.; Dolui, S. K. Synthesis and characterization of polyaniline/graphite composites and study of their electrical and electrochemical properties, *J. Appl. Polym. Sci.* **116**, 1138-1145 (2010)
36. Kim, B. J.; Oh, S. G.; Han, M. G.; Im, S. S. Synthesis and characterization of polyaniline nanoparticles in SDS micellar solutions, *Synth. Met.* **122**, 297-304 (2001)
37. Ni, Y. *et al.* Self-assembly of CuS nanoparticles to solid, hollow, spherical and tubular structures in a simple aqueous-phase reaction, *Apply. Phys. A* **79**, 2007-2011 (2004)
38. Yumashev, K. V. *et al.* Optical transient bleaching and induced absorption of surface-modified copper sulphide nanocrystals, *Appl. Phys. B* **64**, 73-78 (1996)
39. Haram, S. K.; Mahadeshwar, A. R.; Dixit, S. G. Synthesis and characterization of copper sulphide nanoparticles in triton-X 100 water-in-oil microemulsions, *J. Phys. Chem.* **100**, 5868-5873 (1996)
40. Jiang, X. C.; Xie, Y.; Lu, J.; He, W.; Zhu, L. Y.; Qian, Y. T. Preparation and phase transformation of nanocrystalline copper sulphides (Cu_9S_8, Cu_7S_4 and CuS) at low temperature, *J. Mater. Chem.* **10**, 2193-2196 (2000)
41. Lu, X.; Gao, H.; Chen, J.; Chao, D.; Zhang, W.; Wei, Y. Poly(acrylic acid)-guided synthesis of helical polyaniline/CdS composite microwires, *Nanotechnology* **16**, 113-117 (2005)
42. Dey, A.; De, S.; De, A.; De, S. K. Characterization and dielectric properties of polyaniline-TiO_2 nanocomposites, *Nanotechnology* 15, 1277-1283 (2004)

5.1. Conclusions

The combination of inorganic nanoparticles with polymers offers an attractive route to reinforce the polymers as well as to introduce properties of individual components with a synergistic effect. Conducting polymer based nanocomposites have emerged as an area of intense research because of potential applications in diverse fields including electronics, non-linear optics, catalysis, and magnetic and so on. Among conducting polymers, PANI occupies a separate chair because of ease of preparation and processability.

The goal of this thesis is to develop simple synthesis paths to obtain metal and semiconductor nanoparticles, and utilization of synthesized nanoparticles for nanocomposites preparation with PANI to study the influence of nanoparticles on the morphology, optical and electrical properties of the polymer.

The important findings of the thesis are summarised chapter wise below:

Chapter 2: Synthesis of copper (Cu) and nickel (Ni) nanoparticles and their interaction with polyaniline (PANI)

- A one-step synthesis procedure has been achieved successfully for synthesis of stable colloidal dispersion of Cu and Ni nanoparticles. TA, a green reagent is used as reducing as well as capping agent. It has been observed that particle size and morphology of metal nanostructures could be controlled by varying TA concentrations. Growth mechanism based on oriented attachment and Ostwald ripening is proposed. This method opens a new way for shape- and size- controlled synthesis of other metallic nanoparticles.
- XRD analysis reveals face-centred-cubic (fcc) structure for both Cu and Ni naoparticles. Average particle sizes calculated by Scherrer formula are 8.7 ± 1 nm and 5.1 ± 1 nm, respectively, for Cu and Ni nanoparticles synthesized with 0.04 M TA.
- FTIR analysis reveals that TA adheres to the metal nanoparticles and hence, offers stability to the naoparticles. This capping role of TA is further supported by XPS study.

- Weight loss characteristic studied by TGA reveals that less than 8% Cu and 5% Ni nanoparticles synthesized with 0.04 M TA remain in the samples at 800 °C.
- Wire-like, flower-like and cluster-like morphologies are observed for Cu nanostructures synthesized with 0.02, 0.04 and 0.06 M TA, respectively. This implies structure-directing nature of TA.
- PANI and its metal-based nanocomposites of different morphologies have been synthesized utilizing the synthesized metal nanostructures by *in-situ* polymerization technique. FTIR and XPS results indicate sufficient interaction of metal nanoparticles with PANI. From TGA data, it has been found that the thermal stability of bare polymer is enhanced after interaction with metal nanoparticles.
- UV-vis absorption study reveals the absence of surface plasmon resonance band in Cu nanoparticles because of smaller particles and the presence of high conformational surface ordering of TA on the surface of Cu nanoparticles. These Cu nanoparticles are photoluminescent and emit in green light region. In case of all nanocomposites, the PL maximum of Cu nanoparticles is red-shifted.
- For Ni nanoparticles, broad and weak surface plasmon resonance bands are observed in the UV-vis spectra. The two characteristics peaks of PANI at 340 and 635 nm remain unchanged after interaction with Ni nanoparticles. All Ni nanoparticles and their corresponding composites with PANI do not exhibit any photoluminescence property.
- The I-V characteristics of metal and PANI based nanocomposites are asymmetric and nonlinear for forward and reverse directions of applied voltage suggesting the semiconducting behavior and the formation of Schottky barrier in the nanocomposites.

- The temperature dependent DC conductivities of Cu/PANI nanocomposites are found to be significantly higher than that of pure PANI. On the other hand, decrease in conductivity up to 70 °C with respect to bare PANI are observed in case of Ni/PANI composites. However, after rising temperature, the conductivity of the Ni/PANI composites increases as compared to pure PANI.

Chapter 3: Synthesis of cadmium sulphide (CdS) nanoparticles and their interaction with polyaniline (PANI)

- CdS nanoparticles have been successfully synthesized using CdAc, STS and MPA in three different CdAc: STS: MPA proportionate ratios following a simple colloidal dispersion synthetic route.
- XRD patterns indicate the formation of cubic CdS nanoparticles irrespective of the precursor molar ratios used in the synthesis. CdS nanoparticles synthesized with CdAc: STS: MPA molar ratio of 1: 1: 6 give smaller nanoparticles of average particle size 4.1 ± 1 nm.
- Formation of CdS nanoparticles was confirmed by XPS analysis and further quantification of Cd and S peak areas gives the Cd: S atomic ratio as 1: 0.98 that is almost consistent with the stoichiometry of CdS.
- Morphology (SEM, TEM and AFM) studies reveal well ordered near spherical-shape, cube-shape and nanocubes in bunch of flower-like clusters of CdS nanoparticles synthesized with CdAc: STS: MPA molar ratio of 1: 1: 6 (CdS-1), 1: 2: 2 (CdS-2) and 1: 3: 4, (CdS-3), :respectively.
- All three CdS samples were utilised in the synthesis of PANI based nanocomposites via *in-situ* polymerization technique.
- XRD reveals the presence of CdS and PANI in the nanocomposites. However, some changes in peak positions from the original CdS and PANI diffraction peaks are observed.
- FTIR and XPS reveal the interaction of CdS with PANI matrix.

- The thermal property of PANI was improved in the presence of CdS nanoparticles as revealed from TGA analysis.
- SEM, TEM and AFM images reveal bee-hive-like, spike-paddy-like and raspberry-like morphologies for CdS-1/PANI, CdS-2/PANI and CdS-3/PANI, respectively.
- The UV-vis absorption bands for CdS nanoparticles are all blue-shifted with respect to bulk CdS. In CdS/PANI nanocomposites, bands are also blue-shifted with respect to PANI suggesting decrease in conjugation in composites.
- Both CdS nanoparticles and their corresponding PANI composites are photoluninescent.
- The I-V characteristic curves are asymmetric and nonlinear for forward and reverse directions of applied voltage for all CdS/PANI nanocomposites. This suggests semiconducting behavior and the formation of Schottky barrier in the nanocomposites.
- Among all the CdS/PANI nanocomposites, CdS-2/PANI nanocomposite possesses highest DC electrical conductivity value of 6.60 S/cm at room temperature.

Chapter 4: Synthesis of copper sulphide (CuS) nanoparticles and their interaction with polyaniline (PANI)

- Nanosized CuS were synthesized following two different approaches. In one approach, near spherical CuS nanoparticles have been prepared *via* a simple colloidal synthesis route, employing CuAc and THU as copper and sulphur sources, respectively. The CuS dispersion with CuAc: THU molar ratio of 1: 2 and 0.2 g SDS gives the lowest particle size (76 ± 1 nm) and is found stable for 210 days.
- Further study shows that, CuAc: THU molar ratio greatly influences the conversion of golden brown copper sulphide sol to green covellite.

- In the second approach, spherical shaped CuS nanoparticles have been obtained using CuAc and STS as copper and sulphur sources, respectively, in the presence MPA. The average particle size obtained from TEM is 4 ± 1 nm. The second method is advantageous in terms of simplicity and time effective.
- Both types of CuS nanoparticles have been found to be in hexagonal CuS phase. The formation of the covellite CuS phase appears to be concurrent with the development of strong absorption band in the near-IR region of UV-vis absorption spectra.
- These two types of CuS nanoparticles were used in the synthesis of CuS/PANI nanocomposites by *in-situ* polymerization technique. FTIR and XPS results confirm significant interaction of PANI with CuS in the two nanocomposites. Comparison of the thermal properties of pure PANI and the nanocomposites show that the thermal stability of the polymer is improved in the composites.
- Two distinct morphologies of worm-like and shuttle-like are observed for nanocomposites CuS(*THU*)/PANI and CuS(*STS*)/PANI, respectively.
- In both the nanocomposites, the absorption bands of PANI are blue-shifted indicating reduction in conjugation. Both nanoparticles and their corresponding composites do not display photoluminescence property.
- I-V characteristic CuS/PANI nanocomposites suggest semiconducting behaviour and the formation of Schottky barrier in the nanocomposites.
- The electrical conductivity of CuS(*THU*)/PANI nanocomposite is 0.520 S/cm at 100 °C, almost eleven and two times higher than that of pure PANI and CuS(*STS*)/PANI.

Comparative study

The principal focus of the thesis is to study the interaction of nanoparticles with PANI, one of the most studied conducting polymers to gather knowledge whether the property of the existing polymer can be improved or not. Based on the previous chapters, a comparative study is put forwarded.

- ***Effect of nanoparticles on the morphology of PANI*:**
  - Morphologiy of pure PANI can be tailored to various nanostructures such as cypress-leaf-like, raspberry-like, bee-hives like, etc. by interacting with metal or semiconductor nanoparticles of different shape and size.
- ***Effect of nanoparticles on the PL property of PANI*:**
  - Nanocomposites of Cu/PANI and CdS/PANI only exhibit photoluminescence properties.
- ***Effect of nanoparticles on the DC conductivity of PANI*:**
  - DC conductivity of PANI can be enhanced by interacting with metal or semiconductor nanoparticles.
  - CdS nanoparticles synthesized with CdAc: STS: MPA molar ratio of 1: 2: 2 gives highest DC conductivity after interaction with PANI.
  - Though enhancement of DC conductivity is observed in metal/PANI and semiconductor/PANI nanocomposites, yet the results are not upto the expectations due to the effect of capping agent associated with the nanoparticles, which could have interrupted conductivity.

5.2. Future prospects

- Theoretical study of band gap calculation for Cu, Ni, CdS and CuS nanoparticles.
- Utilization of synthesized PANI-based nanocomposites for sensor; light emitting diode applications.
- Anti-microbial property study of Cu and Cu/PANI nanocomposites.
- Magnetic property study of Ni nanoparticles and their corresponding composites.
- Scope for the improvement in the optical and electrical properties of nanocomposites.

List of Publications

Papers in Journals

1. **Dutta, A.**; Dolui, S. K. Preparation of colloidal dispersion of CuS nanoparticles stabilized by SDS, *Mater. Chem. Phys.*, **112**, 448-452 (2008)
2. **Dutta, A.**; Dolui, S. K. Tannic acid assisted one step synthesis route for stable colloidal dispersion of nickel nanostructures, *Appl. Surf. Sci.* (*Article in press*)
3. Pokhrel, B.; Knower, S.; **Dutta, A.**; Huda, M. K.; Ghosh, B.; Dolui, S. K. "Study of photovoltaic performance of host-guest system comprising optically active polyurethane and Rhodamine B dye", *J. Appl. Polym. Sci.* (*Revision submitted*)
4. **Dutta, A.**; Dolui, S. K. Biomolecule mediated synthesis of copper nanostructures, *J. Nanopart. Res.* (*Under review*)
5. **Dutta, A.**; Konwer, S.; Pokhrel, B.; Huda, M. K.; Kalita, A.; Dolui, S. K. Optical and electrical behaviour of Cu/PANI nanocomposite, *Synth. Met*, (*Under review*)
6. **Dutta, A.**; Huda, M. K.; Kamrupi, I. R.; Borthakur, L. J.; Dolui, S. K. Ni/PANI nanocomposites: synthesis, characterizations and their optical and electrical behaviour, *Mater. Lett.* (*Under review*)
7. Kamrupi, I. R.; **Dutta, A.**; Pokhrel, B.; Huda, M. K.; Konwer S.; Kalita, A.; Dolui, S. K. Synthesis of macroporous polymer particles by emulsion polymerization in sc-CO_2 medium, *Polymer Bulletin* (*Communicated*)
8. **Dutta, A.**; Dolui, S. K. CuS/PANI nanocomposites: synthesis, characterization, and their optical and electrical properties, *J. Phys. Chem. C* (*Communicated*)
9. **Dutta, A.**; Dolui, S. K. Effect of reaction parameter from *3-D* CdS to *1-D* CdS and their optical property evaluation, *Appl. Surf. Sci.* (*Communicated*)
10. Kamrupi, I. R.; Pokhrel, B.; **Dutta, A.**; Huda, M. K.; Konwer, S.; Kalita, A.; Boruah, M.; Dolui, S. K. "Synthesis of macroporous polymer particles by suspension polymerization using supercritical carbon dioxide as a pressure adjustable porogen" *Polym. Bull.* (*Communicated*)
11. **Dutta, A**; Dolui, S. K. Electrical and optical properties evaluation of cadmium sulphide/polyaniline nanocomposites, *Mater. Chem. & Phys.* (*Communicated*)

Presentation in Conferences

1. **Dutta, A.**; Dolui, S. K. Synthesis and stabilization of CdS nanoparticles in colloidal dispersion, Inetrnational Seminar on Frontier in Polymer Science and Technology (POLY-2007) Guwahati, Assam, India, November 1-3, **2007**.
2. **Dutta A.**, Konwer, S.; Dolui, S. K. Synthesis of PANI/CdS nanocomposites, structural characterization, optical and electrical properties, The International conference on nanomaterials, (ICN 2010), MG University, Kerela, India, April 27, **2010**.
3. **Dutta, A.**, Konwer, S. Dolui, S. K. Low temperature aqueous synthesis of hexagonal CdS/PANI composite and their optical and electrical properties, Pacifichem 2010 Conference, Hawaii, USA, December 15-20, **2010**.